

ROYAL HOLLOWAY
UNIVERSITY OF LONDON

DEPARTMENT OF PHYSICS

**Superfluid Optomechanics
with
Phononic Nanostructures**

IN PARTIAL FULFILMENT OF THE REQUIREMENTS FOR THE DEGREE
OF DOCTOR OF PHILOSOPHY

Thesis Author:

Sebastian SPENCE

sebtspence@gmail.com

PhD Supervisor:

Dr. Xavier ROJAS

xavier.rojas@rhul.ac.uk

11/07/2022

Abstract

In this work, a novel implementation of superfluid optomechanics is developed, exploiting nanofluidic confinement within a sonic crystal geometry. The aim of which is to enhance the optomechanical coupling strength while preserving the intrinsic properties of superfluid ^4He , via limitation of radiative acoustic effects. These nanostructures are designed and fabricated using cleanroom techniques, with focus on the development of a direct wafer bonding technique. The cleanroom fabricated chips are then integrated into superconducting microwave cavities. For measurements, a dilution refrigerator (capable of mK cooling) was refurbished for modern microwave measurements and work with superfluid ^4He . COMSOL Multiphysics simulations are used to design the optomechanical system, both the acoustics of the sonic crystal and the chip-cavity microwave environment. From these simulations a predicted vacuum optomechanical coupling is calculated giving $g_0/2\pi = 0.63$ mHz; between a superfluid mode of frequency 1.34 MHz, and a microwave cavity mode of 4.2 GHz. Phase sensitive homodyne measurements of the chip-cavity system in the presence of ^4He found mechanical signals close to the predicted resonance frequency, however these signals were insufficient in strength or consistency to determine the optomechanical parameters of the system.

Dedication


To all those who had patience with me, especially in my final year.

“There are more stars in the sky than atoms in the universe.”

—Unknown

Declaration

I Sebastian Spence hereby declare that this thesis and the work presented in it is entirely my own. Where I have consulted the work of others, this is always clearly stated.



Signature

Date: 16/03/2022

Acknowledgements

Firstly I would like to acknowledge my supervisor Xavier Rojas, without whom this project would not have been possible. I also express thanks to my internal and external examiners, Dr Andrew Casey and Professor Richard Haley, whose contributions have greatly improved this thesis. I would also like to acknowledge Professor Vladimir Antonov, the independent chair for my viva examination. I am grateful to my PhD advisor and moderator, Professor John Saunders and Dr Tracey Berry, for their support, especially during the more trying periods.

The final experimental runs would not have been productive without the timely intercession of Angadjit Singh, with his assistance to quickly adapt nanofabrication to silicon wafers; and Sumit Kumar, with his assistance on automating and networking our microwave equipment. I express gratitude to you both, and also to Rais Shaikhaidarov who gave us access to SuperFab in our hour of need. For their less time sensitive but no less critical support (and expansive knowledge of all things cold), I would like to thank the members of the London Low Temperature Lab: Jan Nyeki, Lev Levitin, Petri Heikkinen, and Marijn Lucas. I would like to recognise the support of other PhDs at RHUL specifically: Stefanos Dimitriadis for all the discussions at Egham Services Club and for showing me the end was in sight, Jan Knapp for checking the pumps and letting me in when I forgot my card, and Nathan Eng who kept me somewhat sane between first and final submissions.

Almost all metalwork and woodwork necessary to get the experimental platform up and running was completed by the members of the RHUL machine shop: Ian Higgs, Paul Bamford and Richard Elsom; who have worked tirelessly on the seemingly endless pieces we required. I would also like to acknowledge other members of the Physics Department support staff: Ian Murray for chasing up orders and always being able to find those miscellaneous items I need at short notice, Harpal Sandhu for keeping the helium flowing,

Tom Crane for his extensive electronics knowledge, Andy Alway for chasing up estates, Tracy Webster and Carmela Froggatt for making sure I was paid each year (even though the Doctoral School tried their hardest not to), and Claire Porter for having the patience to chase up the various elements of RHUL admin, ensuring I could continue as a PostDoc in a timely manner. The cleanroom staff at London Centre for Nanotechnology have also provided great support and advice on fabrication, specifically Vijayalakshmi Krishnan and Steve Etienne.

I would be remiss if I did not recognize the patience and support of my friends, especially over the last year and a bit, where I have had to endlessly cancel on social events. Specifically I'd like to thank my old housemates: Chris, Tig, Ed and Rinn; who made lockdown somewhat bearable. Of course I would not have made it this far without the unconditional support of my parents and sister, I am thankful for everything you have given me, and the use of your 'summer house' (wendy house) when lockdown in London became too much. Finally, I must acknowledge the patience and tolerance of Abigail, who truly bore witness to the final six months of experiment running and thesis writing.

Contents

1	Background	17
1.1	Introduction	17
1.2	Cavity Optomechanics	19
1.2.1	Background	19
1.2.2	Optomechanical Coupling	22
1.2.3	Cooperativity and Quality Factor	27
1.3	Helium 4	29
1.3.1	Two-Fluid Model	30
1.3.2	Spectrum of Excitations	32
1.3.3	Sound Propagation	34
1.3.4	Intrinsic Acoustic Attenuation	38
1.3.5	Extrinsic Acoustic Attenuation	43
1.4	Superfluid Optomechanics	47
1.4.1	State of the Art	47
1.4.2	Electrostrictive Coupling	49
1.4.3	Estimated Coupling and Cooperativity	53
2	Optomechanical Scheme	55
2.1	Overview of Our System	55
2.2	Superconducting Cavities	59
2.2.1	Rectangular Cavity Modes	59
2.2.2	Cylindrical Cavity Modes	60
2.2.3	Re-entrant Cavities	61
2.2.4	Circuit Representations	62

2.2.5	Chip - Cavity Modes	65
2.2.6	Cavity Quality Factor	69
2.2.7	Cavity Internal Losses	70
2.3	Nanofluidic Confinement	75
2.3.1	Nanofluidic Helium-4	76
2.3.2	Sonic Crystal	79
2.3.3	Defect Mode	83
2.3.4	Radiative Loss	84
2.3.5	Boundary Condition Loss	89
2.3.6	Substrate Loss	92
2.3.7	Device Imperfections	96
2.3.8	Coupling Capacitor	98
3	Experimental Methods	102
3.1	Dilution Refrigerator	102
3.1.1	Functional Overview	102
3.1.2	Control Wiring	105
3.1.3	Measurement Thermalisation	107
3.1.4	Piezo Drive	112
3.1.5	Fill Line	114
3.1.6	Gas Handling System	117
3.2	Microwave Cavity Design	119
3.2.1	Cavity Resonance	120
3.2.2	External Coupling	126
3.2.3	Hermetic Feedthroughs	130
3.2.4	Indium Seals	132
3.2.5	Differential Thermal Contraction	135
3.3	Nanofabrication	137
3.3.1	Chip Design	137
3.3.2	Transparent Wafer Recipe	141

3.3.3	Silicon Wafer Recipe	142
3.3.4	Room Temperature Wafer Bonding	145
3.3.5	Samples	152
4	Microwave Measurement	158
4.1	Microwave Network Analysis	158
4.1.1	S Matrix	158
4.1.2	RLC Response	159
4.1.3	Capacitively Coupled Response	162
4.1.4	Cavity Photons	165
4.1.5	Real Circuit Response	169
4.2	Fridge Circuit	171
4.2.1	Overview	171
4.2.2	Photon Noise	173
4.2.3	Applied Powers	174
4.3	Cavity Transmission	175
4.3.1	Mechanical Modulation	178
4.3.2	Direct Measurement	182
4.4	Homodyne Detection	184
4.4.1	Principles of Lock-In Detection	184
4.4.2	Cavity Modulated Signal	188
4.4.3	Source Modulated Signal	191
4.4.4	Optomechanical Coupling Calibration	194
4.4.5	Cavity Phase Effect on Modulated Sideband	195
4.4.6	Determination of Delay	197
4.5	Summary	198
5	Experimental Results	200
5.1	Overview	200
5.1.1	Expected Transmission Strength	202
5.2	Run 1	203

5.2.1	Instability and Noise	205
5.2.2	Homodyne	209
5.3	Run 2	212
5.3.1	Room Temperature Investigations	212
5.3.2	Cooling	214
5.4	Run 3	216
5.4.1	Cool and Fill	216
5.4.2	Microwave Power Dependence	219
5.4.3	Two-Level Systems	222
5.4.4	Homodyne	225
5.5	Run 4	228
5.6	Conclusion	228
5.6.1	Outlook	230
	Appendices	255
	A Experiment Cell Drawings	256
	B COMSOL Abstracted Q	265
	C Minor Fridge Alterations	272
	D Fridge Pumping Systems	273
	E Hermetic Pin Solder Recipe	276
	F Transparent Bonding Pictures	278

List of Figures

1.1	Simplified schematic of a Fabry-Perot optomechanical cavity.	20
1.2	A collage of other cavity optomechanical experiments.	21
1.3	The phase diagram for helium-4.	30
1.4	Graph showing the dispersion curve of superfluid ^4He	33
1.5	Fraction of the normal fluid density ρ_n , due to the phonon contribution ρ_n^{ph} and the roton contribution ρ_n^{rot} , as a function of temperature.	35
1.6	Three-phonon Beliaev-Landau process interaction diagrams.	39
1.7	Graph showing quality factor of an acoustic mode limited by three-phonon processes vs frequency of that mode $\Omega_q/2\pi$	41
1.8	Quality factor of an acoustic mode alternatively limited by three and four-phonon processes.	43
1.9	Quality factor of an acoustic mode alternatively limited by three-phonon processes and phonon- ^3He interactions.	46
2.1	Simplified schematic of inside the optomechanical cell.	56
2.2	Diagram of the pseudo 2D sonic crystal	57
2.3	Disassembled experimental cell and microwave cavity.	58
2.4	Left: Electric field norm of a rectangular cavity TE_{101} mode. Right: Magnetic field norm of a rectangular cavity TE_{101} mode.	60
2.5	Left: Electric field norm of a cylindrical cavity TE_{011} mode. Right: Magnetic field norm of a cylindrical cavity TE_{011} mode.	61
2.6	Left: 2D axisymmetric cross section showing the electric field norm of a cylindrical re-entrant cavity's fundamental mode. Right: Magnetic field norm of a cylindrical re-entrant cavity's fundamental mode.	62

2.7	A simple diagram of a parallel RLC circuit terminated with characteristic impedance Z_0	63
2.8	A simple diagram of a coaxial cable impedance Z_{coax} terminated in a capacitor of capacitance C_{cap} and connected to an outside line impedance Z_0	63
2.9	Top: diagram with labelled dimensions of a simple cylindrical re-entrant cavity. Bottom: A circuit diagram of a re-entrant cavity as an equivalent RLC circuit, terminated in characteristic impedance Z_0	64
2.10	RLC lumped element circuit diagram of the chip-cavity system, for the antenna coupling scheme.	66
2.11	Left: Electric field norm for the fundamental mode of the chip-cavity system. Right: Magnetic field norm for the fundamental mode of the chip-cavity system.	67
2.12	Left: Electric field norm for the second mode of the chip-cavity system. Right: Magnetic field norm for the second mode of the chip-cavity system.	68
2.13	Left: Electric field norm for the third mode of the chip-cavity system. Right: Magnetic field norm for the third mode of the chip-cavity system.	69
2.14	The magnetic field magnitude around the on chip wire taper.	73
2.15	A simple acoustic waveguide.	78
2.16	The 2D sonic crystal unit cell.	80
2.17	(a) The phononic band structure of a superfluid ^4He sonic crystal. (b) the reciprocal lattice with its unit cell.	81
2.18	Low frequency phononic band structure around first bandgap.	82
2.19	Mode shape of the $\Omega_m = 1.34$ MHz fundamental point defect acoustic mode.	83
2.20	Pressure field inside the sonic crystal as a function of distance from the central point defect.	84
2.21	Quality factor Q_m^{rad} of the point defect fundamental mode when limited by radiative losses, vs the size of the sonic crystal lattice N ($N \times N$).	86
2.22	A 17×17 2D sonic crystal unit cell, with ^4He acoustic mode shape function, for the 1.34 MHz fundamental acoustic mode.	87

2.23	Quarter view of a 3D FEM simulation of 1.34 MHz modeshape travelling down a rectangular acoustic waveguide.	90
2.24	Sliced view close to the defect, of the 1.34 MHz fundamental mode, from a 3D FEM sonic crystal simulation.	92
2.25	The acoustic mode shape function of the fundamental point defect mode, as disturbed by a $\sim 1\%$ random deviation in pillar radius.	98
2.26	The pressure field contours of the fundamental defect mode.	99
2.27	The acoustic mode shape function of the fundamental point defect mode, as disturbed by the central electrodes and their wires.	100
2.28	An acoustic mode shape function within a single unit cell of a continuous sonic crystal, as disturbed by an additional channel at the x boundaries.	101
3.1	Photo of dilutions fridge's plates.	104
3.2	Control wiring for fridge showing both thermometers and heaters.	106
3.3	Resistance vs temperature graph for the mixing chamber thermometer.	107
3.4	Figure showing the floating braid thermalisation for attenuators.	108
3.5	Figure showing the floating braid thermalisation for coaxial cables themselves.	108
3.6	Lumped element circuit diagram of the piezo impedance check measurement circuit.	114
3.7	Top: The 1.650 MHz piezoelectric buzzer's frequency dependent impedance. Bottom: The 1.650 MHz piezo's approximate frequency dependent capacitance.	115
3.8	Photo of the front of ^4He fill line gas handling system.	118
3.9	Top: Comparison of fundamental chip-cavity mode frequency for the three different chips, as they vary with the gap between the electrodes. Bottom: Comparison of mode frequency fractional detuning from the 150 nm gap value, for the first three modes of the chip-cavity system.	123
3.10	Photo of the two aluminium cavity pieces (pre polishing).	124

3.11	Left: a silicon chip, which has had both ends with contact pads covered in layers of 50 μm thick indium foil, and has then had one end inserted into the slot of the aluminium microwave cavity base. Right: the lid of the closed aluminium cavity, with the slot that the other end of the silicon chip will protrude into.	125
3.12	Image of the full microwave cavity system built within COMSOL.	127
3.13	$\log_{10}(Q_e)$ vs the depth of the coupling pin into the cavity.	129
3.14	Left: Photo of the initial hermetic seal design on an older brass cavity lid. Right: Photo of the new hermetic feedthrough design on a new copper cavity lid.	131
3.15	Figure of two indium seal methods used.	133
3.16	Photo of the aluminium cavity clamped to the copper cell lid.	136
3.17	GDS image of the three layers, to be inverted for production of the three photomasks.	139
3.18	Diagram of the steps of the nano fabrication process.	143
3.19	Left: Camera photo of a bonded transparent chip. Right: Microscope image of the pillar region of a bonded chip.	149
3.20	The silicon wafer bonding setup at SuperFab RHUL.	151
3.21	IR USB microscope images of bonded chips, showing fringes.	152
3.22	Left: A photo of the Q4(A2) chip. Right: False coloured microscope image of the same chip.	153
3.23	Left: A photo of the Q4(A5) chip. Right: False coloured microscope image of the same chip.	154
3.24	Left: FESEM image of the central point defect of diced but not bonded chip. Right: FESM image of a pillar edge.	155
3.25	IR USB microscope images of the Si2(5) chip.	156
3.26	IR USB microscope images of the Si2(5) chip.	156
4.1	Figure showing parallel RLC representation of microwave circuit, set in a two port network with port impedances Z_0	159

4.2	The Thevenin - Norton source transformation for capacitive coupling to an RLC resonator.	163
4.3	Figure showing microwave circuit inside the dilution fridge.	172
4.4	RLC circuit representation of the chip-cavity system, including the capacitive pin coupling.	176
4.5	Diagram of microwave interferometer circuit used.	187
5.1	Photo of the experimental cell attached to the experimental stage of the dilution fridge.	204
5.2	Left: S_{21} logmag and phase detuned around the 4.24 GHz fundamental microwave mode, at 30 mK under vacuum. Right: S_{21} logmag and phase detuned around the 4.21 GHz fundamental microwave mode, at 34 mK and filled with ^4He pressurised to ~ 250 mbar.	205
5.3	Power transmission through the cavity vs time, showing a severe level of noise not expected for the system.	206
5.4	FFT spectrum of a time domain spectrum analyser measurement at the carrier frequency.	207
5.5	S_{21} transmission spectrum on the 4 - 12 GHz operational range of the microwave circuit.	208
5.6	'Best' homodyne measurement of mechanical signal, signal amplitude vs lock-in and piezo frequency.	210
5.7	Individual homodyne measurements.	211
5.8	Transmission spectrum through the empty aluminium cavity, with and without additional tightening	213
5.9	Room temperature phase noise measurements.	214
5.10	S_{21} VNA transmission measurement at 189 mK, during single shot operation of the fridge.	215
5.11	Photo of the experimental stage of the dilution fridge, showing the experimental cell wrapped in lead foil.	216

5.12	Colour plot of continuous single S_{21} measurements over the first cavity resonance.	217
5.13	Plot of the chip-cavity's first microwave mode resonant frequency, vs ^4He filling in arbitrary number of small volumes applied.	219
5.14	S_{21} transmission data over all four resonances for the chip-cavity system of Run 3, for different powers, a temperature of 30 mK, and ^4He pressure 34 mbar.	220
5.15	Q_0 vs source power, for the 4.2 GHz mode/s.	221
5.16	Number of photons in the microwave cavity n_{cav} against source power, for 4.2 GHz modes, taken at various temperatures and helium pressures.	222
5.17	Loaded quality factor Q_L of the 4.2 GHz peaks, normalised to Q_L for a -24 dBm source power, for each temperature and pressure combination, plotted against source power.	223
5.18	Main Figure: Resonant frequency of the 4.2 GHz peak vs temperature. Insert: Loaded quality factor of the 4.2 GHz peak vs temperature.	224
5.19	Transmission of a carrier signal on the second 4.2 GHz peak vs time, with different piezo drive amplitudes.	225
5.20	'Best' homodyne measurement set for Run 3.	226
5.21	Individual sweeps for the best homodyne measurement set of Run 3.	227
A.1	Stainless steel washer for fitting inside aluminium base.	256
A.2	Aluminium cavity base for D type chips.	257
A.3	Aluminium cavity lid for D type chips.	258
A.4	Copper experimental cell base.	259
A.5	Copper cell lid with pilot holes for hermetic feedthrough.	260
A.6	Stainless steel clamp for copper cell base.	261
A.7	Stainless steel clamp for copper cell lid.	262
A.8	Aluminium cavity base for A/B/C type chips.	263
A.9	Aluminium cavity lid for A/B/C type chips.	264
D.1	^3He pumping system, inside of fridge not shown.	274

D.2	1K pot pumping system, which is linked to the 4K helium bath.	275
F.1	Four chip pieces (to create two full chips), suspended on Nalgene forceps into a beaker of 1165 remover, which is itself in a heated bath with sonication. This method was used also for cleaning individual chips with IPA and DI.	278
F.2	Four chip pieces (to create two full chips), placed on a quartz chip holder, within the Diener Plasma Asher, ready to be plasma activated prior to bonding.	279
F.3	Chip piece held on bonding tape, which it Kapton taped to the photomask holder of the mask aligner used for bonding. Ready to be flipped and inserted under the aligner microscope.	279
F.4	Mask aligner used for bonding. Top chip piece is suspended facing downwards under the microscope. The bottom chip piece can be seen on the chuck on the right. Care must be taken with the vacuum settings when bonding.	280

List of Tables

1.1	Table of the figures of merit for a selection of modern superfluid optomechanical systems reported in literature, compared against the proposal for this work.	48
2.1	Table of acoustic properties of possible substrate materials, for use in fabricating nanofluidic sonic crystal chips.	77
2.2	Table of the quality factor reduction coefficient (η) for different substrate materials, obtained by FEM numerical simulations in COMSOL.	95
3.1	Comparison of older COMSOL predicted cavity resonances to measured resonances.	120
3.2	Comparison of first three cavity resonances for different nanofluidic chips, as predicted by COMSOL simulations.	121
3.3	Comparison of first three chip-cavity modes for: vacuum, ^4He film, and ^4He fill.	122
3.4	Comparison of external quality factor for the first three chip-cavity modes.	130
3.5	Fractional thermal contraction, for a variety of materials common to cryogenic and microwave cells.	135
4.1	Comparison of coaxial cables used in microwave circuit. Both attenuations given for 5 GHz signal.	173
5.1	Comparison of simulated chip-cavity resonant frequencies with experimental values.	218

Chapter 1:

Background

1.1 Introduction

This thesis covers development of an optomechanics experiment, combining 3D superconducting microwave cavities with nanofluidic sonic crystals, which are filled with superfluid ^4He . The project falls into the diverse field of cavity optomechanics, interested in the coupling between light or microwaves and mechanical motion; a field with a variety of system designs and applications [1]. A field extending from the macroscopic classical regime, into the microscopic regime of quantum optomechanics, which is pushing the limits of sensing and showing good prospects for quantum technology applications [2].

Most often cavity optomechanics uses a solid material for the mechanical element. Recently however there has been significant interest in developing systems instead using superfluid ^4He as the mechanical element, a material which is a natural quantum fluid, with many properties advantageous to an optomechanics experiment. It has vanishing viscosity at millikelvin temperature, and high natural purity, which leads to ultra low acoustic attenuation, making mechanical quality factors of 10^{10} possible at dilution fridge temperatures of 10 mK [3]. Superfluid ^4He also has high thermal conductivity, quantised excitations such as vortices, and an ultra low dielectric loss tangent of 10^{-10} at 1.5 K [4].

This project aims to measure the optomechanical coupling between a superfluid ^4He acoustic mode, and a 3D microwave cavity mode; partly inspired by the work of De Lorenzo *et al.* [5], using a 3D microwave cavity filled with bulk ^4He , to push the sensitivity of superfluid optomechanics with a ultra high acoustic quality factor. On a much smaller scale superfluid ^4He modes have been trapped between optical fibre ends, enhancing the coupling strength (relative cavity resonance shift), and pushing into the regime of quantum optomechanics [6, 7].

This work then seeks to provide an architecture for reducing the size of a superfluid acoustic mode to a $1000 \mu\text{m}^3$ volume, thereby enhancing the optomechanical coupling, while preserving the ultra high mechanical quality factors normally associated with bulk modes. This is achieved by utilising fabrication methods similar to Souris *et al.* [8], to create shallow near-2D channels between two pieces of etched wafer substrate, using modern cleanroom fabrication techniques. The resulting chips can then be filled with superfluid ^4He , confining the acoustic mode to a small volume, and thereby increasing the optomechanical coupling strength. The acoustic mode confinement is further enhanced by on-chip sonic crystal geometries, similar to those proposed by Safavi *et al.* [9], which block acoustic radiation at frequencies close to the acoustic mode, and help to maintain good acoustic isolation.

The coupling to the superfluid acoustic mode is provided by on-chip fabricated aluminium, which then hybridises with the 3D microwave cavity. The microwave cavity is contained within a superfluid leak tight experimental cell, which can be filled with ^4He , and is mounted on the experimental stage of a dilution fridge.

Chapter 1 gives background to the project and introduces the overarching optomechanical interaction, covering the properties of ^4He at millikelvin temperatures, and focussing on its associated behaviour and losses deep into the superfluid phase. Chapter 2 develops the concept of a 3D microwave cavity coupled to an acoustic sonic crystal, focussing on simulations of the electromagnetic modes of the chip-cavity system, and acoustic modes of nanofluidic ^4He within the sonic crystal. Chapter 3 focusses on the experimental methods for the project, the development of the experimental platform in the lab. This includes refurbishment of the dilution fridge for superfluid optomechanics experiments using microwaves, design of the microwave cavity and experimental cell, and also refinement of nanofabrication techniques for producing the nanofluidic chips. Chapter 4 covers microwave measurement, the readout method for the optomechanical system in this work, focussing on direct transmission measurements through the fridge and chip-cavity system; in addition to the expected response for homodyne measurements using a microwave interferometer setup. Chapter 5 discusses the results of all experimental fridge ‘runs’ where the chip-cavity system was measured. The runs are

discussed in chronological order, with details of measurements, presentation of data, and discussion of experimental difficulties.

1.2 Cavity Optomechanics

1.2.1 Background

Optomechanics is a field concerned with the interaction of electromagnetic radiation and mechanical systems. Or in a more quantum picture, the interaction and coupling of photons with phonons, quasiparticles of mechanical vibrational energy. Classically this interaction originates from radiation pressure, indicating the electromagnetic field's ability to transfer momentum, postulated all the way back in 1619 by Kepler's observation of comet dust trails pointing away from the sun [10], with the same principles being used for much more modern techniques like laser cooling [11]. Optomechanics is a wide field, ranging from the 600 m scale, kg mass LIGO system [12], to zg mass single atoms coupled to optical cavities [13]. Microscopic optomechanics is possible without cavities, usually using optical waveguides to pass light close to or through mechanical oscillators; for example through a nanobeam oscillator [14], or through photonic crystal fibres [15]. However, this work will focus on cavity optomechanics, where electromagnetic radiation at resonant frequencies is trapped within a mode, enhancing its coupling to the mechanics. The quintessential cavity optomechanical system is shown in Figure 1.1, a Fabry-Perot cavity with one moveable mirror attached to a mechanical spring. Cavity optomechanics has been recently reviewed by Aspelmeyer *et al.* [1], and an extensive quantum treatment detailed in a recent book by Bowen *et al.* [2]. Figure 1.2 shows a collage of four cavity optomechanical systems referenced in this section, and two schemes for superfluid optomechanics, discussed further in Section 1.4.1.

This work is concerned with nanoscale mechanical systems; a regime including nanomechanical beams, which have been used to measure motion below the standard quantum limit, both in systems using optical lasers [16], and in systems using on chip microwave circuits [17]. Beams have also been combined with photonic and phononic

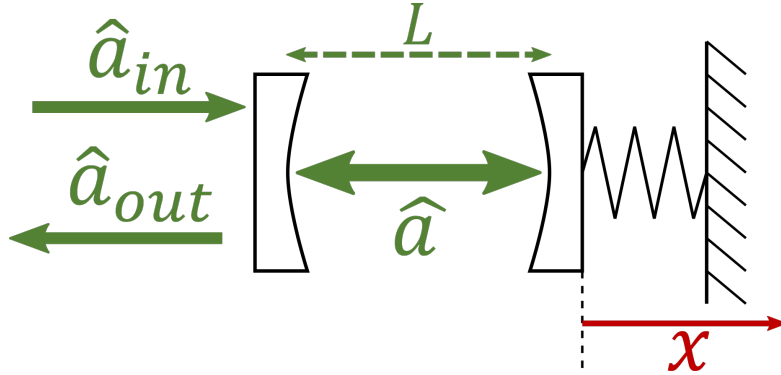


Figure 1.1: Simplified schematic of a Fabry-Perot optomechanical cavity, two concave mirrors with one being fixed, and the other moveable one attached to a mechanical spring. The figure shows cavity field \hat{a} , incident field \hat{a}_{in} , output field \hat{a}_{out} , cavity length L and x the direction of movement.

crystal geometries, similar to those in Section 2.3, in order to reach the mechanical ground state with laser cooling. Reaching the ground state, or having well defined quantum states, is required for integrating optomechanical systems into hybrid quantum information devices. For example the early work of O’Connell *et al.* [18], where a GHz suspended thin film mechanical resonator is cooled into its ground state, and then measured with a coupled qubit, showing single-phonon control.

The optomechanical system in this work is in the microwave regime, where the coupling originates from the mechanical mode altering the capacitance of a microwave cavity, analogous to cleanroom fabricated microwave drum cavities, where a capacitance is formed by between two superconducting surfaces, with the top surface free to oscillate, and a stationary inductance elsewhere on the chip. These drum cavities have been cooled to the ground state [19], used for quantum non-demolition measurement of massive objects [20, 21], and for coherent state transfer between microwave and mechanical modes [22], which has been developed to include coupling to a transmon qubit [23]. The mechanical drum modes tend to be in the 10 MHz frequency range with strong optomechanical coupling, which has enabled their push into the quantum regime including: demonstration of quantum squeezing of the mechanical resonator’s motion [24, 25]; and entanglement between the mechanical mode and microwave fields [26], where the microwave field and mechanical oscillator are in a shared quantum state and separate readout of both systems will produce correlated results.

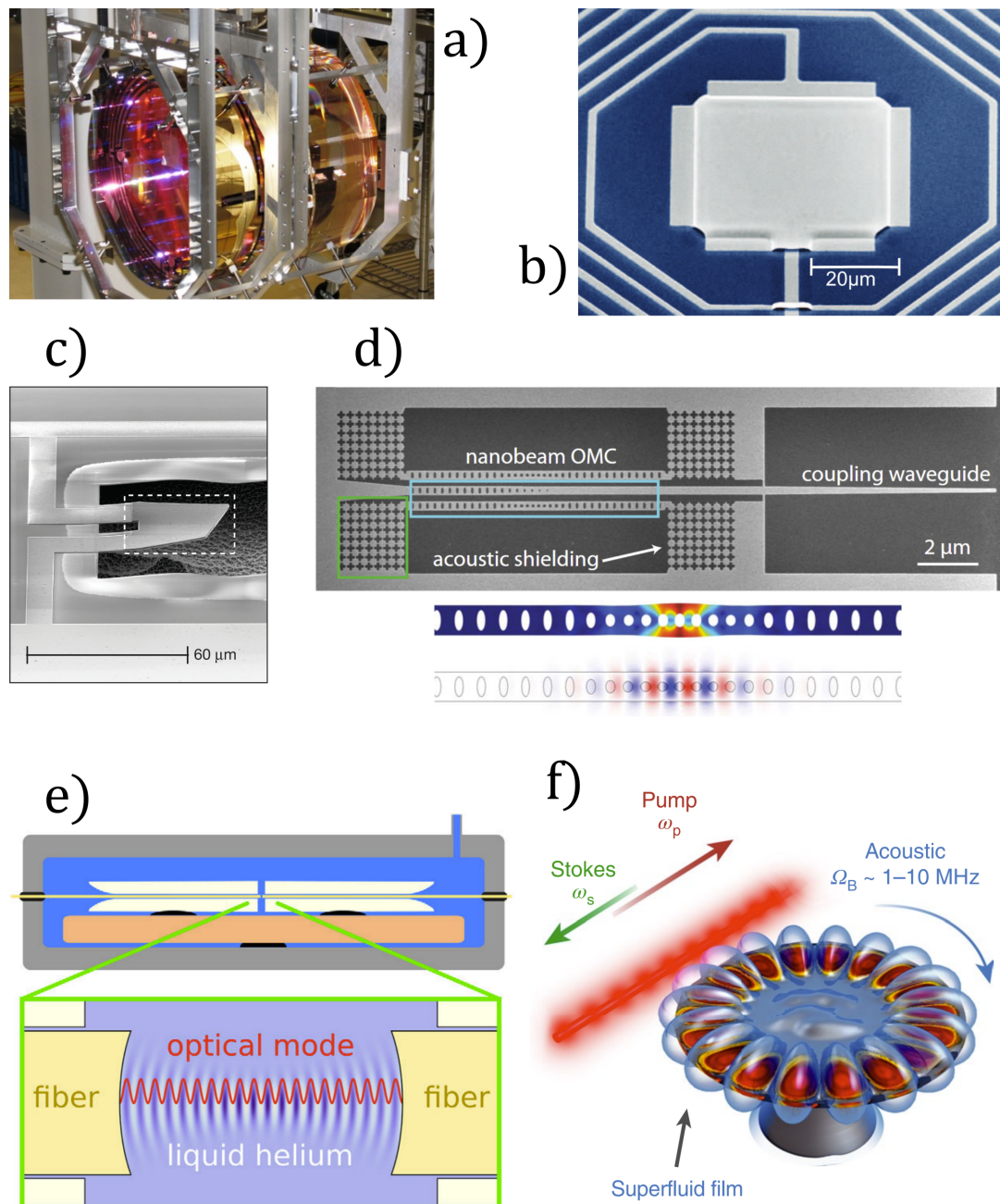


Figure 1.2: Showing a collage of other cavity optomechanical experiments. The individual images are for the experiments: a) LIGO suspended mirror [27], b) microwave drum cavity [20], c) suspended film bulk acoustic resonator [18], d) nanobeam with acoustic shielding [28], optical fibre end superfluid cavity [6], microtoroid with superfluid thin film [29].

Entanglement has also been shown with optical laser systems and mechanical beams, even demonstrating the entanglement of two mechanical beams 20 cm apart [30]. These beams tend to be in the GHz mechanical frequency range, making cooling into the ground state simpler with mK dilution fridge temperatures. The geometry of the beam coupled to an optical waveguide is also suitable for combining with both photonic and phononic crystal geometries, which have been used to enhance lifetime phononic modes in the beam [28]. Phononic crystals have also been incorporated into mechanical drum resonators to increase coherence times to 100 ms for a 1.5 MHz mode [31]. This logic has been extended to create etched patterns of holes, that directly confine both optical and mechanical modes to the same volume [32].

This work seeks to combine phononic crystal geometries with acoustic superfluid ^4He , to form low loss highly confined acoustic modes, for microwave cavity optomechanics. The acoustic and general properties of superfluid ^4He will be covered in Section 1.3, and Section 1.4 will cover its use in optomechanical systems.

1.2.2 Optomechanical Coupling

As described in the historic background, optomechanics is the study of interactions between optical systems and mechanical ones. In quantum mechanical terms it is the study of photon-phonon interactions. Though this work is not quantum in terms of these quasiparticles of excitation, it is still illustrative to consider the system in terms of its Hamiltonian.

Optical Resonator

The first part of the optomechanical system is an optical resonator. The common picture is a Fabry-Perot cavity (shown in Figure 1.1), two slightly concave mirrors that define an optical cavity, capable of trapping optical modes with wavelengths some integer number of half wavelengths, giving cavity resonant frequencies:

$$\omega_{c,m} = \frac{\pi m c}{L}, \quad (1.1)$$

where m is the integer mode number, c is the speed of light, and L is the length of the cavity. The decay rate of photons in the cavity, sometimes called the linewidth of the mode, is then denoted by κ , which is also the inverse of the photon lifetime. The total decay rate of the mode κ_L (using the ‘loaded’ subscript from microwave conventions), can then be decomposed as:

$$\kappa_L = \kappa_0 + \kappa_e , \quad (1.2)$$

where κ_0 is the decay rate from internal losses, and κ_e is from the input coupling, simply that the channel for coupling of photons into the cavity works as a coupling for photons out; though this treatment considers the cavity as an optical one, in line with optomechanics using lasers, the equations of this section are general and valid for a microwave cavity, with frequencies in the GHz range. From the input-output theory of an optical cavity, the cavity field \hat{a} equation of motion can be written:

$$\dot{\hat{a}} = -\frac{\kappa_L}{2}\hat{a} + i\Delta\hat{a} + \sqrt{\kappa_e}\hat{a}_{\text{in}} , \quad (1.3)$$

where $\Delta = \omega_p - \omega_c$ is the detuning of the probe signal from cavity resonance, and \hat{a}_{in} is the signal incident on the input coupling, usually called ‘port’ in microwave networks. This equation is in the frame rotating at the probe frequency, with the lab frame being recovered by taking $\hat{a} \rightarrow e^{-i\omega_p t}\hat{a}$. The thermal noise into the mode is also ignored as the contribution will be small compared to the probe signal, and will average to zero as this project mainly deals with classical observables. \hat{a}_{in} is normalised such that:

$$P = \hbar\omega_p \langle \hat{a}_{\text{in}}^\dagger \hat{a}_{\text{in}} \rangle , \quad (1.4)$$

where P is the power incident on the cavity port. From input-output theory the field coupled back out of the cavity (reflected) is:

$$\hat{a}_{\text{out}} = \hat{a}_{\text{in}} - \sqrt{\kappa_e}\hat{a} , \quad (1.5)$$

which can also be considered as the field reflected from the incident port. For a two port system an additional external coupling term can be introduced into Eq. 1.3, effectively $\sqrt{\kappa_e}\hat{a}_{\text{in}} \rightarrow \sqrt{\kappa_e^{(1)}}\hat{a}_{\text{in}}^{(1)} + \sqrt{\kappa_e^{(2)}}\hat{a}_{\text{in}}^{(2)}$, for ports 1 and 2. This can be extended to a system with any number of ports. Each port will then have an associated version of Eq. 1.5, with variables specific to the port. In this work two port cavities are used, with ports assumed to be approximately identical, so $\kappa_e = \kappa_e^{(1)} + \kappa_e^{(2)} \simeq 2\kappa_e^{(1)}$, and κ_e will be used to refer to the total external coupling from both ports. The average cavity field can then be written [1]:

$$\langle \hat{a} \rangle = \frac{\sqrt{\kappa_e} \langle \hat{a}_{\text{in}} \rangle}{\kappa_L/2 - i\Delta}, \quad (1.6)$$

provided the probe ω_p is near the resonance at ω_c , which is well isolated from any other cavity resonances. Then the average number of photons circulating within the cavity $\bar{n}_{\text{cav}} = \langle \hat{a}^\dagger \hat{a} \rangle$, where $\hat{a}^\dagger \hat{a}$ are the photon creation and annihilation operators respectively, can be rewritten using Eq.'s 1.4 and 1.6 as:

$$\bar{n}_{\text{cav}} = |\langle \hat{a} \rangle|^2 = \frac{\kappa_e}{\Delta^2 + (\kappa_L/2)^2} \frac{P}{\hbar\omega_p}. \quad (1.7)$$

An equivalent equation is also derived from a microwave circuit analysis perspective in Section 4.1.4. The equations presented in this section are general for any photon cavity, and useful to corroborate results from microwave analysis.

Mechanical Resonator

The mechanical resonator part of an optomechanical system can also be treated generally [1], provided the mechanical system can be decomposed into a set of n normal modes with corresponding eigenfrequencies $\Omega_m^{(n)}$, with each mode having an associated mode function $\vec{u}_n(\vec{r}, t)$, for position \vec{r} at time t . This work focusses on a single mode Ω_m , whose mode function can be normalised to a global amplitude $x(t)$, that is $\vec{u}_n(\vec{r}, t) = x(t) \cdot \vec{f}_n(\vec{r})$, where $\vec{f}_n(\vec{r})$ is the normalised modeshape function [33]. This method is common in cavity optomechanics [34, 35], and is formulated specifically for a superfluid ⁴He electrostrictive coupling in Section 1.4.2. The global amplitude can then be described

by the equation of motion for a harmonic oscillator:

$$m_{\text{eff}} \frac{dx^2(t)}{dt^2} + m_{\text{eff}} \Gamma_m \frac{dx(t)}{dt} + m_{\text{eff}} \Omega_m^2 x(t) = F_{\text{ex}}(t) , \quad (1.8)$$

where m_{eff} is the effective mass of the mode, Γ_m is the mechanical damping rate (linewidth), and $F_{\text{ex}}(t)$ is the total external force acting on the resonator. The choice of $x(t)$ normalisation affects m_{eff} , to preserve the potential energy:

$$U = \frac{1}{2} m_{\text{eff}} \Omega_m^2 \langle x^2(t) \rangle . \quad (1.9)$$

This choice is important for comparison between optomechanical systems, discussed in relation to the optomechanical coupling later in this section. The force F_{ex} in Eq. 1.8 includes thermal effects and for a Fabry Perot cavity radiation pressure, with transferred momentum $|\Delta p| = 2h/\lambda$. In the absence of other external forces this gives an average force:

$$\langle \hat{F}_{\text{ex}} \rangle = \frac{\hbar \omega_c}{L} \langle \hat{a}^\dagger \hat{a} \rangle . \quad (1.10)$$

Optomechanical Hamiltonian

The Hamiltonian for a mechanical oscillator in the quantum mechanical picture can be represented as:

$$\hat{H}_m = \hbar \Omega_m \hat{b}^\dagger \hat{b} + \frac{1}{2} \hbar \Omega_m , \quad (1.11)$$

where $\hat{b}^\dagger \hat{b}$ are the phonon creation and annihilation operators respectively. The choice of $x(t)$ defines m_{eff} through the requirement of a consistent potential energy, allowing m_{eff} to define the zero-point fluctuation amplitude of the mechanical oscillator x_{zpf} through the position and momentum operators:

$$\hat{x} = x_{\text{zpf}} (\hat{b} + \hat{b}^\dagger) , \quad (1.12)$$

$$\hat{p} = -im_{\text{eff}}\Omega_m x_{\text{zpf}}(\hat{b} - \hat{b}^\dagger) . \quad (1.13)$$

Equations which obey the commutation relation $[\hat{x}, \hat{p}]$, meaning that the zero-point fluctuation is defined:

$$x_{\text{zpf}} = \sqrt{\frac{\hbar}{2m_{\text{eff}}\Omega_m}} . \quad (1.14)$$

The zero-point fluctuation can be thought of as the amplitude of the mechanical oscillator's ground state, also defined $\langle 0|\hat{x}^2|0\rangle = x_{\text{zpf}}^2$. The average photon number within the mechanical mode is defined similarly to the photon number as $\bar{n}_m = \langle \hat{b}^\dagger \hat{b} \rangle$. The constant $\hbar\Omega_m/2$ contribution is dropped, along with the $\hbar\omega_c/2$ contribution for the cavity mode, as neither term will affect the dynamics of interest to this work. The uncoupled cavity optomechanical Hamiltonian can then be written:

$$\hat{H}_0 = \hbar\omega_c \hat{a}^\dagger \hat{a} + \hbar\Omega_m \hat{b}^\dagger \hat{b} . \quad (1.15)$$

To include the coupling, consider the cavity resonance's dependence on the position $x(t)$ of the mechanical oscillator. The cavity resonance will then be modulated by the position as:

$$\omega_c(x) \approx \omega_c + x \frac{\partial \omega_c}{\partial x} + \dots . \quad (1.16)$$

The linear term can then be used to define a coupling strength $G = -\partial\omega_c/\partial x$, which is sufficient to describe the measurements in this work. For a simple Fabry-Perot cavity this is $G = \omega_c/L$, with the sign convention such that positive x indicates an increase in cavity length, and so drop in frequency. Using this to expand the cavity part of the optomechanical Hamiltonian to first order,

$$\hbar\omega_c(x)\hat{a}^\dagger \hat{a} \approx \hbar(\omega_c - G\hat{x})\hat{a}^\dagger \hat{a} , \quad (1.17)$$

where \hat{x} is the position operator from Eq. 1.12. Here it is useful to highlight that x

need not be length of the cavity, provided a choice of x allows for the expansion of $\omega_c(x)$ as in Eq. 1.16, and it may be more convenient to express the coupling in terms of some other variable, e.g. pressure or density in superfluid optomechanics. However, G is not constant over choice of x , for example $x \rightarrow ax$ will lead to $G \rightarrow G/a$. This also affects the modeshape normalisation via the transformation $m_{\text{eff}} \rightarrow m_{\text{eff}}/a^2$ (and obviously $x_{\text{zpf}} \rightarrow ax_{\text{zpf}}$), to maintain the system's energy as in Eq. 1.9 [33, 35]. Taking advantage of these interconnected quantities a more universal 'vacuum optomechanical coupling strength' can be defined:

$$g_0 = x_{\text{zpf}}G . \quad (1.18)$$

Substituting this into Eq. 1.17 and then Eq. 1.15, gives the general cavity optomechanical Hamiltonian as [1]:

$$H = \hbar\omega_c a^\dagger a + \hbar\Omega_m b^\dagger b - \hbar g_0 a^\dagger a (b^\dagger + b) , \quad (1.19)$$

where $-\hbar g_0 a^\dagger a (b^\dagger + b)$ is the interaction term, and g_0 describes the cavity resonant frequency shift due to the mechanical oscillator's ground state, or as a quantification of the single photon single phonon interaction. This coupling strength is more fundamental than G , and useful to directly compare very different optomechanical experiments; g_0 is also called the single photon coupling rate, from the definition of the 'optomechanical coupling strength' $g = \sqrt{\bar{n}_{\text{cav}}}g_0$, for $\bar{n}_{\text{cav}} = 1$.

1.2.3 Cooperativity and Quality Factor

Another useful quantity for categorising optomechanical systems is the cooperativity, giving a value for the efficiency of a system for converting a mechanical signal into an optical one. The cooperativity is usually defined:

$$C = \frac{4g^2}{\kappa\Gamma_m} , \quad (1.20)$$

where κ is the optical linewidth, and Γ_m is the mechanical linewidth, and $g = \sqrt{n_{\text{cav}}}g_0$ is the optomechanical coupling strength with n_{cav} photons in the cavity. Cooperativity is sometimes defined as an effective quantum cooperativity $C_{\text{eff}} = C/n_{\text{cav}}$, the single photon value. The cooperativity can also be defined:

$$C = \frac{4g^2 Q_c Q_m}{\omega_c \Omega_m}, \quad (1.21)$$

Where Q_c and Q_m are the cavity and mechanical quality factor's respectively, related to linewidth as $\omega/Q = \Delta\omega$ with $\Delta\omega$ the general linewidth. When already working with the frequency, quality factor can be a useful intuitive parameter, and will be used more commonly throughout this work. Quality factor (or Q / Q-factor) is a dimensionless parameter giving the ratio of the total energy stored in a mode and the energy lost in a single cycle, and can be defined:

$$Q = \omega \frac{e_{\text{stored}}}{P_{\text{loss}}} = \frac{\omega}{\Delta\omega}, \quad (1.22)$$

where e_{stored} is the stored energy, and P_{loss} is the lost power. The quality factor can also be considered as the average lifetime of energy (photons or phonons) in terms of cycles. The total quality factor of a mode can be broken up into individual sources of loss as:

$$\frac{1}{Q} = \sum_n^M \frac{1}{Q_n}, \quad (1.23)$$

for M loss sources. Where Q_n , the quality factor due to loss source n , considers the total energy of the mode. For electronic circuits this is conveniently the same form as addition of resistors in parallel, allowing reformulation of loss sources into resistive components. Total linedwith can be decomposed similarly as a simple sum of constituent linewidths.

1.3 Helium 4

The second element of the periodic table, helium is an inert gas of single atoms at room temperature. Natural helium gas contains majority helium-4 (^4He) isotopes, composed of two protons and two neutrons, and therefore behaving as a boson. The other naturally occurring stable isotope is helium-3 (^3He), composed of two protons and a neutron, a fermion with natural fractional abundance in the ppm to ppb range [36].

Due to its low mass, two electrons, and bosonic nature, ^4He has only incredibly weak van der Waals forces for interatomic binding and liquid formation. This leads to the second lowest boiling point of any known atomic substance at 4.21 K, with the lowest being ^3He at 3.19 K. ^4He does not naturally form a solid at its own vapour pressure, instead a pressure of 25 bar is required for solid formation.

Cool either helium isotope well below its boiling point and it will begin to show exotic behaviours. Of chief interest to this work is superfluidity. In the superfluid phase the helium liquid's viscosity vanishes [37] and acoustic losses are heavily suppressed [38, 39]. Both these properties make superfluid helium an ideal acoustic medium, especially for nanofluidic confinement where viscous effects such as capillary forces can clamp a normal fluid. This section will cover the fundamentals of this superfluid phase and its associated acoustic losses, while Section 1.4 will cover its integration into optomechanical systems, leaving Section 2.3 to cover the specifics of its confinement into a sonic crystal environment.

^4He is the focus of this work as its superfluid transition temperature is much higher than ^3He , meaning that at the mK temperatures of a dilution fridge it is much deeper into its superfluid phase; thus allowing it to be treated as an idealised acoustic medium with vanishing dissipation. It is also possible to achieve a superfluid state in ^3He , but at much lower temperatures around 0.9 mK and 2 mK at low and high pressure respectively. Though as ^3He is fermion its low temperature behaviour is very different to ^4He , and may prove an interesting topic of future studies using systems similar to those developed here. The work in this section is also covered in the group's paper [40].

1.3.1 Two-Fluid Model

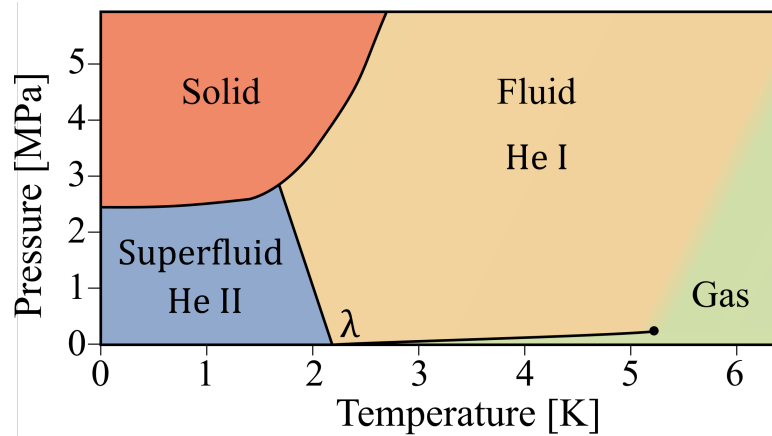


Figure 1.3: The phase diagram for helium-4, showing the normal fluid (He I) and superfluid (He II) phases, along with the solid and gas phases. The lambda point is shown at $T_\lambda = 2.17$ K and low pressure. The solid dot at the end of the solid-gas boundary is a critical point.

As mentioned above, liquid helium behaves as a normal fluid (He slowromancapi@) down to its superfluid transition temperature $T_\lambda = 2.17$ K, named the ‘lambda point’ due to the shape of specific heat vs temperature through the transition. Figure 1.3 shows the phase diagram for helium-4. Below this critical temperature helium begins to exhibit the unique behaviours of its superfluid (He slowromancapii@) phase. From early experiments superfluid ^4He seemed to provide a low but non-zero resistance to the motion of a submerged torsional oscillator [41], a level of resistance expected from a gas. While for superfluid ^4He emptying from a volume via a small capillary, a flow rate independent of the remaining liquid (pressure) was observed [42], implying dissipationless flow up to some critical velocity. These seemingly contradictory behaviours, of low viscosity vs dissipationless flow, were reconciled in the development of the non-interacting ‘two-fluids’ model for this novel new material; where the ‘normal’ element provides the resistance to motion, which is clamped in small geometries, allowing only the ‘superfluid’ element to flow through thin capillaries. The two-fluid model originally proposed by Tisza [43] was then reformulated by Landau [44] into the form presented here. A deeper discussion of superfluid helium’s discovery and the development of the two fluid model can be found in Ref. [45], while Ref. [46] gives an introduction to the modern theory of superfluids. The superfluid ^4He is treated as a Bose liquid (sometimes Bose-Einstein Liquid), which

is similar to a Bose-Einstein Condensate in that some large fraction of the atoms are in the lowest energy state so quantum statistics must be considered. However, for a Bose liquid the ^4He atoms are considered strongly interacting, rather than as a weakly or non-interacting dilute gas as in the Bose-Einstein Condensate.

The two-fluid model separates helium below the lambda point into two non-physical components, the purely superfluid component of mass density ρ_s and velocity \mathbf{v}_s , and the purely normal fluid with mass ρ_n and velocity \mathbf{v}_n . These two fluids occupy the same space, together making up the total density ρ and momentum density \mathbf{j} of the He

$$\rho = \rho_n + \rho_s , \tag{1.24}$$

$$\mathbf{j} = \rho_n \mathbf{v}_n + \rho_s \mathbf{v}_s . \tag{1.25}$$

In this formulation the superfluid fraction represents the macroscopic quantum state of the Bose liquid, a collective phenomena with neither entropy nor viscosity (S_s and $\eta_s = 0$), where the distinction of single atoms is no longer meaningful; while the normal fraction accounts for the fluid's entropy and viscosity, representing the quasi-particle excitations within the superfluid medium. This phenomenon begins at the transition temperature T_λ where $\rho_s = 0$ and $\rho_n = \rho$, then as the zero temperature limit is approached the superfluid fraction increases, until at the limit $\rho_s = \rho$ and $\rho_n = 0$. Of course this absolute zero limit of total superfluid is impossible as the normal fraction holds the fluids entropy ($S = S_n$), which cannot be reduced to zero in a physical system, though at low mK temperatures the superfluid fraction is sufficiently close to unity to approximate the fluid to a pure superfluid. This entropy from the normal fraction provides viscosity as the elementary excitations within the superfluid scatter off the container walls, transferring momentum and opposing motion. A sound wave (acoustic mode) within the ^4He can be considered as a bulk collection of coherent phonons, which is then attenuated via scattering from the container walls and other quasi-particles. The reduction of quasi-particles as the normal fraction vanishes with temperature, is then responsible for the vanishing of intrinsic losses.

1.3.2 Spectrum of Excitations

T_λ can be thought of as the point where the thermal de Broglie wavelength of ^4He atoms, becomes comparable with their interatomic spacing. Then as the helium atom's wave functions begin to overlap, the distinction between the individual identical ^4He atoms becomes less meaningful as they transition into the superfluid phase, becoming a background within which excitations are defined.

Therefore at low temperatures, especially below 1.5 K where non-interacting is a good approximation, the dynamic properties of He slowromancapii@ are determined by the spectrum of these excitations and their interactions, rather than the interactions of the helium atoms themselves. Of key interest here is the phonon-maxon-roton dispersion curve, originally proposed for non-interacting excitations by Landau [44], and confirmed via neutron scattering experiments [47]. This curve is defined by excitations with energies related to their wave number q . The low energy linear section of the dispersion curve, corresponding to phonons, is approximated away from the zero temperature limit to $\varepsilon_{\text{ph}} = c\hbar q$, where c is the speed of first-sound. Here the phonon corresponds to the gapless Goldstone modes of the Bose liquid [48], rather than the quantised vibrations on a crystal lattice. A more rigorous treatment of these modes approximates, to order q^3 , as [49]:

$$\varepsilon_{\text{ph}}(q) \simeq c\hbar q(1 - \gamma\hbar^2 q^2), \quad (1.26)$$

where γ is the dispersion coefficient, negative at low pressure (anomalous dispersion), and positive at high pressure (normal dispersion). The sign change of γ alters the prevalence of three phonon-phonon interactions, and therefore their contribution to sound attenuation in the superfluid. For a negative γ the dispersion relation is convex at low energy, making energy and momentum conservation easier for a process involving three phonons, leading to their dominance of attenuation at low temperatures and pressure. While for positive γ the dispersion relation is concave, forbidding three phonon processes with certain wave vectors, suppressing the interaction and allowing four phonon processes to become significant.

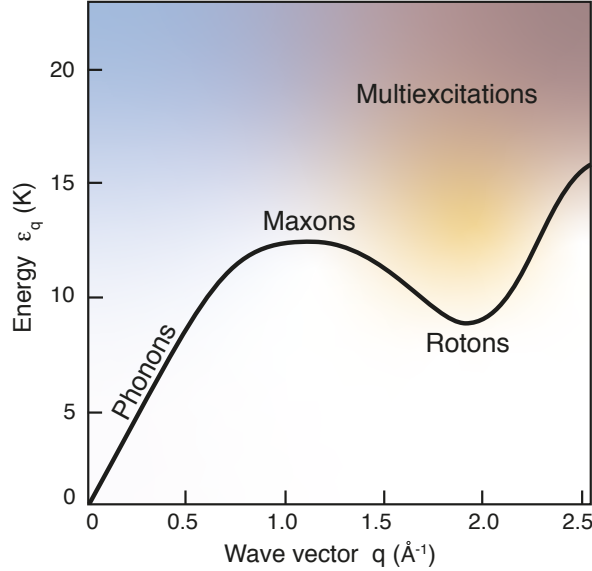


Figure 1.4: Graph showing the dispersion curve of superfluid ${}^4\text{He}$, with regions labelled by their characteristic excitation. The solid line denotes the low-energy branch of the spectrum. The curve only depends on $|\mathbf{q}|$ due to the isotropy of superfluid ${}^4\text{He}$.

While phonons account for the low q region of the dispersion curve in Figure 1.4, around the minimum corresponds to roton excitations. The dispersion curve around this roton minimum can be approximated to:

$$\varepsilon_{\text{rot}}(q) \simeq \Delta_r + \frac{\hbar^2}{2\mu_r}(q - q_e)^2, \quad (1.27)$$

where the energy and momentum coordinates of the minimum are $\Delta_r/k_B = 8.594$ K and $q_r = 1.926 \text{ \AA}^{-1}$ respectively, and $\mu_r = 0.124 m_4$ is the roton effective mass, corresponding to the changing curvature of the dispersion curve at the roton minimum. These values are extracted from more modern neutron scattering experiments at saturated vapour pressure [50]. Though shown to exist by these neutron scattering experiments, the roton quasiparticle still does not have a universally agreed form. An early proposal by Feynman [51] considered a toroidal vortex ring, closed with itself rather than pinned to a wall, small enough that only a single atom could pass through. Alternatively rotors could be related to backflow caused by a travelling excitation or atom [52, 53], or as recently suggested the “precursor of a crystallization instability” [54], where the roton minimum indicates the superfluid is close to solidifying.

At the temperatures well below T_λ relevant to this work phonons and rotons are the dominant excitations, and so the contributions from maxons and mutliexcitations are ignored here. The normal fluid density is then the sum of both the phonon and roton contributions $\rho_n = \rho_n^{\text{ph}}(T) + \rho_n^{\text{rot}}(T)$, with each of these contributions being [46]:

$$\rho_n^{\text{ph}}(T) = \frac{2\pi^2 k_B^4}{45\hbar^3 c^5} T^4, \quad (1.28)$$

$$\rho_n^{\text{rot}}(T) = \frac{1}{3} \sqrt{\frac{\mu_r}{2\pi^3 k_B T}} \hbar q_r^4 e^{-\Delta_r/k_B T}, \quad (1.29)$$

where γ has been ignored. The relative densities as a proportion of the normal fluid density are shown in Figure 1.5. These densities are equal at ~ 570 mK, with the roton contribution falling off sharply with temperature as $e^{-\Delta_r/k_B T}$. Below about 500 mK the phonon contribution can be considered dominant, and the fraction of normal liquid follows temperature as $\rho_n/\rho \propto T^4$. At the lowest temperatures of dilution refrigerators around 10 mK, ^4He is far below its superfluid transition with $T/T_\lambda \sim 0.005$, giving an achievable normal fraction in the 10^{-12} range. This enables experimentally a stable temperature regime of vanishing acoustic losses in ^4He . In comparison a very low ^3He temperature of 100 μ K achieves $T/T_c \sim 0.04$ [55], and the colder Bose-Einstein condensates are in the region of $T/T_c \sim 0.25$ [56], both requiring arguably more complex experimental implementations.

In the phonon dominated temperature range, where intrinsic losses are dominated by phonon-phonon interactions, the specific heat of ^4He drops with temperature as [57]:

$$C_V = \frac{2\pi^2 k_B^4}{15\rho\hbar^3 c^3} T^3, \quad (1.30)$$

as expected recovering the T^3 expected when dominated by phonons.

1.3.3 Sound Propagation

This work will treat superfluid helium as an acoustic medium, using the standard plane wave solutions, approximated from the nonlinear hydrodynamic equations. This

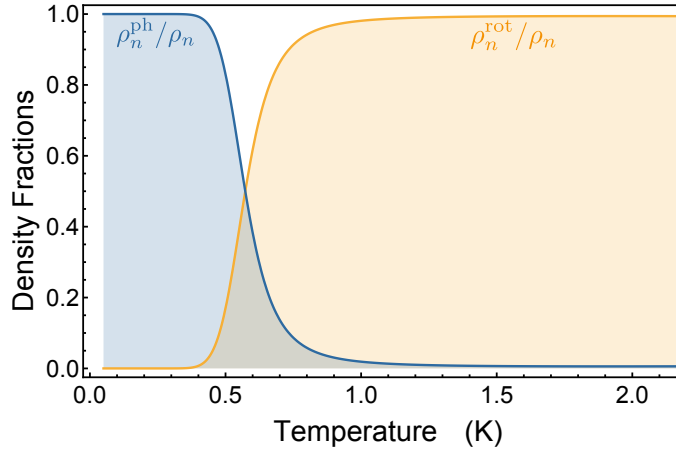


Figure 1.5: Fraction of the normal fluid density ρ_n , due to the phonon contribution ρ_n^{ph} (blue) and the roton contribution ρ_n^{rot} (orange), as a function of temperature. The contributions are equal at ~ 600 mK.

decomposes states of the acoustic field into a linear superposition of plane waves, valid for long wavelengths and pure ${}^4\text{He}$ [44]. A full treatment of the motion of He slowromancapii@ involving solving the equations of motion of the two-fluids is derived in textbooks on the subject [48, 58]. However, as this work is concerned with ‘bulk’ ${}^4\text{He}$ far into the superfluid phase, it will focus on the regime of small disturbances from a $\mathbf{v}_n = 0$ and $\mathbf{v}_s = 0$ steady state, reducing normal and superfluid fraction velocities to:

$$\mathbf{v}_n = \delta\mathbf{v}_n(\mathbf{r}, t), \quad (1.31)$$

$$\mathbf{v}_s = \delta\mathbf{v}_s(\mathbf{r}, t). \quad (1.32)$$

This also means the thermodynamic properties of the system are close to equilibrium values:

$$\rho = \rho_0 + \delta\rho(\mathbf{r}, t), \quad (1.33)$$

$$p = p_0 + \delta p(\mathbf{r}, t), \quad (1.34)$$

$$T = T_0 + \delta T(\mathbf{r}, t), \quad (1.35)$$

$$s = s_0 + \delta s(\mathbf{r}, t), \quad (1.36)$$

where ρ , p , T and s , are the density, pressure, temperature, and entropy per unit mass respectively; with the δ perturbations being assumed small compared to the subscript

zero equilibrium value, including $\delta\mathbf{v}_n(\mathbf{r}, t)$ and $\delta\mathbf{v}_s(\mathbf{r}, t)$ which are small compared with the speed of sound. Assuming no dissipative effects, these approximations can then be used to find linearised approximations for the equations of motion by discarding δ^2 terms [40]:

$$\frac{\partial(\delta\rho)}{\partial t} + \nabla \cdot \delta\mathbf{j} = 0 , \quad (1.37)$$

$$\rho_0 \frac{\partial(\delta s)}{\partial t} + s_0 \frac{\partial(\delta p)}{\partial t} + \rho_0 s_0 \nabla \cdot \delta\mathbf{v}_n = 0 , \quad (1.38)$$

$$\frac{\partial(\delta\mathbf{j})}{\partial t} + \nabla\delta p = 0 , \quad (1.39)$$

$$\frac{\partial\mathbf{v}_s}{\partial t} + \nabla\delta\mu = 0 , \quad (1.40)$$

where $\delta\mathbf{j} = \rho_{n,0}\delta\mathbf{v}_n + \rho_{s,0}\delta\mathbf{v}_s$ is the mass current, and $\delta\mu = \delta p/\rho_0 - s_0\delta T$ is the chemical potential perturbation from equilibrium (per unit mass). The first equation derives from conservation of mass and the second from conservation of entropy. The third equation shows a pressure gradient causes a mass flow. While the fourth equation is more unique to the two-fluid model, where a chemical gradient drives a flow of only the superfluid fraction. Combining Eq.'s 1.37 and 1.39 gives the acoustic wave equation for 'first-sound' [46]:

$$\frac{\partial^2(\delta\rho)}{\partial t^2} - \nabla^2\delta p = 0 . \quad (1.41)$$

This first-sound is analogous to the density wave form of a classical sound mode in a normal fluid. To rewrite in a more recognisable form, first consider the isentropic differential of the superfluid's equation of state $p = p(\rho, s)$:

$$\delta p = \left. \frac{\partial p}{\partial \rho} \right|_s \delta \rho . \quad (1.42)$$

It is then possible to define the isentropic first-sound velocity c_1 via:

$$c_1^2 = \left. \frac{\partial p}{\partial \rho} \right|_s , \quad (1.43)$$

representing the propagation speed of pressure or density waves in He slowromancapii@. This gives, to a first order approximation, the constitutive equation:

$$\delta p = c_1^2 \delta \rho , \quad (1.44)$$

which when substituted back into Eq. 1.41 gives:

$$\frac{\partial^2(\delta p)}{\partial t^2} - c_1^2 \nabla^2 \delta p = 0 . \quad (1.45)$$

Or in a density wave form:

$$\frac{\partial^2(\delta \rho)}{\partial t^2} - c_1^2 \nabla^2 \delta \rho = 0 . \quad (1.46)$$

Both are in the more standard wave equation form, with simple plane wave solutions of the form:

$$\delta p(\mathbf{r}, t) = A e^{i(\mathbf{k} \cdot \mathbf{r} - \Omega t)} , \quad (1.47)$$

where A is the amplitude of the acoustic waves, \mathbf{k} its wave vector, and Ω its angular frequency. Eq.'s 1.38 and 1.40 can be similarly combined to give a wave equation describing the 'second-sound' in He slowromancapii@, instead of pressure or density these waves correspond to temperature and entropy, responsible for the fountain effect [59]. These equations for first and second sound are valid in the hydrodynamic regime, where the respective density and entropy field variations are slow compared to the relaxation time required for the excitations to reach thermal equilibrium [48]. The condition for this regime is:

$$\Omega \tau_r \ll 1 , \quad (1.48)$$

where $\tau_r = 1.43^{-10}/T^5$ is the phonon relaxation time to achieve local thermodynamic equilibrium [60]. The hydrodynamic regime is valid for lower frequencies and higher temperatures. However, at relatively high frequencies around 1 MHz and low temper-

atures around 10 mK, this work is in the collisionless $\Omega\tau_r \gg 1$ regime, where phonon lifetimes can be considered as much greater than their period. In the collisionless regime sound propagation is via phonons, also called a ‘quasiparticle sound mode’ or the ‘zero-sound’ mode [48]; where the average field of these quasiparticles provides the restoring force. This zero-sound is similar to the first-sound, but with an expected modification to the sound velocity of $c_0 = c_1(1 + \rho_n/\rho)$, a slight increase to the velocity at low temperatures. A more important distinction between the two sounds is the different treatment required for acoustic attenuation, covered in the following sections.

1.3.4 Intrinsic Acoustic Attenuation

For a hydrodynamic fluid, sound attenuation originates as losses from viscosity and heat conduction. This is not true for the collisionless regime where the gas of excitations is unable to reach a local thermodynamic equilibrium. Instead sound in this regime must be treated as phonon quasiparticles travelling through the superfluid medium, on which viscosity and heat conduction are not well defined, and attenuation must be derived from interactions with other particles. A full treatment of this is complex and much beyond the scope of this work. However, deep into the superfluid phase (~ 10 mK) where the gas of excitations can be assumed as only phonons, and with a low enough ^3He concentration ($< \text{ppm}$) to be considered single particles which don’t collide with one another, dissipation is much simplified. In this regime of simplified dissipation the only sources of loss intrinsic to the ^4He are phonon-phonon processes, and extrinsic losses can be reduced to only phonon- ^3He interactions and boundary losses, both covered in the next section.

The original theoretical treatment of phonon-phonon processes was developed in [39, 61–63], predicting the three phonon $\sim T^4$ dependence of attenuation below 0.6 K, with some higher order effects, consistent with low pressure experiments [64]. A summary of these concepts can be found in [49], introducing γ the phonon dispersion limit from correction to phonon energy in Eq. 1.26; γ was initially considered to be positive for all pressures. This was inconsistent with experiments at the time [38, 65–68], underestimating low pressure attenuation below ~ 100 mK while overestimating the attenuation

at higher pressures. The inconsistency was due to a positive γ disallowing three-phonon processes, and was corrected in [69–71]. It is now accepted that γ is negative at low pressure where three-phonon processes dominate, accurately measured more recently in Ref. [72]. Note, this provides an interesting prospect of using high pressure to further reduce attenuation in an experiment which has sufficiently isolated an acoustic mode from extrinsic losses. Early work considered only the Landau process, where an acoustic phonon is absorbed by a thermal phonon, leading to attenuation [73]:

$$\alpha_q = \frac{3}{2} \frac{\rho_n^{\text{ph}}}{\rho_0} (u + 1)^2 q [\arctan(2\Omega_q \tau_r) + \arctan(3\gamma \bar{q}_{\text{th}} \Omega_q \tau_r)] , \quad (1.49)$$

where q is the acoustic phonon wave number, Ω_q its frequency, τ_r is the typical phonon relaxation time [60], $\bar{q}_{\text{th}} = 3k_B T / c_0$ is the average thermal phonon momentum, and:

$$u = \frac{\rho_0}{c_0} \frac{\partial c_0}{\partial \rho_0} , \quad (1.50)$$

is the Gröneisen constant, a dimensionless parameter [74]. Eq. 1.49 considers a finite phonon lifetime, set by τ_r and giving rise to the frequency dependence. In the collisionless regime ($\Omega_q \tau_r \gg 1$) this lifetime is long and Eq. 1.49 can be approximated to:

$$\alpha_q = \frac{\pi^3}{30} \frac{(u + 1)^2 k_B^4}{\hbar^3 \rho_0 c_0^6} \Omega_q T^4 . \quad (1.51)$$

This expression is valid for low acoustic phonon frequencies, below the frequency of typical thermal phonons, e.g. $\hbar\Omega_q \ll k_B T$.

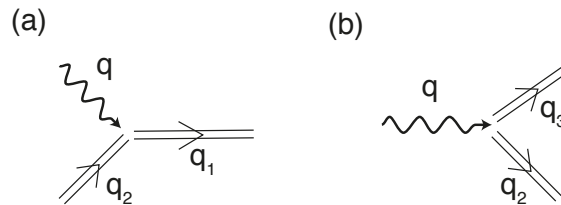


Figure 1.6: Three-phonon Beliaev-Landau process interaction diagrams, wavy lines represent acoustic phonons and double lines thermal phonons. (a) The Landau process, where an acoustic phonon absorbs a thermal phonon, producing a thermal phonon ($q + q_2 \rightarrow q_1$). (b) The Beliaev process, where an acoustic phonon decays into two thermal phonons ($q \rightarrow q_2 + q_3$)

At higher frequencies Beliaev processes become significant, where an acoustic phonon can decay into two thermal phonons [75]. An acoustic phonon being one within a coherent acoustic mode, whereas a thermal phonon represents momentum with random direction from the thermal noise background (Figure 1.6). From the work of Kurkjian *et al.* [75], where the three-phonon damping rates are calculated for a quantum gases, a simplified expression for the low temperature limit damping rate is:

$$\Gamma_q^{\text{Bel/Lan}} \underset{T \rightarrow 0}{\simeq} \frac{(u+1)^2 (k_B T)^5}{8\pi \rho_0 \hbar^4 c_0^5} \tilde{\Gamma}^{\text{Bel/Lan}}(\tilde{q}), \quad (1.52)$$

where \tilde{q} is the dimensionless wave number:

$$\tilde{q} = \frac{\hbar c_0 q}{k_B T}, \quad (1.53)$$

which has been scaled to the typical thermal phonon wave number $k_B T / \hbar c$, and Γ_q^{Lan} is the decay rate due to Landau processes (absorption) while Γ_q^{Bel} is due to Beliaev (decay). $\tilde{\Gamma}^{\text{Bel/Lan}}(\tilde{q})$ are their associated universal functions of \tilde{q} , given by:

$$\begin{aligned} \tilde{\Gamma}^{\text{Bel}}(\tilde{q}) = & \frac{1}{30} \tilde{q}^5 - \frac{4\pi^4}{15} \tilde{q} + 48[\zeta(5) - g_5(e^{-\tilde{q}})] \\ & - 24\tilde{q} g_4(e^{-\tilde{q}}) + 4\tilde{q}^2[\zeta(3) - g_3(e^{-\tilde{q}})], \end{aligned} \quad (1.54)$$

$$\tilde{\Gamma}^{\text{Lan}}(\tilde{q}) = \tilde{\Gamma}^{\text{Bel}}(\tilde{q}) - \frac{1}{30} \tilde{q}^5 + \frac{8\pi^4}{15} \tilde{q}, \quad (1.55)$$

where the Riemann zeta functions correspond to $\zeta(i) = g_i(1)$, and $g_i(z)$ are the Bose functions (also known as polylogarithms $Li_i(z)$), given by:

$$g_i(z) = \sum_{n=1}^{+\infty} \frac{z^n}{n^i}. \quad (1.56)$$

Taking the limit $\tilde{q} \rightarrow 0$ for low frequency phonons well below typical thermal phonon frequencies ($\hbar\Omega_r \ll k_B T$), simplifies the Landau associated universal function to:

$$\tilde{\Gamma}^{\text{Lan}}(\tilde{q}) \underset{\tilde{q} \rightarrow 0}{\simeq} \frac{8\pi^4}{15} \tilde{q}, \quad (1.57)$$

from the limit of the polyarithm. Feeding this into Eq. 1.52 recovers a damping rate equivalent to the attenuation given in Eq. 1.51 ($\Gamma^{\text{Lan}}(q) = 2c_0\alpha_q$):

$$\Gamma^{\text{Lan}}(q) \underset{\substack{T \rightarrow 0 \\ \tilde{q} \rightarrow 0}}{\simeq} \frac{\pi^3}{15} \frac{(u+1)^2 k_{\text{B}}^4}{\hbar^3 \rho_0 c_0^5} \Omega_q T^4, \quad (1.58)$$

corresponding to the Landau dominated regime of very little frequency dependence. The total damping rate is then $\Gamma_q = \Gamma_q^{\text{Lan}} + \Gamma_q^{\text{Bel}}$. This damping has been calculated numerically for various mK temperatures, converted into quality factor $Q_q = \Omega_q/\Gamma_q$ and then plotted against frequency Ω_q in Figure 1.7. The figure shows a near constant quality factor at constant temperature below a certain cutoff frequency, above which the quality factor then tends towards decreasing as Ω_q^{-4} . Even at the lowest dilution fridge temperatures, around 10 mK, this cutoff is much greater than 1 MHz, the expected helium mode frequency in this work.

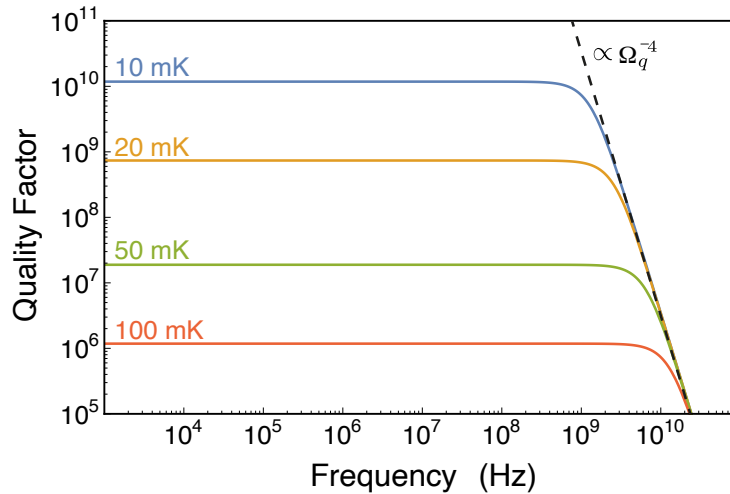


Figure 1.7: Graph showing quality factor of an acoustic mode limited by three-phonon processes vs frequency of that mode $\Omega_q/2\pi$, computed using $\Gamma_q = \Gamma_q^{\text{lan}} + \Gamma_q^{\text{Bel}}$. Plotted for varying dilution fridge mK temperatures: 10 (blue), 20 (orange), 50 (green), 100 (red). The dashed Ω_q^{-4} line represents the frequency dependence once Beliaev processes become significant for $\Omega_q > k_{\text{B}}T/\hbar$.

Now all three-phonon processes have been considered, it is interesting to look at the regime where $\gamma > 0$ and wave number is low enough for a concave dispersion relation.

The regime corresponding to a suppression of three-phonon processes and where four phonon processes become the dominant intrinsic loss. The $\gamma > 0$ regime is entered at ~ 20.4 bar, as measured in neutrino scattering experiments by Beauvois *et al.* [50, 76, 77]. This is a reasonably simple pressure to achieve within a microwave cell mounted on a dilution fridge.

The four-phonon damping rate was originally calculated by Landau and Khalatnikov [78], by considering the anharmonic contributions to the interaction Hamiltonian, though this work ignored certain four-phonon processes of the same magnitude, as proposed by Tucker and Wyatt [79]. A full derivation is beyond the scope of this work, however the work of Kurkjian *et al.* [75] takes into account all significant terms, giving the damping in the low-temperature limit due to four-phonon processes as:

$$\Gamma_q^{2\leftrightarrow 2} \underset{T \rightarrow 0}{\simeq} \frac{(u+1)^4}{128\pi^4} \frac{(k_B T)^7}{\rho_0 |\gamma| c_0^8 \hbar^5} \tilde{\Gamma}^{2\leftrightarrow 2}(\tilde{q}). \quad (1.59)$$

The complete form of $\tilde{\Gamma}^{2\leftrightarrow 2}(\tilde{q})$ is given in Ref. [58], however for this work it is sufficient to consider the asymptotic limits in \tilde{q} . The low \tilde{q} limit is given by:

$$\tilde{\Gamma}^{2\leftrightarrow 2}(\tilde{q}) \underset{\tilde{q} \rightarrow 0}{\simeq} \frac{16\pi^5}{135} \tilde{q}^3, \quad (1.60)$$

and the high \tilde{q} limit is:

$$\tilde{\Gamma}^{2\leftrightarrow 2}(\tilde{q}) \underset{\tilde{q} \rightarrow \infty}{\simeq} \frac{16\pi\zeta(5)}{3} \tilde{q}^2. \quad (1.61)$$

These two limits can be used to calculate an approximate quality factor due to four-phonon processes for expected experimental parameters. Figure 1.8 shows a comparison between the quality factor due to three and four-phonon processes. As expected this shows three-phonon being dominant over four-phonon for expected experimental temperatures, however if it is possible to sufficiently suppress extrinsic losses, then it will be possible to increase the pressure and enter the four-phonon dominated regime. This level of isolation from the environment is difficult, and in a regime of such low loss other quasiparticle interactions could also become significant. A review of phonon-phonon

processes for ^4He can be found in Ref. [80].

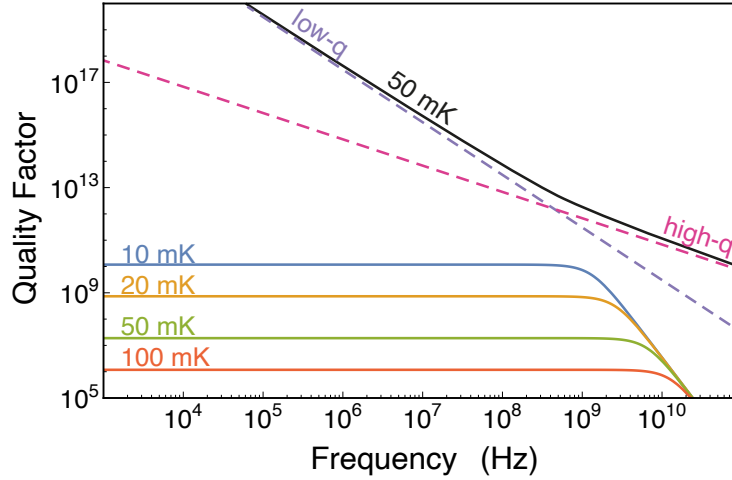


Figure 1.8: Showing quality factor of an acoustic mode alternatively limited by three and four-phonon processes, vs the frequency of that mode $\Omega_q/2\pi$. Blue, orange, green and red lines correspond to three-phonon processes as in Figure 1.7. The dashed lines indicate a quality factor dominated by the asymptotic limits of four-phonon damping at 50 mK, purple for low \tilde{q} , and pink for high \tilde{q} , from Eq.'s 1.60 and 1.60 respectively. The solid black line indicated an approximate quality factor from a qualitative combination of these two limits.

1.3.5 Extrinsic Acoustic Attenuation

^4He is a substance that interacts very little with electromagnetic fields, and for low enough temperatures all non-helium particles are absorbed onto the walls of the container. In this regime ^4He can be considered to have only two sources of extrinsic acoustic losses. Losses due to ^3He particles acting as impurities, and losses associated with the walls of the container.

^3He Losses

Much of the work on sound attenuation due to ^3He has focussed on ‘dilute solutions’, where ^3He makes up roughly a percent of the mixture [81–83]. At this level of concentration, sound attenuation is calculated by solving the Boltzmann equation, including ^3He - ^3He collisions, in the relaxation time approximation [84–86]. A methodology where the ^3He atoms are described as a Fermi gas, whereas for the ultra low concentrations

considered in this work, the ^3He atoms are well above their Fermi temperature ($T \gg T_F$), and are better described as a classical gas.

For the higher concentration viscous regime, the primary loss mechanism is ^3He - ^3He collisions, which maintain a local thermodynamic equilibrium. This regime is for $\Omega_q \tau_\eta \ll 1$, where τ_η is the viscous relaxation time [83]. The relaxation time τ_η should be of similar order to the ^3He - ^3He collision time τ_{33} :

$$\tau_{33} = \frac{l_{33}}{\bar{v}_3}, \quad (1.62)$$

where $l_{33} \approx 8.66 \times 10^{-10}/x_3$ m is the mean free path of a ^3He atom [87], and $\bar{v}_3 = \sqrt{3k_B T/m^*}$ is the RMS thermal velocity of the ^3He . At a temperature of 10 mK and concentration of 1 ppm, this gives $\tau_{33} \approx 0.1$ ms, meaning $\Omega \tau_\eta \ll 1$ is only satisfied below kHz frequencies. Therefore this work at MHz acoustic frequencies (and most superfluid optomechanics) is well outside of this regime, and a different approach is needed.

Natural ^3He impurities can vary from the ppm to ppb range, with purification to the ppt level possible [88]. The Fermi temperature is $k_B T = \hbar^2 k_F^2 / 2m^*$, where m^* is the effective mass and $k_F = (3\pi x_3 \rho_0 / m^*)^{1/3}$ is the Fermi wave number, x_3 being the ratio of ^3He . In the ppm and ppb ranges this corresponds to Fermi temperatures of ~ 0.3 mK and ~ 3 μK respectively, far below dilution fridge temperatures. Above Fermi temperature, the ^3He atoms remain nondegenerate and act as a gas of quasiparticles within the superfluid medium. At these low concentrations, and the ^4He at rest, the ^3He quasiparticles have the energy spectrum [89]:

$$\epsilon_3(k) = \epsilon(0) + \frac{\hbar^2 k^2}{2m^*}, \quad (1.63)$$

where k is the wave vector of the quasiparticle, and m^* is the effective mass of a ^3He atom within the ^4He superfluid at zero pressure [84]. The effective mass is larger than ^3He 's bare atomic mass as it drags ^4He atoms with it, which carry the additional momentum.

For concentrations around the ppm range and frequencies above low kHz acoustic attenuation can be calculated using a classical viscous gas approximation in the viscous regime [90]. As in the work of De Lorenzo [91], where a Q limited by ^3He is calculated to

be $\sim 1 \times 10^8$ at dilution fridge temperatures, for a ~ 10 kHz mode and 0.1 ppm concentration. The dependence on frequency of this attenuation is $\propto \Omega^2$, so would give a quality factor $\sim 1 \times 10^4$ for a 1 MHz resonance. However for MHz frequencies, and especially in below ppb concentrations, the collisionless regime is reached and this approximation is no longer valid. Instead it is possible to estimate the attenuation from the existing theory on transport properties in very dilute solutions [87, 92, 93].

In this regime phonon absorption and emission by ^3He atoms are forbidden, ^3He do not collide with one another and no other quasiparticles are significant; therefore, the ^3He can only provide attenuation via phonon scattering. From Ref. [87] it is possible to calculate the damping rate due to this scattering as:

$$\Gamma_q^{\text{ph-3}} = \frac{x_3 m_4 c_0 q^4}{4\pi \rho_0} J, \quad (1.64)$$

where J is the angular integral:

$$\begin{aligned} J &= \frac{1}{2} \int_0^\pi (A + B \cos \theta)^2 \sin \theta \, d\theta \\ &= A^2 + \frac{B^2}{3}, \end{aligned} \quad (1.65)$$

with $A = -1.2 \pm 0.2$ and $B = 0.70 \pm 0.04$ [84, 94–96].

Figure 1.9 shows the quality factor from this damping rate, at different helium concentrations, compared to three-phonon processes. Clearly damping from phonon- ^3He scattering should not provide a significant loss channel for this work, however care must be taken to remain in the collisionless regime. Outside of this regime phonon absorption and emission will become significant, along with other excitations, and the relationship of ^3He concentration to damping will be greatly enhanced.

Boundary Losses

So far only losses within the helium itself have been considered, whether this be the interactions of excitations with themselves or with ^3He impurities, both loss channels

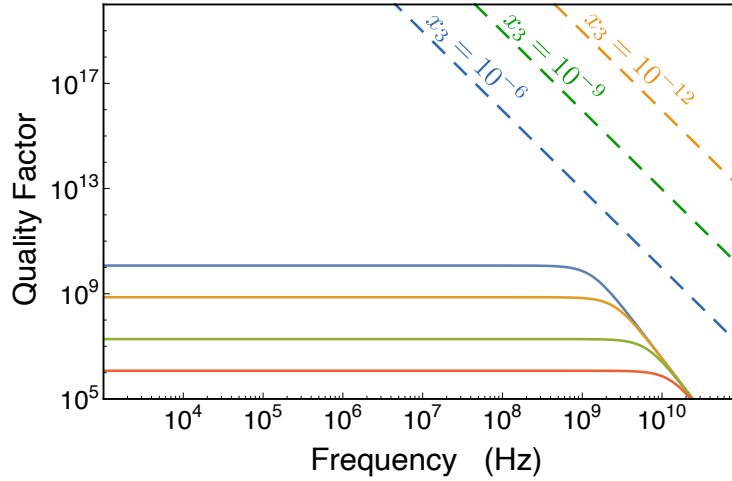


Figure 1.9: Showing quality factor of an acoustic mode alternatively limited by three-phonon processes and phonon- ^3He interactions, vs the frequency of that mode $\Omega_q/2\pi$. Blue, orange, green and red lines correspond to three-phonon processes as in Figure 1.7. The dashed lines indicated a quality factor due to phonon-h3 interactions, calculated from Eq. 1.64 for various ^3He concentrations x_3 : 10^{-6} (blue), 10^{-9} (green), and 10^{-12} (orange).

consider mean free path / phonon lifetime. For a truly bulk helium volume these losses would limit the mean free path, however for a nanoscale confined mode the physical boundaries enclosing the mode can provide a dominant limiting factor. Intuitively, rough walls can completely destroy a mode, as reflected acoustic waves are scattered out of a coherent mode. For smooth walls, especially for the extreme smoothness achievable with modern nanofabrication techniques [97], this effect can be sufficiently minimised to be described by a roughness-dependent mean free path [98]:

$$l_B = l_B^0 \frac{1+S}{1-S}, \quad (1.66)$$

where l_B^0 is the boundary mean free path, defined by the characteristic size of the geometry, and S is the fraction of incident quasiparticles specularly reflected from the walls, a parameter of wall roughness varying from 0 to 1. $1-S$ would then give the fraction of quasiparticles diffusively scattered out of the mode. In addition to the extreme smoothness possible from nanofabrication, superfluid ^4He may uniquely increase S . In the recent work of Heikkinen *et al.* [99], it was shown that 3-4 atomic layers of ^4He on surfaces lead to an enhancement of the specular reflection of ^3He cooper pairs. This

effect was related to the Fermi wavelength of these cooper pairs ($\sim 1 \text{ \AA}$), and so may be greatly enhanced at the longer wavelengths of phonons and ^3He quasiparticles.

Phonons incident on liquid-solid boundaries may be transmitted as well as reflected, which contributes to losses as these transmitted phonons are absorbed by the substrate forming the boundary. An overly simple picture would be to treat the MHz acoustic phonons as thermal and calculate the time constant of cooling $\tau_k = R_k C_{\text{He}}$, where R_k is the Kapitza resistance between the helium and substrate or cavity and then C_{He} is the total helium heat capacity. However, typical thermal phonons at dilution fridge temperatures are an order of magnitude higher in frequency ($\sim \text{GHz}$), and so this picture is insufficient.

Thermal phonons and Kapitza resistance will be covered in more detail in Section 3.1.3, which will also cover transmission of phonons through an impedance mismatch boundary. Phonon transmission across an impedance mismatch can be extended to acoustic phonons which is discussed in Section 2.3.1. Beyond this Section 2.3 treats acoustic attenuation at a boundary by considering the mode as a bulk acoustic wave, where instead of individual phonon reflections or absorptions the substrate participates in the mode, and the material dependent attenuation of the energy within the substrate is the source of loss.

1.4 Superfluid Optomechanics

1.4.1 State of the Art

As introduced in Section 1.1 and then developed in Section 1.3, superfluid helium is a promising material for optomechanics experiments, with low acoustic and dielectric losses. This section will then cover developments in the sub-field of superfluid optomechanics, and give comparison to this work. Table 1.1 gives a list of key optomechanical parameters for this work and other projects in the field.

The most similar experiment to, and a key inspiration of, this project is the work of De Lorenzo *et al.* [3, 5], which utilises a cylindrical 3D superconducting microwave

Table 1.1: Table of the figures of merit for a selection of modern superfluid optomechanical systems reported in literature, compared against the proposal for this work, taking 10^{10} as the mechanical quality factor. Note Childress *et al.* is also a proposal.

Systems	$\Omega_m/2\pi$	$\omega_0/2\pi$	$g_0/2\pi$	C_{eff}
This Work Proposed [40]	1.34 MHz	5 GHz	6.3×10^{-4} Hz	2.81×10^{-6}
De Lorenzo <i>et al.</i> [5]	8.1 kHz	10.6 GHz	4×10^{-8} Hz	3.58×10^{-14}
Kashkanova <i>et al.</i> [7]	317.5 MHz	194.5 THz	~ 3 kHz	1.47×10^{-4}
Shkarin <i>et al.</i> [6]	319 MHz	196 THz	3.6 kHz	5.50×10^{-4}
Childress <i>et al.</i> [100]	0.02 - 1 kHz	300 THz	0.2 - 10 kHz	3.16×10^2
He <i>et al.</i> [29]	1 - 10 MHz	193 THz	133 kHz	2.94×10^{-3}

cavity, which is superfluid leak tight and filled with ^4He . The optomechanical coupling for this system is electrostrictive, where bulk acoustic modes in the superfluid ^4He cause changes in density, and therefore the dielectric properties of a region also containing the microwave cavity mode. The experiment seeks to isolate the bulk acoustic helium mode from vibrational losses, maximising its quality factor. Meanwhile a high microwave quality factor is also achieved via use of a niobium superconducting microwave cavity. These properties make the system viable as a proposed gravitational wave detector [101], with a similar prototype system having now been constructed [102].

While the bulk ^4He resonator system shows low dissipation and high sensitivity, it has very low optomechanical coupling strength. The coupling strength is key to quantum information technologies, which presents another route for optomechanical systems [103]. The obvious way to an enhanced coupling strength is to confine the mechanical and optical modes to a much smaller volume; the path taken by Kashkanova *et al.* [7] and Shkarin *et al.* [6]. Where instead of a 3D microwave cavity, a small optical cavity is created between two single mode optical fibre ends. The fibre ends are machined concave, and turned into distributed Bragg reflectors with alternating deposited layers of different refractive index. The concave shape of the fibre ends then also functions to confined a superfluid ^4He acoustic mode, with good overlap to the optical mode. This confinement and greater overlap works to enhance the electrostrictive optomechanical coupling. However, in these experiments the mechanical quality factor is reduced to $\sim 10^5$, from 10^8 for

the bulk experiment.

Ideally a superfluid optomechanical system would provide a stronger coupling while also maintaining a high mechanical quality factor, which is what this work is seeking to provide, combining a 3D superconducting microwave cavity with a nanofluidic chip. This approach comes with the added advantage of having the optomechanical system be ‘on-chip’, and so easier to integrate with other chip based systems. The idea of an on-chip resonator has been around for some time, with an early proposal by Schwab *et al.* [104], for an on-chip electromechanical Helmholtz resonator. However, it has only been recently that techniques for effective confinement within a nanofluidic chip have been developed, for both ^4He [105], and ^3He [106], with the on-chip Helmholtz resonator being somewhat analogous in terms of fabrication to this work [8, 107]. Moving towards a nanofluidic regime also expands the behaviours of ^4He that can be studied, including the finite scale dependence of the superfluid transition [108], the superfluid correlation length [109], and the bistability of turbulence [110].

Beyond this, another avenue of superfluid optomechanics research is using microtoroid resonators [29, 111], also requiring precise cleanroom fabrication. Here the microtoroids are covered in a thin film of superfluid ^4He , whose whispering gallery mode couples to optical modes in tapered fibres, a system proposed for creating a mechanical qubit and for integration with a phononic crystal [112]. An optomechanical system using a levitated helium droplet has also been proposed [100], combining techniques from levitated optomechanics with superfluid optomechanics, where the focus is on a strong coupling and low optical losses.

1.4.2 Electrostrictive Coupling

Considering the definitions of optomechanical coupling $g_0 = Gx_{\text{zpf}}$ and $G = -\partial\omega/\partial x$, the vacuum coupling can be thought of as $g_0 = -\delta\omega_c^{\text{zpf}}$, with $\delta\omega_c^{\text{zpf}}$ being the cavity resonance shift due to the zero-point motion of the mechanical resonator. The mechanical resonator for this work is formed by oscillating helium pressure waves confined within an on-chip nanofluidic environment, with the chip itself inside the greater microwave cavity. These acoustic pressure waves are density fluctuations of the helium acting as a dielectric

for the microwave cavity mode, causing fluctuations of the permeability and permittivity (dielectric properties) inside the cavity, which in turn changes the energy density and therefore resonant frequency of the cavity mode. So by first relating $\delta\omega_c$ to $\delta\varepsilon$, then to $\delta\rho$, and writing in terms of zero point fluctuation, an equation for the electrostrictive cavity optomechanical coupling g_0 can be obtained.

From Pozar section 6.7 [113] the fractional change in microwave cavity resonant frequency due to material dielectric fluctuations are:

$$\frac{\delta\omega_c}{\omega_c} \simeq -\frac{\int_V \delta\varepsilon |E_0(\mathbf{r})|^2 + \delta\mu |H_0(\mathbf{r})|^2 d^3\mathbf{r}}{\int_V \varepsilon |E_0(\mathbf{r})|^2 + \mu |H_0(\mathbf{r})|^2 d^3\mathbf{r}}, \quad (1.67)$$

where $E_0(\mathbf{r})$ and $H_0(\mathbf{r})$ are the unperturbed fields, \int_V is over the cavity volume, and $\delta\varepsilon$, $\delta\mu$ are the change in permittivity and permeability respectively. The magnetic susceptibility of ^4He , $\chi_M \sim -10^{-7}$ [114], is very small compared to the electric susceptibility $\chi_H = 0.057$ [115]. The above equation can then be simplified via the approximation $\delta\mu \ll \delta\varepsilon$, the fields having equal energy on resonance, and by cancelling ε_0 factors. The equation becomes:

$$\delta\omega_c \simeq -\frac{\omega_c}{2\varepsilon_r} \frac{\int_V \delta\varepsilon_r |E_0(\mathbf{r})|^2 d^3\mathbf{r}}{\int_V |E_0(\mathbf{r})|^2 d^3\mathbf{r}}, \quad (1.68)$$

with $\delta\varepsilon_r$ being the change in relative permittivity of the dielectric. To relate permittivity to density the Clausius-Mosotti Equation [116] is used:

$$\frac{\varepsilon_r - 1}{\varepsilon_r - 2} = \frac{4\pi\rho\alpha_M}{3M}, \quad (1.69)$$

where ρ is the density, α_M is the molar polarisation, and $M = 4.0026$ g/mol is the ^4He the molar mass [117]. Differentiating with respect to ρ , and relating molar polarisation and mass to ε_r via the electric susceptibility gives:

$$\frac{\partial\varepsilon_r}{\partial\rho} = \frac{(\varepsilon_r + 2)(\varepsilon_r - 1)}{3\rho}. \quad (1.70)$$

Using this to write $\delta\varepsilon_r$ in terms of $\delta\rho$:

$$\delta\varepsilon_r = \frac{(\varepsilon_r + 2)(\varepsilon_r - 1)}{3} \frac{\delta\rho}{\rho}. \quad (1.71)$$

To relate to g_0 , $\delta\rho$ must be written as changes due to zero-point motion of the mechanical resonator. Also $\delta\varepsilon_r$ in Eq. 1.68 must be dependent on \mathbf{r} , so expressing $\delta\rho$ in terms of the mode shape function $f(\mathbf{r})$ and zero point motion [33]:

$$\delta\rho(\mathbf{r}) \equiv \delta\rho_{\text{zpf}} f(\mathbf{r}), \quad (1.72)$$

where $\delta\rho_{\text{zpf}}$ is the maximum amplitude of the zero-point density fluctuations due to the superfluid helium resonant mode, and $f(\mathbf{r})$ is the mode shape function. $f(\mathbf{r})$ is normalised from zero to ± 1 such that $|f(\mathbf{r})| \leq 1$, with $f(\mathbf{r}) = 1$ corresponding to the point of maximum acoustic field, this normalisation is valid provided ρ_{zpf} is the maximum physical density fluctuation [33]. Substituting Eq. 1.72 and Eq. 1.71 into Eq. 1.68 gives:

$$g_0 = -\delta\omega_c^{\text{zpf}} \simeq \omega_c \frac{(\varepsilon_r + 2)(\varepsilon_r - 1)}{6\varepsilon_r} \left(\frac{\delta\rho_{\text{zpf}}}{\rho} \right) \frac{\int_V f(\mathbf{r}) |E_0(\mathbf{r})|^2 d^3\mathbf{r}}{\int_V |E_0(\mathbf{r})|^2 d^3\mathbf{r}}. \quad (1.73)$$

To write this equation in terms of factors calculable via finite element modelling (FEM) $\delta\rho_{\text{zpf}}$ must be rewritten, this is achieved via the acoustic energy of the mode and definition of compressibility. On resonance the kinetic and potential energy of an acoustic mode are equal, giving the total energy e :

$$e = \int_V e_{\text{PE}}(\mathbf{r}) + e_{\text{KE}}(\mathbf{r}) d^3\mathbf{r} = 2 \int_V e_{\text{PE}}(\mathbf{r}) d^3\mathbf{r}, \quad (1.74)$$

with $e_{\text{PE}}(\mathbf{r})$ and $e_{\text{KE}}(\mathbf{r})$ the potential and kinetic energies respectively. By definition the energy of the ground state or zero point energy is:

$$\begin{aligned} e &= \frac{\hbar\Omega_m}{2} \\ &= 2 \int_V e_{\text{PE}}(\mathbf{r}) d^3\mathbf{r}, \end{aligned} \quad (1.75)$$

where this has been related to Eq. 1.74 in the second line. Writing the acoustic potential

energy in terms of pressure [118]:

$$e_{\text{PE}}(\mathbf{r}) = \frac{1}{2\rho c^2} (\delta P(\mathbf{r}))^2, \quad (1.76)$$

where c is the speed of sound within the material and $\delta P(\mathbf{r})$ is the pressure differential. Pressure can be related to density via the definition for compressibility:

$$\beta = -\frac{1}{V} \frac{\partial V}{\partial P} = \frac{1}{\rho} \frac{\partial \rho}{\partial P}, \quad (1.77)$$

where V is the volume, and the differential of $\rho = M/V$ is used in the second equality. In the isentropic case:

$$\beta_S = \frac{1}{\rho c^2}, \quad (1.78)$$

where β_S is the compressibility at constant entropy. Using this and Eq. 1.77 to rewrite Eq. 1.76:

$$e_{\text{PE}}(\mathbf{r}) = \frac{1}{2\rho c^2} \left(\frac{\delta \rho(\mathbf{r})}{\rho} \right)^2. \quad (1.79)$$

Substituting this into Eq. 1.75 and rewriting $\delta \rho(\mathbf{r})$ using Eq. 1.72 gives:

$$\frac{\hbar \Omega_m}{2} = \frac{1}{\rho c^2} \left(\frac{\delta \rho_{\text{zpf}}}{\rho} \right)^2 \int_V f(\mathbf{r})^2 d^3 \mathbf{r}. \quad (1.80)$$

Rearranging this to be in terms of $\delta \rho_{\text{zpf}}/\rho$:

$$\frac{\delta \rho_{\text{zpf}}}{\rho} = \sqrt{\frac{\hbar \Omega_m}{2\rho c^2 \int_V f(\mathbf{r})^2 d^3 \mathbf{r}}}. \quad (1.81)$$

Finally substituting this into Eq. 1.73 gives the electrostrictive optomechanical vacuum coupling constant, for an acoustic helium mode within a microwave cavity:

$$g_0 = \omega_c \frac{(\varepsilon_r + 2)(\varepsilon_r - 1)}{6\varepsilon_r} \sqrt{\frac{\hbar \Omega_m}{2\rho_h c_h^2 \int_V f(\mathbf{r})^2 d^3 \mathbf{r}} \frac{\int_V f(\mathbf{r}) |E_0(\mathbf{r})|^2 d^3 \mathbf{r}}{\int_V |E_0(\mathbf{r})|^2 d^3 \mathbf{r}}}. \quad (1.82)$$

To summarise: ρ_h and c_h are the bulk density and speed of sound of the ^4He (acoustic medium), $f(\mathbf{r})$ is the acoustic modeshape function normalised as $|f(\mathbf{r})| \leq 1$, and $|E_0(\mathbf{r})|$ is the electric field magnitude at point \mathbf{r} . $V_{\text{eff}} = \int_V f(\mathbf{r})^2 d^3\mathbf{r}$ represents the effective volume of the acoustic mode, which with ρ_h gives the effective mass. $\int_V f(\mathbf{r})|E_0(\mathbf{r})|^2 d^3\mathbf{r}$ represents an overlap integral between the electronic and acoustic modes, normalised by the denominator below. Eq. 1.82 can also be written in terms of pressure using $g_0 = \partial\omega_c/\partial P \cdot \delta P_{\text{zpf}}$ as [91]:

$$g_0 = \omega_c \beta \delta P_{\text{zpf}} \frac{(\varepsilon_r + 2)(\varepsilon_r - 1)}{6\varepsilon_r} \frac{\int_V f(\mathbf{r})|E_0(\mathbf{r})|^2 d^3\mathbf{r}}{\int_V |E_0(\mathbf{r})|^2 d^3\mathbf{r}}, \quad (1.83)$$

where δP_{zpf} is the maximum pressure difference due to zero point motion of the mode, which when expanded causes the above equation to become Eq. 1.82. This formulation then becomes a powerful tool in designing optomechanical systems, as g_0 is an absolute measure of coupling strength. A measure which is independent of scheme or cavity field, and so can not only be used to compare between different geometries, but also entirely different optomechanical schemes, as in Table 1.1.

1.4.3 Estimated Coupling and Cooperativity

This section will cover the estimation of g_0 and C_{eff} , in Table 1.1, for the optomechanical system in this work. Eq. 1.82 gives the equation with which g_0 is calculated. The system estimated for is a sonic crystal with 100 μm unit cell size, 80 μm pillars, and a height of 250 nm, see Section 2.3 for more details. The capacitive electrode region is approximated to a 40 μm radius circle, at the central defect which hosts the acoustic mode. For this system the microwave frequency is ~ 4.21 GHz, from Section 3.2.1, and the mechanical frequency ~ 1.34 MHz, from Section 2.3.3. $\varepsilon_r^{\text{He}} = 1.057$ is used, along with $\rho_h = 145.1$ kg/m³ and $c_h = 229.5$ m/s¹ [119].

Assuming that the electric and acoustic fields are approximately constant within the capacitive region, the integrals in Eq. 1.82 can be estimated using finite element modelling (FEM), simulating the acoustic and electromagnetic modes separately. For the normalised overlap integral, if acoustic field is assumed constant between the

electrodes, then the integral becomes a constant for the acoustic field, multiplied by the fraction of electric field energy within the capacitor. Which is the participation ratio \mathcal{R}_{gap} from Section 3.2.1, and for the chosen parameters and a silicon chip is $\mathcal{R}_{\text{gap}} = 0.13$. Then the constant value for $f(\mathbf{r})$ between the electrodes, can be estimated by the ratio α_1 of the acoustic field $f(\mathbf{r})$ integrated over the capacitive region, to the integral of $f(\mathbf{r})$ over the entire acoustic mode. For the stated parameters this is calculated as $\alpha_1 = 0.76$.

As mentioned at the end of the previous Section 1.4.2 $V_{\text{eff}} = \int_V f(\mathbf{r})^2 d^3\mathbf{r}$, gives the effective volume of the mode, proportional to its effective mass. For the simulated system in Section 2.3.8 $V_{\text{eff}} = 3.04 \times 10^{-15} \text{ m}^3$, which can also be thought of in terms of the ratio of the volume within the capacitive region V_{gap} , to $\int_V f(\mathbf{r})^2 d^3\mathbf{r}$ integrated over acoustic mode. This then gives $V_{\text{eff}} = V_{\text{gap}}/\alpha_2$, where a larger α_2 means a more concentrated mode, a smaller effective mass, and therefore stronger coupling. For the parameter set above $\alpha_2 = 0.414$.

Combining all the parameters from this section gives an estimated $g_0/2\pi$ of 0.63 mHz, small compared to optical experiments, however four orders of magnitude greater than the other microwave system in Table 1.1. When moving from simulation to experimental testing it will be important to determine the accuracy of simulated factors going into this g_0 estimate. For the estimate of the effective cooperativity, as defined in Section 1.2.3, frequencies and g_0 from this section are used, along with: a mechanical quality factor of 10^{10} , as an upper estimate from the discussion of Sections 1.3 and simulations from Section 2.3; and a microwave quality factor of 10^6 , as discussed in Section 2.2.6. This gives the effective cooperativity C_{eff} of 2.81×10^{-6} , roughly two orders of magnitude below the optical fibre experiments, but eight orders of magnitude above the microwave one.

Chapter 2:

Optomechanical Scheme

This chapter separately covers the microwave and mechanical elements of this work’s optomechanical coupling scheme. Section 2.1 gives a general introduction to the system, a cleanroom fabricated nanofluidic chip with a sonic crystal geometry and on-chip aluminium circuit, which is enclosed within a 3D superconducting microwave cavity. The cavity itself is then filled with superfluid helium, which penetrates the chip, filling the sonic crystal geometry. Section 2.2 covers superconducting microwave cavities, and the expected chip-cavity microwave modes used for the optomechanical coupling. Then Section 2.3 covers nanofluidic confinement of superfluid helium on-chip, and develops the on-chip sonic crystal geometry as a method of confining an acoustic mode for optomechanics experiments, with a specific focus on identifying which loss mechanisms could spoil ^4He ’s ultra-high intrinsic quality factor.

2.1 Overview of Our System

As introduced in Sections 1.1 and 1.4, the motivations for this project are recent advancements in superfluid optomechanics, the importance of confining low dissipation mechanical modes to the future of the field, and the ongoing development of cleanroom fabrication techniques for nanofluidics. This work then proposes and develops the combination of superfluid ^4He nanofluidics, with 3D superconducting microwave cavities. A diagram of the combined nanofluidic ‘chip’ - superconducting microwave cavity system is shown in Figure 2.1.

In more specific terms, the mechanical element of the optomechanical system is an acoustic superfluid helium mode, within a sonic crystal type geometry. The sonic crystal is a square lattice (at least 17×17) of $\sim 80 \mu\text{m}$ diameter cylindrical pillars, with even

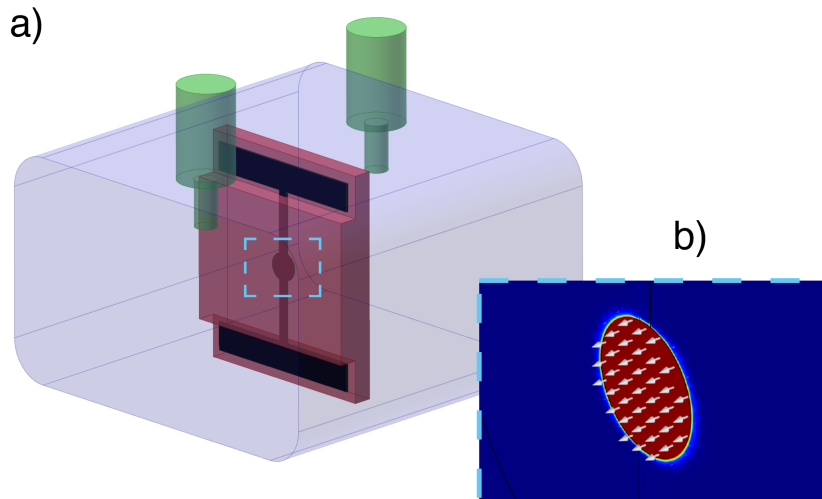


Figure 2.1: Simplified schematic of inside the optomechanical cell. (a) Inside the experimental cell with exaggerated components. The microwave cell volume to filled with helium is shown in blue, with green cylinders representing the two microwave ports and pin couplers. The nanofluidic chip, represented in red, is mounted centrally inside the cavity, with black exposed antennae grounded to the aluminium microwave cavity. These antennae are connected to the central capacitor contained within the chip (dark red), which encloses the point defect of the sonic crystal geometry etched into the nanofluidic chip. (b) shows a zoomed image of the electric field concentrated within this capacitive region, modelled with FEM for the full chip-cavity system. Red showing maximum field and blue minimum, white arrows indicate field direction.

lattice spacing $100\ \mu\text{m}$. ^4He then fills the geometry in between these pillars. Removing a single pillar from the lattice creates a ‘point defect’, a region that can traps the acoustic mode of the system. Figure 2.2 shows a diagram of the sonic crystal geometry, with the point defect highlighted. To fabricate the sonic crystal geometry, the pattern between pillars is etched ($100\text{--}500\ \text{nm}$ deep) into a wafer substrate, and another piece of substrate is bonded on top. This forms a pseudo 2D nanofluidic geometry, of wide and flat pillars, creating a small ^4He volume that can host a concentrated acoustic mode. The physics of the sonic crystal will be developed in Section 2.3, while the cleanroom fabrication of the nanofluidic chips will be covered in Section 3.3, with Figure 3.17 in this section showing a schematic of the full chip design.

For a stronger optomechanical coupling the electric field also must be concentrated to the same region as the acoustic mode. To achieve this, thin ($\sim 50\ \text{nm}$ deep) aluminium electrodes are fabricated above and below the point defect region, forming a parallel plate capacitor around the acoustic mode. To electronically connect to these electrodes two narrow ($10\ \mu\text{m}$ wide) aluminium wires are deposited, leading from the central electrodes

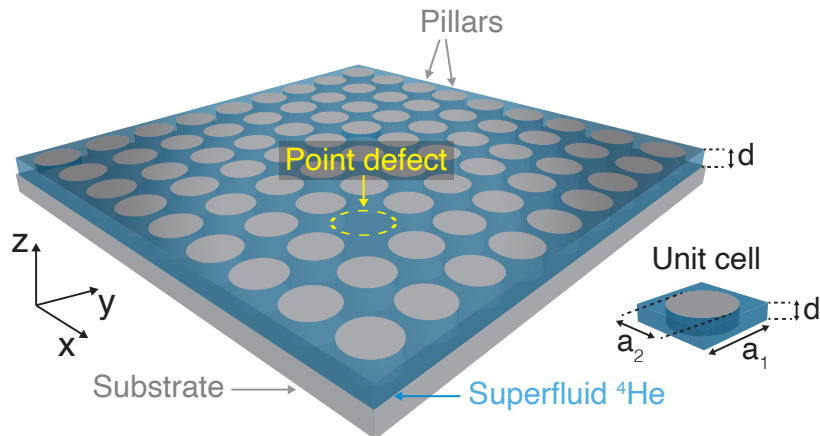


Figure 2.2: Diagram of the pseudo 2D sonic crystal, formed by a regular square array of cylindrical substrate pillars (grey), with the volume between pillars filled with superfluid ^4He (blue). The physical crystal is enclosed by another flat substrate bonded on top. The lattice’s ‘point defect’, shown in yellow, is a unit cell without a pillar that will trap the acoustic mode of the optomechanical system. On the RHS is shown a unit cell with typical size $a_1 \sim 100 \mu\text{m}$, pillar diameter $a_2 \sim 80 \mu\text{m}$, and height $d \sim 100 \text{nm}$.

to large aluminium contact pads on the top and bottom of the nanofluidic ‘chip’. The two pieces of wafer substrate that form the chip enclose the nanofluidics, and most of the deposited aluminium, excluding the contact pads which are exposed. The chip is $\sim 10 \times 10 \text{mm}$ and is placed within a microwave cavity of similar size.

The contact pads on the nanofluidic chip are left exposed so they can be grounded to the 3D superconducting aluminium microwave cavity, with indium foil, creating a hybrid microwave resonator. The central chip electrodes become the dominant capacitance of the cavity, concentrating the electric field to same region as the acoustic mode. The aluminium microwave cavity is itself enclosed within a superfluid leak tight copper cavity (not involved in the microwave mode), which is closed using soft soldered connections and an indium seal. Figure 2.3 shows the disassembled cell, including a silicon chip, the superconducting aluminium microwave cavity, and the superfluid leak tight copper cavity. The physics of the microwave cavity is covered in Section 2.2, and then from a microwave network analysis perspective in 4.1. The practical aspects of designing and fabricating the aluminium and copper cavities are covered in 3.2, with technical drawings in Appendix A.

The cavity is mounted on the experimental stage of a dilution fridge capable of

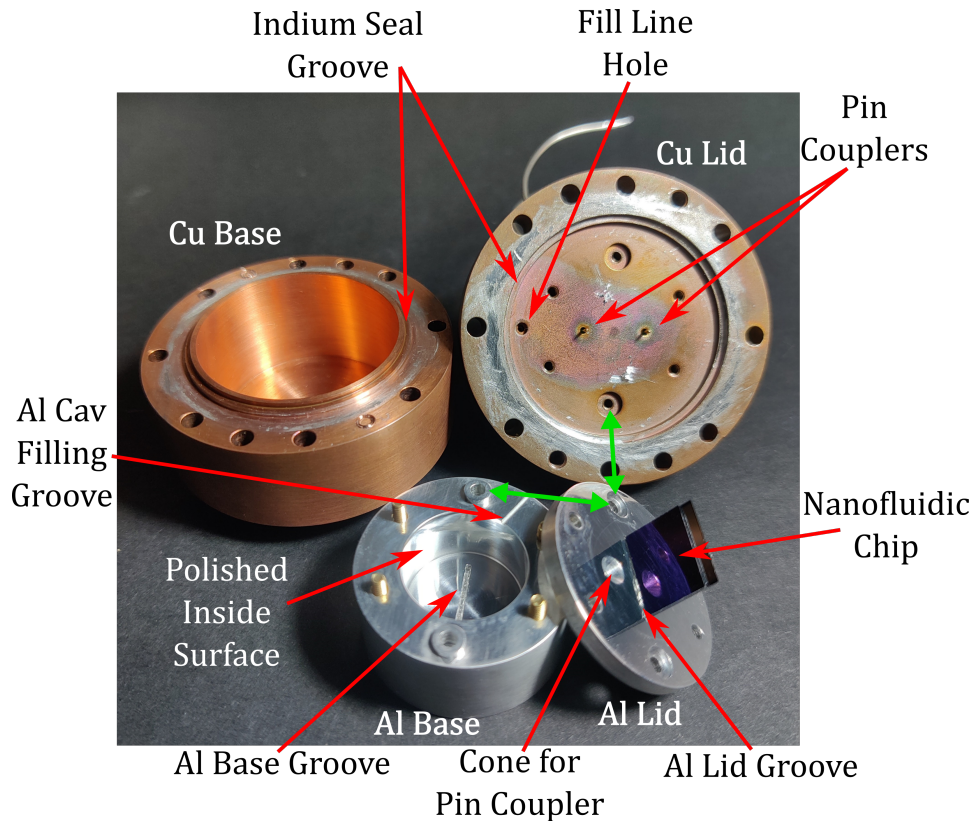


Figure 2.3: Back left: copper cavity base. Back Right: copper cavity lid, with two central pin couplers, and six threaded holes for attaching the aluminium cavity, the fill line enters via the extra hole on the LHS of the inner surface. Front Left: the aluminium cavity base, with polished inside surface and slot for the chip to sit in. The screws through the aluminium base screw through the aluminium lid and into the copper lid, clamping the aluminium cavity together and to the copper, as indicated by the green arrows. Front right: the aluminium cavity lid with the silicon chip inserted with indium foil. The other end of the chip will then slot into the aluminium base. Slightly to the left of where the chip meets the aluminium the ‘coupling cone’ can be seen, which is the region the copper lid’s pin couplers will protrude into.

reaching 23 mK. To fill both the cavities and the nanofluidic chip with superfluid ^4He , a fill line is brought from room temperature (RT), with thermalisation at each fridge stage, and connected to the lid of the copper cavity. Microwave signals are coupled into the cavity via an attenuated ‘in’ microwave line from RT, while signals are coupled out via a superconducting and amplified ‘out’ line from the cavity to RT. Both lines are thermalised between RT and the experimental stage. Details of the dilution fridge experimental platform are found in Section 3.1, while the treatment of the total microwave circuit can be found in Chapter 4

For the chip-cavity system the size of the sonic crystal determines the acoustic

frequency, which is of order 1 MHz; while the combination of cavity size and electrode capacitance determines the microwave resonance frequency, which is ~ 5 GHz, and kept within the 4 – 12GHz operating range of the greater microwave circuit. The microwave mode is normally dominated by the central electrode capacitance, with area ~ 0.01 mm² giving a capacitance ~ 1 pF, which then corresponds to an inductance in the nH range for the expected frequency. The expected optomechanical coupling strength of this system is $g_0/2\pi \approx 1$ mHz, from Section 1.4.3.

2.2 Superconducting Cavities

Due to strong reflection of electromagnetic waves at conductive surfaces, it is possible to trap eigenmodes of specific wavelengths inside conductive boxes. These modes are found by solving Maxwell's equations with appropriate boundary conditions. For rectangular and cylindrical cavities it is possible to use the Transverse Electro-Magnetic (TEM) waveguide solutions with short conditions at both ends (as in Pozar [113]).

2.2.1 Rectangular Cavity Modes

TEM modes of waveguides are split into: Transverse Electric (TE) modes and Transverse Magnetic (TM) modes, where there is either no electric or no magnetic field in the direction of propagation. The resonant TEM frequencies of a rectangular cavity can be calculated by taking a rectangular waveguide shorted at both ends. The mode shape of the electric field is a standing wave with nodes at the cavity edges. The frequencies f_{mnl} of the resonant TE_{*mnl*} and TM_{*mnl*} modes are given by the equation [113]:

$$f_{mnl} = \frac{ck_{mnl}}{2\pi\sqrt{\mu_r\epsilon_r}}, \quad (2.1)$$

where the numbers *mnl* refer to the number of half wavelengths of the TE or TM standing wave in the $x - y - z$ planes of the cavity, c is the speed of light in the medium, μ_r and ϵ_r are the relative permeability and permittivity respectively, and k_{mnl} , the wave number of the mode, is given by:

$$k_{mnl} = \sqrt{\left(\frac{m\pi}{a}\right)^2 + \left(\frac{n\pi}{b}\right)^2 + \left(\frac{l\pi}{d}\right)^2}, \quad (2.2)$$

where a, b, d are the dimensions of the sides of planes m, n, l respectively. This TM and TE naming convention depends on the choice of propagation direction (z), which is less meaningful for a cavity. However the choice is important to distinguish between modes such as TM_{111} and TE_{111} , which are degenerate in frequency. Note on resonance an equal proportion of energy is stored in the electric and magnetic fields, this is true for all cavities and is analogous to energy storage in an LC circuit resonator.

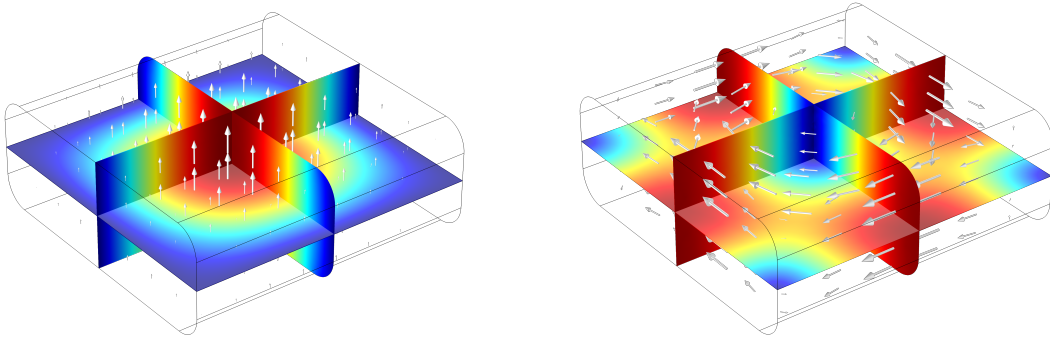


Figure 2.4: Left: Electric field norm of a rectangular cavity TE_{101} mode. Right: Magnetic field norm of a rectangular cavity TE_{101} mode. Arrows show field direction and have size proportional to strength, while the heat map shows relative magnitude of the norm.

Figure 2.4 shows the TE_{101} mode of a rectangular cavity, with arrows showing field direction. This is the fundamental (lowest f_0) mode of a cavity of this shape. Filleted corners in one direction simplify fabrication while helping to remove degeneracies.

2.2.2 Cylindrical Cavity Modes

Similarly to rectangular cavities, the TE and TM modes of a cylinder can be found with short conditions on the two ends of a cylindrical waveguide, giving the same standing wave form in the \hat{z} direction. The TM and TE cylindrical modes do not follow the same equations for frequency, which can lead to unexpected degeneracies based on cavity dimensions. Both modes are specified by the indices n, m, l which give the number of nodes in the electric field for directions ϕ, ρ, z respectively [113].

The frequency of the TE_{nml} modes are given by:

$$f_{nml} = \frac{c}{2\pi\sqrt{\mu_r\epsilon_r}} \sqrt{\left(\frac{p'_{nm}}{a}\right)^2 + \left(\frac{l\pi}{d}\right)^2}, \quad (2.3)$$

where p'_{nm} is the m -th zero of the derivative of the n -th Bessel function. Then the frequency of the TM_{nml} modes is given by:

$$f_{nml} = \frac{c}{2\pi\sqrt{\mu_r\epsilon_r}} \sqrt{\left(\frac{p_{nm}}{a}\right)^2 + \left(\frac{l\pi}{d}\right)^2}, \quad (2.4)$$

where p_{nm} is the m -th zero of the n -th Bessel function. The fundamental TM_{010} mode shape is very similar to the TE_{101} mode of the rectangular cavity. Figure 2.5 shows the TE_{011} mode, useful for being a lower frequency mode with the highest potential quality factor. This is due to minimum electric field and low magnetic field at all cavity walls, minimising dielectric and conductor losses respectively. This mode also allows for locating seams at minima of both electric fields minimising associated losses. These effects are discussed further in Section 2.2.7.



Figure 2.5: Left: Electric field norm of a cylindrical cavity TE_{011} mode. Right: Magnetic field norm of a cylindrical cavity TE_{011} mode. Arrows show field direction and have size proportional to strength, while the heat map shows relative magnitude of the norm.

2.2.3 Re-entrant Cavities

Re-entrant cavities differ from cylindrical or rectangular cavities by the inclusion of, at least one, conductive re-entrant ‘stub’ or ‘pillar’ which extends from one of the interior

surfaces. An example of this geometry is shown in the first image of Figure 2.9. This stub usually extends close to the opposite interior surface, concentrating the electric field of the fundamental mode within the region between the two surfaces, forming a ‘capacitive’ region. The magnetic field is then concentrated around the pillar in the $\pm\phi$ direction. The concentrated fields of the fundamental mode and the well separated higher modes [120], are advantages of this cavity geometry. Both the electric and magnetic fields of the fundamental mode are shown in Figure 2.6. These differ from the quarter wavelength stub style cavities becoming popular in quantum information studies [121], where the stub acts to define the wavelength of the resonator, rather than the dominant capacitance of the cavity. These cavities, at small gap sizes, work well as analogies to the nanofluidic chip-cavity system as they also contain dominant capacitive regions with surrounded by larger inductive volumes. This analogy may also prove useful for creating multi-stub simulations that mimic more complex on chip geometries [122].

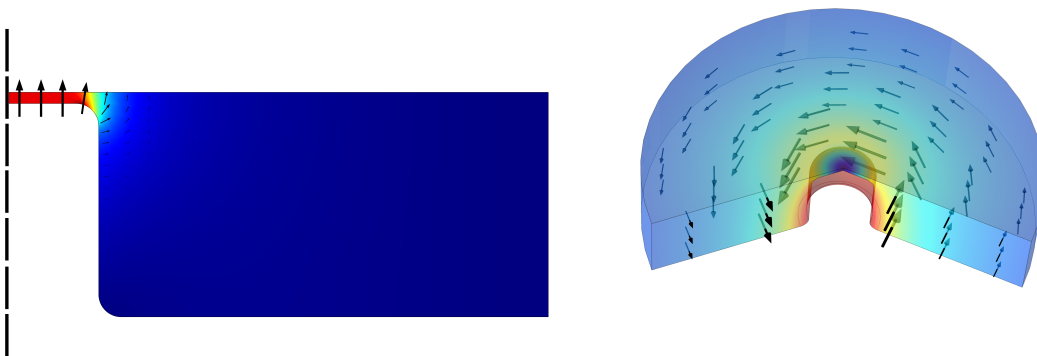


Figure 2.6: Left: 2D axisymmetric cross section (rotated around the dashed line) showing the electric field norm of a cylindrical re-entrant cavity’s fundamental mode. Right: Magnetic field norm of a cylindrical re-entrant cavity’s fundamental mode, a slice of the cylinder has been removed from the plot for clarity. Arrows show field direction and have size proportional to strength, while the heat map shows relative magnitude of the norm.

2.2.4 Circuit Representations

Any microwave cavity can be generalised to an RLC lumped element resonator, in either series or parallel equivalent representations. The parallel arrangement is shown in

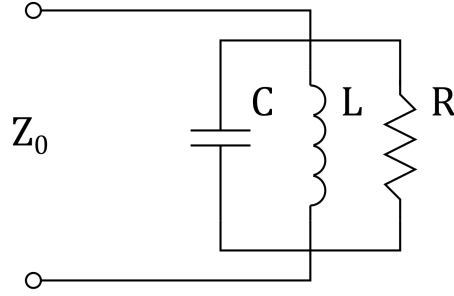


Figure 2.7: A simple diagram of a parallel RLC circuit terminated with characteristic impedance Z_0 .

Figure 2.7. A simple equation for the resonant frequency f_0 of an RLC circuit is:

$$f_0 = \omega_0/2\pi = \frac{1}{2\pi\sqrt{LC}}, \quad (2.5)$$

where L is the inductance and C the capacitance. Using this and the knowledge that on resonance energy stored in the electric field is equal to energy stored in the magnetic, the L and C parameters can be written in terms of the TE and TM modes as:

$$L_{mnl} = \mu k_{mnl}^2 V, \quad (2.6)$$

$$C_{mnl} = \frac{\epsilon}{k_{mnl}^4 V}, \quad (2.7)$$

where V is the volume, mnl the mode number, μ the absolute magnetic permeability and ϵ the absolute permittivity.

Capacitor Terminated Coax

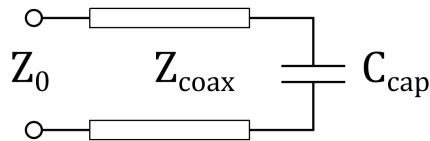


Figure 2.8: A simple diagram of a coaxial cable impedance Z_{coax} terminated in a capacitor of capacitance C_{cap} and connected to an outside line impedance Z_0 .

The RLC analogy can also be used for a re-entrant cavity, however the simple equations for L_{mnl} and C_{mnl} will not hold as the mode is no longer TE or TM. Instead the entire cavity can be approximated to a coaxial cable terminated in a capacitor (Figure 2.8) [123]. This approximation works, including modifications for conical stubs, provided the capacitance of the gap region is significant compared to that of the coax $C_{\text{cap}} \gtrsim C_{\text{coax}}$.

This simple diagram is useful but the circuit can be redrawn in a way analogous to the RLC circuit, where the L and C parameters can be calculated. Figure 2.9 shows a diagram for the dimensions of a re-entrant cell, along with its RLC representation. Only coaxial inductance is present, as the gap is assumed small enough to treat the outer region as a single inductance.

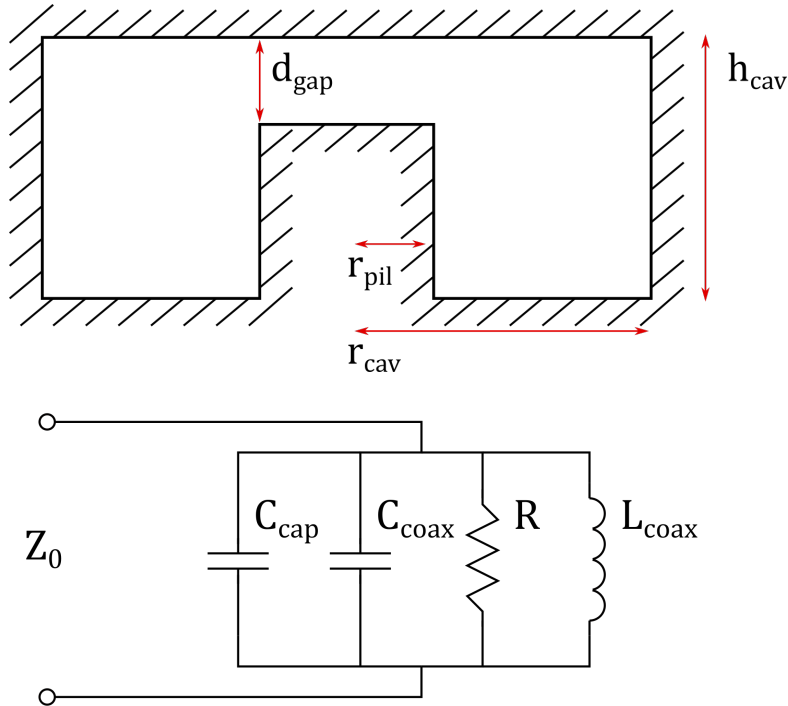


Figure 2.9: Top: diagram with labelled dimensions of a simple cylindrical re-entrant cavity. Bottom: A circuit diagram of a re-entrant cavity as an equivalent RLC circuit, terminated in characteristic impedance Z_0 .

For a capacitive region with a small d_{gap} to r_{pil} aspect ratio the electric field in the gap can be treated as linear, in this case the equation for a parallel capacitor can be used:

$$C_{\text{cap}} = 2\pi\epsilon r_{\text{pil}}^2/d_{\text{gap}} , \quad (2.8)$$

where r_{pil} is the radius of the re-entrant pillar, and d_{gap} is its distance to from the opposing surface. Using the standard equations for a coaxial cable the coaxial capacitance C_{coax} can be written:

$$C_{\text{coax}} = \frac{2\pi\epsilon h_{\text{cav}}}{\ln(r_{\text{cav}}/r_{\text{pil}})} , \quad (2.9)$$

where h_{cav} is the height of the cavity (length of the coax) and r_{cav} is the radius of the cavity (outer radius of the coax). This can then be related to a general parallel RLC cavity via $C = C_{\text{cap}} + C_{\text{coax}}$. L_{coax} the coaxial inductance can then be written:

$$L_{\text{coax}} = \frac{\mu h_{\text{cav}}}{2\pi} \ln(r_{\text{cav}}/r_{\text{pil}}) , \quad (2.10)$$

with all terms defined as previously. Note if the internal system is assumed lossless $Z_{\text{coax}} = \sqrt{L/C}$, though in practise this will be modified by internal and external losses. The capacitor terminated coax approximation works well for small gaps and cylindrical/conical stubs, while for larger gaps the RLC parameters of a re-entrant cavity can also be treated generally as in [124]. For more complex geometries finite element modelling (FEM) becomes more accurate and convenient [125].

2.2.5 Chip - Cavity Modes

For the chip-cavity system, the chip is mounted vertically in a cylindrical cavity, with two small overlapping electrodes at the cavity centre (forming a parallel plate capacitor), and thin wires running vertically from these electrodes to large antennae. An exaggerated example of this is shown in Figure 2.1, while Figure 3.17 show the on-chip circuitry in greater detail. Though the geometry of the chip-cavity system differs from a simple re-entrant stub, it still contains a dominant capacitive region with small gap size (central electrodes), and lengths of conductor running through the centre of the cavity (electrode-antenna wires). Instead of a stub extending close to an opposing face, there are thin

wires propagating from opposing surfaces to a central capacitor. These similarities to the re-entrant cavity allow use of the capacitor terminated coax approximation, though due to the more complex geometry and dielectric effect of the chip substrate, FEM is required for accurate results. FEM of the microwave cavity will be discussed in more detail in Section 3.2.

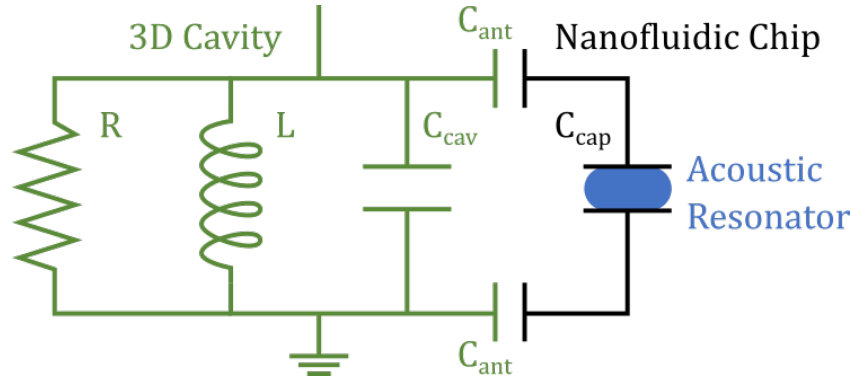


Figure 2.10: RLC lumped element circuit diagram of the chip-cavity system, for the antenna coupling scheme. Green represents the 3D aluminium cavity, black the on-chip circuit, and blue the acoustic resonator which alters C_{cap} .

Figure 2.10 show an LC circuit representation of the chip-cavity system. The on-chip capacitor formed by the electrodes tends to dominate the capacitance of the system $C_{cap} \gg C_{cav}$, for a 250 nm gap and 60 μm square electrode C_{cap} is of order 100 fF, while C_{cav} is around 5 fF for the cavities used in this work. There are two options considered for connecting the on-chip circuit to the cavity mode. The first is via large antennae that capacitively couple to the cavity mode [126], and the second is via ‘galvanic coupling’ where the antenna are grounded to the inside cavity surface [127], which is equivalent to both antenna capacitances, C_{ant} in Figure 2.10, becoming direct connections. Galvanic coupling is chosen as it avoids introducing hard to calculate additional capacitances that are sensitive to chip position inside the cavity.

Although the ^4He acts as the dielectric for the dominant capacitor, the expected $\delta\epsilon$ from the mechanical oscillations is low, leading to a low expected δC . Meaning the system can be treated similarly to more standard optomechanical systems, where an on chip coplanar waveguide is capacitively coupled to a mechanical oscillator. Coupling into and out of the chip-cavity system will be covered in Section 3.2.

For a chip-cavity system with a fundamental mode ~ 4 GHz, there should be three modes (including fundamental) within the 4 - 12 GHz operating range of the measurement circuit, taking into account the chip substrate's dielectric effect. The fundamental mode is the focus of this work, as its electric field is most concentrated within the defect. It may also be possible to detect optomechanical coupling for the third mode, while the second mode is not useful for this purpose as its electric field is distributed along the on-chip wire.

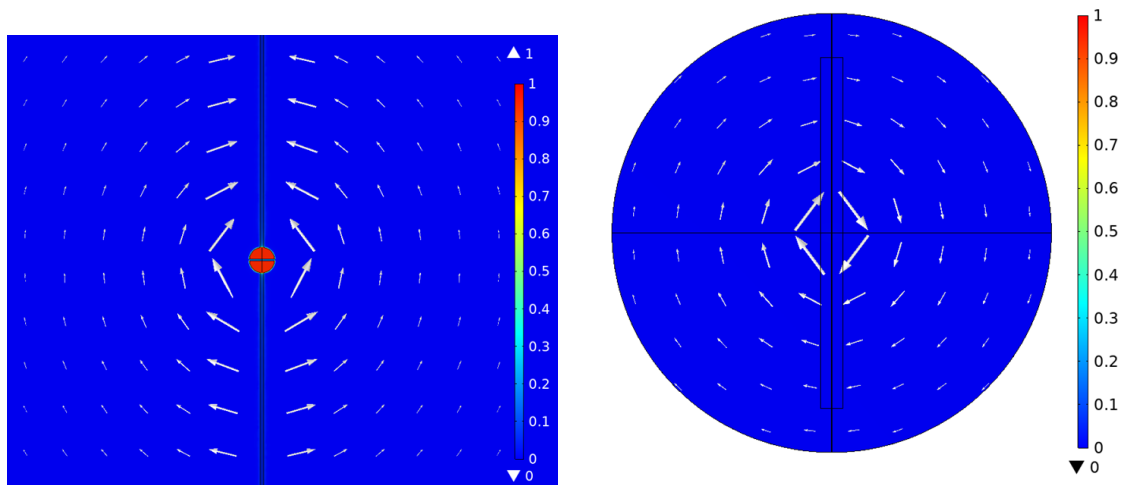


Figure 2.11: Left: Electric field norm for the fundamental mode of the chip-cavity system, zoomed into the central electrode region. Right: Magnetic field norm for the fundamental mode of the chip-cavity system, for a ‘top down’ $x - y$ plane cut at the the electrode level. Fields have been normalised from 0 to 1 and arrows show field direction with size proportional to strength.

Figure 2.11 shows the electric and magnetic fields of the first mode, as in Figure 2.1 the chip sits vertically in the cylindrical cavity, with the electrodes overlapping at the centre; however, here the on chip circuitry matches more closely to that in Figure 3.17, with the two large antennae not visible as they are grounded within the top and bottom of the cylindrical cavity. Similarly to the re-entrant cavity, the electric field of this system is concentrated within the capacitive region formed by the electrodes, and the magnetic field circles the central conductor (antenna-electrode wires). The electric field in the wider cavity follows lines from the bottom to top wire, and can be approximated as vertical far from the centre radially. This simple mode is ideal for the optomechanical scheme in this work, with its electric field highly concentrated at the centre, and low but predictable elsewhere.

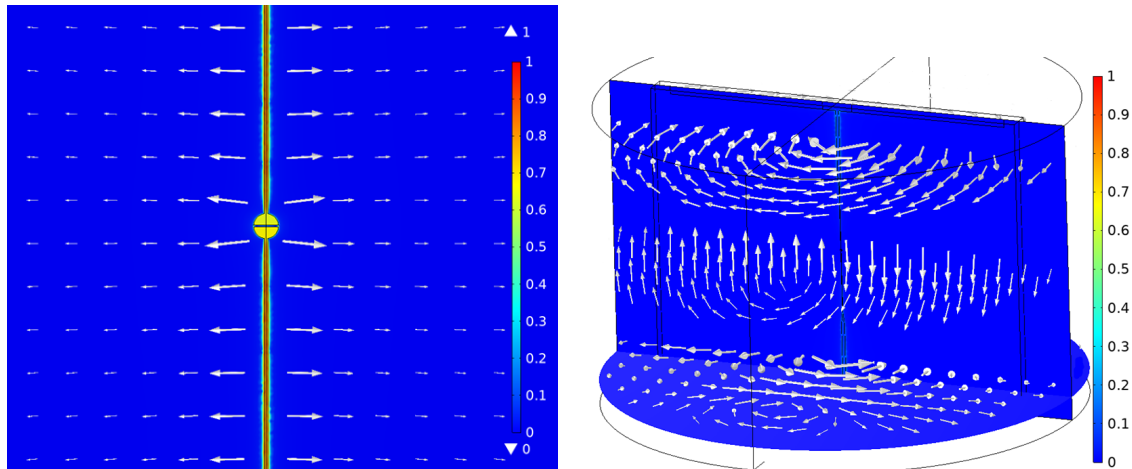


Figure 2.12: Left: Electric field norm for the second mode of the chip-cavity system, zoomed into the central electrode region. Right: Magnetic field norm for the second mode of the chip-cavity system, with arrows in three $x - y$ planes above, below and at the electrode level. Fields have been normalised from 0 to 1 and arrows show field direction with size proportional to strength for electric and logarithmically for magnetic.

Figure 2.12 shows the electric and magnetic fields of the second mode. The Electric field is concentrated along the on chip aluminium, with generally radial field direction, though curving away from the cavity centre at larger distances from the electrodes. The modeshape is similar to a coaxial mode, with the capacitor playing a less significant role than the other two modes. The magnetic field circles the central wire, similarly to the first mode, but then changing direction of circulation as the $x - y$ plane passes the electrodes. An effect of the microwave port (not shown) causes the smaller circulating magnetic field at the base of the diagram, this effect is visible due to how weak the magnetic field is away from the central wire.

Figure 2.13 shows the electric and magnetic fields of the third mode. Similar to the first mode the electric field is concentrated in the capacitive region. The direction is also similar, however the vertical field further from the central wire is of opposing direction to the field across the electrodes. The magnetic circulates the central wire in the $x - y$ plane, but with a change of direction fairly close to the electrodes.

The magnetic field density for all modes is concentrated around the central electrode to antenna wires, and so is low in the greater cavity volume, though it is useful to consider as it gives another window into the mode number.

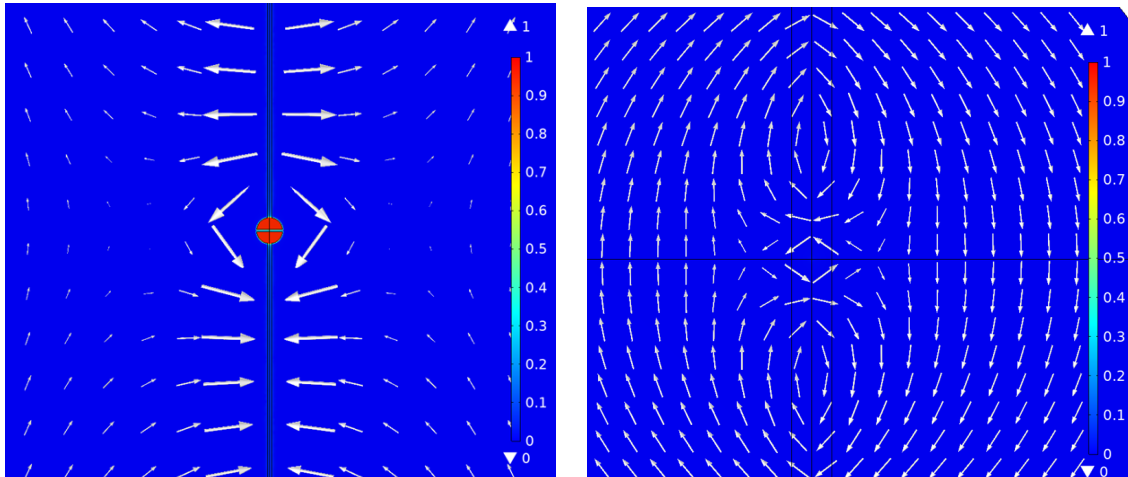


Figure 2.13: Left: Electric field norm for the third mode of the chip-cavity system, zoomed into the central electrode region. Right: Magnetic field norm for the third mode of the chip-cavity system, for a ‘top down’ $x - y$ plane cut at the the electrode level. Fields have been normalised from 0 to 1 and arrows show field direction with size proportional to strength for electric and logarithmically for magnetic.

2.2.6 Cavity Quality Factor

So far the cavities have been primarily considered in terms of resonant frequency and fields, to fully characterise the cavities dissipative effects must also be considered. This work focusses on quality factor as a generalisation of losses, as introduced in Sections 1.2.3, with cavity losses broadly being broken up into internal and external effects with associated quality factors Q_0 and Q_e . Q_e will be discussed in Section 3.2 when considering the cavity coupling design, and the relationship of these factors to the total Q_L will be explored in Section 4.1 in the language of microwave network analysis.

3D cavities are selected over more common on-chip resonators as they have the potential for much higher quality factors (above 10^6). The capacitive pin coupling into the cavity also has the potential to provide a lower loss connection and more controllable impedance mismatch than wire bonding, with the additional bonus of not requiring an on chip ground plane, which may disturb the nanofluidic environment and complicate chip fabrication.

Q_0 , the internal cavity quality factor, accounts for dielectric losses and losses at cavity walls, and so is generally determined by material choice and surface preparation. In general the lower frequency modes of a cavity have higher quality factors, which are

often selected for use in experiments. For room temperature applications polished high conductive copper is often used, with quality factors $\sim 10^5$ possible [128], but values $10^3 - 10^4$ more common [129]. Cooling to cryogenic temperatures can help improve this quality factor by up to an order of magnitude [130].

To achieve much higher quality factors superconducting materials are used in cavity fabrication. For this work aluminium is chosen due to the relative availability in high purity and simplicity of machining. Aluminium superconducting microwave cavities can routinely exceed quality factors of 10^6 , with values greater than 10^8 possible with pure samples and surface treatments [131, 132].

Alternatively copper cavities plated in a superconducting material can be used, with tin plating giving quality factors $\sim 10^5$ [133] and lead plating achieving $> 10^{10}$ [134]. Pure niobium cavities are also sometimes used, achieving the highest quality factors $\sim 10^{11}$ [135], though $> 10^8$ is more routinely achievable [136]. Generally achieving a temperature far below the superconducting transition temperature T_c gives a higher quality factor, though surface quality and any oxide layer will also play a role.

Though aluminium produces quality factors on the lower end for superconductors, the introduction of the nanofluidic chip into the cavity is expected to produce microwave losses that would dominate over the higher aluminium quality factors. Moving to niobium on-chip may reduce these additional losses, and also allow testing of the chip-cavity system at liquid helium temperature (4.2 K). Reduction of on-chip microwave losses remains an important area of study for optomechanics and quantum information technologies [137].

2.2.7 Cavity Internal Losses

There are many types of internal losses associated with microwave cavities: dielectric loss, conductor loss and contact resistance (seam loss), tend to dominate 3D cavities and will be discussed in this section [138, 139]. For very pristine 3D cavities and concentrated on chip circuits, other factors can become significant to the internal quality factors, including two level systems (TLS) when approaching a quantum regime [137]. As introduced in Section 1.2.3, the quality factor from a specific loss mechanism is the

ratio of total energy stored in the entire mode, to energy dissipated by that mechanism per cycle. This is complicated slightly in a physical 3D cavity, where the energy distribution of the system must be considered, as the power dissipated by a loss mechanism is usually expressed as a function of the energy stored in specific regions. To account for this participation ratios are used to account for the ratio of energy stored in a dissipative medium, to the total energy stored in the mode. A general ratio is then defined [140]:

$$\mathcal{R} = \frac{\text{Energy Stored in Medium}}{\text{Total Energy}} . \quad (2.11)$$

Dielectric Loss

Dielectric loss is associated with the material filling the cavity volume, usually expressed as loss tangent $\tan \delta$, which for a single dielectric filling the whole volume relates to quality factor as $\tan \delta = 1/Q_{\text{diel}}$. This is negligible for the areas of helium dielectric as $\tan \delta_{\text{h}} < 10^{-10}$ at 1.5 K [4]. However for the nanofluidic chip material $10^{-3} < \tan \delta_{\text{sub}} < 10^{-7}$ are expected [141], which may limit the overall quality factor depending on the substrate's participation ratio. The aluminium used within the superconducting cavity and chip may also cause dielectric loss due to the surface layer of aluminium oxide [142, 143]. Therefore the participation ratio's for each individual dielectric $\mathcal{R}_{\text{diel}}$ becomes important:

$$\mathcal{R}_{\text{diel}} = \frac{\int_{\text{diel}} \epsilon_{\text{diel}} |E(\mathbf{r})|^2 d^3\mathbf{r}}{\int_V \epsilon(\mathbf{r}) |E(\mathbf{r})|^2 d^3\mathbf{r}} , \quad (2.12)$$

where $E(\mathbf{r})$ is the electric field and point \mathbf{r} , ϵ_{diel} is the permittivity of the dielectric corresponding to $\mathcal{R}_{\text{diel}}$, and $\epsilon(\mathbf{r})$ is the permittivity at point \mathbf{r} . The integral in the numerator is over the volume of the dielectric corresponding to $\mathcal{R}_{\text{diel}}$, while the denominator is over the entire mode volume. This is equivalent to the electric field energy distribution between the materials, and shows the importance of the aluminium oxide within the central capacitor, a material with a much higher permittivity and loss tangent than ${}^4\text{He}$, where the electric field density is already most concentrated.

Conductor Loss

Conductor loss, associated with magnetic fields at surfaces, is usually the dominant loss factor for room temperature cavities [113]. For superconductors this is not necessarily the case, though some conductive effects are still expected at the surfaces and may still dominate in certain regimes. The quality factor due to conductive losses can be written generally in terms of the sheet resistance R_s as:

$$Q \approx \mathcal{G}/R_s, \quad (2.13)$$

where \mathcal{G} is a geometric factor expressed in Ohms. This geometric factor can be written as:

$$\mathcal{G} = \frac{\omega_c \mu_0 \int_V |H(\mathbf{r})|^2 d^3 \mathbf{r}}{\int_S |H(\mathbf{r})|^2 d^2 \mathbf{r}}, \quad (2.14)$$

where $H(\mathbf{r})$ is the magnetic field at point \mathbf{r} , \int_V is over the mode volume, and \int_S covers the material surface seen by the mode. Inverting the two integrals and multiplying the surface integral by a skin depth (converting to a volume) gives a form similar to \mathcal{R} , which allows writing the conductive participation ratio of a material as:

$$\mathcal{R}_{\text{cond}} = \frac{\delta_s \int_S |H(\mathbf{r})|^2 d^2 \mathbf{r}}{\int_V |H(\mathbf{r})|^2 d^3 \mathbf{r}}, \quad (2.15)$$

where δ_s is the skin depth, also known as λ the penetration depth of a superconductor, typically of order 10 nm, and for aluminium specifically 16 nm [144]. This participation ratio is also known as α the ‘kinetic inductance fraction’ [145]. Substituting Eq. 2.15 into Eq. 2.14, and then Eq. 2.13, a quality factor due to conductive losses can be written:

$$Q_{\text{cond}} = \frac{\omega_c \mu_0 \delta}{R_s \mathcal{R}_{\text{cond}}}. \quad (2.16)$$

$\omega_c \mu_0 \delta$ can also be understood as the surface reactance of a superconductor X_s [144]. This inverse relationship of Q_{cond} to $\mathcal{R}_{\text{cond}}$ highlights the potential for losses in the highly concentrated magnetic field running from electrodes to the contact pads. For re-entrant

cavities, conical stubs can be used to reduce conductor losses by reducing the value of $|H(\mathbf{r})|^2$ at surfaces [123]. Considering this, it may prove effective to have the on-chip wire coming from the central electrode widen as it exits the sonic crystal geometry heading towards the antenna, as seen in Figure 2.14. This can be seen later in Figure 3.17 in Section 3.3 on nanofabrication.

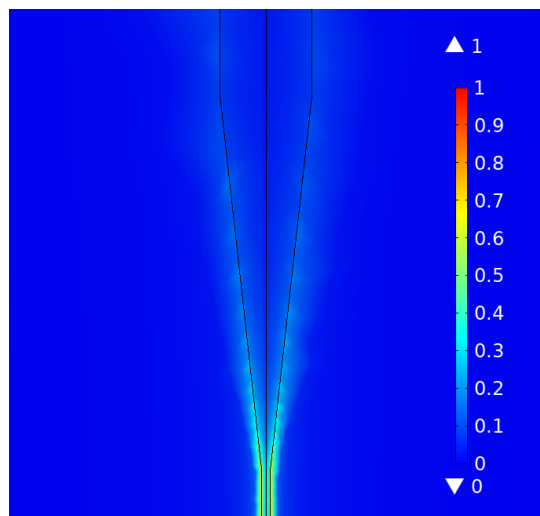


Figure 2.14: Showing the magnetic field magnitude around the on chip wire taper, as the wire from the central electrode leaves the sonic crystal region its width increases. This is associated with a drop in magnetic field amplitude at its surface. The thin wire at the bottom is $10 \mu\text{m}$ wide, while the thick wire at the top is $100 \mu\text{m}$ wide.

Seam Loss

Contact resistance will be present for any material connections in the microwave environment, including SMA connections and the ‘seams’ formed at the boundaries when closing a microwave cavity, hence the term seam loss. The clamping together of a microwave cavity becomes important for producing high quality factor microwave cavities [132, 139, 146].

Following the method of Brecht *et al.* [147], the microscopic quality and size of a cavity seam cannot be directly quantified, as the seam is enclosed it acts as a defect on the cavity mode. Instead the effect of the entire seam is modelled as a generic conductance G_{seam} , across a seam of loop length to close the cavity L_{seam} , giving a constant loss profile $g_{\text{seam}} = G_{\text{seam}}/L_{\text{seam}}$. For a small section of the seam this is:

$$dG_{\text{seam}} = g_{\text{seam}} dl . \quad (2.17)$$

Which allows calculation of the power dissipated over the element as:

$$dP = \frac{1}{2} \frac{(dI)^2}{dG_{\text{seam}}} = \frac{1}{2} \frac{(J_{\perp} dl)^2}{g_{\text{seam}} dl} = \frac{J_{\perp}^2 dl}{2g_{\text{seam}}} , \quad (2.18)$$

where dI is the current across seam element dl , and J_{\perp} is the surface current across the seam, defined:

$$J_{\perp} = \hat{\mathbf{n}} \times H_{\parallel} , \quad (2.19)$$

where $\hat{\mathbf{n}}$ is the surface normal vector and H_{\parallel} is the magnetic field parallel to the seam. The power lost due to the seam can then be calculated:

$$P_{\text{seam}} = \frac{1}{2g_{\text{seam}}} \int_L |H_{\parallel}|^2 dl , \quad (2.20)$$

where \int_L is along the seam. Converting this to a quality factor gives:

$$Q_{\text{seam}} = \omega \mu_0 g_{\text{seam}} \frac{\int_V |H(\mathbf{r})|^2 d^3 \mathbf{r}}{\int_L |H_{\parallel}|^2 dl} , \quad (2.21)$$

where \int_V here is over the whole mode volume. The loss profile g_{seam} is minimised by creating a seam with a good electrical contact, whose profile is as flush to the cavity walls as possible. The total seam loss can then also be reduced by choosing a seam location at the surface magnetic field minimum of the mode intended for study. For a cylindrical cavity this is with a cup and lid shaped pieces. For the chip-cavity system the chips clamping into the cavity must also be considered for how it influences seam loss.

From simulations of the chip-cavity system, for the first mode, the electric field within the capacitor is a factor of 10^6 higher than that at the cavity edges. While the magnetic field is concentrated around the thinnest section of on chip wire, which is a factor of 10^3 higher than at the top and bottom surfaces of the cavity, and a factor of 3×10^4 higher than the outer cavity edges. As the losses outlined in this section are

proportional to the square of these fields, these values indicate why the chip plays a significant role in the total cavity quality factor.

2.3 Nanofluidic Confinement

As discussed in Section 1.4, for superfluid optomechanics to move towards a stronger optomechanical coupling and/or quantum regime, the obvious strategy is to reduce the effective size and therefore mass of the helium mode. The method of confinement then becomes critically important, as the electric field must be concentrated to the same volume, and the helium must enter, while minimising and disturbance to the acoustic mode. This work proposes using a sonic crystal type geometry, as in Figure 2.2 at the start of this chapter, to confine a ^4He acoustic mode while limiting dissipation; a move to smaller acoustic mode volumes, and potentially lower dissipation than existing on chip ^4He helmholtz resonators [8, 148].

This section will cover the confinement of helium into a nanofluidic sonic crystal, constructed from a wafer substrate using cleanroom fabrication techniques [149, 150]. The bulk of the discussion will focus on computational acoustic simulations of sonic crystal geometries, with and without the presence of the confining substrate.

Simulations of superfluid helium for optomechanics are useful for efficiently evaluating and refining proposed systems. These methods have been used recently to model the interaction of surface sound waves and vortices on microtoroidal resonators [151], and to propose a quantum travelling Brillouin resonator using superfluid ^4He [152]. The sonic crystal itself also lends itself to simulations, as more complex geometries can be quickly assessed and refined [153] before lengthy cleanroom fabrication and cryogenic experimental implementations. Helium deep in the superfluid regime is ideal to simulate, as its lack of viscosity allows simulation as a perfect acoustic medium, especially relevant to nanofluidic simulations.

2.3.1 Nanofluidic Helium-4

Helium-4 at mK temperatures is deep into the superfluid phase ($\rho_s \rightarrow \rho$), with vanishing viscosity, and can therefore be approximated to an ideal fluid, allowing for complex simulations without oppressive computing requirements. Vanishing viscosity, unique to superfluid helium, also means reduced capillary forces and minimal surface tension, enabling nanofluidic geometries that would not be possible for any other fluid. Low temperature superfluid helium can be treated as an acoustic medium, governed by the classical wave equation (Section 1.3.3):

$$\frac{\partial^2 p}{\partial t^2} - c_h^2 \nabla^2 p = 0, \quad (2.22)$$

where $p = p(\mathbf{r}, t)$ is the scalar pressure field of the ^4He at position \mathbf{r} and time t , and c_h is the speed of sound in ^4He at zero temperature and saturated vapour pressure (SVP) [119], equivalently the first or zeroth-sound. These values are chosen as the experiment is expected to operate in a low temperature and low pressure regime, however the methodology of this section can be used for any regime where the ^4He can be approximated to a pure superfluid. Solving the wave equation in Eq. 2.22, gives solutions as a linear superposition of plane wave, simplifying simulation. However, in a physical system the superfluid geometry will be enclosed by some other material. In this work we consider helium confined within a nanofluidic geometry inside a ‘chip’ fabricated from a cleanroom wafer substrate. A full treatment would require simulating for the entire chip-helium system, looking for mode matching between the helium modes of interest and the chip. It would also include a material dependent treatment of the crystal axes in the substrate. At this stage, the complexity is avoided by considering the chip as a continuous isotropic acoustic medium, bounding the helium geometry. The modes of the chip can largely be ignored as its material’s characteristic wavelengths are much longer than ^4He , due to the substrate’s much greater speed of sound:

$$c_{\text{sub}} = \sqrt{\frac{E(1-\nu)}{\rho_{\text{sub}}(1+\nu)(1-2\nu)}}, \quad (2.23)$$

where E is the Young's modulus and ν the Poisson ratio, for the isotropic material. Values for substrate materials are presented in Table 2.1. This picture can be simplified further, by considering the acoustic impedance mismatch between the two materials. Assuming a continuous pressure across the ^4He -substrate interface, the normal incidence reflection coefficient of acoustic wave amplitude at the interface can be calculated as:

$$r = \left| \frac{Z_h - Z_{\text{sub}}}{Z_h + Z_{\text{sub}}} \right|, \quad (2.24)$$

where $Z_h = \rho_h c_h$ and $Z_{\text{sub}} = \rho_{\text{sub}} c_{\text{sub}}$ are the acoustic impedances of the ^4He and substrate respectively. The concept of phonon transmission across the solid-liquid boundary is further covered in Section 3.1.3, in the context of thermal phonons. Table 2.1 shows material parameters for different wafer substrates commonly used in nanofabrication.

Table 2.1: Table of acoustic properties of possible substrate materials, for use in fabricating nanofluidic sonic crystal chips. The acoustic impedances are given in *rayl* (Pa.s/m). The sound velocity for solid materials was derived from the literature using Eq. 2.23.

Material	ρ_{sub} (kg/m ³)	c (m/s)	Z (<i>rayl</i>)
Liquid ^4He ^a	145.1	229.5	3.33×10^4
Fused silica [154]	2200	5900	1.30×10^7
Crystal quartz ^b	2650	7000	1.86×10^7
Borosilicate glass [154]	2230	5460	1.22×10^7
Crystal Silicon ^c	2330	8560	1.99×10^7
Sapphire [155]	3910	9940	3.89×10^7

^aAt saturated vapour pressure and T= 0 K, values from [119].

^bAT cut crystal quartz values from [155].

^c[100] orientation, values from [156].

Clearly there will be a large impedance mismatch between the ^4He and substrate material ($Z_h \ll Z_{\text{sub}}$), giving reflection coefficients ~ 0.995 , and so almost all the ^4He acoustic wave will be reflected at the interface. This means a ‘sound hard’ boundary condition is a good approximation for this system, given by:

$$\hat{\mathbf{n}} \cdot \nabla p = 0, \quad (2.25)$$

where $\hat{\mathbf{n}}$ is the unit vector normal to the boundary surface. Imposing this Neumann boundary condition, where the normal derivative of the pressure is zero at the surface, produces total reflection of incident waves. This allows further simplification of initial simulations, to only consider the ${}^4\text{He}$ geometry with sound hard boundaries, as the substrate's effect on mode shape are expected to be small.

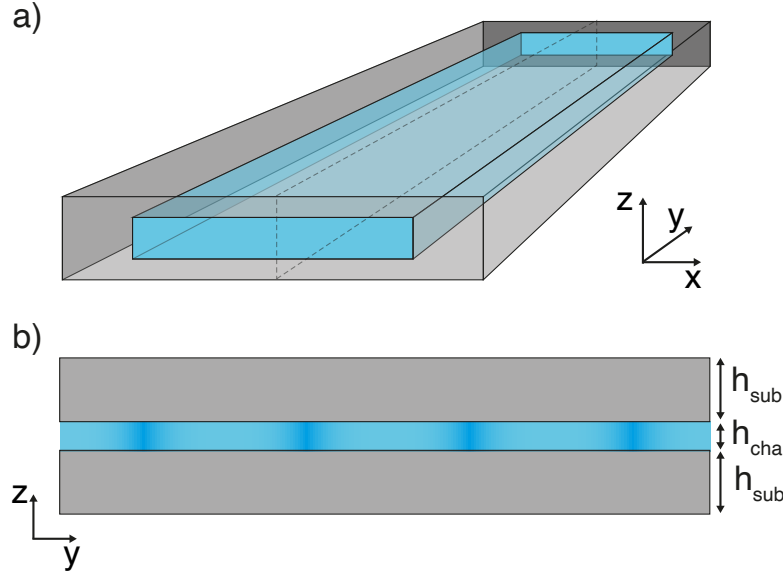


Figure 2.15: Showing a simple acoustic waveguide, considered in this work to be a nanofluidic channel formed between two wafer substrates (grey), filled with superfluid ${}^4\text{He}$ (blue). (a) shows a section of waveguide, open at both ends, which can be treated as ports for acoustic waves. While (b) shows the dashed cross section of (a), with light and dark regions indicating a travelling acoustic wave.

Another advantageous feature of the proposed geometry is a small aspect ratio between height (z) and the sonic crystal plane ($x - y$), similar to traditional waveguides, as illustrated in Figure 2.15, where the $x - z$ dimensions of the channel are small compared with the y . For plane wave solutions and sound hard boundaries, the wavevector of these solutions (k) can be split up into quantised $x - y - z$ components as:

$$k_{n,i} = \frac{n\pi}{h_i} \quad i \in x, y, z, \quad (2.26)$$

where n is a positive integer denoting the wave number in the i direction, and h_i is the size of the waveguide in the i 'th direction. Waveguides are designed such that, in the non-propagation directions, the $n = 1$ mode is associated with frequencies much larger than those travelling down in the direction of propagation. The $n = 1$ mode then defines

the cutoff frequency as:

$$\frac{\Omega_{\text{co}}}{1\pi} = \frac{c_{\text{h}}}{2h_i} \quad i \in x, y, z, \quad (2.27)$$

where c_{h} is the speed of sound inside the waveguide (^4He). For the sonic crystal geometries in the next section, the $x - y$ plane is ‘open’ to acoustic propagation, while the z dimension is enclosed to a height of ~ 100 nm scale, giving a cutoff frequency $\Omega_{\text{co}} \sim 1$ GHz. Acoustic waves below the cutoff frequency are forbidden from propagating in the cutoff direction, effectively disallowing any wave around ~ 1 MHz (expected Ω_{m}) with $k_z \neq 0$ within the sonic crystal. Waves below the cutoff are called ‘evanescent’, and do not have a propagating wave form, instead decaying quickly in the cutoff direction. The strong cutoff in z with $\Omega_{\text{m}} \ll \Omega_{\text{co}}$, means the system can be considered as approximately 2D ($x - y$). Therefore the initial simulations in the next few sections neglect the z direction, setting $k_z = 0$, in addition to the sound hard and ^4He as a perfect acoustic medium assumptions. The simulations are then developed to include the the z direction and substrate in Sections 2.3.6, 2.3.5 and 2.3.7.

2.3.2 Sonic Crystal

As introduced previously the mechanical aspect of the optomechanical system in this work is a superfluid ^4He sonic crystal, formed from wafer substrate pillars surrounded by ^4He (shown in Figure 2.2). The sonic crystals in this work are a type of engineered phononic crystal, a little like a solid atomic lattice, they are formed from repeated periodic structures, and are used for manipulating elastic or acoustic modes. The structures are either fabricated in bulk as a material with controllable acoustic properties, or as defined patterns for controlling the propagation of waves [157], e.g an acoustic waveguide. Early proposals for sonic crystals were for composite metals [158], formed from repeated cylinders of one metal within another bulk bulk metal, itself inspired by early photonic crystals. More recent proposals have even suggested developing repeated dielectric structures that can act both as a photonic and phononic crystal simultaneously [9], which are now being incorporated into optomechanical systems [28, 30, 32]. These novel

structures are an exciting research avenue for superfluid optomechanics, and have been recently proposed by Sfindla *et al.* [112], as a method to extend the physics of superfluid thin films on micro-toroid resonators into the single phonon regime. Where, instead of helium confined within a sonic crystal structure, the phononic crystal is formed from a thin dielectric with periodic holes, itself covered in a thin film of helium.

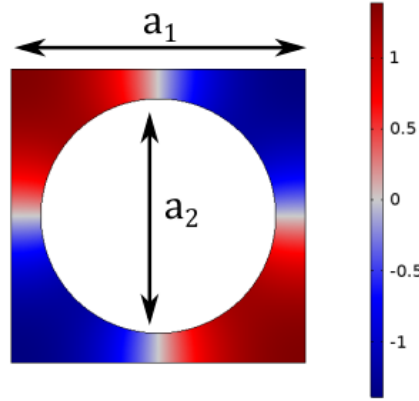


Figure 2.16: Showing the 2D sonic crystal unit cell, with ^4He acoustic mode shape function (normalised pressure), for the 1.19 MHz acoustic mode of the first band. The dimensions of the unit cell are labelled, with unit cell size $a_1 = 100 \mu\text{m}$ and pillar diameter $a_2 = 80 \mu\text{m}$.

Given the assumed regime from the previous section, the nanofluidic geometry here is an artificial crystal formed by the lattice of substrate pillars which strongly reflect incident acoustic waves within the ^4He superfluid helium. The periodic nature of the pillar lattice causes Bragg scattering of these acoustic waves and so, following the classical Bloch theorem of solid state physics, the solutions for propagating modes are Bloch waves, with pressure field of form:

$$p(\mathbf{r}) = e^{-i\mathbf{k}\cdot\mathbf{r}}\tilde{p}(\mathbf{r}), \quad (2.28)$$

where \mathbf{k} is the 2D wave vector ($k_z = 0$), and $\tilde{p}(\mathbf{r})$ is a periodic function with the same periodicity as the sonic crystal geometry. The solutions are still a linear superposition of plane waves, now modulated by $\tilde{p}(\mathbf{r})$. The \mathbf{k} dependence of these Bloch waves defines a phononic band structure, analogous to an electronic band structure but for phonons. To determine the phononic band structure of a specific crystal, finite element modelling (FEM) using COMSOL Multiphysics is employed. Initially an infinite, or continuous, 2D

sonic crystal is simulated by modelling a single crystal unit cell, with a sound hard pillar. Figure 2.16 shows the simulated unit cell. This single unit cell can simulate a continuous crystal using Floquet periodic boundary conditions, linking the opposing faces of the unit cell to create a continuous lattice defined as [159, 160]:

$$p(x = 0) = p(x = a_1)e^{-k_x a_1} , \quad (2.29)$$

$$p(y = a_1) = p(y = 0)e^{-k_y a_1} , \quad (2.30)$$

for a square unit cell of size a_1 , spanning $(x = 0, y = 0) \rightarrow (x = a_1, y = a_1)$.

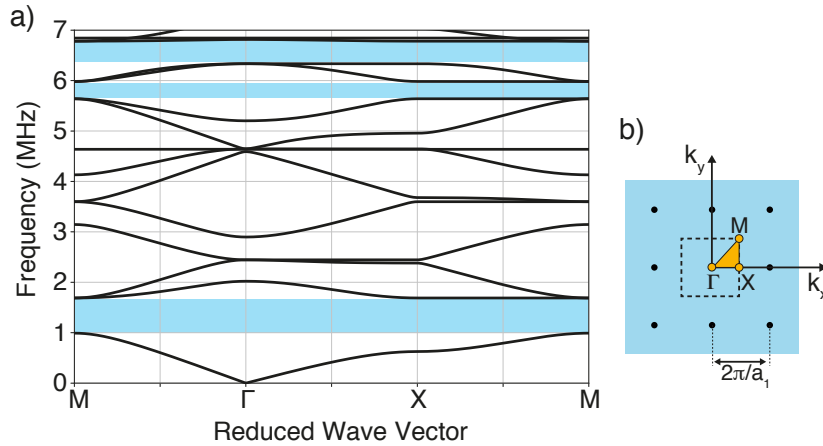


Figure 2.17: (a) The phononic band structure of a superfluid ^4He sonic crystal, extracted from a simulation of a continuous lattice of square unit cell size $a_1 = 100 \mu\text{m}$ and pillar diameter $a_2 = 90 \mu\text{m}$, using sound hard and Floquet boundaries. Highlighted in blue are the three lowest frequency bandgaps. (b) the reciprocal lattice with its unit cell outlined by the dashed line; containing its irreducible Brillouin zone highlighted in orange, with characteristic points Γ , M and X .

Figure 2.17 shows one such band structure, and the irreducible Brillouin zone, for a square unit cell of side length $a_1 = 100 \mu\text{m}$ and circular pillar diameter $a_2 = 90 \mu\text{m}$. Figure 2.17 also shows the three lowest frequency ‘complete’ bandgaps (nearest the fundamental mode). These bandgaps are due to Bragg interference of reflections from the ^4He -pillar boundaries. They are ‘complete’ as they open for all values of \mathbf{k} , meaning the bandgap defines a region of frequency where acoustic wave propagation is forbidden for all directions. For Figure 2.17, these first three bandgaps are centred at frequencies 1.34, 5.81 and 6.56 MHz, with widths of 0.7, 0.34 and 0.45 MHz respectively. Within

this frequency region sound waves can only exist as evanescent waves, with imaginary wave vectors, defining an exponential amplitude decay of characteristic length close to the unit cell size.

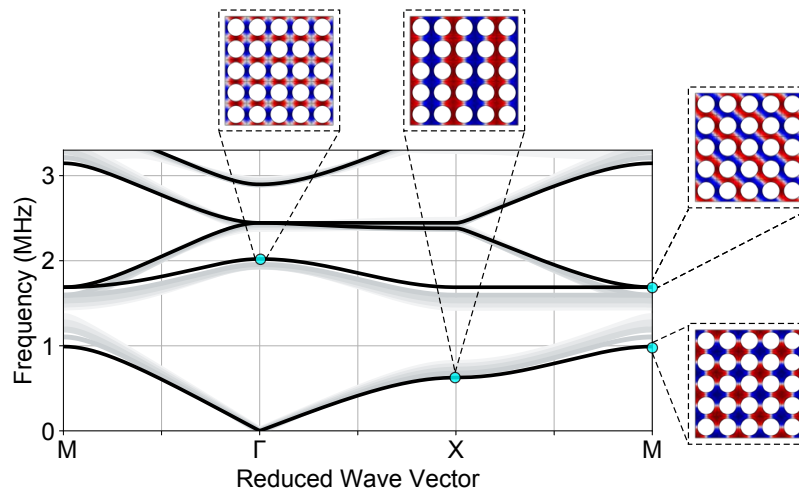


Figure 2.18: Low frequency phononic band structure around first bandgap, for pillar spacing $a_1 = 100\mu\text{m}$. For varying pillar diameter a_2 , from $90\mu\text{m}$ in black, lightening as diameter decreases to $70\mu\text{m}$ in the lightest grey. The acoustic mode shape is also shown, in colour plots, at different characteristic positions either side of the bandgap.

The unit cell size of the sonic crystal crystal will also determine the frequency range of it's bands, while the ratio a_2/a_1 will determine their structure. Figure 2.18 shows the effect of changing the a_2/a_1 ratio, and also the mode shape of the pressure field at different points either side of the bandgap. Bandgaps are found for a_2/a_1 ratios from ~ 0.65 to ~ 0.95 . Above this the pillars become large enough to effectively separate the helium into separate volumes which weakly couple together, while below this the Bragg interference is not strong enough to complete the bandgap for all \mathbf{k} , and instead the sonic crystal merely suppresses sound waves in certain directions.

The shape of the unit cell and pillar will determine the phononic band structure, with many novel pillar shapes and crystal structures being possible, however this work will focus on square unit cells and circular pillars as these produce the largest first bandgap and therefore acoustic isolation for any mode within.

2.3.3 Defect Mode

This work aims to take advantage of this phononic bandgap behaviour to confine a low dissipation acoustic mode, whilst still leaving it open to filling and thermalisation with bulk ^4He inside the greater microwave cavity. By removing a single pillar at the centre of the sonic crystal a ‘point’ defect is created, as introduced in Figure 2.2. The point defect defines a region capable of hosting acoustic modes at bandgap frequencies. The centre of the first bandgap then also corresponds to the frequency of the fundamental point defect mode. For a $a_1 = 100 \mu\text{m}$ unit cell and $a_2 = 80 \mu\text{m}$ diameter pillar, this gives a fundamental mode frequency of $\Omega_m = 1.34 \text{ MHz}$.

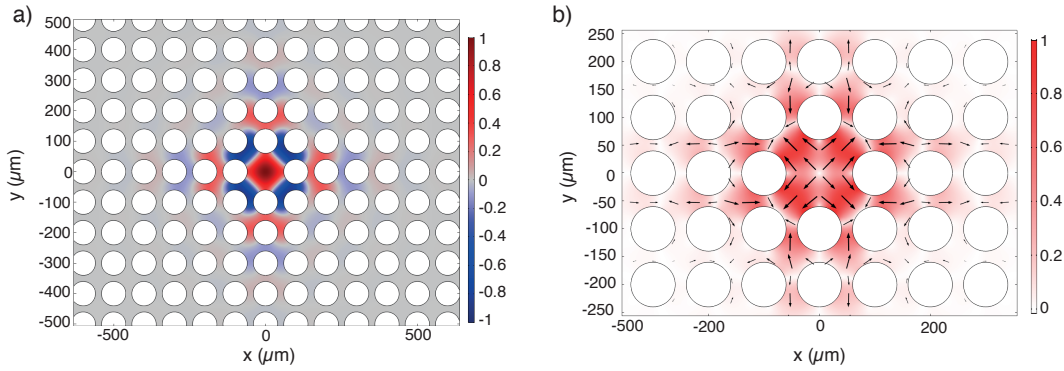


Figure 2.19: Mode shape of the $\Omega_m = 1.34 \text{ MHz}$ fundamental point defect acoustic mode, for a crystal unit cell $a_1 = 100 \mu\text{m}$ square with $a_2 = 80 \mu\text{m}$ diameter pillars. (a) The acoustic mode shape function (normalised pressure field); and (b) the velocity field magnitude (colour scale) and its direction (black arrows).

Figure 2.19 shows the fundamental defect mode shape in terms of both pressure and velocity fields. For this mode the center of the defect itself contains a highly concentrated pressure antinode, with the next opposing phase antinode between the pillars neighbouring the defect. Beyond the defect there are repeating antinodes of rapidly diminishing amplitude roughly every unit cell, indicating the evanescent nature of the mode beyond the defect. The rapid decay of the field indicates a concentration of the mode and suppression of dissipation, making these modes interesting candidates for optomechanical experiments.

Figure 2.20 shows the pressure field as a function of distance from the defect centre, for the fundamental defect mode. Here the envelope of the pressure field is fitted to

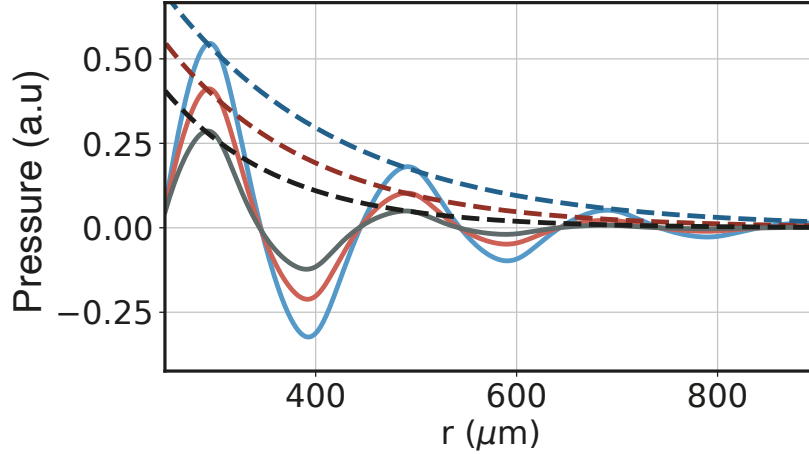


Figure 2.20: Pressure field inside the sonic crystal as a function of distance from the central point defect (solid lines), calculated for the $\Omega_m/2\pi \approx 1.34$ MHz fundamental mode of a $a_1 = 100\mu\text{m}$ unit cell crystal, with varying pillar diameter a_2 : $75\mu\text{m}$ (blue), $80\mu\text{m}$ (red), and $85\mu\text{m}$ (black). For each line the pressure field is normalised against the maximum field of the defect. The envelope of each roughly sinusoidally varying pressure field has been fitted to an exponential decay $p(r) = \exp(-r/l_c)$ (dashed lines), giving l_c the characteristic decay length of the acoustic field. For each line these are: blue $l_c = 176\mu\text{m}$, red $l_c = 143\mu\text{m}$, and black $l_c = 115\mu\text{m}$.

e^{-r/l_c} , where l_c is the characteristic decay length, defining the evanescent nature of the wave. This decay length is roughly the unit cell size a_1 , depending on the ratio a_2/a_1 , and for $a_2 \rightarrow a_1$ gives $l_c \rightarrow a_1$. The results presented here are for finite lattices, due to unnecessary difficulty simulating a continuous lattice with a single defect. However, for even a moderately sized finite lattice the defect mode remains highly confined, and the modeshape within regions closer to the defect than crystal edge obeys the expected sinusoidal exponentially decaying field profile. For losses a more careful approach must be taken, whereas an infinite crystal will have a perfectly reflected mode with no loss (ignoring ^4He 's internal losses). A finite crystal will have losses associated with finite size effects, which must be considered as a radiative loss channel.

2.3.4 Radiative Loss

Mechanical Quality Factor

For FEM simulations it is simplest to split mechanical losses into two main categories: ‘intrinsic’ to the ^4He , and ‘extrinsic’ to the ^4He . Intrinsic losses are covered in

Section 1.3, with intrinsic being used here to mean any loss mechanism present in the bulk superfluid (including ^3He processes), and are modelled with a simple attenuation factor for the ^4He acoustic medium. While extrinsic refers to any confinement related losses, including geometric and boundary related factors. These both contribute to the overall mechanical Q_m as:

$$\frac{1}{Q_m} = \frac{1}{Q_m^{\text{int}}} + \frac{1}{Q_m^{\text{ext}}}, \quad (2.31)$$

where Q_m^{int} is the quality factor from intrinsic losses, and Q_m^{ext} is the quality factor from extrinsic losses. For the simulations presented here Q_m^{ext} can then itself be split up into the two main factors: radiative losses, where the wave escapes the sonic crystal geometry; and substrate losses, associated with a substrate's intrinsic loss mechanisms where the substrate participates in the mode. Similar to Q_m , Q_m^{ext} can then be separated as:

$$\frac{1}{Q_m^{\text{ext}}} = \frac{1}{Q_m^{\text{rad}}} + \frac{1}{Q_m^{\text{sub}}}, \quad (2.32)$$

where Q_m^{rad} is the quality factor due to radiative losses, and Q_m^{sub} is the quality factor due to substrate losses. Note, the relationship between quality factors means that the lowest Q will often 'dominate', and if it is lower by orders of magnitude then $Q_{\text{total}} \rightarrow Q_{\text{lowest}}$ is a good approximation. Ideally the choice of geometry and substrate would produce extrinsic quality factors above Q_m^{int} . However for a study looking at the internal loss mechanisms of ^4He , an extrinsic quality factor Q_m^{ext} of similar order would be sufficient to allow Q_m^{int} to be extracted, provided the quality factors behaved differently with varying system parameters (e.g. temperature).

2D Radiative

The simplest model for radiative losses out of the sonic crystal (Q_m^{rad}), is a 2D crystal ($k_z = 0$) with sound hard pillars (perfect reflections). In this model radiative loss can be thought of as the portion acoustic waves in the $x - y$ plane which, through pillar reflections, propagate ('radiate') out of the sonic crystal. For a continuous lattice the bandgap is perfectly complete, and no radiative loss occurs, however finite size effects

allow for some energy to escape. The escaping energy originates from the exponentially decaying evanescent field, from Figure 2.20, that makes it to the edge of the crystal.

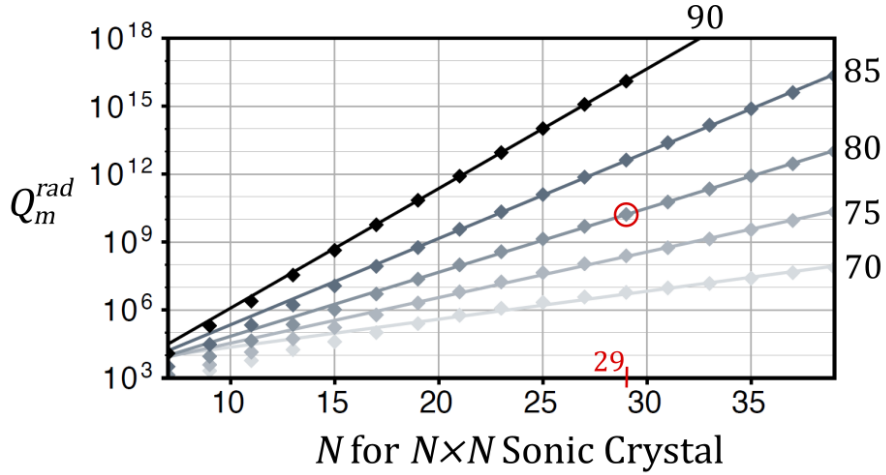


Figure 2.21: Quality factor Q_m^{rad} of the point defect fundamental mode when limited by radiative losses, vs the size of the sonic crystal lattice N ($N \times N$). For a crystal with unit cell size $a_1 = 100 \mu\text{m}$ and varying pillar diameter a_2 , ranging from $90 \mu\text{m}$ (darkest diamonds), in $5 \mu\text{m}$ steps to $70 \mu\text{m}$ (lightest diamonds). The lines represent log-linear fits for data of corresponding colour with $N > 17$.

To study the effects of finite lattices, sonic crystals of increasing size N are simulated, where N refers to a lattice of $N \times N$ square unit cells, with a centrally located defect. The radiative loss in these systems is modelled via a ^4He ‘perfectly matched layer’ (PML). This is a numerical method for simulating an open boundary condition for a system, where a PML region is added at the boundary to non-reflectively absorb incoming waves. The PML simulates a truncated continuous domain, with matched impedance to the bulk, through which waves are quickly attenuated [161]. For the 2D sonic crystal simulations a circular ^4He PML is used around the entire lattice, beginning at a distance of two characteristic wavelengths away, and extending for another 5 wavelengths radially. Figure 2.22 shows the full simulated geometry. Q_m^{rad} is then calculated from the energy dissipated in the PML, intentionally representing a ‘worst case’ for loss, where no energy returns to the lattice. The PML is advantageous over other non-reflective boundary conditions as it is less reflective for more oblique incident waves, though very oblique ($\geq 70^\circ$) waves will still be partially reflected [162]. The PML works well for the sonic crystal system, as waves exiting the sonic crystal tend to be fairly radial, and any waves reflecting from the PML are unlikely to make it back into the lattice due to the

bandgap. Starting the PML a small distance from the lattice further improves these characteristics.

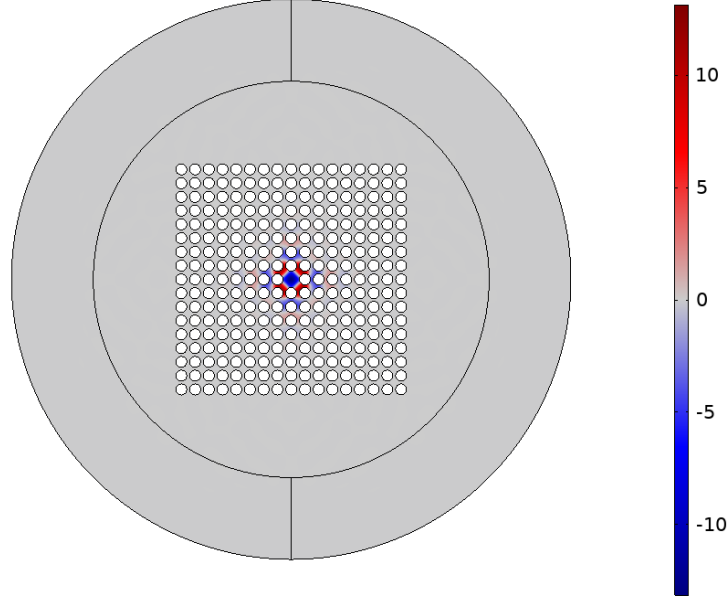


Figure 2.22: Showing a 17×17 2D sonic crystal unit cell, with ^4He acoustic mode shape function (normalised pressure), for the 1.34 MHz fundamental acoustic mode. Size of the crystal unit cell is $a_1 = 100 \mu\text{m}$ and pillar diameter is $a_2 = 80 \mu\text{m}$. The sonic crystal is surrounded by a PML layer (the two halves of the outer ring).

The simulations of increasing N are repeated for different a_2/a_1 ratios (changing l_c), and extracted quality factors Q_m^{rad} show in Figure 2.21. There is a clear exponential increase in Q_m^{rad} with increasing N , due to increasing the distance a wave must travel through the lattice before escaping, while decaying at e^{-r/l_c} . Increasing a_2/a_1 also improves Q_m^{rad} as l_c is decreased. For an a_2/a_1 ratio of 0.8, used in fabricated chips, a $Q_m^{\text{rad}} > 10^{10}$ is achieved for $N \gtrsim 29$. This Q_m^{rad} is approximately the ^4He intrinsic quality factor at 10 mK, and is very achievable for a $100 \mu\text{m}$ unit cell, as the sonic crystal would occupy ~ 3 mm on a device with dimensions of order 10×10 mm. The relationship between N and Q_m^{rad} is closely log-linear for $N \gtrsim 17$ (fitted in Figure 2.21), above this the mode shape can be considered evanescent, while below finite size effects disturb the mode shape in addition to providing a loss channel. Though high Q_m^{rad} 's are still achievable, even with very small lattices, where the modeshape deviates from close to the ideal evanescent due to reflections from the lattice's edge.

To produce accurate high quality factor acoustic FEM simulations sufficient mesh density must be included. Generally six mesh points per characteristic wavelength is sufficient [163], which would be $\sim 200/6 \mu\text{m}$ for a 1.34 MHz ^4He mode. However, for significantly smaller geometry mesh density must be increased to achieve high Q 's. For fabricated devices $N = 37$ is chosen to be well above intrinsic losses, while maintaining a compact design.

3D Radiative

So far the sonic crystal has been considered 2D with sound hard pillar boundaries. If radiative loss accounts for all acoustic energy that makes it outside the pillar region, then a contribution from the substrate should be simulated for. The simplest model would be a 2D lattice with substrate pillars, however the pillar boundary conditions are difficult to define in COMSOL, due to how the pillars are clamped.

Simulating for the ^4He -substrate system in 3D should allow for more physical pillar boundary conditions. As a consistency check, the 3D sonic crystal is simulated for ^4He only with sound hard boundaries. This recovers almost exactly the 2D results, due to the aspect ratio of the pillar height ($\sim 100 \text{ nm}$) to the unit cell size ($a_1 = 100 \mu\text{m}$). Next the substrate pillars are added as solid medium, clamped top and bottom to the sound hard $x - y$ planes confining the ^4He . This simulation also recovers similar results to the 2D sound hard model, with some small modifications due to the solid pillars participating slightly in the mode, though the energy radiating into the PML is largely unchanged as the impedance mismatch between the pillars and ^4He is sufficient for near perfect reflection, and the pillars are too small to host their own acoustic modes.

The final step in complexity is to add the substrate above and below the sonic crystal, allowing for reflections with k_z into the substrate, yet it proves too computationally intense to simulate the entire ^4He -chip object. So instead a square waveguide is modelled, to check for any radiation of energy away from the propagation direction, in analogy to radiation out of the sonic crystal plane. Such a waveguide is shown in Figure 2.23, and these simulations will be covered in detail in the next section. In short, no truly radiative effects through the substrate are found, however the substrate shows

significant participation in the acoustic mode, and finite size effects of the substrate must be considered.

2.3.5 Boundary Condition Loss

Boundary effects, including any k_z radiative effects, must be accounted for before moving on to assess the impact of a substrate's internal losses on the ^4He acoustic mode. Ideally the entire chip would then be modelled, clamped at the antenna ends, but as mentioned above this is difficult to model for the full substrate- ^4He system. The chip is roughly a $10\text{ mm} \times 10\text{ mm} \times 1\text{ mm}$ object, and its volume overwhelms the ^4He inside the sonic crystal, pushing simulations beyond available computational limits. Any choice of a reduced geometry boundary conditions will then introduce geometric errors which must be considered. Because of this difficulty an analogy is made to an acoustic waveguide, swapping the $x - y$ plane of the sonic crystal for the x direction of propagation in a waveguide, simplifying simulations, and allowing isolation of different boundary conditions effects.

Waveguide Simulations

Figure 2.23 shows an acoustic wave propagating down a ^4He filled acoustic waveguide at 1.34 MHz, pressure field in the helium is shown, along with displacement field inside the solid substrate. Waveguide simulations focussed on square waveguides of cross sections $100\text{ }\mu\text{m} \times 100\text{ nm}$. These simulations find the substrate participation is in the form of evanescent waves, that extend a short distance from the ^4He channel into the surrounding substrate. The acoustic waves inside ^4He essentially move parallel to the boundaries, under conditions of total internal reflection, similar to the conditions of an optical fibre or microwave waveguides for electromagnetic waves. The evanescent field inside the substrate does not propagate acoustic energy, and again with a continuous substrate all energy would be returned to the ^4He . For the physical system, finite size effects must be taken into account, and the boundary conditions on the outside substrate surface considered.

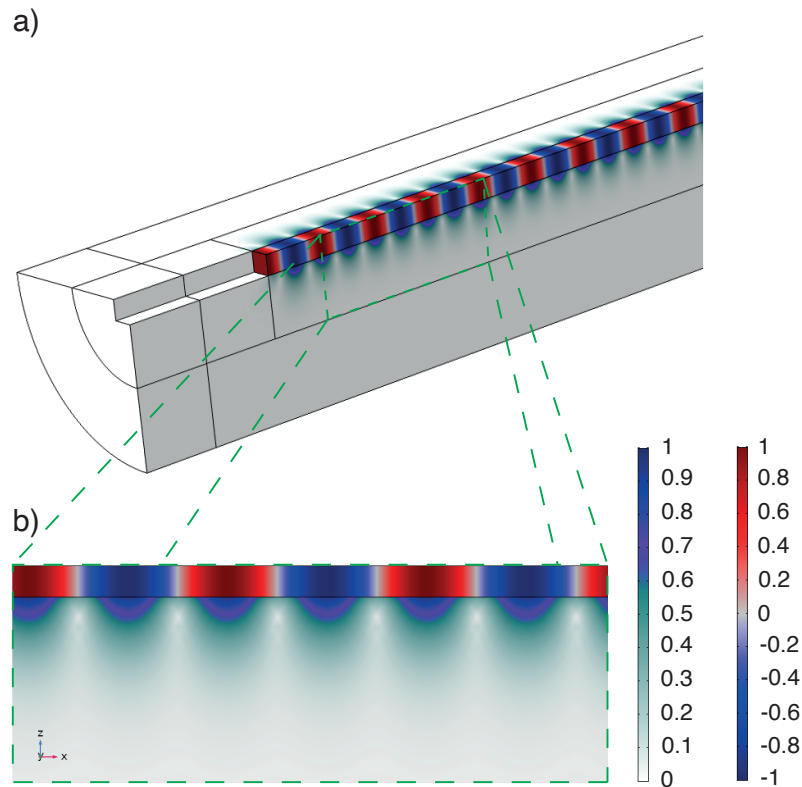


Figure 2.23: Quarter view of a 3D FEM simulation of 1.34 MHz modeshape travelling down a rectangular acoustic waveguide, of cross sections $100 \times 100 \mu\text{m}$ (height exaggerated from 100 nm for clarity) and length 5 mm. The red-blue colour scaled region shows the acoustic pressure field within the ^4He , which fills the waveguide channel. While the white-purple colour scaled region shows the displacement field within the solid substrate, defining the dimensions of the waveguide. Both fields have been normalised to their maximum value. (a) show the 3D view, where the inner substrate region is modelled as a normal isotropic solid, while the outer (white) substrate region is a PML. (b) then shows the cross section of the rectangular channel indicated by dashed green lines.

The first boundary condition considered is a substrate PML, some distance from the waveguide (Figure 2.23). As expected, the wave travelling down the waveguide is attenuated as the portion of its energy within the substrate evanescent field which crosses into the PML. However a reasonably thick pre-PML substrate layer ($> 200 \mu\text{m}$) can easily suppress this below the substrate or helium's internal loss. To achieve this the substrate must also be extended around the acoustic ports, as a PML starting at the port plane begins at a higher displacement field. Pillars can then be added to these waveguide simulations as an additional check for radiative effects. These simulations find little

change to the loss of the system (insignificant reflection into $y - z$), though the frequency dependent transmission and reflection properties in the direction of propagation are modified.

Sonic Crystal Simulations

Considering the sonic crystal, the substrate is more finite in the z direction (300–500 nm above and below) than in the $x - y$ direction. The substrate in z then ends in a boundary to the bulk ^4He inside the microwave cavity, which may even help reflect the wave due to the large acoustic impedance mismatch. There is a significant difference here when compared with the $x - y$ radiative losses (Section 2.3.4). For the $x - y$ plane the acoustic wave is evanescent inside the sonic crystal, while outside it is free to radiate away, with the transition being modelled as part of the simulation. In z the wave is instead evanescent inside the substrate up to a material boundary, making a substrate PML unsuitable.

Accurate modelling of the ^4He and substrate requires too many mesh points. As the ^4He demands a small maximum distance between mesh points ($\sim 20 \mu\text{m}$), even though the characteristic wavelength in the substrate is much longer, and an appropriate growth factor still produces a dense substrate mesh close to the ^4He . Using a swept mesh inside the thin sonic crystal plane, and exploiting the sixteen-wise symmetry of the geometry can reduce the mesh significantly. Allowing for a simplified simulation of the sonic crystal immediate region, with free outer boundaries in z ; as a transition back to ^4He would require a transition back to high mesh density. The boundaries at the edges of this model in $x - y$ are fixed. These boundaries introduce additional losses, as the substrate evanescent field in z penetrates significantly deeper than in the waveguide, as seen in Figure 2.24. The field is able to drive the reduced chip geometry, dissipating energy at the fixed boundaries.

Within COMSOL these boundary losses can be considered as geometric errors from finite mesh density, and are more significant in solid objects than in acoustic mediums. It is even possible for the energy flux through the boundary to be negative, adding energy to the system, and providing a non-physical negative effective quality factor. Simplifying

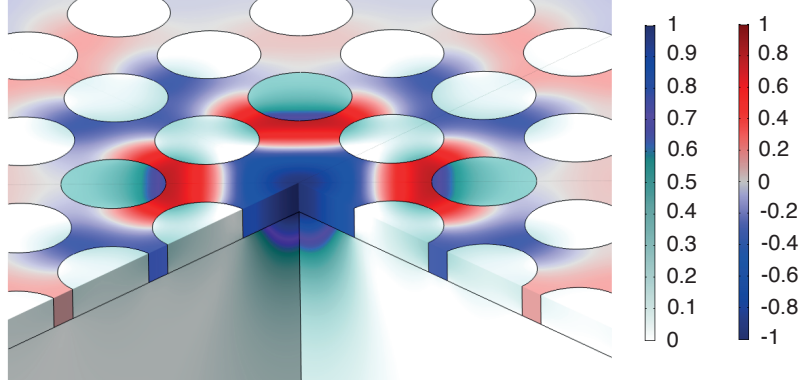


Figure 2.24: Sliced view close to the defect, of the 1.34 MHz fundamental mode, from a 3D FEM sonic crystal simulation. The red-blue colour scaled region shows the acoustic pressure field within the ${}^4\text{He}$, which fills the sonic crystal. While the white-green-blue colour scaled region shows the displacement field within the solid substrate, enclosing the helium. Both fields are normalised to their maximum values.

the sonic crystal to a single disc of ${}^4\text{He}$ surrounded by substrate confirms these errors to be mesh density dependent. The errors produce effective quality factors $|Q_m^{\text{eff}}| > 10^6$ for the sonic crystal geometry, and so limit the accuracy of simulations above this. Which can be calculated numerically via:

$$Q_m^{\text{eff}} = \frac{\Omega_e e_{\text{tot}}}{I}, \quad (2.33)$$

where e_{tot} is the total energy of the acoustic mode, and I is the surface integral of the energy flux, either through all outer boundaries, or a single boundary if its associated effective Q is required.

2.3.6 Substrate Loss

Internal substrate losses are expected to be a significant loss factor compared to those intrinsic to the helium. This internal loss is modelled as an isotropic attenuation factor applied to the field within the substrate, associated with its participation in the mode. The dimensionless isotropic loss factors are defined in terms of dissipation per cycle and so for the substrate can be written:

$$\alpha_{\text{sub}} = \frac{1}{Q_m^{\text{lit}}}, \quad (2.34)$$

where $Q_m^{\text{lit}'}$ is a high mechanical quality factor from literature values (Table 2.2). This assumes the literature values are limited by internal material losses, which should be reasonably accurate for high $Q_m^{\text{lit}'}$, and if not will still give upper bounds of attenuation for this work. The attenuation factors α_{sub} and α_{int} are for attenuation in bulk substrate and bulk helium respectively. Hence this section will use $Q \rightarrow Q'$ to refer to bulk material quality factors, and Q to refer to quality factors of the total acoustic mode. This is to show the significance of energy distribution between materials in a ^4He acoustic mode where the substrate participates.

The goal of the sonic crystal system is to preserve the ultra-low loss ^4He superfluid environment, so a $Q_m^{\text{int}'}$ of 10^{10} is chosen for simulation, representing intrinsic ^4He losses limited by three-phonon processes at 10 mK. For such a low loss system with high quality factor, the $|Q_m^{\text{eff}}| > 10^6$ boundary losses/errors discussed in the previous section become an issue. To isolate only the intrinsic material associated losses, it is possible to proportionally increase both their strengths, to solve the problem in terms of how the substrate reduces the pristine ^4He intrinsic Q' . For a regime where $Q_m^{\text{sub}}, Q_m^{\text{int}} \ll |Q_m^{\text{eff}}|$:

$$\frac{Q_m}{Q_m^{\text{int}}} = \frac{1}{1 + \frac{Q_m^{\text{int}}}{Q_m^{\text{sub}}}}, \quad (2.35)$$

from the standard form of Q_m . If Q_m^{int} and Q_m^{sub} can be reduced while maintaining the ratio $Q_m^{\text{int}}/Q_m^{\text{sub}}$, this would give a practical method of assessing the reduction of Q_m^{int} due to the presence of the substrate. These quality factors are not directly accessible, and so are rewritten as:

$$Q_m^{\text{int}} = \frac{1}{\alpha_{\text{int}} \mathcal{R}_m^{\text{int}}}, \quad (2.36)$$

$$Q_m^{\text{sub}} = \frac{1}{\alpha_{\text{sub}} \mathcal{R}_m^{\text{sub}}}, \quad (2.37)$$

Where $\mathcal{R}_m^{\text{int}}$ and $\mathcal{R}_m^{\text{sub}}$ are the fraction of acoustic energy in the ^4He and substrate respectively. A full derivation for both equations, from the equations of motion solved for in COMSOL, is shown in Appendix B. Note that there is some ambiguity to the \mathcal{R}_m 's,

as they are defined as a ratio of the maximum potential energy during a cycle in the material, divided by the total acoustic energy (potential and kinetic) across the entire system. This is due to COMSOL related definitions and explored further in Appendix B.1. From these two equations Equation 2.35 can be rewritten:

$$Q_m \alpha_{\text{int}} = \frac{Q_m}{Q_m^{\text{int}'}} = \frac{1}{R_{\text{int}}} \left(1 + \frac{\alpha_{\text{sub}} \mathcal{R}_m^{\text{sub}}}{\alpha_{\text{int}} \mathcal{R}_m^{\text{int}}} \right), \quad (2.38)$$

for $\mathcal{R}_m^{\text{int}} \gg \mathcal{R}_m^{\text{sub}}$, $Q_m \alpha_{\text{int}} \simeq Q_m / Q_m^{\text{int}}$ and $1 / \mathcal{R}_m^{\text{int}} \simeq 1$. The method of abstracting the quality factors is to reduce both α_{sub} and α_{int} , from their known literature values, while maintaining the ratio $\alpha_{\text{sub}} / \alpha_{\text{int}}$. It is then possible to simulate the sonic crystal for Q_m , and use these values to calculate $Q_m \alpha_{\text{int}} = Q_m / Q_m^{\text{int}'}$, which should remain constant with the known literature values. This method assumes the distribution of energy in the system remains constant.

Performing consistency checks for the sonic crystal finds this method is effective for reduced substrate quality factors $10^2 < Q_m^{\text{sub,red}} < 10^6$. Checking for consistency with a simple enclosed helium disc confirms the results, and is effective for $10^2 < Q_m^{\text{sub,red}} < 10^8$, while waveguide simulations are effective for $10^2 < Q_m^{\text{sub,red}} < 10^{11}$, though it may be possible to push the upper bound higher. The consistent lower bound for all three simulation types corresponds to a regime where the substrate attenuation becomes significant on the length-scale of it's associated evanescent wave, modifying the energy distribution of the system.

An alternate method of calculating Q_m is used for the waveguide simulations. The ^4He and substrate are still given their associated attenuation factors, but instead the energy in/out of the acoustic ports is used for calculation of the total quality factor using:

$$Q_m = \frac{\Omega_m L}{c_0 [1 - (P_{\text{out}}^1 + P_{\text{out}}^2) / P_{\text{in}}^1]}, \quad (2.39)$$

where L is the length of the waveguide, c_0 is the speed of sound in helium (approx the acoustic wave speed), P_{in}^1 is the acoustic power in through port 1, then P_{out}^1 and P_{out}^2 are the acoustic power out of port 1 and 2 respectively. For the waveguide simulations the

physical attenuation factors can be used as sufficient mesh density to push $|Q_m^{\text{eff}}|$ above 10^{10} is possible.

Using this methodology simulations with different available substrates are run for a $N = 19$ sonic crystal (the largest solvable 3D lattice with the lab’s computing capabilities), with $a_1 = 100 \mu\text{m}$ and $a_2 = 80 \mu\text{m}$, 200 nm deep and surrounded by $200 \mu\text{m}$ of substrate, with substrate attenuation reduced to $\alpha_{\text{sub}}^{\text{red}} = 10^{-4}$, and with ^4He attenuation reduced from $\alpha_{\text{int}} = 10^{-10}$ to a value that maintains the $\alpha_{\text{sub}}/\alpha_{\text{int}}$ from literature. The results of these simulations were then used to calculate the ‘reduction coefficient’ η , the fractional decrease to the pristine ^4He quality factor due to substrate losses:

$$\eta = 1 - Q_m \alpha_{\text{int}} = 1 - \frac{Q_m}{Q_m^{\text{int}}} . \quad (2.40)$$

The results of these simulations presented in Table 2.2. η is of course closely linked to α_{sub} , but is also dependent on the portion of acoustic energy inside the substrate. This is reduced for a higher acoustic impedance mismatch at the ^4He -substrate boundary. For the given materials this ratio varies from 0.7% (sapphire) to 3.8% (borofloat) of the energy in the substrate.

Table 2.2: Table of the quality factor reduction coefficient (η) for different substrate materials, obtained by FEM numerical simulations in COMSOL. Typical materials properties values: substrate density (ρ_{sub}), Young’s modulus (E), and Poisson’s ratio (ν) have been extracted from an online database [164]. The isotropic loss factor was computed from the quality factor values reported in the cited references.

Material	ρ_{sub} (kg/m^3)	E (GPa)	ν	α_{sub}	η
Silicon [165]	2330	170	0.06	5×10^{-10}	4.3%
Quartz [166]	2649	97	0.08	5×10^{-10}	7.6%
Sapphire [156]	3910	330	0.24	1.7×10^{-9}	8.5%
Fused Silica [167]	2203	70.4	0.15	1.7×10^{-8}	82.2%
Borofloat [168]	2230	64	0.2	1×10^{-6}	96.8%

Waveguides are also simulated for transmission of a 1.35 MHz acoustic wave, down a square cross section of $100 \mu\text{m} \times 250 \text{nm}$, and length 6 mm, dimensions chosen to produce similar energy distributions to the sonic crystals, and so provide a consistency

check. These simulations produce results within 5% of their sonic crystal counterpart. They also find a higher energy concentration within the ^4He for more square channels and higher frequency waves.

2.3.7 Device Imperfections

So far simulations have focussed on perfectly smooth devices with identical unit cells. For a physical nanofluidic chip there will always be some level of imperfection, either pre existing on the wafer substrate or introduced during fabrication. It is important to consider the size and associated effect of these imperfections as they have the potential to significantly perturb the acoustic mode.

Modern cleanroom nanofabrication techniques are expected to produce surface defects on a much smaller scale than the μm feature size within the sonic crystal chip. The top and bottom surfaces confining the ^4He into the $x - y$ plane may have surface RMS roughness down to 0.3 nm, the atomic surface roughness of commercially available silicon wafers. This roughness will be increased by etching, but with careful processing can easily be maintained on the nm scale [150].

Surface roughness on the pillar side walls could contribute to losses, especially as the defect mode is dependent on reflections from these surfaces. Optimisation of smooth side walls is an ongoing area of study [169], with many practical methods available. For the fabrication techniques used in this work, nm scale defects are expected on the pillar side, producing a surface roughness of the same scale. Simulating for this level of roughness on a $80\mu\text{m}$ object is beyond the scope and computation power of this work, though these defects may contribute as a geometric factor incorporated into a roughness-dependent mean free path as in Section 1.3.5.

While small nm scale defects can be considered to only cause acoustic scattering loss, larger defects may also cause perturbations to the acoustic mode, which may inhibit the concentration of mode and increase its radiative loss. To establish the significance of these effects, disorder is introduced into the pillar circumferences of a 2D sonic crystal simulation. The form of this disorder is random noise on parametric parametric functions for the radius of the pillar, around its normal value of $a_2/2 = 40\mu\text{m}$. Noise is produced

with a sum of cosine functions over increasing spectral frequency but decaying amplitude. The amplitude of the cosine noise is Gaussian, while its phase comes from a uniform distribution. The x coordinate of a pillar around its centre is then defined:

$$x = \frac{a_2}{2} \cos(2\pi s) \left(1 + A \sum_{m=-M}^M \frac{1}{|m|^\beta} g(m) \cos[2\pi m s + a(m)] \right), \quad (2.41)$$

for $m \neq 0$. $a_2/2$ is the radius of the pillar, s is the parametric variable sweeping $0 \rightarrow 1$ that defines the circle, A is the amplitude of the oscillations relative to the radius, $m = k/2\pi$ is the spectral frequency, summed from $-M$ to M , β is the spectral exponent defining the decay rate with frequency, $g(m)$ is a Gaussian noise function centred at 1 with standard deviation 1, and $u(m)$ is a uniform noise function from 0 to π . To generate a lattice of pillars with unique noise profiles in COMSOL, an additional $\times n$ variable is added to both noise functions, where n is the individual pillar number.

Simulations are run for the $a_1 = 100\mu\text{m}$ and $a_2 = 80\mu\text{m}$ sonic crystals, with $A = 0.01$ corresponding to a 1% noise on the pillar radius, $\beta = 0.2$ and $M = 20$. The resulting mode shape of one of these simulations is shown in Figure 2.25. A low β is chosen to preserve the amplitude of higher frequency noise, which is closer to what is expected from fabrication. With much greater computing power it may be possible to simulate some approximation of surface roughness, by beginning at higher m and increasing M .

Even though the simulations include noise with much greater amplitude than expected from fabrication, the resulting reducing in Q_m^{rad} is only around 10%, indicating the effect will not be significant for the physical devices. The likely reason for this is that sonic crystal is not reliant on the circular shape of the pillar, it is just the optimal choice, and so deviations still produce a lattice of objects that will on average reflect waves back into the defect.

The nm scale roughness remains a challenge to account for. While extensive literature exists for photonic systems [170, 171], the problem has yet to be solved for phononic crystals, especially for a sonic crystal where the interface is between a solid substrate and superfluid ^4He .

Considering the first in-plane pillar mode would be in the 10's of MHz range, far

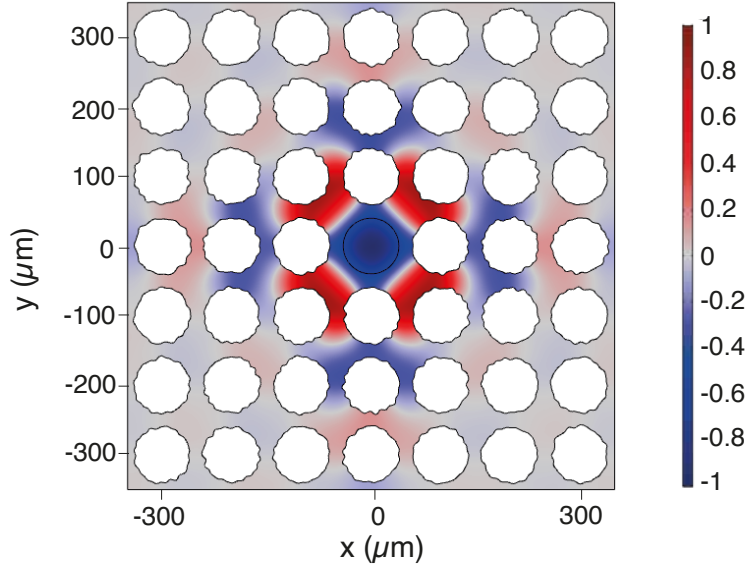


Figure 2.25: Showing the acoustic mode shape function (normalised pressure colour scale), of the fundamental point defect mode, as disturbed by a $\sim 1\%$ random deviation in pillar radius. The mode is only slightly disturbed by the deviations (with $< 10\%$ shift in defect mode frequency), which are much greater than what is expect from fabrication. The crystal unit cell is $a_1 = 100 \mu\text{m}$ and $a_2 = 80 \mu\text{m}$.

above the 1.34 MHz defect mode, the radiative efficiency into the pillar should be low. The loss into the substrate can then be considered in terms of scattering off an infinite pillar [172], using the vertical stress of an infinite cylinder as that within the pillar, which can then be treated as force onto the upper and lower substrate planes. By analogy to a shear transducer, the integral in Ref. [173] can be used to calculate the fraction of the incident power radiated into the substrate as 10^{-6} .

2.3.8 Coupling Capacitor

So far only the geometry necessary for the nanofluidics has been considered, while for the physical system the electric field must be also brought into the defect. The full microwave mode shape is discussed in Section 2.2.5, here the important feature of the mode is that the electric field will be concentrated between the central electrodes. To maximise the optomechanical coupling, the electrodes should be shaped to maximise the overlap integral in Eq. 1.82 for g_0 from Section 1.4.2. As the electric field is maximum everywhere between the electrodes, the shape of the electrodes should be chosen maximise

the acoustic modeshape integral $\int_V f(\mathbf{r})$ from Eq. 1.82, where V is the volume between electrodes.

Considering the defect modeshape in Figure 2.19, an electrode over almost the entire defect region would maximise coupling. However, a larger electrode also increases the capacitance, decreasing the microwave cavity's resonant frequency, which must be kept in the 4 – 12 GHz operating range of the measurement circuit. It is possible to decrease the capacitance by increasing the pillar height and so the electrode separation, but this will increase the effective mass of the acoustic mode through $\int_V f(\mathbf{r})^2$, and also decrease the concentration of the electric field within the capacitor.

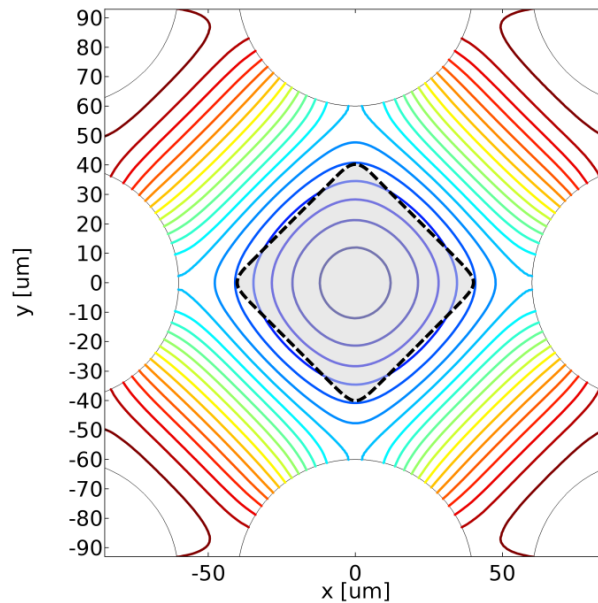


Figure 2.26: Showing the pressure field contours of the fundamental defect mode, for a sonic crystal of $a_1 = 100 \mu\text{m}$ and $a_2 = 80 \mu\text{m}$. The rough area covered by the coupling capacitor is outlined with a dashed black line, and highlighted in grey.

To maximise g_0 a balance must be found between: the portion of $f(\mathbf{r})$ enclosed by the electrodes and the effective mass of the acoustic mode, proportional to total $f(\mathbf{r})^2$ integrated over the entire geometry. A balance found all the while keeping the capacitance, related to electrode area and gap height, above 4 GHz the minimum operating frequency of the microwave circuit. Figure 2.26 shows a topographical map of the defect mode for a $a_1 = 100 \mu\text{m}$ by $a_2 = 80 \mu\text{m}$ sonic crystal, with contours lines of constant acoustic pressure field. From this a $60 \times 60 \mu\text{m}$ square electrode with rounded corners is

selected, approximately matching the fifth contour from the defect centre. As mentioned in Section 1.4.3, the key acoustic field quantities can be considered as α_1 and α_2 . α_1 is the ratio of $f(\mathbf{r})$ integrated over capacitor volume, to total $f(\mathbf{r})$ integrated over the entire mode; while α_2 is the ratio of volume between the capacitors, to the effective volume of $f(\mathbf{r})^2$ integrated over the entire mode. For the chosen electrode and sonic crystal geometry $\alpha_1 = 0.76$ and $\alpha_2 = 0.41$, a significant but not excessive reduction in g_0 .

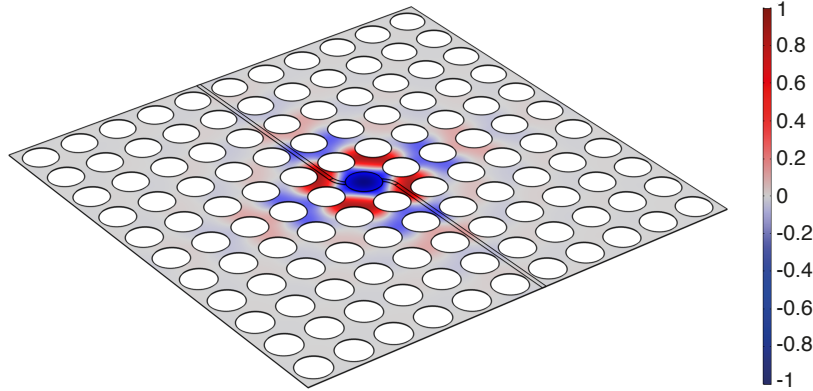


Figure 2.27: Showing the acoustic mode shape functions (normalised pressure colour scale), of the fundamental point defect mode, as disturbed by the central electrodes and their wires. The simulation is for a pillar height of 100 nm with the aluminium recessed by 10 nm. The field shape is also shown concentrated within the capacitive region. The crystal unit cell is $a_1 = 100 \mu\text{m}$ and $a_2 = 80 \mu\text{m}$.

With the shape of the electrodes chosen, a scheme must exist to connect them to the rest of the microwave cavity. The on chip aluminium wiring is grounded via large antenna on the edges of the chip to the outside of the microwave cavity, as in Section 2.2.5. Then to make an electrical connection from the electrodes within the central defect to the antenna, small wires $10 \mu\text{m}$ thick and $\sim 50 \text{ nm}$ deep are used, running in $\sim 50 \text{ nm}$ deep channels between the pillars. Channels that the electrodes are also contained within, which have the purpose of recessing the on chip wiring to minimise the disturbance of the ^4He acoustic field.

The recessing of the on chip aluminium should hopefully minimise its impact on the acoustic mode, but it is still useful to simulate for any potential effects. Figure 2.27 shows one such simulation for a 10 nm deep trench, within a 100 nm height 3D sonic crystal. This represents a reasonable worst case scenario of a 20 % mismatch between the

trench etch depth and aluminium deposition thickness, or a 10 % deviation in the height of the sonic crystal in the metallised regions. Simulations of this order of disturbance (recessed or protruding aluminium), find a negligible reduction in the quality factor or change in shape of the mode. The resistance to this form of disturbance is likely due to the $x - y$ mode being well below the k_z cut-off.

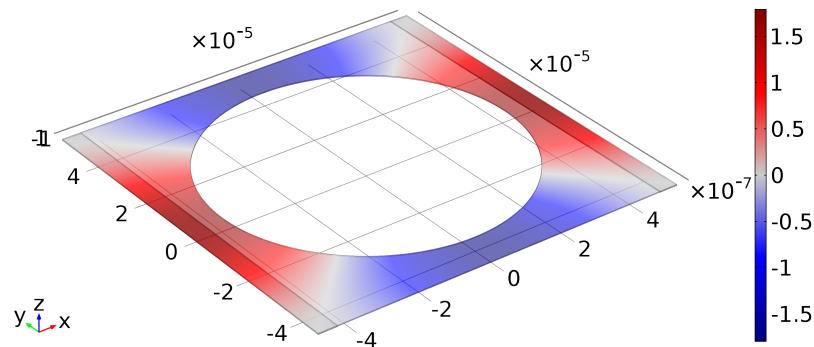


Figure 2.28: Showing an acoustic mode shape function within a single unit cell of a continuous sonic crystal, as disturbed by an additional channel at the x boundaries. The simulation is for a pillar height of 250 nm, with the channels 50 nm deep and 5 μm wide. The crystal unit cell is $a_1 = 100 \mu\text{m}$ and $a_2 = 80 \mu\text{m}$.

To corroborate this result, similar simulations were run for a 3D continuous crystal using Floquet boundaries, including 5 μm wide 50 nm deep channels at the left and right boundaries, for a 250 nm height sonic crystal. An example of one of the band modes is shown in Figure 2.28. These simulations found a $\sim 1\%$ change in the band structure of the sonic crystal, with the bandgap remaining complete, confirming the resistance of the system to these kinds of disturbances. Further exaggerating the channels in the simulations, to 50 nm deep in a 100 nm high crystal, a reduction in the bandgap height is found for the continuous crystal. While for the defect simulation a mode is found at ~ 1.6 MHz with field density concentrated along the channels. This mode may coincide with the lowering of the bandgap, and effectively represents a lowering of the phononic mode at the top of the first bandgap for \mathbf{k} vectors in the channel direction.

Chapter 3:

Experimental Methods

This chapter covers physical development of the experimental platform, including development of procedures for creating and running the experiment. Section 3.1 details the overhaul of a ‘wet’ dilution fridge, used to create the millikelvin experimental conditions required for work with superfluids (and superconductors), including details of the microwave measurement line thermalisation, and of the gas handling system used to supply helium-4 into the experimental cell. Section 3.2 then covers design of the experimental cell, including simulations to optimise its microwave properties, and design of features necessary to keep the cell superfluid leak tight (for filling with ^4He). Finally, Section 3.3 covers nanofabrication of the sonic crystal nanofluidic chips. An overview of the on-chip design is given, along with recipes for both transparent and silicon wafers, with specific focus on the room temperature wafer bonding technique developed to enclose nanofluidic geometry. The chapter and section end with a summary of the final samples (or chips) which are then used in the full optomechanics experiments.

3.1 Dilution Refrigerator

3.1.1 Functional Overview

Initial State

The group inherited a 1986 Oxford Instruments top loading dilution refrigerator, capable of cooling an experimental stage to low millikelvin temperatures. This ‘fridge’ had been adapted for many different generations of experiments, with no comprehensive documentation provided, and had laid dormant for many years. Due to these factors and the increased space required for modern microwave components, all on-fridge electronics

were removed. A new control setup was then fitted and tested on an initial run to base temperature, before finally installing a new microwave circuit.

This new setup allows controlled cooling to a base temperatures around 25 mK, sufficient for ^4He experiments deep into the superfluid phase. Through running the fridge to base temperature with the new control setup, an operational procedure was developed, while also giving an opportunity to identify problems and solve them where necessary. A list of minor alternations to the fridge not covered in this chapter are listed in Appendix C.

Description of Fridge

The fridge is an older design of ‘wet’ helium dilution refrigerator. The coldest section, the dilution unit, is held under vacuum inside the inner vacuum can (IVC), which is itself immersed in a bath of liquid helium. The bath is held inside a cryogenic super-insulated dewar or outer vacuum can (OVC), shielding the liquid helium from ambient temperatures. This setup provides six stages of cooling with distinct ‘plates’ of decreasing temperature to anchor to, these are (with approximate temperatures):

1. 300 K - Room Temperature Plate (RT)
2. 4.2 K - Liquid Helium Bath (4K)
3. 1.4 K - 1K pot (1K)
4. 0.7 K - Still Plate (Still)
5. 100 mK - Heat Exchangers (HX)
6. 25 mK - Mixing Chamber (MC) and Experiment (EX)

The stages EX - 4K are held within the IVC with the 4K plate forming the top surface of this vacuum can. Figure 3.1 shows the exposed plates EX - 4K. The IVC and 4K plate are kept at ~ 4.2 K by immersion in the helium bath. The IVC is connected through the bath to the fridge ‘top plate’ (RT) via a series of stainless steel tubes, held under the same vacuum as the IVC. These tubes contain everything needed for cooling, measurement and control within the IVC. The RT plate forms a seal closing the bath

from the top of the OVC. The OVC is bolted to a frame, suspending the fridge centrally in the screen room, with pumping lines and electronics feeding in from above. When the fridge is ‘open’ the OVC is stored directly below the dilution unit in a pit below the floor. The fridge does not have a nitrogen jacket, so when running only the helium bath must be refilled to keep it above the level of the 1K pot intake.

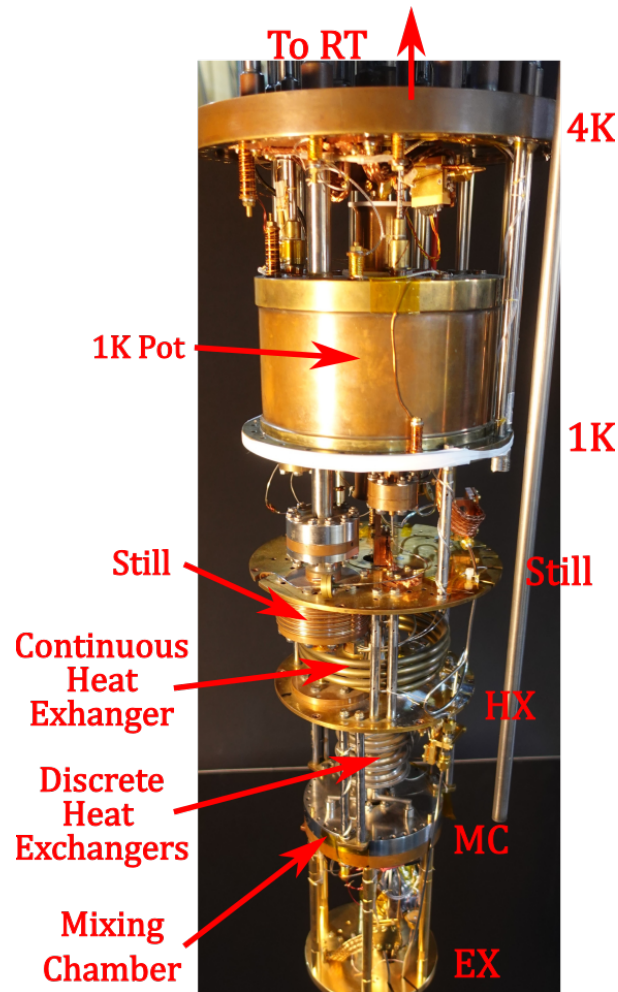


Figure 3.1: Photo of dilutions fridge’s plates, contained within the IVC during operation. On the RHS the plates have been labelled, while the LHS points to the sections of the fridge responsible for cooling.

The cooling of each plate will be covered in the next section as this is common to most wet fridges. All gas lines (pumping, recovery and return) connect from the RT plate to a gas handling system (GHS) in a box on the other side of the screen room. There are two distinct systems, covered in Appendix D, the helium 3 circuit and the 1K pot / recovery system.

3.1.2 Control Wiring

Figure 3.2 shows the ‘control’ wiring installed on the fridge to replace legacy systems, consisting of two thermometers, two heaters, and associated lines. The heaters are 1 k Ω resistors located at the Still and MC plates; wired with 44 *SWG* (81 μm diameter) copper twisted pairs from RT to 1K, superconducting NbTi (100 μm core, CuNi insulation) twisted pairs from 1K to the heated plate, and finally soldered connections to the resistors with short copper twisted pairs. The thermometers, from *LakeShore Cryotronics*, are located at the 1K and MC stages; a *Cernox CX-1030-AA-0.3L* thermometer purchased pre-calibrated down to 300 mK, is located on the 1K plate; and a Ruthenium Oxide *RX-102B-CB* thermometer calibrated down to 8 mK locally, is located on the MC plate, Figure 3.3 shows its resistance vs temperature calibration curve. Both thermometers are wired from RT to their respective plates with 4 wire *36 AWG phosphor bronze* ribbons, transitioning to their factory wiring close to the thermometer. The MC thermometer line also has two 5500 pF Pi filters (low pass), thermalised at MC, to reduce RF heating directly on the thermometer, reducing the measured base temperature from 27 mK to 23 mK. Transitions between different wire types have been achieved with small 4 pin plugs (*CMD Direct, 4-way connector for cryogenic use*) to allow easy modification and repair.

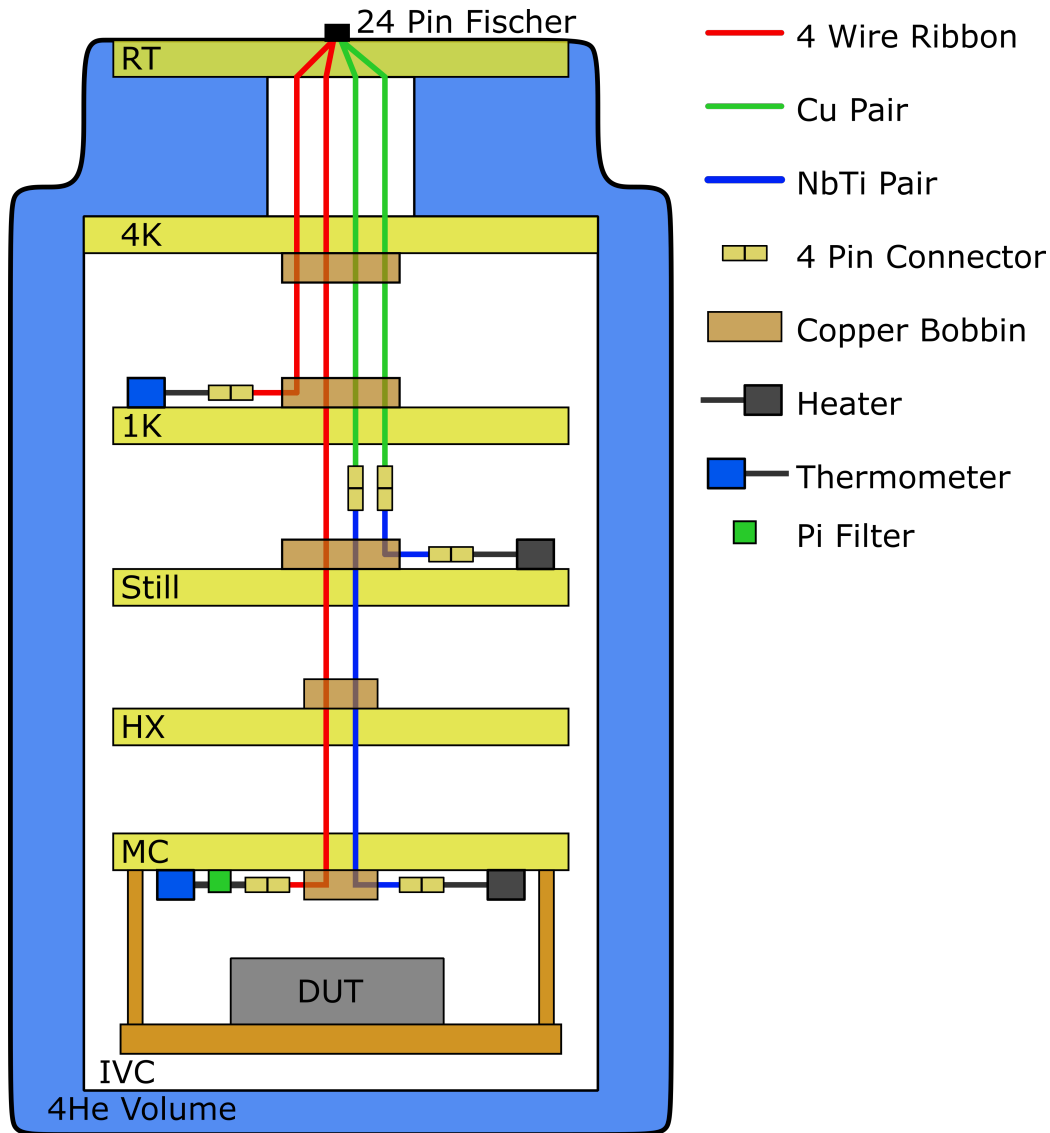


Figure 3.2: Control wiring for fridge showing both thermometers and heaters. Turns around the copper bobbins are not shown, all wires are thermalised to the same bobbin at each stage.

All control wiring is thermalised at each plate with 10+ turns around copper bobbins and coated in GE varnish, using a small piece of cigarette paper between the wires and copper bobbin to help electrical isolation. Dental floss and Kapton tape have been used to secure wiring to the fridge structure within the IVC. The control wiring exits the IVC volume via a 24 pin vacuum Fischer connector at RT, and is connected to the *Lakeshore 372 AC Resistance Bridge and Temperature Controller* via shielded cables.

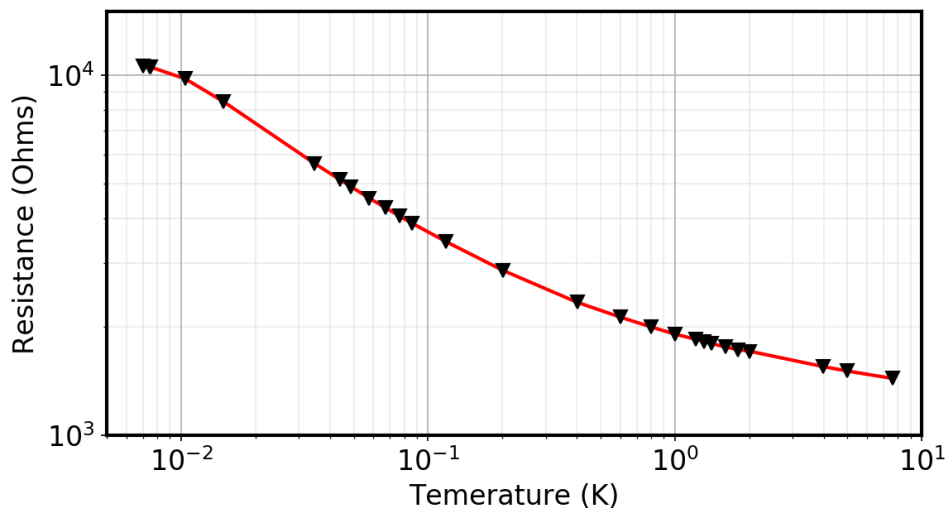


Figure 3.3: Resistance vs temperature graph for the mixing chamber thermometer, showing the region of calibration against a noise thermometer, with calibration carried out on another fridge in the department by Dr. Lev Levitin. Black Triangles are data points, while the red lines show what the temperature will read for specific resistances. Additional points have since been added up to 77 K using the 1K pot thermometer, however these are rough and only used to detect direction of change.

3.1.3 Measurement Thermalisation

Due to the older style of dilution fridge SMA mountings directly on each plate was not practical, instead a ‘floating’ scheme of thermalisation was used. From RT to 4K both the in and out lines run through the helium bath in the central tube (previously for top loading), these cables are mounted to a set of copper baffles with skirts that provide thermal contact with the inside of the tube, thermalising the cable on the way down while blocking thermal radiation from RT. From 4K to EX most components are thermalised to one end of copper (or gold plated copper) braids, which are then thermalised at the other end to the fridge plates. There are two main types of these thermalisation clamps, one that clamps the attenuator (Figure 3.4), and the other that clamps the coaxial line itself (Figure 3.5). The cryogenic preamp is also thermalised via a floating braid. These braids are used where the space provided is not sufficient for direct mounting according to the minimum bend radii of the coaxial cables.

Towards the MC thermalisation becomes increasingly important, especially thermalisation of EX stage components to the MC base temperature. As contact surface area can be up to a factor of 10^{-6} less than ideally smooth surfaces [174], the copper



Figure 3.4: Figure showing the floating braid thermalisation for attenuators.

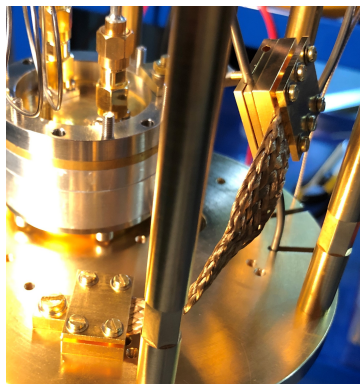


Figure 3.5: Figure showing the floating braid thermalisation for coaxial cables themselves.

components from HX down are gold plated to increase thermal contact and stop the copper surfaces from oxidising. The microwave cells (DUT) are thermalised by clamping directly to the EX plate, and the circulator directly to a pillar on the bottom of the EX plate. The EX plate itself is then clamped to the MC plate via six gold plated copper rods.

NbTi Thermalisation Issue

During an early run of the fridge there was an intermittent issue with $S_{21}(\omega)$ measurements of the cavity resonance at base temperature (see Chapter 4 for discussion of microwave measurements). Often the signal would abruptly drop in magnitude close to

the resonance, then recover at a frequency above the resonance. It was determined this drop would occur when the helium bath level was low and the input signal strength was above a certain point, with the lower the bath level the lower the input power threshold. The issue was likely caused by the 4K plate rising in temperature as the bath level drops, leading to a lower cooling power on the cryogenic preamp, and so higher temperature of the connected NbTi coax close to its superconducting transition. Then as the microwave signal nears resonance the transmitted power through the cavity increases to a point where it heats the NbTi normal near the preamp, causing a sudden jump in attenuation.

Two methods were successfully employed to mitigate this effect. Firstly a copper braid was attached to the top of the 4K plate, running outside the IVC and down into the bath volume, helping the 4K plate remain closer to 4K. Secondly a small heat leak was created using a copper wire from the 1K pot to the small section of copper coax between the preamp and NbTi cable, providing additional cooling to ensure the NbTi remains below its superconducting transition temperature. The heat leak was estimated to be around 1 mW, from its length and RRR.

Heating and Cooling

So far in this section thermalisation and heat leaks have been treated qualitatively, this subsection will cover some heat equations relevant to thermalisation. From the Fourier's law of thermal conduction, the heat \dot{Q} down a rod or wire of constant cross section A can be written as [175]:

$$\dot{Q} = \frac{A}{L} \int_{T_{\text{cold}}}^{T_{\text{hot}}} K(T) dT, \quad (3.1)$$

where L is the length of the rod or wire, T_{hot} and T_{cold} are the hot and cold ends of the rod respectively, and $K(T)$ is the thermal conductivity in W/(m·K). The heating can be approximated to $\dot{Q} = \bar{K}(T_{\text{hot}} - T_{\text{cold}})$, where \bar{K} is the average thermal conductivity over the temperature range. This is useful for quickly calculating the heat leak through components that span the different temperature plates within the fridge. For example

the thermometers are connected via a ribbon of four 36 AWG phosphor bronze wires, assuming the wires are thermalised at each plate, with 10 cm of the ribbon between the 1K and 4K plates. The values for $K(T)$ provided by the manufacturer can then be used to calculate the heat leak from 4K to 1K [176], which is $\sim 50 \mu\text{W}$, acceptable for the 1K pot with mW's of cooling power. A similar process can be repeated for all the on-chip circuitry.

For metals $K(T)$ tends to decrease proportional to temperature, at the temperatures inside the dilution fridge, which gives a T^2 dependence from the integral. This dependence and the decreasing temperature gap of the plates towards the mixing chamber, means for the same wiring the heat leak between each successive plate is lower, e.g. for the same length of phosphor bronze above the heat leak between the 1K plate and still plate is $\sim 0.25 \mu\text{W}$.

Another method for metals is using the ‘residual-resistance ratio’ (RRR), the ratio of a materials resistivity at 300 K and 0K, though often approximated to room temperature and 4.2 K (liquid helium temperature) [174]. The RRR of a normal metal is roughly equal to its thermal conductivity at 1 K, with some material dependent constant adjustment factor. For example copper’s thermal conductivity can be written:

$$K = \frac{RRR}{0.76} T . \quad (3.2)$$

This allows for quick measurement of RRR by dipping in liquid helium, followed by a quick calculation of the heat leak, using the RT and 4K RRR method for the NbTi thermalisation issue described above. A RRR of 130 was measured for some 28 SWG copper wire, which was then used to select 25 cm as the length required to create a $\sim 1 \text{ mW}$ heat leak, between the 4K plate (at 4.2K) and the 1K plate (at 1.4K). Note this method does not work for superconductors, instead their thermal conductivity can generally be approximated to zero below their critical temperature.

Superfluid ^4He ’s thermal conductance near base temperature is sufficient to consider the ^4He in the cell at thermal equilibrium. Instead the concern is whether the helium volume is well thermalised to base temperature. Assuming the existing fill line

infrastructure is sufficient to thermalise the helium down to the heat exchanger plate, then the mixing chamber heat sink outlined in Section 3.1.5 will provide the cooling to base temperature. For cooling helium the acoustic mismatch at the liquid-solid interface determines the rate at which thermal phonons can be transferred. Firstly, only phonons with angle of incidence below the critical angle will be transmitted. The critical angle is calculated from Snell's law:

$$\frac{\sin \theta_h}{\sin \theta_s} = \frac{c_h}{c_s}, \quad (3.3)$$

where θ_h is the angle of phonon incidence from the superfluid ^4He , θ_s is the angle of refraction into the solid, then c_h and c_s are the speed of sound in the ^4He and solid respectively. From this the critical angle can be calculated:

$$\theta_{\text{crit}} = \arcsin \left(\frac{c_h}{c_s} \right), \quad (3.4)$$

which is equal to a few degrees for most solids. The critical angle can then be used to calculate the fraction of phonons with sufficiently low angle of incidence from transmission:

$$f = 2 \sin^2 \left(\frac{\theta_{\text{crit}}}{2} \right) \approx \frac{1}{2} \left(\frac{c_h}{c_s} \right)^2, \quad (3.5)$$

which is usually of the order 10^{-3} . Those photons below the angle of incidence then have a chance of transmission based upon the acoustic mismatch (as introduced in Section 2.3.1):

$$t = \frac{4Z_h Z_s}{(z_h + Z_s)^2} \simeq \frac{4Z_h}{Z_s} = \frac{4\rho_h c_h}{\rho_s c_s}, \quad (3.6)$$

assuming the angle of incidence is small enough to approximate all the phonons are incident perpendicular to the surface. A further approximation has been made for $Z_s \gg Z_h$. This transmission also tends to be of the order 10^{-3} . The fraction of thermal phonons transmitted from the helium into the solid, can then be approximated to:

$$ft \simeq \frac{2\rho_h c_h^3}{\rho_s c_s^3}, \quad (3.7)$$

for the heat sink made from a CuNi capillary, wound around and sintered to a copper bobbin, from Section 3.1.5. The solid parameters are $c_s = 2500$ m/s and $\rho_s = 8.94 \times 10^3$ kg/m³, and using the values of $c_h = 229.5$ m/s and $\rho_h = 145.1$ kg/m³, from Table 2.1; giving $\theta_{\text{crit}} = 5.27^\circ$, $f = 4.22 \times 10^{-3}$, and $t = 5.96 \times 10^{-3}$. Which relates to a total fraction of phonons transmitted $ft \approx 2.5 \times 10^{-5}$. The transmitted energy flux from helium into the solid is then:

$$\begin{aligned} \dot{Q} &= \frac{2\pi^2 k_B^4 T^4 \rho_h c_h}{30\hbar^3 \rho_s c_s^3} A \\ &= \frac{2\pi^2 k_B^4 T^4 ft}{60\hbar^3 c_h^2} A. \end{aligned} \quad (3.8)$$

The capillary used for the heat sink has an inner radius of 0.14 mm, and is wrapped around the copper bobbin 44 times at a major radius of 4 mm, giving an inside surface area in contact with the ⁴He of $\sim 1 \times 10^{-3}$ m². Substituting this surface area and ft into Eq. 3.8 gives a cooling power at 25 mK of 9.50×10^{-10} W, which is approximately 1 nW. This appears to be a very small cooling power, however, using the heat capacity in Eq. 1.30 from Section 1.3.2, for a ~ 1 cm³ volume of ⁴He at 25 mK gives $C_V = 5.27 \times 10^{-8}$ J K⁻¹ kg⁻¹. This means that a temperature change of 1 mK would be cooled in 0.055 s, and so the helium within the cell should be at roughly the mixing chamber temperature. Of course this ignores the contribution of thermal phonons travelling from the CuNi capillary, and other sources of heat onto the helium volume.

3.1.4 Piezo Drive

As an external source of acoustic energy at a specific frequency (or as white noise), a piezoelectric buzzer (piezo) is used. The piezo's used are PZT resonators enclosed by two electrodes, from *Boston Piezo Optics*, which can be driven with an electric signal at the intended frequency. The PZT acts as a transducer converting the alternating

electric field into acoustic energy at the same frequency. The piezo is mounted, using Stycast 1266, onto a small plate which is then screwed to the top of the experiment cavity. A small piece of cigarette paper is glued between the piezo and the plate to prevent electrical contact.

To bring AC signal down from RT miniature coax cables from CMR Direct are used. These cables have a 0.2 mm stainless steel core and 0.7mm braided stainless steel shield shield. Their small size and flexibility allows them to be thermalised by being wrapped around, and then GE varnished to, copper bobbins at each plate. The cables have a characteristic impedance of 40Ω at 10 MHz, and attenuation of 5.7 dB/m at 100 MHz, so working close to 1 MHz the cable attenuation should not be significant. To create a hermetic feedthrough at the RT plate, the outer conductor and dielectric are stripped back, and the inner conductor is fixed with Stycast 1266 through a brass piece, with dimensions matching one of the RT plate ports. The outer conductor of the coax is grounded to this brass piece, and the inner conductor is soldered to the central pin of an SMA conductor fixed to the lab side.

To check the piezo is functioning before an experimental run the room temperature impedance is checked, including the mini coax cables inside the fridge. A simple check with a multimeter should give 30Ω for the resistance from the RT plate to the piezo outer surface, through the outer conductor of the mini coax. while through inner conductor to the piezo inner surface gives 90Ω .

When making alterations to the cavity a more rigorous frequency dependent impedance check is carried out using a lock-in amplifier, the measurement circuit is shown in Figure 3.6. The lock-in measures V_1 and V_2 on its two inputs, sweeping the frequency of both inputs and the source simultaneously. The current through the system will then be:

$$I = \frac{V_g}{50 + R + Z_c} . \quad (3.9)$$

For large enough R to produce a constant current through the circuit, $R \gg Z_c$, the piezo impedance can be expressed as:

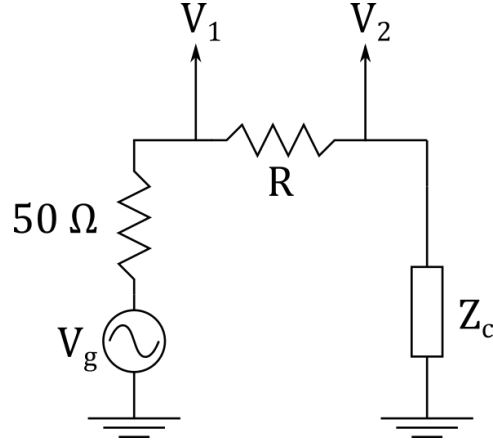


Figure 3.6: Lumped element circuit diagram of the piezo impedance check measurement circuit. Where V_g is the lock-in source voltage, R is a large known resistance (normally 10 k Ω), Z_c is the impedance of the mini coax and the piezo.

$$Z_c \simeq \frac{V_2}{V_1 - V_2} R. \quad (3.10)$$

Two piezo's have been used, one with a fundamental resonance frequency 538 kHz, which was then replaced with one resonant at 1.650 MHz. This was to avoid any higher PZT resonances near the expected fundamental defect resonance at 1.34 MHz. The piezo is expected to be mainly capacitive away from its resonance, so give an impedance approximately proportional to $1/i\omega C$. Multiplying the measured impedance by the source frequency and then taking the inverse, will give an approximate frequency dependent capacitance of the piezo and mini coax.

Figure 3.7 shows the measured frequency dependant impedance and approximate capacitance of the piezo line, as measured before the most recent fridge run with the 1.650 MHz piezo. The peak around 1.650 MHz is the expected piezo's fundamental resonance, possibly altered slightly by clamping to the cavity. Then the lower 100-200 kHz peak is likely the fundamental mode of the small plate the piezo is attached to.

3.1.5 Fill Line

The simplest way to fill the experimental cell with helium, is to bring a small tube or 'fill line' down from room temperature to the experimental stage. Then the flow of

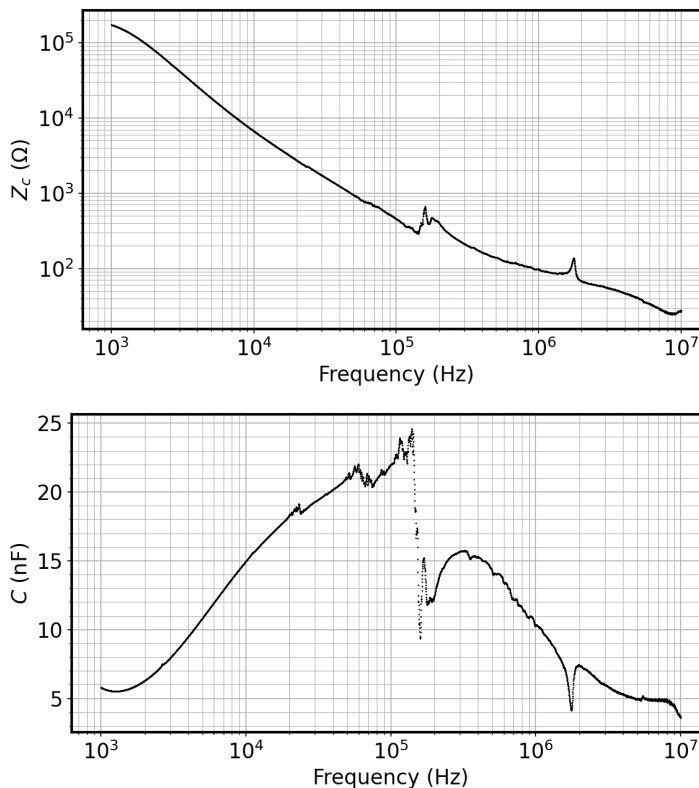


Figure 3.7: Top: The 1.650 MHz piezoelectric buzzer’s frequency dependent impedance, as measured for the most recent fridge run. Bottom: The 1.650 MHz piezo’s approximate frequency dependent capacitance, as measured for the most recent fridge run.

helium can be controlled at room temperature using a gas handling system as described in the following Section 3.1.6. The fill line must then be thermalised on its way down from room temperature, to avoid sudden heat loads to the MC, to efficiently cool the ^4He to base temperature, and to avoid excessive heat leaks once the cell is full.

The dilution fridge used for this project had existing fill lines, thermalised at each stage by: running through the liquid helium bath, through the 1K pot, around the still, and then finally through the continuous heat exchanger. As thermalisation at base temperature was missing, a heat sink was added at the mixing chamber, created from a length of CuNi capillary wrapped around and brazed to a copper bobbin, details of the construction are in the following sub-subsection. As the heat sink is only a length of capillary, it does not provide a large impedance to the fill line. While this makes filling the cavity quick, it provides slightly too strong of a thermal contact between the helium volume in the cavity and the HX plate, meaning a full cell will provide a heat leak, and

raise the base temperature of the fridge. At low pressures close to SVP this is minimal and only raises the base temperature by a few mK, however at higher pressure closer to 1 bar this can push the base temperature towards 50mK.

A ballast volume could be added above the cell, thermalised to the MC, which could then be partially filled, eliminating the heat leak at SVP, however higher pressures would not be possible. Another option is to add a silver sinter heat exchanger, where the helium must flow through the sinter, creating a larger impedance and reducing the heat leak. A way to eliminate the heat leak entirely would be to add a superfluid valve at the mixing chamber [177–179], so the cell could be filled to a certain pressure, the valve closed, and then the fill line pumped out.

To create and modify the fill line a selection of CuNi capillaries are used. These capillaries fit snugly inside one another with decreasing outer radius, making leak tight soft solder connection simple. To connect fill lines to cavities, thin walled brass or copper tubes with inner diameter matching a capillary, are brazed to the cavities over small through-holes. This then gives the freedom to soft solder capillaries, while not needing to heat the entire cavity piece, which may disturb the hermetic feedthroughs discussed in Section 3.2.3. Conversely the feedthroughs can be reheated and repaired without remelting the fill line solder join.

MC Heat Sink

As the existing fridge fill lines were only thermalised down to the HX plate, a heat sink was added to the MC, to aid thermalisation of helium in a cell to base temperature. The heat sink was created from length of CuNi capillary wound around and brazed to a copper bobbin; 72% silver, 28% copper brazing wire was used, according to the recipe:

- Ramp up to 805 °C at 7 °C/min
- hold for 20 min
- Ramp down to 20°C at 7 °C/min with a hold back of 10 °C

A volume of brazing wire was estimated from the assumption that the 0.5 mm outer diameter capillary would be tightly wound around the entire bobbin surface. This

underestimated the volume by a little over 50%, as brazing the first time did completely cover the wound capillary. A second braze on the same piece with $1.33\times$ the volume of silver sinter covered the capillary but caused the sinter to begin pooling at the bottom; so $2\times$ the initial estimate may be appropriate.

3.1.6 Gas Handling System

As mentioned in the previous section, filling and pressuring the experimental cell with ^4He at base temperature is controlled by a gas handling system (GHS) at room temperature. The existing gas handling system was insufficient: it leaked; was not capable of pressure much over 1 bar; and its LN_2 cold trap would boil dry overnight. Therefore a new gas handling system was designed and built, using primarily Swagelok components, fitted to a black anodised aluminium board, mounted to a wheeled frame with room for gas cylinders below. The front of this board is shown in Figure 3.8.

The board allows filling and pressuring of the experimental cell, from either the pure ^4He or dump cylinders below the board. The dump is used to recover ^4He from one run to be used in the next, which helps keep the pure ^4He volume free from impurities. The cell is normally filled through the LN_2 cold trap (CT), to freeze out any air or moisture in the system, though there is also a bypass to avoid the large CT volume. The bypass and CT connect the upper fill line section of the system with the lower ^4He volumes and vent section. The CT sits behind the board in a new nitrogen dewar, which stays cold for over a week. The current CT is an old repurposed low pressure CT, which has been converted to Swagelok $1/4''$ fittings, but should still not be pressurised over a few bar. A new high pressure (> 30 bar) CT has been designed and awaits filling with charcoal and welding.

During experiments at low pressure the filled cell is left open to the CT volume, a measure to reduce cell pressure in case a fault causes a sudden warming of the ^4He . Leaving the cell open to the CT also reduces the risk of any small leak from atmosphere, which could lead to ice blocking the fill line, presenting a hazard on warming up, though no noticeable leaks have been found during operation or a thorough leak checking of the GHS. As an additional safety mechanism, and for higher pressure operations, an over

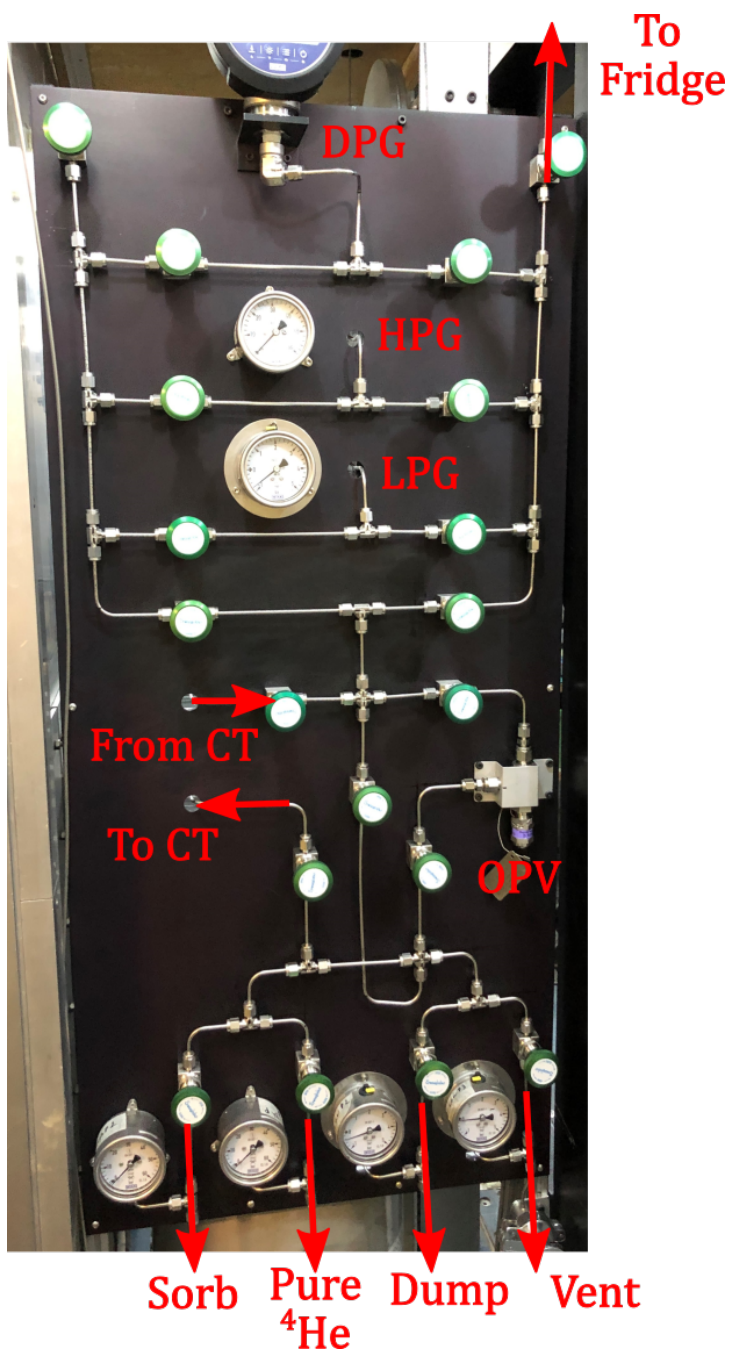


Figure 3.8: Photo of the front of ^4He fill line gas handling system, used to deliver pure ^4He to the experimental cell mounted on the fridge, a complete description of its function is in Section 3.1.6. On the fill line section the GHS includes: a digital pressure gauge (DPG) from 0 to 40 bar, an analogue low pressure gauge (LPG) from -1 to 5 bar, and an analogue high pressure gauge (HPG) from 0 to 60 bar. On the bottom of the GHS the sorb and pure ^4He are each connected to a HPG, while the dump and vent (with KF connector) are each connected to a LPG. All gauges are from Wika [180]. Lines travel to and from an LN_2 cold trap (CT) sitting behind the board, and an over pressure valve (OPV) set to 65 bar is fitted.

pressure valve (OPV) is installed, which can be left open to the fill line on one side and dump on the other. In the event of a fill line pressure over 65 bar this valve will open and let pressure into the dump.

The ‘sorb’ is a small (25 mm OD, 300 mm long) cylinder filled with charcoal on the end of long tube, which can be dipped into a liquid helium dewar, cooling the large surface area of charcoal and encouraging helium to quickly condense in the volume. This allows pressuring the cell by removing all the ^4He from the dump (down to a few mbar), and also returning almost all the ^4He to the dump at the end of a run. The sorb has been designed to be able to cycle to 60 bar, and so should be sufficient for high pressure liquid ^4He experiments.

The GHS is constructed from *Swagelok 1/8" 316 Stainless Steel Tubing*, certified up to 1000 bar, connected via stainless steel ferrules to Swagelok welded stainless steel valves, certified up to 68.9 bar. The system was constructed using a Swagelok 1/8" tube bender, pipe cutter and improvised de-burring tool.

There is room on the top left of the GHS for a second fill line connection, and there is also a second fill line connection and valve on top plate of the fridge. The second fill line could be pressurised and then monitored in parallel to the first fill line, however they would both need to share the CT volume and overpressure valve. Fitting a needle valve would also prove useful to slowly fill the cavity. As during the Run 1, applying only 35 mbar of ^4He from the GHS CT volume, was sufficient to mostly fill the nanofluidic geometry, due to its 100 nm scale height. Filling was taken much slower in Run 3, however it only took six times ~ 20 mbar in the smallest volume (digital gauge and connected tubing), to fill the nanofluidics.

3.2 Microwave Cavity Design

This section focusses on the specifics of designing a superfluid leak tight superconducting aluminium microwave cavity, to create a chip-cavity microwave mode as introduced in Section 2.2. First the isolated chip-cavity system is simulated without microwave ports, the goal of which is to establish the expected frequency for a given chip

size and material. Then the microwave ports are added to the simulation, varying the depth of the pin couplers to achieve the desired coupling strength. This is covered in the following Section 3.2.2. The size variation of these simulated cavities is kept within the limits set by the physical materials and the space on the experimental stage. Once the internal cavity dimensions are established the experimental cell can be designed, taking extra care for the hermetic microwave feedthroughs (Section 3.2.3), indium seals (Section 3.2.4), and the differential thermal contraction between components of different materials (Section 3.2.5).

3.2.1 Cavity Resonance

Table 3.1: Comparison of older COMSOL predicted cavity resonances to measured resonances.

Cavity Type	$\omega_{\text{FEM}}/2\pi$ GHz	$\omega_{\text{meas}}/2\pi$ GHz	Fractional Change
Al Square	7.37	7.60	3.03%
Al Re-entrant	4.36	4.19	3.90%

Similar to the acoustic simulations of Section 2.3, COMSOL is also a powerful tool for designing microwave cavities, typically able to predict the microwave resonances of a geometry to within $\sim 10\%$ of the physical measured values. Table 3.1 shows the COMSOL predicted resonant frequencies ω_{FEM} vs the measured frequencies ω_{meas} , for a couple of earlier aluminium cavities, where measurements are at base temperature.

The current design of superconducting microwave cavity-chip system is a cylindrical microwave cavity. With the nanofluidic chip sitting vertically, such that the chip’s central capacitive region is right at the centre of the cavity, with the thin on chip wires running vertically, until they meet the ‘contact pads’ which ground the on chip aluminium to the inside surface of the microwave cavity. This is similar to Figure 2.1, but with a cylindrical cavity, and the antennae recessed into the cavity walls Giving expected microwave modes as discussed in Section 2.2.5, which can be solved for using COMSOL, solving for the electromagnetic waves in the frequency domain.

The chip-cavity geometry is more difficult to mesh and solve for than a macroscopic cavity, due to the large difference in scale between the mm scale cavity and μm scale on chip aluminium, plus the nm thinness of this aluminium. To solve for this more complex geometry, a triangular mesh is created over a 2D projection of all the on chip geometry, out to the cavity radius. This 2D mesh is then swept to an identical projection, over a distance equal to the electrode gap, creating a thin slice of order 100 nm thick. This approach allows the on chip aluminium to then be defined as 2D ‘perfectly conducting boundaries’, on the outer surfaces of the swept domains. Also included in the 2D plane before sweeping the mesh, are two concentric circles of increasing radius, centred on the electrodes, which allow for defining a higher mesh density in the regions closer to the electrode. Figure 3.12 shows the COMSOL geometry, including the pin couplers.

The rest of the 3D geometry can then be built up around this thin slice. For a cylindrical cavity this involved splitting the cylinder in half along the slice, and shifting each half away from each other by half the gap size. This creates a cavity that is cylindrical to a good approximation, and can take advantage of the swept mesh technique. This methodology allows for a high mesh density where it is needed (electrode region), and a low density where it is not (cavity volume), keeping the total mesh just within current available computing power.

Table 3.2: Comparison of first three cavity resonances for different nanofluidic chips, as predicted by COMSOL simulations, all for an electrode gap of 150 nm, and a cylindrical cavity of diameter 15 mm and height 9.5 mm.

Chip Material	Chip Type	Electrode Width μm	1st Mode GHz	2nd Mode GHz	3rd Mode GHz
Quartz	A	30	4.86	11.45	14.87
Quartz	A	60	2.88	11.43	14.63
Silicon	D	60	3.90	7.71	11.25

Table 3.2 presents COMSOL predictions of the first three microwave modes of the chip-cavity system, for three different chips in the same cavity. These chip materials and parameters are chosen as they represent the ‘best’ chips produced from nanofabrication, Section 3.3.5. The predictions are for a 150 nm gap, the minimum gap simulated. Ideally

the predicted first mode would be greater than 4.4 GHz, within the reasonable maximum deviation expected for the physical system, to still get a mode above 4 GHz.

Figure 3.9 then shows how these resonances change with electrode gap, showing the absolute frequency for the fundamental chip mode, and the detuning from each mode's 150 nm value. The physical chips have gaps ~ 500 nm for quartz and ~ 250 nm for silicon. As expected from the discussion of chip-cavity mode shape in Section 2.2, the first mode's frequency varies the most, followed by the third mode, and finally the second. This mirrors the concentration of the electric field into the central capacitive electrode region. The silicon chip is generally less sensitive to the gap due to its higher dielectric constant, which occupies a portion of the cavity volume and helps concentrate more of the mode's energy there.

Table 3.3: Comparison of first three chip-cavity modes, for a silicon chip of 250 nm gap, in a cylindrical cavity of diameter 15 mm and height 9.5 mm. Shown are the resonant frequencies of the chip-cavity system in vacuum, with ^4He film covering the central electrodes, and with ^4He filling the entire cavity. \mathcal{R}_{gap} is the fraction of the mode's total electric energy within the gap between the electrodes.

$\omega_c^{\text{vac}}/2\pi$ GHz	$\omega_c^{\text{film}}/2\pi$ GHz	$\omega_c^{\text{full}}/2\pi$ GHz	\mathcal{R}_{gap}
4.125	4.095	4.088	0.130
7.767	7.7674	7.717	1.34×10^{-4}
11.412	11.407	11.311	7.20×10^{-3}

Focussing on a silicon chip with a 250 nm gap, it is useful to calculate the expected mode frequencies in vacuum, with a thin film of ^4He filling the capacitive region, and with the entire cavity volume filled with liquid ^4He . The results of these calculations are shown in Table 3.3. As expected the first mode shifts in frequency mainly due to the capacitive volume, while the second mode shifts almost entirely due to the volume, and the third mode presents some mix of the two. The participation ratio \mathcal{R}_{gap} of the central capacitive region has also been calculated via:

$$\mathcal{R}_{\text{gap}} = \frac{\int_{\text{gap}} \epsilon_h |E_0(\mathbf{r})|^2 d^3\mathbf{r}}{\int_V \epsilon(\mathbf{r}) |E_0(\mathbf{r})|^2 d^3\mathbf{r}}, \quad (3.11)$$

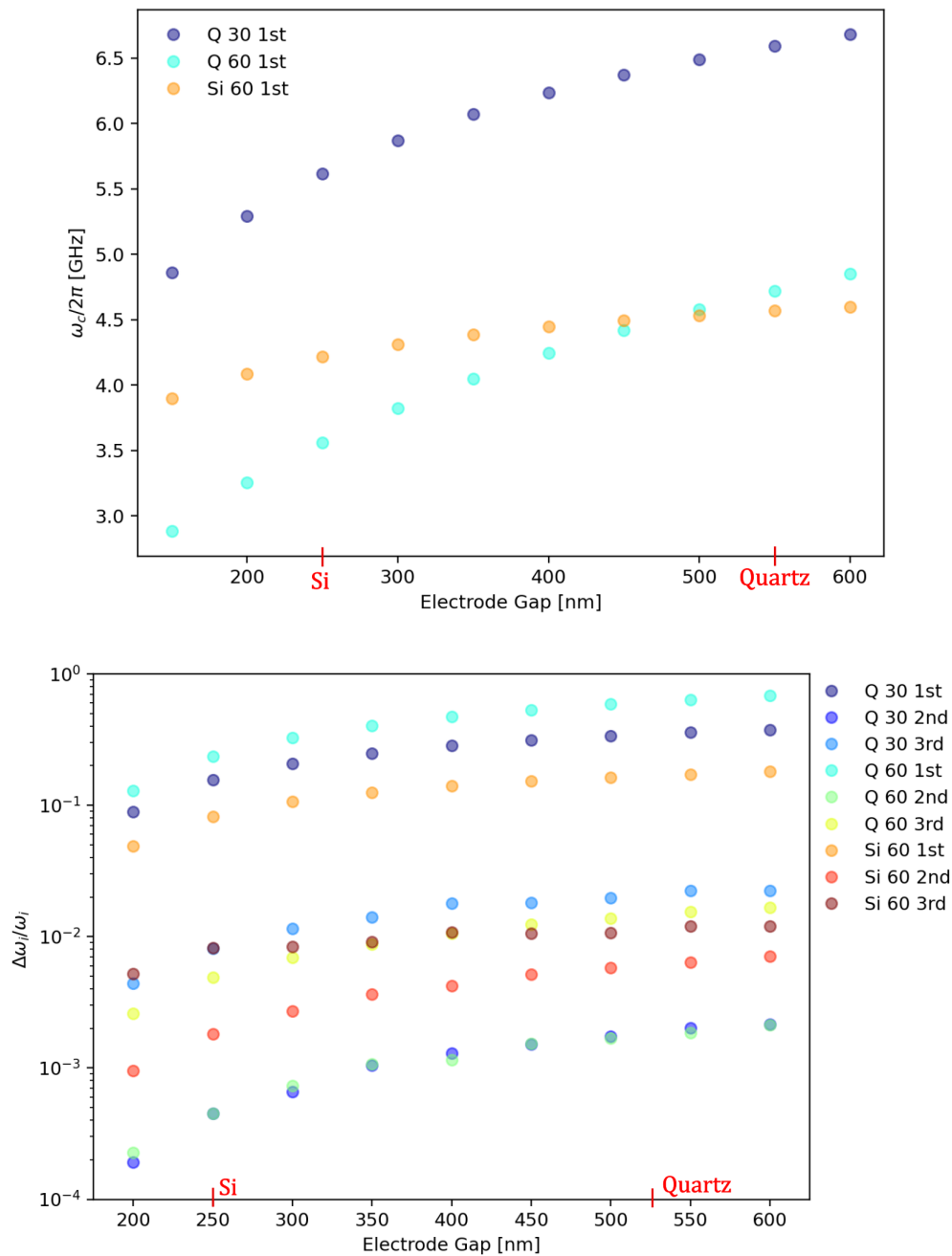


Figure 3.9: Both graphs show results of COMSOL simulations for a cylindrical cavity of diameter 15 mm and height 9.5 mm. Different chips from Table 3.2, Q referring to Quartz, Si to silicon, followed by the electrode width and finally mode number. Marked in red are the approximate gaps for the physical chips produced for the experiment. Top: Comparison of fundamental chip-cavity mode frequency for the three different chips, as they vary with the gap between the electrodes. Bottom: Comparison of mode frequency fractional detuning from the 150 nm gap value, for the first three modes of the chip-cavity system, for all three different chips.

where ε_h is the dielectric constant of helium, $E_0(\mathbf{r})$ is the electric field magnitude at point \mathbf{r} , $\varepsilon(\mathbf{r})$ is the dielectric constant of the material at point \mathbf{r} , \int_{gap} is over the capacitive gap region between electrodes, and \int_V is over the entire mode volume. \mathcal{R}_{gap} is equivalent to the fraction of the mode's total energy concentrated between the electrodes. For the case where the acoustic mode of the nanofluidic chip is entirely within the ^4He , and the electric field can be considered constant between the electrodes, this equation becomes similar to the terms at the end of Eq. 1.82 for g_0 . In fact, \mathcal{R}_{gap} should be approximately proportional to g_0 , meaning the relative coupling strength of the modes can be calculated from the values in Table 3.3 via $g_0 \propto \omega_c^{\text{full}} \mathcal{R}_{\text{gap}}$. From this, the 4.1 GHz mode gives the highest potential g_0 , while the third mode gives just under an order of magnitude weaker coupling, and the second mode is weaker again by an over an order of magnitude. Values which fit with the more qualitative descriptions of field distribution discussed in Section 2.2.5.

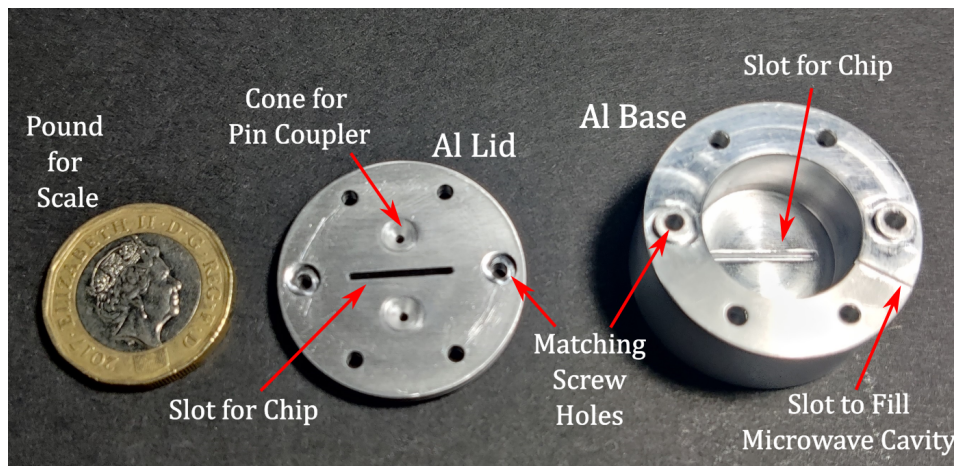


Figure 3.10: Photo of the two aluminium cavity pieces (pre polishing). The inside face of the lid piece that will form one surface of the microwave cavity is shown. The slots into which the chip will sit are shown for both pieces, along with the two coupling cones and holes for the microwave pin couplers in the lid. There is also a slot in the base where it will meet the lid to ensure ^4He can easily enter the aluminium volume.

This chip-cavity combination was chosen as it has two modes, in the 4 – 12 GHz operating region, that have an electric field concentrated to the capacitive region. The second mode may not be useful for coupling, but may be used to assess the helium level in the cavity, as its electric field concentrated along the thin on chip wire may be sensitive to this. Once an appropriate cavity size has been chosen, in this case to fit the nanofluidic

chip and have the three modes in the 4–12 GHz operating region, the physical object can be designed and fabricated. Figure 3.10 shows the bare aluminium cavity, while Figure 2.3 in Section 2.1 shows an entire dissembled cell with a silicon chip, and Appendix A contains technical drawings of the cell. Aluminium is chosen as it is superconducting at low temperatures (as discussed in Section 2.2.6), and it can be machined with relative ease.

As mentioned previously, the current design is for an aluminium cavity that encloses the chip, which is then itself enclosed by a superfluid leak tight copper cavity. Due to the pandemic affecting local fabrication, the cell was fabricated externally. This limited the aluminium cavity to 1060 ‘commercially pure’ aluminium, greater than 99.6% pure by weight, which will limit the internal quality factor to around 10^6 [131].

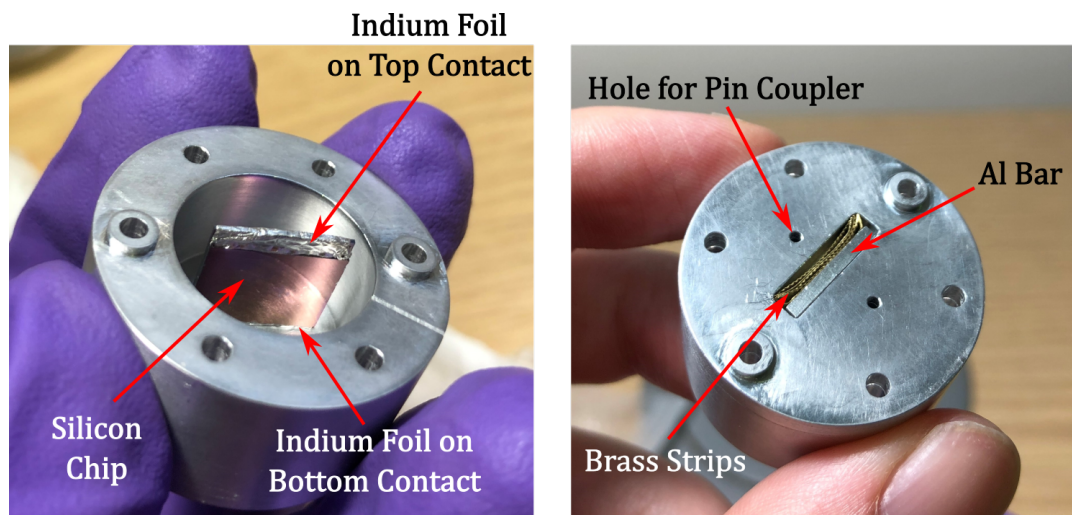


Figure 3.11: Left: a silicon chip, which has had both ends with contact pads covered in layers of 50 μm thick indium foil, and has then had one end inserted into the slot of the aluminium microwave cavity base. Leaving the other indium covered end protruding out the cavity base. Right: the lid of the closed aluminium cavity, with the slot that the other end of the silicon chip will protrude into. The small aluminium bar is then placed across the slot, and secured in place with some bent strips of brass, which hopefully apply sufficient force for good electrical contact.

Though a good galvanic bond is critical to ensure three microwave modes are within the measurement window, and to achieving a high quality factor. The current cavity design does not clamp the indium foil to the chip, avoiding unnecessary stress, instead relying on a good contact when the chip is pressed into the slot. This may be the cause of reductions in quality factor when thermally cycling the cavity without reseating the

chip, where thermal contraction and expansion has deteriorated the contact. To try to mitigate this the contact pads of the chip are covered in successive layers of 50 μm thick indium foil, such that the indium is tightly squeezed when fitting into the cavity. One pad end of the chip is pressed firmly into the base's slot, then the lid is fitted over the top of the other chip's pad. The chip protrudes through the lid's slot, such that on the other side an aluminium bar can be pushed against it with small strips of brass acting as springs, helping to maintain electrical contact between the cavity and on chip aluminium. The galvanic coupling process is shown in Figure 3.11.

3.2.2 External Coupling

The concentration of electromagnetic fields away from cavity surfaces makes strong microwave coupling difficult. However, for a high internal quality factor the low field is actually beneficial, as FEM (here COMSOL, as earlier in this section and in Section 2.2) techniques can be used to design a cavity with a specific weak coupling, preserving the internal quality factor. The two common methods for coupling to a cavity mode are: pin couplers which couple capacitively to the electric field, and loop couplers which couple inductively to the magnetic field [138]. Pin coupling was chosen as loop size, position, and insertion depth cannot be tuned accurately while maintaining a hermetic seal. Adjustment at room temperature with reference to the chip-cavity mode, is also not possible for either method, due to low Q above aluminium's superconducting transition. Pin couplings therefore allow a more accurate estimation of coupling strength via tunable dimensions at the simulation stage of cell design.

The microwave signal is brought to and from the cavity via coaxial microwave lines, which are discussed further in Section 4.2. The coaxial cables are then connected to the copper lid of the experimental cell via SMA connectors, which are in turn connected to the hermetic microwave feedthroughs from Section 3.2.3 next, with Figure 2.3 in Section 2.1 showing the pin on the other side of the copper lid. The feedthrough has a central pin which provides a continuation of the coaxial line's central conductor, which passed into the copper cavity, through the aluminium cavity's lid, and into the microwave mode's volume, coupling to the electric field with matching direction to the pin.

To estimate the coupling strength of this type of microwave port requires evaluating the field strength at the pin, which is difficult analytically for the combined chip-cavity system. Instead FEM with COMSOL is used to directly simulate the coupling strength, Figure 3.12 shows the chip-cavity-port geometry, as constructed in COMSOL.

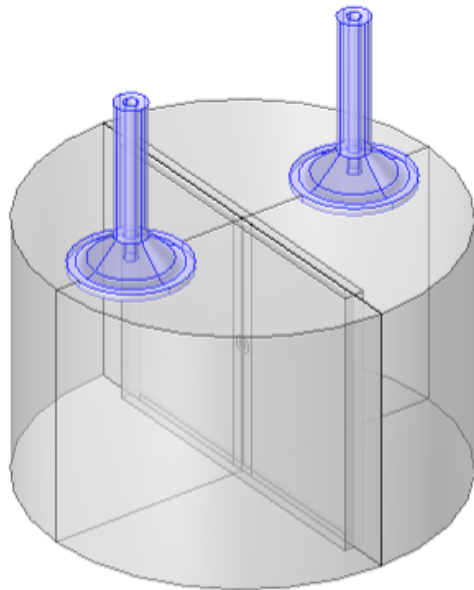


Figure 3.12: Image of the full microwave cavity system built within COMSOL. The cylindrical cavity is shown in grey with nanofluidic chip positioned vertically in the centre, including the on-chip aluminium and chip dielectric, but ignoring the sonic crystal geometry to reducing computing requirements. The two microwave ports and coupling cones have been highlighted in blue.

The method for tuning the coupling uses the concept of quality factor introduced in Sections 1.2.3 and 2.2.6. Quality factor can be extended to coupling to microwave cavities by treating the ports as additional loss channels with their own Q . The quality factor of the microwave cavity including ports is called the loaded quality factor Q_L , it is then convention to split internal and external losses into separate factors giving:

$$\frac{1}{Q_L} = \frac{1}{Q_e} + \frac{1}{Q_0}, \quad (3.12)$$

where Q_0 is the ‘unloaded’ quality factor from internal cavity losses, and Q_e is the external quality factor due to energy coupled out of the system through ports. The relative strength of the coupling between a microwave cavity and its ports can then be expressed as β :

$$\beta = \frac{Q_0}{Q_e}. \quad (3.13)$$

This β can also be thought of as the ratio of energy dissipated within the cavity and the energy coupled out of the mode through the ports, with $\beta < 1$ representing the undercoupled regime, $\beta > 1$ the overcoupled regime, and $\beta = 1$ the critically coupled regime, where half the energy is dissipated in the cavity and half leaves via the couplers. For a two port cavity sometimes $\beta = 1/2$ is given as critical coupling, where Q_e is for a single port, however in this work external coupling will always refer to the sum of all ports. For a cavity with two identical ports and $\beta = 1$, half the power is dissipated inside while a quarter is transmitted out each port.

Coupling towards the upper limit of internal quality factor is chosen as an initial target for external quality factor [132], that is $Q_e = 1 \times 10^7$. This allows a first run to accurately determine Q_0 which should dominate Q_L , refinements can be made to approach critical coupling at this measured Q_0 . To achieve the target Q_e , the cavity is simulated and the length of the coupler's pin is varied.

For the centrally concentrated electric field of the chip-cavity system, the optimal pin depth is approximately on the border of the cavity. This presents an issue for fabrication as small errors in depth can alter the pin from being slightly recessed from, to slightly protruding into, the cavity itself. These two regimes represent a significant jump in coupling strength. To mitigate this 45° ‘coupling cones’ were added in between the microwave ports and cavity volume, creating regions of weaker and more slowly varying cavity field. The pins can then protrude a distance into the cones, providing coupling less vulnerable to small errors in fabrication. The cones are included in Figure 3.12.

Three distinct methods have been used to extract Q_e from COMSOL simulations. Firstly the unloaded zero port cavity can be simulated with lossy boundaries, whose conductance can be varied to get the required Q_0 . This conductance can then be used in the full two port cavity eigenfrequency simulation to get Q_L , from which Q_e can be extracted due to a known Q_0 . Secondly the frequency response of a two port cavity can be simulated, with a single incident signal on one port. Then from the transmission

and reflection the Q_e can be extracted, using methods similar to those discussed later in Chapter 4. Lastly an eigenfrequency simulation of the two port cavity with perfect conducting boundaries will directly give Q_L , which is then equal to Q_e , provided other geometric error related losses are minimal. In testing it was found that these methods gave identical results for Q_e , so the simple perfect conducting eigenfrequency method was chosen.

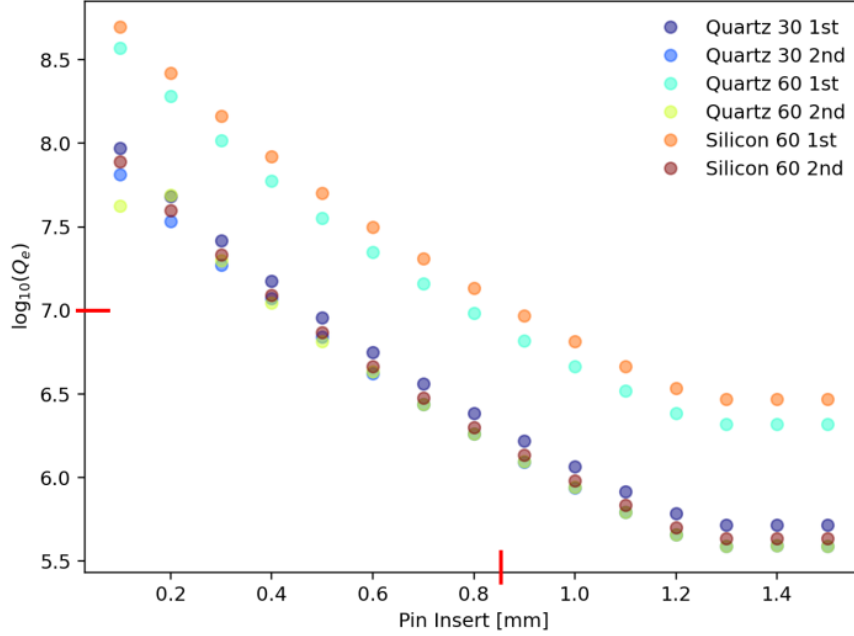


Figure 3.13: $\log_{10}(Q_e)$ vs the depth of the coupling pin into the cavity. For the first two modes of the chip-cavity system for the three different chips discussed in the previous Section 3.2.1. The chosen pin depth of 0.85 mm, giving $Q_e \approx 1 \times 10^7$ for the 60 μm electrodes has been marked in red on the axes. See text for discussion.

Figure 3.13 shows the results of these simulations, the external quality factor as a function of the the pin depth, from where the port meets the coupling cone. For the first two modes of the chip-cavity system for the three chips discussed in the previous Section 3.2.1. The initial log linear drop in Q_e is for the pin within the 1 mm deep coupling cone, where the electric field strength varies more slowly than at a cavity boundary, but much faster than within the cavity volume. Then Q_e levels out at a 1.2 mm insert as the pin enters the cavity volume proper, where the electric field varies much slower. The third mode is not shown as its Q_e is near constant around $10^4 - 10^5$, indicating either a higher participation of the coupling cone volume in the cavity mode, or some significant

error due to insufficient mesh density. A pin insert depth of 0.85 mm is chosen to give a Q_e of around 10^7 for the chips with 60 μm electrodes, a value just above a reasonable maximum Q_0 expected from the chip-cavity system, so that Q_0 can be directly measured without too much loss of signal strength. Technical drawings of the cavity can be found in Appendix A.

Table 3.4: Comparison of first three chip-cavity modes, for a silicon chip of 250 nm gap, in a cylindrical cavity of diameter 15 mm and height 9.5 mm. Shown are the resonant frequencies of the chip-cavity system with ^4He filling the entire cavity. Q_e the external quality factor, and E_{gap} the electric field within the central capacitive region between electrodes, for 20 and -50 dBm incident microwave power on one port P_{in} .

$\omega_c^{\text{full}}/2\pi$ GHz	Q_e	$E_{\text{gap}}(P_{\text{in}} = 20 \text{ dBm})$ V/m	$E_{\text{gap}}(P_{\text{in}} = -50 \text{ dBm})$ V/m
4.09	1.35×10^7	9.00×10^5	292
7.72	1.70×10^6	1.75×10^5	-
11.4	1.10×10^5	7.20×10^8	4.22×10^4

Focussing again on the 250 nm gap silicon chips, Table 3.4 gives key values for the first three modes of the chip cavity system. From Table 3.3 and its discussion in the previous subsection g_0 is expected to be an order of magnitude smaller for the third mode than the first, however Q_e is roughly two orders of magnitude higher than for the first mode, which is inversely proportional to \bar{n}_{cav} the average number of photons in the cavity (discussed more fully in Section 4.1.4). The square root of the photon number is then proportional to the coupling strength $g = g_0\sqrt{\bar{n}_{\text{cav}}}$, meaning it may be possible to measure the optomechanical coupling of the third mode with a comparable signal strength to the first mode. The values for the electric field in the capacitive region between the chip electrodes reinforces this, though these exact values cannot be fully trusted as they originate from simulations with no internal loss.

3.2.3 Hermetic Feedthroughs

As the superconducting microwave cavities used in this experiment will be filled with superfluid helium, microwave couplers are required which can remain superfluid leak

tight (hermetic) at mK temperatures and with differential pressure, while maintaining reasonable impedance matching. To achieve this soldered-in glass bead hermetic seals from Southwest Microwave were used, a full recipe for the installation can be found in Appendix E. Due to difficulty soldering aluminium, the seals were soldered into copper or brass pieces with the necessary dimensions drilled into them. The pieces were designed to be mounted to the aluminium cavity, such that they created a microwave connection from SMA connectors on the outside to the superconducting cavity mode, with the feedthrough's central conductive pin protruding into the coupling cone region, acting as the pin coupler described in the previous Section 3.2.2.

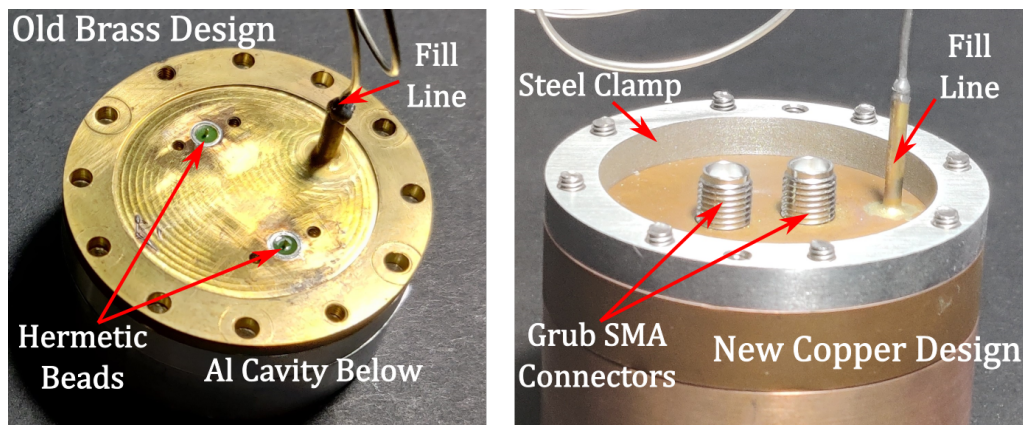


Figure 3.14: Left: Photo of the initial hermetic seal design on an older brass cavity lid. The green regions are the glass of the feedthrough bead, which has been soldered almost flush with brass lid. The SMA connectors which would connected to the central pin have been removed, but would attach to the lid via the two screw holes either side of the bead. Right: Photo of the new hermetic feedthrough design on a new copper cavity lid. The two grub screws SMA connectors are attached, screwing into the copper lid such that they connect to the central pin of the hermetic bead. The hermetic bead seal is identical in dimensions to the older design, however instead of being flush with the lid surface, the seal is recessed into the lid, with a tapped hole matching the grub style connector leading down to the seal level.

Initial tests with cavities regularly found leaks, especially after thermal cycling to base temperature and unmounting then remounting to the fridge. The initial designs used beads with the outer conductor almost flush with the face of their brass mounting pieces, and the hermetic seal produced with tin-silver solder (LHS Figure 3.14). In an attempt to reduce leaks, later cavities were designed with ‘thread in’ connectors, where the bead is recessed and the SMA coupler is a grub screw shape that screws into the mounting itself (RHS Figure 3.14). This reduces any potential force applied on the bead

by mounting the coax cables. Lead-tin flux free solder was also used for later cavities, which required use of a hydraulic press to create solder rings, but provided more even solder joins. Figure 3.14 shows both types of cavity, with the grub connectors screwed in on the new design. Both methods proved effective at forming superfluid leak tight seals, tested up to 2 bar, with acceptable impedance matching. However leaks after thermal cycling persisted, this issue has been consistent across all cavities, including those of other groups in the department, and prevents dip testing of cavities in liquid ^4He or N_2 . Cavities that leak after cycling can be made leak tight again by remelting their solder with a little flux. However, cavities that are robust to thermal cycling are desired, and so stycast feedthroughs, similar to low frequency lines but engineered to be $\sim 50 \Omega$, may be used. As low external coupling is required, a moderate impedance mismatch can be tolerated if symmetry between the two ports can be maintained.

3.2.4 Indium Seals

A microwave cavity is, by necessity of fabrication, formed of two or more conductive pieces, which when clamped together form a ‘cell’ with the cavity volume enclosed within. To then fill the cavity with superfluid helium the cell must form superfluid leak tight seams when clamped together, the most common way of achieving this is via an indium seal [181].

Initial Designs

For the initial design of a two port cavity, components mounted to the cell were soldered into individual small brass pieces, each with its own indium seal. This meant a total of four separate indium seals were necessary: one for each port, one for the fill line to bring helium into the cell, and one between the two pieces of aluminium to close the cavity itself; similar to the designs of De Lorenzo [91]. However for this cell the central pin length of the hermetic feedthrough limited the aluminium lid thickness, which compounded with the softness of pure aluminium, to make tight enough screwing of the brass piece to create a leak tight seal difficult. Helicoils were used to try and

increase thread strength but were insufficient.

The next generation of cavities were designed to mitigate this by combining all brass pieces into a single brass ‘lid’ which mimicked the dimensions of the aluminium lid it would be clamped on top of. This reduced the number of indium seals to two, one between the aluminium base and lid, and the other between the brass and aluminium lids. The updated design also includes two steel clamping rings, for above and below, with one including threaded holes, so that both indium seals could be tightened at the same time without the need to screw into soft aluminium. For both versions two distinct seal geometries were used. Both geometries assumed the 0.7 mm diameter indium wire used would compress to $\sim 50\mu\text{m}$, and their volumes were calculated to ensure no indium flows into the screw holes or cavity itself.

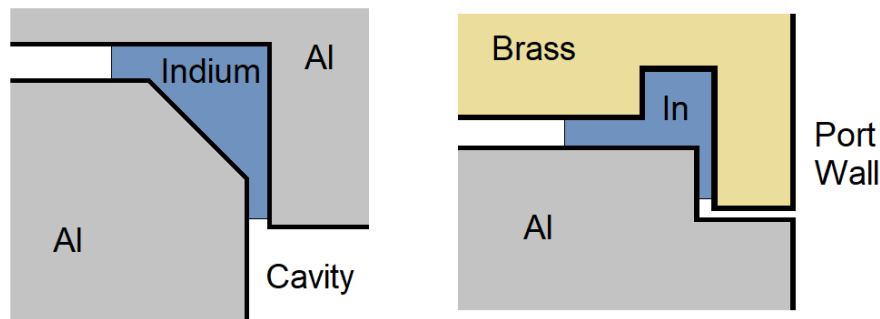


Figure 3.15: Figure of two indium seal methods used. Left: seal between top of aluminium cavity and base. The LHS thin section of indium is assumed to be $50\mu\text{m}$. Right: seal between brass pieces with SMA ports and aluminium cavity lid, shown is the LHS of an axisymmetric cross-section where the RHS would be mirrored. This is the initial design, with the seal being further from the ports in the improved design but following the same principle. The LHS thin section of indium is again assumed to be $50\mu\text{m}$.

Figure 3.15 shows both types of geometry used. Firstly the diagram on the left shows the seal geometry used between the aluminium lid and base. The seal is formed from by a winding an indium wire around the inside corner of the lid piece before placing it in contact with the 45° surface of the base piece. The protrusion of the lid piece, which defines the top of the cavity, is machined to be as close to the inside diameter of the base as possible, thus reducing and deformity along the upper edge and minimising seam losses [139]. The flush seam also encourages the indium to flow into larger channel

away from the cavity. The simple shape of this seal allows cleaning without significant deforming soft aluminium. This design of seal initially proved leak tight, however over multiple resealings the walls of the aluminium base deformed, increasing the 45° volume, and preventing a leak tight seal. The deformation also caused a deterioration of the microwave cavity mode's Q. Breaking the indium seal between the brass and aluminium also posed a threat to the feedthroughs, as the pieces separating at an angle could easily bend the pins.

The second seal geometry is shown on the right shows of Figure 3.15, the seal geometry used between the brass pieces and the aluminium cavity lid. The aim of this design is to maintain the impedance of the cavity's microwave ports, from SMA pin to cone volume. To achieve this the height of the brass lip on the RHS of the diagram is $50\ \mu\text{m}$ closer to it's opposing aluminium surface than the flat on the LHS. This means, for a compression of the indium to $50\ \mu\text{m}$, the brass surface on top of the lip will makes contact with the aluminium surface opposite, creating a more continuous inner surface, which minimises impedance mismatch. Similarly to above there is a volume for the indium to be compressed into, reducing the flow distance and giving a more reliable compression to $50\ \mu\text{m}$. The brass lip diameter is also machined flush with the aluminium to encourage indium flow away from the port. This design proved reliably leak tight with sufficient clamping force, however for the second generation the centrally located ports were far from clamping screws, so contact between the surfaces could not be ensured.

Final Designs

Due to difficulty producing reliable indium seals while maintaining a good microwave environment, the cells were redesigned to separate the aluminium microwave environment from the superfluid leak tight cavity. Essentially the designs in Appendix A are a superconducting microwave cavity inside a superfluid leak tight copper box, the disassembled cell and cavity are shown in Figure 2.3. The aluminium cavity (Figure 3.10) is bolted together and to the copper 'lid' (RHS Figure 3.14), which houses the feedthroughs and fill line. This removes the need to clamp soft pure aluminium with enough force to form an indium seal, reducing risk of deformation. The elimination of indium provides

a better microwave environment, reduces the reliance on high tolerance fabrication, and eliminates the risk of bending the pins. Then the copper box encloses the aluminium, and is tightened using steel clamps to form the single required indium seal, the geometry of which is a simple set of two opposing steps (which can be seen in Figure 2.3). The copper provides good thermal contact between the aluminium, EX stage and helium inside; while being strong enough to be resealed without deformation. These cavities also used the ‘thread in’ type SMA connectors, allowing a thicker lid, required for designs to accommodate higher pressures.

3.2.5 Differential Thermal Contraction

As mentioned earlier in this section, thermal contraction and expansion is a concern for low temperature experiments. Mentioned so far with regards to the hermetic feedthroughs which start leaking after thermal cycling, and also for the galvanic chip contact, which may also degrade after cycling to base temperature. Both of these issues are likely caused by the differential thermal contraction between the different materials used for the physical cell, Table 3.5 gives the percentage change in length for commonly used materials.

Table 3.5: Fractional thermal contraction, from room temperature to 0 K, for a variety of materials common to cryogenic and microwave cells, presented as a percentage of their original dimensions [182].

Material	Al	Brass	SS 316	Cu	In	Mo	Nb
$\Delta L_{RT \rightarrow 0K}$ [%]	0.425	0.384	0.297	0.326	0.706	0.095	0.143

A good rule of thumb, for making a good thermal contact at base temperature, is using brass through screws with nuts and steel washers to connect copper pieces together. This ensures the copper surfaces are pushed together with increased force at low temperature, as brass contracts more than copper and steel contracts less. The cell is attached to the experimental stage in this way, ensuring it is thermalised to base

temperature. The same logic is not used for the copper cell's indium seal, where steel screws are used, because steel screws can be tightened with more force without damaging the screw head, and this tightening is sufficient to create a superfluid leak tight indium seal.

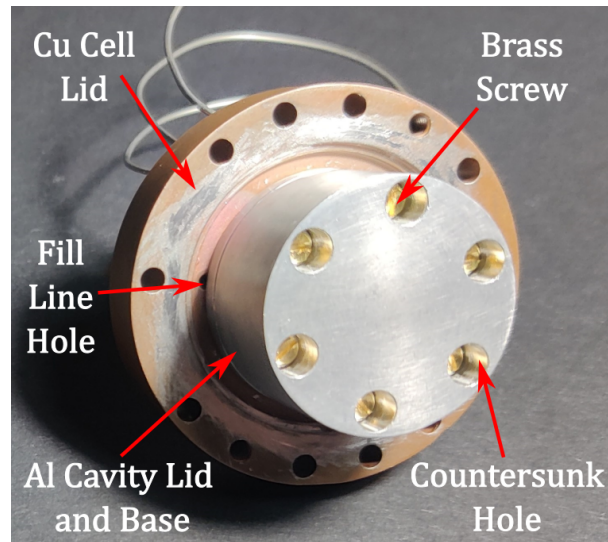


Figure 3.16: Photo of the aluminium cavity (with chip inside) clamped to the copper cell lid, using brass screws and stainless steel washers, within the countersunk holes of the aluminium cavity base.

Removing the indium seal from the aluminium cavity seam should create a cleaner microwave environment, provided good contact is made between the aluminium base and lid. This presents a problem as the thermal contraction of aluminium is greater than brass, and over tightening can easily tear soft copper or aluminium threads. On the older design of cavity, with the indium seal, this was avoided with steel braces either side of the cavity with threaded holes. For the new design the screws must remain inside the leak tight volume and screw into soft OFHC copper, so the thermal contraction must be more directly accounted for. To do this the aluminium cavity base is designed with countersunk holes, reducing the thickness of the clamped aluminium to 6 mm (lid plus base). Using brass screws the differential thermal contraction between aluminium and brass is 0.031 %. Then accounting for this with thick stainless steel washers, the differential contraction between brass and steel is 0.084 %. Taking the ratio of these two gives 0.369, which gives the ratio of stainless steel required for the depth of aluminium, resulting in 2.2 mm stainless steel washers. Figure 3.16 shows the aluminium cavity clamped to the copper

cell lid, with brass screws and stainless steel washers, into countersunk holes.

It may be more beneficial to go further and have the aluminium cavity further tighten with cooling, however approximately matching the differential thermal contractions was chosen to avoid additional stresses on the chip. Molybdenum washers are another option with very little contraction, where the thickness of washer required is a concern. Niobium instead of aluminium is an alternative option for creating a superconducting microwave cavity, and has the benefit of low thermal contraction, though is difficult to machine as it is so soft.

3.3 Nanofabrication

Due to the small dimensions and complex design of the nanofluidic sonic crystals, a fairly involved cleanroom process is required to fabricate the geometry from wafer substrates. The near 2D nanofluidic channels are enclosed, between two bonded pieces of cleanroom wafer, which forms the complete ‘chip’. Borosilicate, quartz and silicon have been used to create chips. Initial fabrication was using transparent wafers at London Centre for Nanotechnology (LCN) and nanoFAB at University of Alberta (UofA), however due to interruptions of access due to the COVID-19 pandemic, fabrication was moved to SuperFab at Royal Holloway (RHUL); where Silicon with thermal oxide was more in line with local processing.

3.3.1 Chip Design

The purpose of the cleanroom fabrication is to produce chips which house both the nanofluidic environment and superconducting circuits, concentrating the electric field of the microwave cavity and the acoustic mode field of the superfluid mode into a small volume. As mentioned previously the nanofluidic environment and superconducting circuit are patterned onto and then enclosed between two pieces of cleanroom wafer. As alignment of these pieces will be required for bonding, it makes sense to pattern the wafers with photolithography, as the resolution for both processes will be $\sim 1 \mu\text{m}$ (as a limit with $5 \mu\text{m}$ being regularly achievable). This choice simplifies fabrication as

photolithography tools are more routinely accessible within cleanrooms.

The devised process involves three photolithography steps: the first two are for etches into the substrate, the first to define the nanofluidic environment, then the second to create channels for depositing aluminium. The last photolithography is followed by the aluminium deposition step, which defines the superconducting readout circuit. The aluminium must be on the ‘inside’ surface of the bonded chip to provide a small enough capacitive gap, so the second etch was added to provide trenches for aluminium to be evaporated into, hopefully disturbing the superfluid acoustic mode less than aluminium directly within the sonic crystal.

Given the choice of photolithography and optical alignment for bonding, the chips were designed around a $5\ \mu\text{m}$ minimum resolvable distance for features. Using this as the default size of the sonic crystal unit cell was set as $100\ \mu\text{m}$, with $80\ \mu\text{m}$ diameter pillars, leaving enough room for a $20\ \mu\text{m}$ wide trench, to fit a $10\ \mu\text{m}$ thick superconducting wire. These dimensions also allowed for $\sim 60\ \mu\text{m}$ wide central electrodes, which should be fairly resistant to a $< 5\ \mu\text{m}$ misalignment. With this choice of electrode size the required electrode gap, for a 4-12 GHz mode, is $\sim 250\ \text{nm}$, achievable in most cleanrooms with acceptable tolerances ($< 50\ \text{nm}$). Initial 4” photo-mask designs had many designs of chip, varying the dimensions from a best case of possible resolution, half of dimensions above, to a worst case doubling of the dimensions. This is the origin of the $30\ \mu\text{m}$, $60\ \mu\text{m}$ and $120\ \mu\text{m}$ electrode widths, from the analysis in Section 2.3.8, which details the expected cavity resonant frequency vs electrode gap. A higher frequency is beneficial to g_0 , however a wider gap will increase the acoustic mode’s effective mass, so as small a possible unit cell gives the best possible coupling as the gap can be reduced while maintaining a higher ω_0 .

Three photomasks are required for fabrication, one per photolithography step (or layer), having both halves of the chips defined on the same wafer. CNST Toolbox was used to create a GDS file with geometry of the three photolithography patterns as separate layers [183], sent off to produce three separate photomasks, one for each later. Figure 3.17 shows an image of the geometry of the top and bottom pieces of a ‘D’ type chip, from the GDS using KLayout. The image would then be inverted for photomask

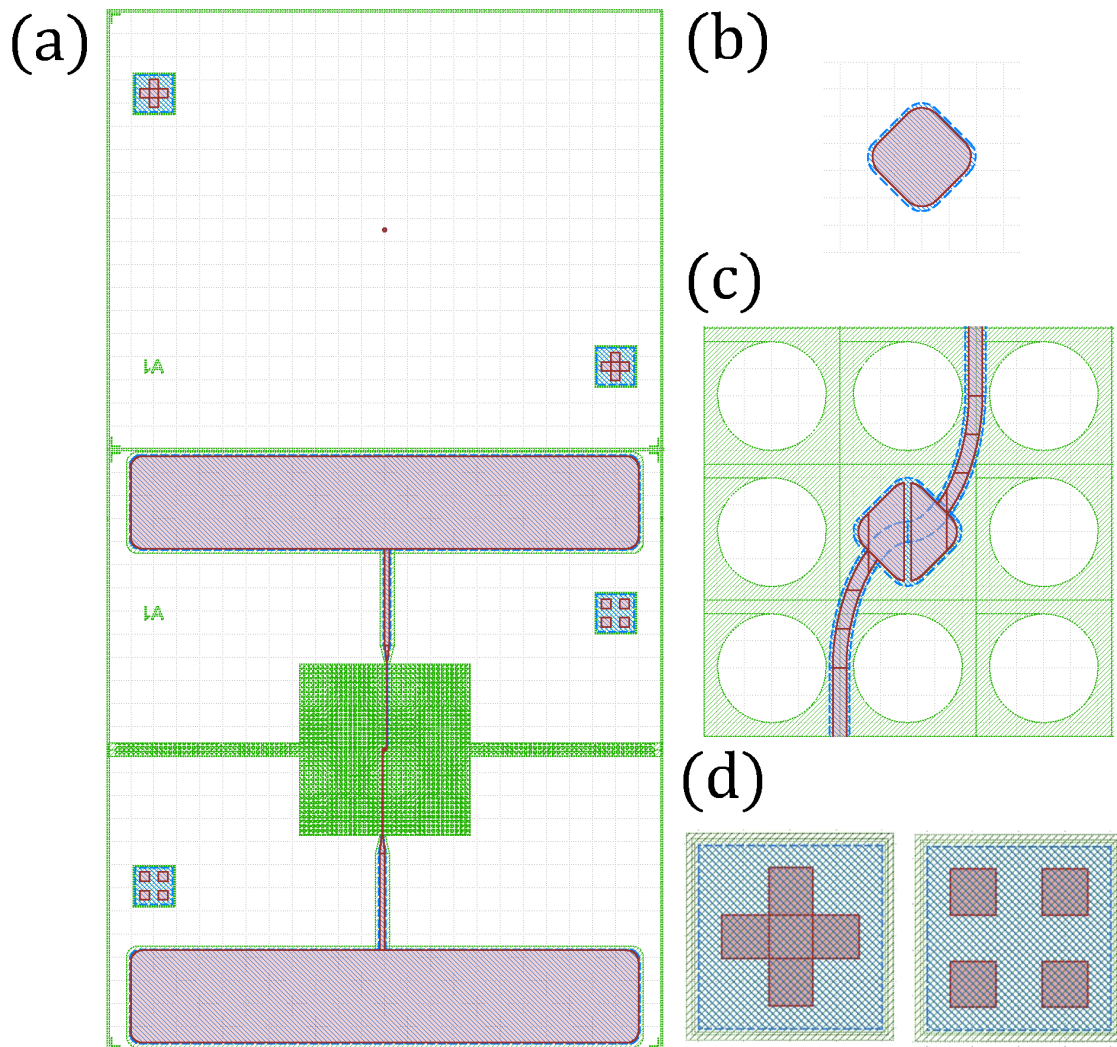


Figure 3.17: Showing the GDS image of the three layers, to be inverted for production of the three photomasks. First etch defining the geometry is in green, second etch to defined the channels for aluminium is in blue, and aluminium evaporation layer is in red. (a) showing the entirety of both the ‘top’ and ‘bottom’ chip pieces. (b) zoomed into the floating electrode from the centre of the top chip.

(c) zoomed into the central defect region defined on the bottom chip. (d) zoomed image of both bonding marks side by side, one from either chip piece.

production.

The figure shows diagrammatically how the geometry would look on the chip. The green first etch geometry defines: the sonic crystal pillar lattice (the nanofluidic plane), wide channels to keep all aluminium at a consistent depth, the nanofluidic filling channels to the left and right of the crystal, and the chip name (in this A1, though it should be D1). The second etch in blue defines the shallow 50 nm channel for the aluminium to fill, and some regions to keep aluminium depth consistent. Then the third layer in red defines the areas for aluminium deposition, which are $> 5 \mu\text{m}$ from the edges of the second etch to avoid overlap. The aluminium defines the large antenna top and bottom, leading via tapering wires to the split bottom electrodes, within the crystal defect. The deposited areas also include the floating top electrode and the alignment marks, which are used to align the matching top and bottom pieces for bonding. The cross of one alignment mark fits within the four squares of the other, leaving a $5 \mu\text{m}$ gap between the two. This gap is resolvable with a microscope and makes bonding alignment much clearer, necessary as the image is blurred due to dicing tape.

The initial 4" photomasks contained three distinct types of chip: A and B type chips whether the central electrode is a parallel plate and the chip-cavity coupling is galvanic, so the top and bottom pieces are essentially mirrored, with exposed antennas overlapping at both ends; C type chips with parallel plate electrode and antenna coupling, similar to A and B but with enclosed antenna closer to the centre of the chip; and D type chips (Figure 3.17) using a 'floating electrode' style central capacitor and galvanic coupling, this leads to a top piece with only an electrode and bonding marks, with both exposed antenna on the bottom piece.

Early trials focussed on the A and B chips, however the antenna facing in opposing directions meant that, to create a galvanic coupling, force must be applied from both sides of the chip. Often this would break the chip along the bond, either when it was tightened into a cavity or a some stage of returning from base temperature and opening the cavity. To remove this unreliability focus was switched to the D type chips, as force is applied in the same direction and not across the bond. Success has been found with this kind of floating electrode design and galvanic coupling with membranes [127]. When

switching from LCN to Superfab 3" masks were required, so a new gds was created using L-Edit which contained six copies of a single repeated D chip. The choice to focus on a single design was made to allow parallel design of a cavity, while minimising the time to produce the specific chip it required.

3.3.2 Transparent Wafer Recipe

Quartz and Borosilicate glass wafers were used for the first generation of chips, with a similar recipe for both. A complete run of fabrication was carried out at nanoFAB UofA, before adapting the recipe for LCN. The recipe revolves around the three photolithography steps described above, bonding will be covered in Section 3.3.4. After acquiring photomasks and other equipment an outline of the wafer processing recipe is:

1. **Clean:** 5 min O_2 plasma and 10 min Piranha, not necessary if wafers not exposed to air since manufacture.
2. **First Photolithography:** spin, bake, expose and develop S1818 photoresist.
3. **First Etch:** ~250 nm RIE etch with SF_6 .
4. **Strip Photoresist:** 1165 remover + heat + sonication.
5. **Characterisation:** Microscope inspection and profilometry.
6. **Clean:** 10 min Piranha.
7. **Second Photolithography:** spin, bake, expose and develop S1818 photoresist.
8. **Second Etch:** 50 nm RIE etch with SF_6 .
9. **Strip Photoresist:** 1165 remover + heat + sonication.
10. **Characterisation:** Microscope inspection and profilometry.
11. **Clean:** 10 min Piranha.
12. **Third Photolithography:** spin, bake, expose and develop two layer S1818 and LOR B photoresist.

13. **Aluminium Deposition:** 50 nm thermal evaporation of pure aluminium.
14. **Lift Off:** 1165 remover + heat + sonication.
15. **Characterisation:** Microscope inspection and profilometry. Alignment of aluminium in trench and cleanliness are key.
16. **Dicing:** protect with S1818 photoresist and then dice into pieces. More intensive characterisation possible on individual chips.
17. **Bonding:** Clean individual chips then align and then bond. Bonding discussed in detail Section 3.3.4.

The Figure 3.18 shows diagrammatically this process, with some simpler steps missing or combined.

After aluminium deposition it is no longer possible to thoroughly clean, O_2 plasma will oxidise the aluminium, while Piranha will remove it. Inspection must show clean surfaces before the third lithography is begun, if not additional cleaning or a new wafer is required. Wafers are most clean immediately after manufacture, so it may be beneficial with new wafers to skip the first cleaning step. In addition to this it may be possible to skip cleaning after photoresist stripping if the wafers are still pristine, thereby reducing total wafer handling.

Some difficulties with fabrication at LCN were: a perfectly even crystal bond and a long conditioning run are required for the DRIE to give repeatable even etch rates, optical mask alignment to a 50 nm etch into a transparent wafer is only just resolvable, and aluminium can drop off the coil when thermally evaporation (instead use a boat).

The process outline above showed potential for creation of chips at LCN, however due to the COVID-19 pandemic access to the cleanroom facilities became limited, and so the decision was made to move fabrication to SuperFab, local to RHUL.

3.3.3 Silicon Wafer Recipe

As mentioned above, fabrication was moved to SuperFab at RHUL. Due to time constraints and local processing facilities the decision was made to use 3" silicon wafers

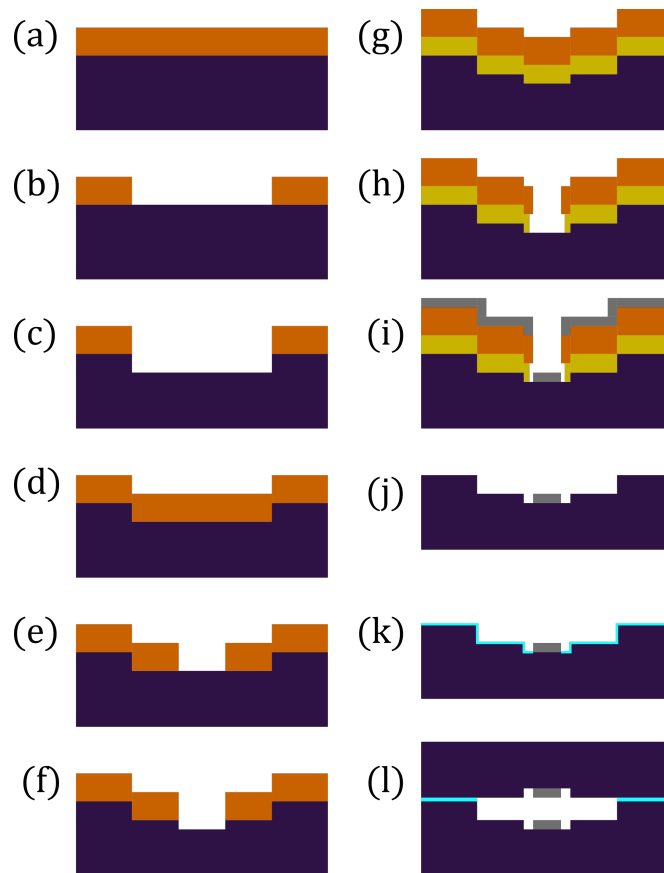


Figure 3.18: Diagram of the steps of the nano fabrication process, as a cross section of a region approximating the electrodes. Purples represents the wafer, orange the S1818 photoresist, yellow the LOR B photoresist, grey deposited aluminium, and cyan as the plasma activated surfaces with absorbed H_2O monolayers. Corresponding to the transparent wafer recipe: (a) the fresh wafer with spun photoresist, (b) expose and develop resist, (c) first etch, (d) resist strip and spin new resist, (e) expose and develop, (f) second etch, (g) resist strip and spin two layer resist, (h) expose and develop resist with undercut, (i) evaporate aluminium, (j) lift off, (k) clean and plasma activate, and (l) bond. Not shown is the dicing step, the two pieces bonded in (l) will originate on the same wafer.

with thermal oxide, specifically 300 nm of thermal oxide. This enabled a first etch of ~ 250 nm and then a second etch through the Si to the SiO_2 , reducing the time required to refine the recipe. Switching to 3" also required new masks, this is where the focus was switched to a single D chip ($100 \mu m$ unit cell). The chip design remained constant, however due to problems with photolithography equipment, direct laser writing was used for the first layer, then electron beam lithography (EBL) was used for the second and third layers. In principle laser writing could be used for all layers, but the laser writing equipment could not align reliably within $10 \mu m$. Although EBL can be used align to then expose patterns with much greater resolution than the $5 \mu m$ tolerance designed for,

the process was still limited by the need to resolve and align features using IR imagery during bonding. The final process was:

1. **Laser Writer Lithography:** spin, bake, direct write and develop S1813 photoresist.
2. **First Etch:** ~250 nm RIE etch with $CHF_3 + Ar$.
3. **Strip Photoresist:** 1165 remover + heat + sonication.
4. **First EBL:** spin, bake, expose and develop two layer Copoly MER 6% and ARP 6200.09 photoresists.
5. **Second Etch:** ~50 nm RIE etch with $CHF_3 + Ar$.
6. **Strip Photoresist:** ARP remover + heat + sonication.
7. **Second EBL:** spin, bake, expose and develop two layer Copoly MER 6% and ARP 6200.09 photoresists.
8. **Aluminium Deposition:** 50 nm electron beam evaporation of pure aluminium.
9. **Lift Off:** ARP remover + heat + sonication.
10. **Characterisation:** Microscope inspection and profilometry. Alignment of aluminium in trench and cleanliness are key.
11. **Dicing:** protect with S1813 photoresist and then dice into pieces. More intensive characterisation possible on individual chips.
12. **Bonding:** Clean individual chips then align and then bond. Bonding discussed in detail Section 3.3.4.

Harsher chemical cleaning is not present in this recipe as Piranha was not available, RCA cleaning may prove possible but introduction was delayed beyond the scope of this project. O_2 plasma cleaning was used to remove any photoresist left after stripping. Visual inspection prior to bonding with a microscope was possible, however profilometry

proved difficult due to problems with equipment. Even with these difficulties it was possible to produce samples of high enough quality for bonding.

3.3.4 Room Temperature Wafer Bonding

Low Temperature Direct Bonding

There are many methods of bonding cleanroom wafers, such as: fusion bonding, anodic bonding, thermo-compression bonding, eutectic bonding [150], glass fritting and polymer adhesive bonding [184]. The purpose of the bonding in this fabrication is to enclose the nanofluidic sonic crystal geometry, maintaining the designed acoustic profile as closely as possible, ruling out methods requiring additional material such as adhesive bonding. Anodic and fusion bonding can be used to produce ‘shallow’ channels with height of order 10 nm [185, 186], however both these methods require temperatures $\gg 200\text{ }^\circ\text{C}$ which will damage and oxidise the on chip aluminium.

Instead a low temperature ‘direct’ bonding method is used [187], this type of bond is created instantaneously by contacting two wafers or wafer pieces together. The initial temporary bond is weak and a more permanent bond is created by annealing at some temperature, though higher temperatures are often used it is possible to get a strong bond with $< 200\text{ }^\circ\text{C}$, and even a strong room temperature bond can be achieved with a long anneal time [188]. Direct bonding can be used for many different types and combinations of wafer substrate. The main condition for bonding is surface roughness [189], with RMS roughness below 0.6 nm providing a good bond (as a rule of thumb). Though the profile of the roughness is important as contact area determines bond strength, ignored by RMS, so instead using a bearing ratio (proportion of surface above a certain depth) provides a more accurate gauge of potential bond strength [190].

Creating strong bonds at low temperatures between Si , and similar material, wafers requires activation of surface SiO_2 groups. This is usually achieved with plasma but is possible with detergent [191] or certain acids, even enabling this type of bonding outside a cleanroom environment [192]. The plasma method creates a hydrophilic bond via the surface oxide, hydrophobic bonding is also possible between Si groups if surface oxide

is removed [193]. The plasma activated method uses a short burst of plasma, usually O_2 , N_2 or Ar , to transform surface $Si - O$ groups into $Si - OH$ groups [188]. These $Si - OH$ groups are very hydrophilic, and trap 2-3 monolayers of water (H_2O) via hydrogen bonds. Bringing two activated surfaces together, the hydrogen bonds between each surfaces trapped H_2O is enough to form a weak bond. The bonded pieces can then be left to anneal at room temperature, where the water molecules diffuse out through the interface and surface SiO_2 , causing hydrogen bonds to form between $Si - OH$ groups on opposing surfaces. These OH groups come close enough for the oxygen to form covalent bonds, creating additional water, $Si - OH + OH - Si \rightarrow Si - O - Si + H_2O$. Over ~ 400 hours at room temperature, or 48 hours at $50^\circ C$, this creates a strong bond, limited by surface roughness to a bond strength of $\sim 1.5 \text{ J/m}^2$. This limit is for wafers with minimal surface roughness, though the water monolayers form an initial bond $\sim 1.2 \text{ nm}$ wide, giving some additional tolerance for surface roughness, especially if a strong bond is not required. A maximum bond strength of 2.5 J/m^2 (close to bulk SiO_2) is achievable by softening the SiO_2 with heating to $100 - 200^\circ C$, which may be possible with aluminium in vacuum. For whole wafers and especially thin SiO_2 layers, excess water and produced hydrogen gas can cause voids to form [194], to improve bond reliability dedicated plasma and bonding equipment has been developed [195–198]. The temperatures in this section are for plasma activate surfaces, the same bond is possible without plasma activation using temperatures $> 800^\circ C$.

N_2 plasma may provide a marginally stronger bond than O_2 for this process [199], avoiding O_2 plasma is also preferable as it will further oxidise the aluminium, slowly increasing oxide thickness [200]. This bonding method can be used on quartz or glass due to the presence of surface $Si - O$ groups, and can even be used to bond SiN to any of these materials by plasma activating the SiN surface to create $Si - O$ groups. Though the plasma activation method removes the need to high temperatures or strong chemicals that would damage the Al, it still requires an effective surface roughness near and preferably below 1 nm . Any surface contamination via particles, leftover resist, or scratching can easily disturb the surface, making careful wafer handling and cleaning throughout processing key.

Transparent Chips

The general bonding process is cleaning, plasma activation, then alignment. Direct bonding requires pristine surfaces, sensitive to even a single particle on the wafer surface, so a thorough pre-bond cleaning procedure is key to a reliably strong bond. Cleaning procedures from the literature referenced earlier in this section almost always include strong acid steps (Piranha or RCA), these would remove Aluminium, and even weaker chemical processes like ozone and peroxide can oxidise the aluminium [193,201]. Through trial and error a harsh chemical free cleaning procedure has been developed that gives a reliable bond. This chip piece cleaning procedure, including the plasma activation, begins with the wafer diced but still protected with resist, then proceeds as follows:

1. Microscope inspection to determine viable chip.
2. Cold 1165 bath 5 min.
3. IPA rinse, N_2 dry
4. Mount pieces on Nalgene forceps and suspend face down over heated sonication bath.
5. Hot 65 °C 1165 bath with sonication 5 min.
6. IPA bath with sonication 5 min.
7. DI water bath with sonication 5 min.
8. DI gun rinse, N_2 dry.
9. 30 s O_2 plasma.
10. Remount, DI gun rinse, N_2 dry.

After this procedure the pieces are ready to align and bond. Cleanliness of equipment is key and so all equipment is washed with DI and IPA ahead of each bonding attempt, also a separate ‘clean’ set of tweezers and other equipment is kept for piece handling

after the sonication steps. The Nalgene forceps minimise piece handling and allow the maximum pressure of the DI gun to be used. Without ‘mechanical’ cleaning, provided by DI gun and sonication, bonding was unsuccessful. Prior to the use of forceps, the pieces were scrubbed with a soft material and detergent, this allowed bonding but scratched the aluminium surface. Oxygen plasma will slowly oxidise the aluminium [200], so it may be possible to replace plasma activation with a detergent wash, especially for second bonding attempts which fail due to introduction of additional particles or failure to remove particles from the first attempt. Though the bond strength without plasma activation may be weaker. The final DI gun rinse may be redundant as the surface will rehydrate with the 2-3 monolayers of water from the cleanroom air, and it may be that the additional handling introduces more particles than it removes.

After this cleaning process the pieces are aligned with the aid of a mask aligner and bonded by contact and a small force, photos illustrating the process are in Appendix F. To align the pieces while maintaining a microscope image, the window of the photomask holder is covered with bonding tape. The tape is placed on the bottom of the holder, sticky side to face the chuck below, with Kapton tape to secure it in place. One piece is then placed on the tape in the centre of the holder window, facing away from the tape, and the second piece is placed face up on the mask aligner chuck. The mask holder can then be inserted and the chuck slid in below. Keeping the bonding tape taught prevents the pieces coming into contact at an angle, which makes alignment more difficult and can prevent bonding if bonding surfaces are scratched. Rough alignment is achieved by moving the piece on the chuck around using tweezers, then fine alignment using the mask aligner’s micrometers. A fine alignment is first achieved using the bonding marks (Figure 3.17), with the pieces as close as possible but not in contact with one another. Then as the pieces are slowly brought into contact with one another, the overlap of the central electrodes is monitored and small adjustments made. The designs are tolerant to a small theta misalignment, but the central electrode overlap is key to maximising g_0 . Once in contact the pieces are gently pressed together by hand, forming a strong enough bond for the now complete chip to be removed from the bonding tape.

If the bond is unsuccessful the pieces will separate as the chuck is dropped, cleaning

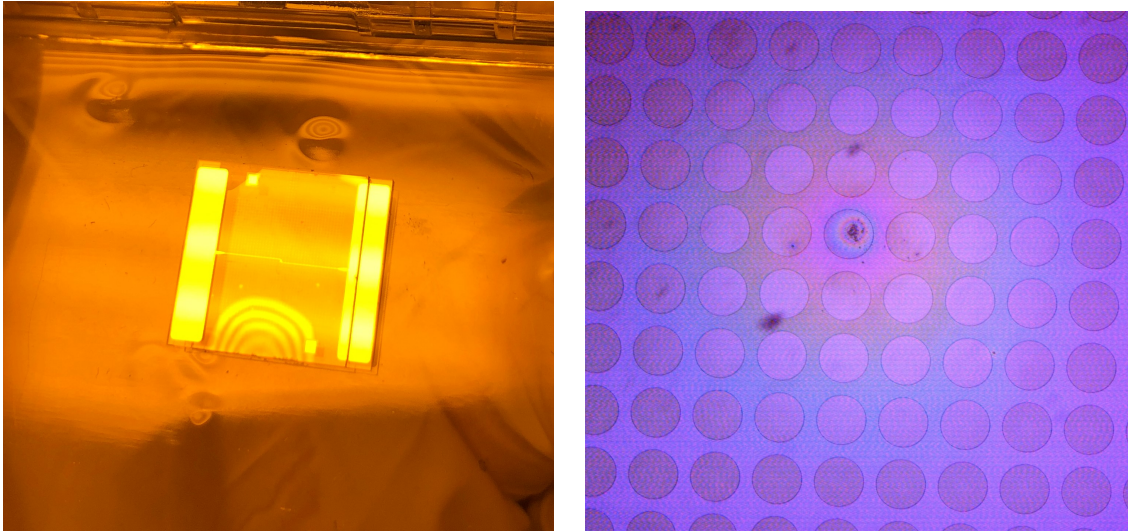


Figure 3.19: Left: Camera photo of a bonded transparent chip, showing Newton fringes originating at the chip edge. Right: Microscope image of the pillar region of a bonded chip, showing Newton fringes originating at some impurity inside.

must then be repeated if another attempt is to be made. If bonding is successful the chip should be checked for Newton rings or fringes [202]. The rings are interference fringes indicating a small gap between the pieces, the light and dark fringes showing the gradient of the gap, and at the centre of rings a particle can normally be found using a microscope. If these fringes appear across the sonic crystal region of the chip, it can still be easily separated at this stage and bonding reattempted. The cleaning process has been sufficiently refined that most bonding attempts are successful without particles. However the bonding is sufficiently sensitive that the failure rate increases drastically with number of people in the cleanroom, with an over 60 % failure rate on LCN training days and an ~ 80 % success rate possible alone. Of the attempts which succeed without clear particles Newton rings are still often present, originating instead from the edges of the chip. It is not clear if these fringes are due to particles introduced from handling during the cleaning process, or are caused by edge defects from dicing [191]. Coverage from Newton fringes originating at edges can be minimised with pressure on the chip, this is best achieved immediately after removal from the mask aligner, with force being applied by hand. If any present Newton rings do not propagate into the sonic crystal region, the complete chip can then be left to anneal at room temperature for a number

of days, creating a permanent bond. Figure 3.19 shows two completed chips, one with edge Newton rings and the other with particle ones. Complete chips are then imaged under a microscope to determine the quality of the central capacitor alignment.

Silicon Chips

As mentioned earlier fabrication was moved from LCN to SuperFab at RHUL, this also meant a switch from quartz or borosilicate to silicon wafers with thermal oxide. The cleaning and plasma activation procedure for these chips was the same as for the silicon chips, however due to silicon being opaque to visible light, and no infra red (IR) capable mask aligners at SuperFab, a home made IR bonding setup was developed. Figure 3.20 shows this bonding setup, utilising a halogen lamp to produce IR below a X-Y-Theta stage. A blank silicon wafer is taped to the top of the X-Y-Theta stage, over its central hole, forming an opaque to visible light ‘platform’ for the bottom chip. The top piece is then suspended by bonding tape on a forked brass piece, facing the bottom chip and attached to its own X-Y-Z stage. To view the alignment a USB microscope is held above both the chip pieces. A second blank single side polished silicon wafer was added in front of the halogen bulb to act as a diffuser.

Following the bonding process developed via trial and error, bonding tape was placed sticky side down on the platform wafer over the X-Y-Theta stage hole, this tape provides friction for the bottom piece so that it remains stationary when in contact with the top piece, however the tape must be pre-pressed with dummy silicon pieces so that it does not adhere to the bottom with enough strength to break the initial bond. The bottom piece can then be placed on this tape, using the microscope to align with the most intense region of IR. More bonding tape is then attached with electrical tape to the brass forked piece, and the top piece attached, similarly to the transparent chip process it is critical to alignment for the top piece to hang flat. Having the two chips flat relative to one another was more difficult with this setup and proved a limiting factor for alignment. Once both pieces are mounted the entire X-Y-Z stage is moved to bring them into rough alignment, and the Z used to bring the two pieces close together. The USB microscope can then be lowered close to the top piece, to monitor the alignment. Close alignment is

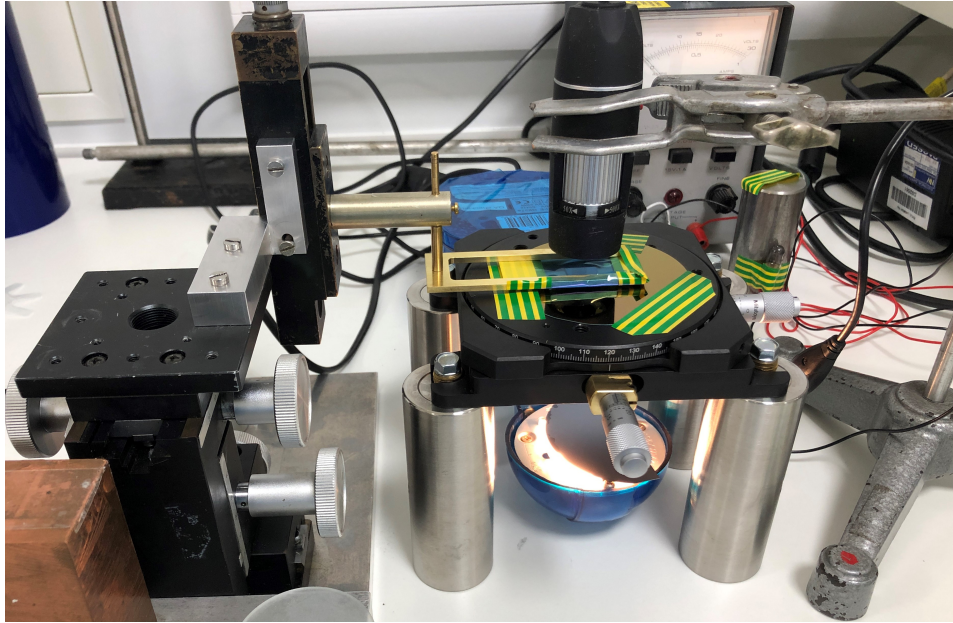


Figure 3.20: Showing the silicon wafer bonding setup at SuperFab RHUL. On the left is the X-Y-Z stage, which holds the brass arm, suspending the top piece. Above the bottom piece, on a silicon wafer, on the X-Y-Theta stage. A halogen lamp is placed below the central hole of the X-Y-Theta stage, with a single side polished silicon wafer acting as a diffuser. An IR capable USB microscope is then suspended above the chips.

achieved using the X-Y-Theta stage and the bonding marks, bringing the pieces together with the X-Y-Z. The microscope being held on a lab stand and it needing to be moved between the two bonding marks made it difficult to maintain a vertical position, adding to alignment uncertainty from any angle between the chips. Once fully in contact the pieces can be lightly pressed together, usually causing interference fringes to become visible on the microscope output. At this point the weakly bonded chip can be removed from the setup and pressed together on a desk to create a more permanent bond.

The central electrodes were not resolvable with this setup, and so the alignment was checked and imaged at a later date using an IR capable mask aligner. This procedure made reliable alignment within $\sim 10 \mu\text{m}$ difficult and time consuming, though within $5 \mu\text{m}$ is possible with a sufficient numbers of attempts and bond ready pieces. IR interference fringes, similar to the transparent Newton fringes, were seen with these chips, with the same problem of fridges originating at the edges. In addition to these fringes and those between the chip and platform wafer, another anomalous type of fringe was present. These new fringes had no clear origin point, covered the whole bonded region, and did

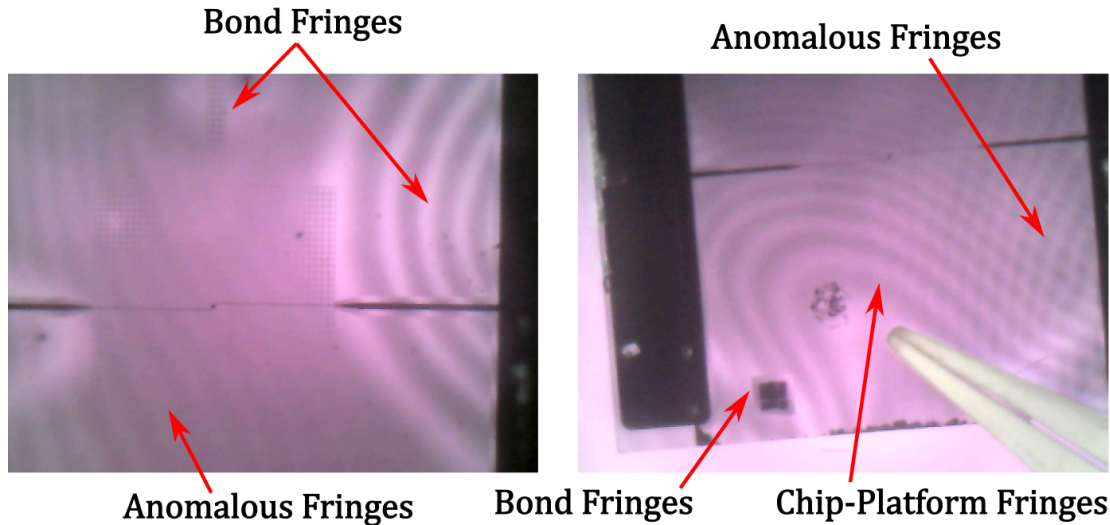


Figure 3.21: Left: IR USB microscope image of a bonded chip, showing fringes from the bond of the two chip pieces, and the anomalous fringes. The bond related fringes clearly originate at the chip edges or at particles, and exhibit a phase change where they meet an etched region, as the gap height is affected. Right: IR USB microscope image of a bonded chip, showing the anomalous fringes and the fringes between the chip and the silicon wafer platform. White tweezers are used to press on the chip, which clearly alters the chip-platform fringes, while the anomalous fringes remain unchanged. Some bond fringes can also be seen at the bottom left and right corners of the chip.

not move with pressure or interact with the other fringes. As these fringes could not be altered with pressure and were not present with transparent chips under IR, they were not considered to show a gap, and may be from some reflection within the chip, perhaps due to the thermal oxide. Figure 3.21 shows microscope images illustrating all three types of fringes.

Fringes originating at edges that indicate a gap have not been eliminated by refinement of the cleaning process, for either type of chip. If over handling is causing this, it may be possible to mitigate with chips which overlap in a cross (similar to [8]), so that handled edges are never at a bonding surface. Future designs should also develop the bonding marks to resolve closer alignment (similarly to common mask alignment marks).

3.3.5 Samples

This section will give key information for finished chips. All ‘usable’ chips had some Newton fringes originating at edges, and so the ‘best’ chips have been selected to have a good overlap of the central electrodes, and no fringes within the sonic crystal area.

Quartz Chips

The borosilicate and quartz chip processes were first developed at nanoFab, and then adapted for LCN. From the many nanofabrication runs and bonding attempts, the two best chips will be discussed here. These two chips both originated from the fourth quartz wafer (Q4), initially processed at nanoFab, with dicing and bonding occurring at LCN. From profilometry measurements this wafer has: first etch depth ~ 550 nm, second etch depth ~ 43 nm, and aluminium evaporation ~ 60 nm thick. So the aluminium is assumed to be protruding from the trench by ~ 17 nm, which is assumed to not be significant compared to the 550 nm height of the sonic crystal volume. These parameters would give an electrode separation of ~ 516 nm, a fairly large separation, though still a pseudo 2D geometry compared to the sonic crystal unit cell size of $100 \mu\text{m}$.

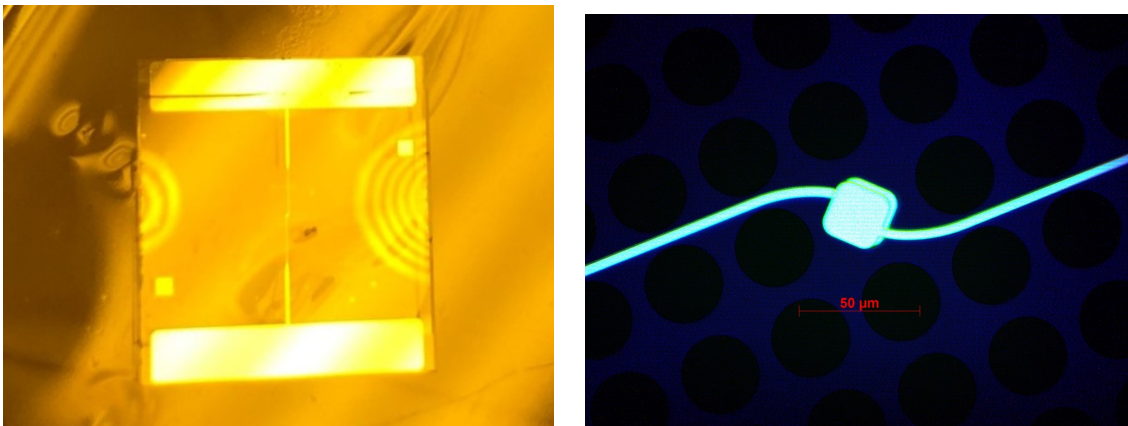


Figure 3.22: Left: A photo of the Q4(A2) chip, showing the Newton fringes, indicating an unbonded area due to some imperfection at the edge. Right: False coloured microscope image of the same chip, showing the crystal defect region. Of specific interest here is the overlap of the two electrodes, which appears to be misaligned by $\sim 5 \mu\text{m}$. The scale is incorrect and should be $100 \mu\text{m}$

Figure 3.22 shows images of the first ‘good’ quartz chip, Q4(A2) meaning chip A2 from the fourth quartz wafer. This is a parallel plate galvanic bonding chip, with a central electrode $60 \times 60 \mu\text{m}$, unit cell $a_1 = 100 \mu\text{m}$ and pillar diameter $a_2 = 80 \mu\text{m}$. The central electrodes are slightly misaligned ($\sim 5 \mu\text{m}$). This is not too concerning as this level of misalignment will still leave a fundamental resonance in the 4–12GHz operating range of the microwave circuit. There are also Newton fringes from both non-antenna edges, however they do not propagate into the sonic crystal region, and as the chip is firmly

bonded it is assumed the bond covers the central area.

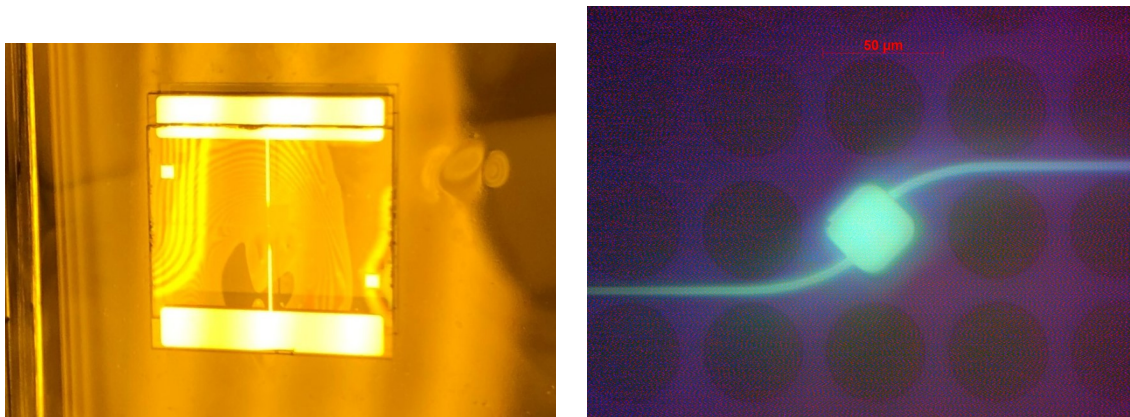


Figure 3.23: Left: A photo of the Q4(A5) chip, showing the Newton fringes, indicating an unbonded area due to some imperfection at the edge. The more central fringes are between the chip and the gel pack it is resting in. Right: False coloured microscope image of the same chip, showing the crystal defect region. Of specific interest here is the overlap of the two electrodes, which appear to be in almost perfect alignment.

Figure 3.23 shows images of the second good quartz chip Q4(A5). This is another parallel plate galvanic bonding chip, with a smaller unit cell $a_1 = 50 \mu\text{m}$ so smaller $30 \times 30 \mu\text{m}$ central electrode, and pillar $a_2 = 40 \mu\text{m}$. The central electrodes are almost perfectly aligned, though it is difficult to see as the misalignment is at the edge of the microscope resolution. There is a greater Newton fringe from one non-antenna edges, however they still do not propagate into the sonic crystal region, and again as the chip is firmly bonded it is assumed the bond covers the central area.

Figure 3.24 shows FESEM images of the surfaces of a wafer from NanoFab. On the scale of the electrode or pillars, the surface looks pristine, with very little disturbance at the edges of the aluminium or trench. Though for the zoomed image on the right some nm scale surface roughness is present, much more significant within the etched areas and the pillar wall. These images also give a visualisation of just how flat and close to 2D the geometry is.

These chips were not initially used for the full superfluid optomechanics experiments, as from some initial testing, the parallel plate galvanic chips tended to split / break when being fitted into a cavity and cycled to mK temperatures. However in light of the results later in Chapter 5, and the development of the fitting process, the upcoming run of the

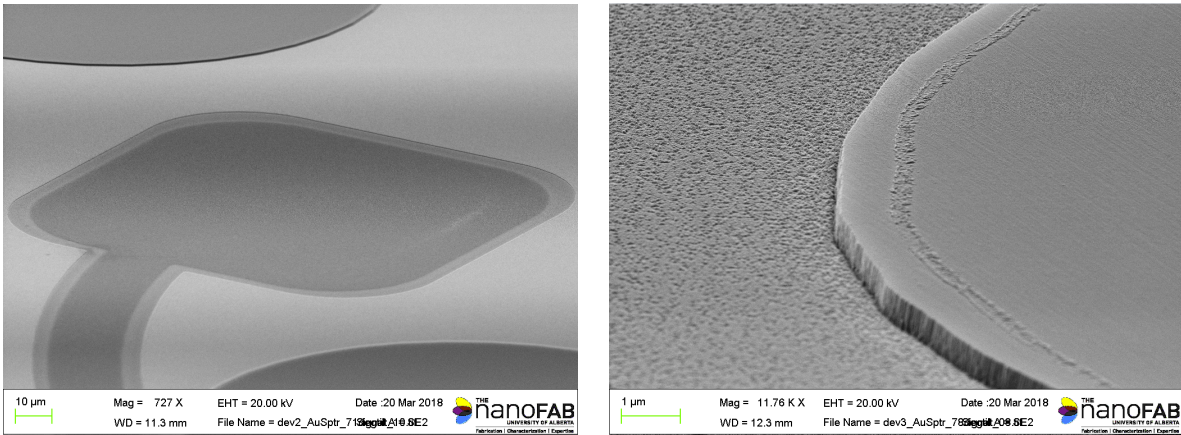


Figure 3.24: Left: FESEM image of the central point defect of diced but not bonded chip, showing the central aluminium electrode within the etched trench, with wire leading in, and a pillar above and below. Right: FESM image of a pillar edge, showing the etched surface on the LHS and the pristine un-etched surface on the RHS. Bottom left the edge of the trench for aluminium can also be seen.

dilution fridge will involve one of these chips.

Silicon Chips

As mentioned previously, the pandemic caused disruption to use of LCN, and so existing silicon with thermal oxide techniques were adapted to produce sonic crystal chips. All trials were with Silicon wafer with 300 nm of thermal oxide, with etching only applied to the oxide. The first three complete wafers were sent off for bonding at Michigan University, which was unsuccessful. For the next three wafers the bonding apparatus was developed at SuperFab, achieving a higher portion of successful bonds but worse average alignment when compared to LCN. The two best chips are from the second and third wafer of those bonded at SuperFab. Both chips are of the floating electrode style, with a central electrode $60 \times 60 \mu\text{m}$, with a $5 \mu\text{m}$ split, unit cell $a_1 = 100 \mu\text{m}$ and pillar diameter $a_2 = 80 \mu\text{m}$. The images of the bonds for these chips were taken using the ‘home made’ bonding setup at SuperFab, while the alignment images are from a mask aligner at LCN with IR capabilities. Even with the IR capable mask aligner, the images are photos of an old CRT screen, making accurate assessment of the overlap impossible.

Figure 3.25 shows images of the first good silicon chip, Si2(5) meaning the fifth chip from the second silicon wafer. For this wafer the first etch was $\sim 236 \text{ nm}$, second etch $\sim 72 \text{ nm}$, and aluminium deposition 74 nm thick, giving an electrode gap of ~ 232

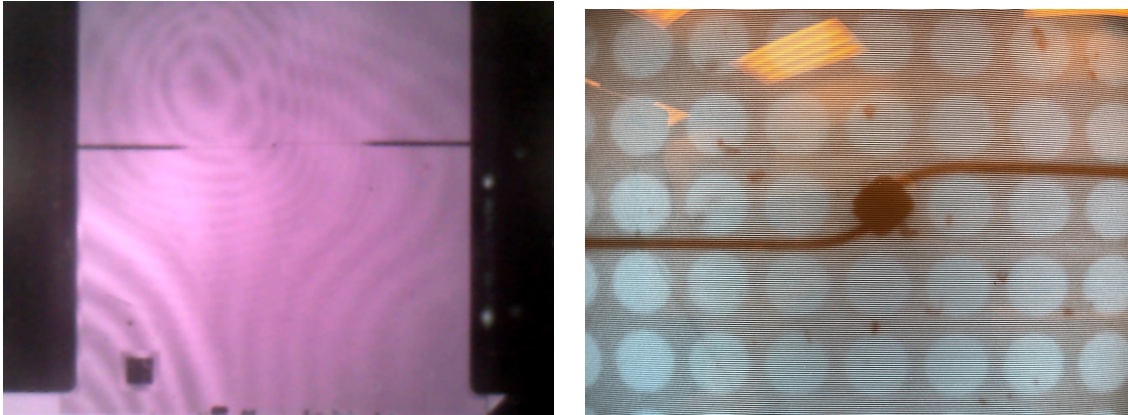


Figure 3.25: Left: An IR USB microscope image of the Si2(5) chip, showing the Newton fringes, indicating an unbonded area due to some imperfection at the bottom left corner. The less prominent fringes over the remainder of the chip are either anomalous or between the chip and the wafer it is resting on. Right: IR mask aligner image of the same chip, showing the crystal defect region. Of specific interest here is the overlap of the two electrodes, which appear to be in good alignment.

nm. The central electrodes look to be well aligned. There are bond related Newton fringes originating at the bottom left corner of the chip, though they do not propagate into the sonic crystal region. This chip was used for run one of the dilution fridge with a nanofluidic chip.

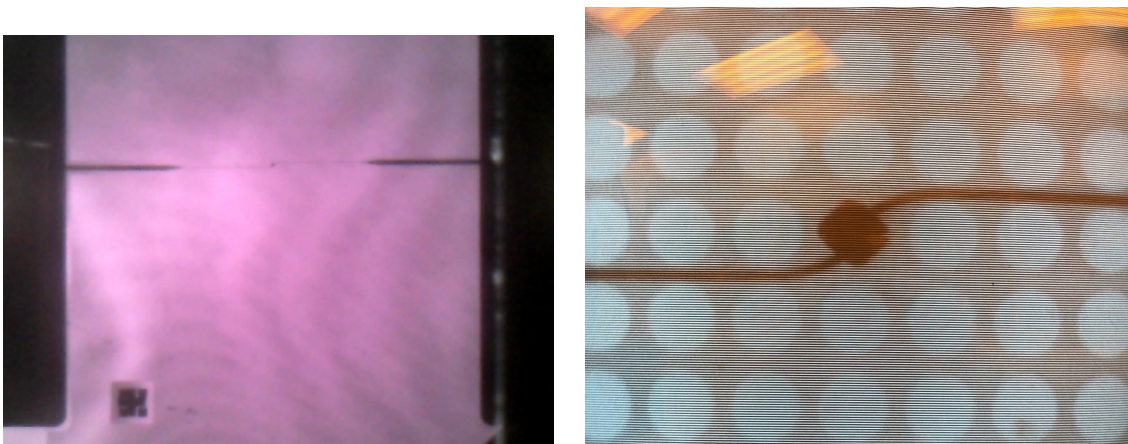


Figure 3.26: Left: An IR USB microscope image of the Si2(5) chip, showing the Newton fringes, indicating an unbonded area due to some imperfection at the bottom left corner. The less prominent fringes over the remainder of the chip are either anomalous or between the chip and the wafer it is resting on. Right: IR mask aligner image of the same chip, showing the crystal defect region. Of specific interest here is the overlap of the two electrodes, which appear to be in good alignment.

Figure 3.26 shows images of the second good silicon chip, Si3(5) meaning the fifth chip from the third silicon wafer. For this wafer the first etch was ~ 252 nm, second etch

~ 47 nm, and aluminium deposition 71 nm thick, giving an electrode gap of ~ 212 nm. The central electrodes look to be less well aligned than the previous chip, as the split in the electrode can be faintly seen on the RHS. A single bond related Newton fringe can be seen originating at the bottom left coner of the chip, indicating a stronger bond than the first silicon chip. This chip was used for runs two and three of the dilution fridge with a nanofluidic chip.

Chapter 4:

Microwave Measurement

This chapter covers equations relevant to microwave measurement of the chip-cavity optomechanical system. Section 4.1 introduces microwave network analysis, and considers the chip-cavity system as an capacitively coupled RLC circuit, giving equations for complex transmission through the system near the chip-cavity resonances, as measured by a vector network analyser. Section 4.2 gives details of the microwave measurement circuit mounted on the dilution refrigerator, which delivers signal from room temperature equipment to the experiment at base temperature, and vice versa. The optomechanical coupling is introduced in Section 4.3, which considers the effect of the time varying cavity resonant frequency on a transmitted microwave signal at constant frequency. This effect is then used to outline a method for direct measurement of the vacuum optomechanical coupling strength. The direct measurement technique is not possible for weaker couplings, and so Section 4.4 develops a homodyne detection technique to enhance the measurement sensitivity, which is the primary method for detecting optomechanical signals used in this work. Theory for a calibrated homodyne detection using a phase modulation at the microwave source is also developed in this section, giving a methodology for direct calculation of the vacuum optomechanical coupling from a single measurement.

4.1 Microwave Network Analysis

4.1.1 S Matrix

General circuits can be decomposed into their ‘lumped elements’. A linear complex impedance Z ($Z = V/I$) can be broken down into capacitors, inductors and resistors. At low frequencies this can be literal physical components, however at higher frequencies

these lumped elements become an abstraction and applied voltages begin to act as waves closer to optics. Therefore much of microwave network analysis instead uses the scattering (S) matrix, which gives a complete description of a system as seen at its N ports. This matrix relates voltage waves incident on ports to those reflected from ports [113]. This is the formulation Vector Network Analysers (VNA's) measure in. The S matrix [S] relates incident waves to reflected via:

$$[V^-] = [S][V^+], \quad (4.1)$$

where V_i^- is the reflected voltage wave at the i 'th port, and V_i^+ is the incident wave at the i 'th port. The individual S matrix parameters S_{ij} are then defined:

$$S_{ij} = \left. \frac{V_i^-}{V_j^+} \right|_{V_k^+ = 0 \text{ for } k \neq j}, \quad (4.2)$$

describing driving port j with incident voltage V_j^+ , while measuring the reflected wave V_i^- at port i , with all other ports terminated in matched loads. Usually the matched loads are equal to the characteristic impedance of the microwave lines used for measurement $Z_0 = \sqrt{l/c}$, where l and c are the inductance and capacitance, per unit length. From this S_{ij} represents transmission from port j to port i , while S_{ii} is the reflection coefficient Γ of port i .

4.1.2 RLC Response

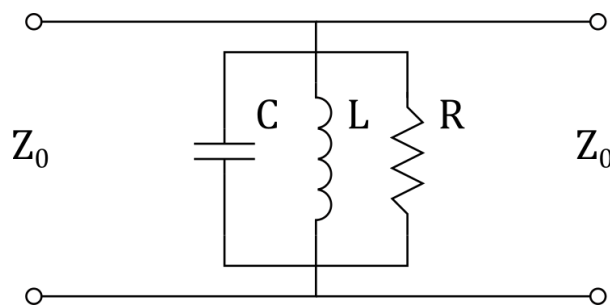


Figure 4.1: Figure showing parallel RLC representation of microwave circuit, set in a two port network with port impedances Z_0 .

Using the abstraction to RLC lumped elements from Section 2.2.5 and the definition of S_{21} above, transmission across a microwave cavity can be modelled according to Figure 4.1. The RLC components here giving a combined characteristic parallel impedance:

$$Z(\omega) = \left(\frac{1}{R} + i\omega C + \frac{1}{i\omega L} \right)^{-1}, \quad (4.3)$$

where ω is the angular frequency of the signal incident on the circuit, R is the characteristic resistance, C the capacitance, and L the inductance. This circuit describes a cavity with resonant frequency $\omega_0 = 1/\sqrt{LC}$ and quality factor $Q = \omega_0 RC = R/\omega_0 L$. Using the substitution $\Delta\omega = \omega - \omega_0$, $\delta\omega = \Delta\omega/\omega_0$, and the approximation:

$$\omega^2 - \omega_0^2 \approx 2\omega(\omega - \omega_0), \quad (4.4)$$

valid near resonance ω_0 . This allows simplification of the impedance into the form:

$$Z = \frac{R}{1 + 2iQ\delta\omega}. \quad (4.5)$$

Switching to admittance $Y = Z^{-1}$ gives:

$$Y = \frac{1}{R} + \frac{2iQ\delta\omega}{R}. \quad (4.6)$$

Then using the ABCD transmission matrix for a general admittance in parallel [113]:

$$\begin{bmatrix} A & B \\ C & D \end{bmatrix} = \begin{bmatrix} 1 & 0 \\ Y & 1 \end{bmatrix}, \quad (4.7)$$

with the expression of S_{21} for a two port transmission measurement of admittance Y with characteristic port impedances Z_0 (Figure 4.1):

$$S_{21} = \frac{2}{A + B/Z_0 + CZ_0 + 1}, \quad (4.8)$$

gives an expression for the complex transmission:

$$S_{21} = \frac{\beta}{(\beta + 1) + 2iQ_0\delta\omega}, \quad (4.9)$$

where $Q = Q_0$ from above, and the substitution $\beta = 2R/Z_0$ has been made. This β is again the coupling constant of the microwave system $\beta = Q_0/Q_e$, with $Q_e = Z_0/2\omega_0L$ coming from the definition of an RLC loaded on two ports with Z_0 impedances. Here the internal quality factor Q_0 represents energy dissipated within the cavity itself, while the external quality factor Q_e represents energy lost out of the ports, including the energy terminated in a measurement device. The total quality factor of the combined system is $Q_L = (Q_0^{-1} + Q_e^{-1})^{-1}$, known as the loaded Q.

Often when discussing optomechanical resonators, linewidth is used instead of quality factor. This linewidth can be thought of as the photon decay rate or as the bandwidth of a measured resonance, it is related to quality factor by:

$$\kappa = \frac{\omega}{Q}. \quad (4.10)$$

Similarly to quality factor the total or loaded linewidth κ_L can be broken up into the internal linewidth κ_0 and external linewidth κ_e , these linewidths are related via $\kappa_L = \kappa_0 + \kappa_e$.

Reflection Coefficient S_{11}

S_{11} represents the reflection of the incoming voltage wave at the ‘in’ port and is equivalent to the reflection coefficient Γ , it can be used to calculate the average power into the system $P_{\text{avg}} = (1 - |\Gamma|^2)|V_0^+|^2/2Z_0$, where V_0^+ is the amplitude of the incident voltage wave. Modelling the RLC as a load Z_L terminating a transmission line of characteristic impedance Z_0 , the reflection coefficient can be expressed:

$$S_{11} = \Gamma = \frac{Z_L - Z_0}{Z_L + Z_0}. \quad (4.11)$$

For a cavity with a single port Z_L is simply Z from Equation 4.5, which can be substituted into the above equation and then simplified to give:

$$S_{11} = \frac{2\beta_1}{(\beta_1 + 1) + 4iQ_0\delta\omega}, \quad (4.12)$$

where $\beta_1 = R/Z_0$ has been used to represent the coupling constant of a single port system. For a two port system the reflection coefficient from one port assumes a matched load on the second port, this can be added as a 50Ω Z_0 in parallel to the RLC. This modification to the circuit changes its effective resistance $R \rightarrow Z_0R/(R + Z_0)$. Keeping all terms defined as in S_{21} gives $Q \rightarrow Z_0Q_0/(R + Z_0)$. Using these modifications to Equation 4.5 for Z_L and then substituting into Equation 4.11 gives:

$$\begin{aligned} S_{11} &= \frac{-Z_0 - 2iQ_0\delta\omega}{2R + Z_0 + 2iQ_0\delta\omega} \\ &= \frac{Z_0\beta}{Z_0(\beta + 1) + 2iQ_0\delta\omega} - 1. \end{aligned} \quad (4.13)$$

The single port equation can be recovered by setting the second port to open, the form of this equation depends greatly on the choice of definition for the Q 's, this form is chosen to be consistent with S_{21} , [203] gives a single port alternative.

4.1.3 Capacitively Coupled Response

For the simple circuit of a RLC resonator directly shunted to the standard Z_0 of 50Ω , a high Q_0 resonance is easily destroyed by a low Q_e . This, along with the impracticality of coupling directly to a cavity mode, means some coupling scheme must be employed to mediate the flow of energy out of the resonator. The two usual methods are loop couplers which couple inductively to the magnetic field of the cavity, and pin couplers which couple capacitively to the electric field [138]. Pin couplers are used here, one port represented by C_e on the LHS of Figure 4.2, while the source impedance is represented by Z_0 , the other port can be mirrored on the RHS.

It is possible to reformat the capacitively coupled circuit into an equivalent form where Equation 4.9 can be used. This can be achieved using the Thevenin - Norton source transformations while taking the coupling capacitance C_e into the complex source

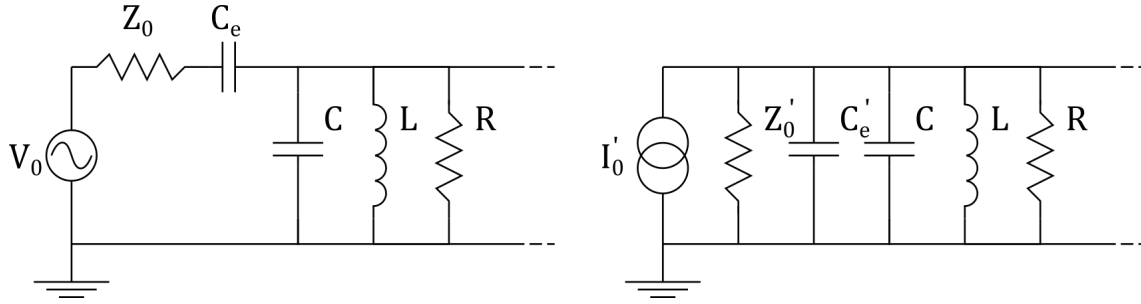


Figure 4.2: Figure showing the Thevenin - Norton source transformation for capacitive coupling to an RLC resonator. The RHS of the circuit is connected to a mirrored C_e and Z_0 , where the Z_0 is for the HEMT amplifier, which is also transformed into a parallel impedance and capacitance.

impedance [204]. These source transforms hold that a series voltage source impedance is equivalent to a parallel current source impedance of equal value, where the current of the transformed source is equal to the original source voltage divided by this impedance (an application of Ohms law). A visualisation of the process is shown in Figure 4.2, where the more intuitive series circuit is transformed into its equivalent parallel one. This only shows the transform for one port, but the process can be mirrored on the RHS for the second port. The $2V_0$ in series with Z_0 is to maintain $V_{\text{load}} = V_0(1 + \Gamma)$, where V_0 is the voltage applied by a microwave source V_{in} , attenuated by some $\sqrt{\text{loss}}$ before reaching the port (the $x = 0$ reference plane) [113].

The series source impedance and coupling capacitor components represent a combined impedance of:

$$Z_s = Z_0 + \frac{1}{i\omega C_e}. \quad (4.14)$$

While the parallel components represent a combined impedance of:

$$Z_p = \left(\frac{1}{Z'_0} + i\omega C'_e \right)^{-1}. \quad (4.15)$$

To draw an equivalence between the two representations, there exists Z'_0 , C'_e such that $Z_s = Z_p$, giving a transformed current source $I'_0 = 2V_0(Z_0 + 1/i\omega C_e)^{-1}$. The equivalence is also true for admittance and simpler to solve in this form. The equivalent admittances are:

$$Y_s = \left(Z_0 + \frac{1}{i\omega C_e} \right)^{-1}, \quad (4.16)$$

$$Y_p = \frac{1}{Z'_0} + i\omega C'_e. \quad (4.17)$$

Y_s can be expanded and simplified into the form:

$$Y_s = \frac{q^2/Z_0 + i\omega C_e}{1 + q^2}, \quad (4.18)$$

where $q = Z_0\omega C_e$ can be thought of as the charge on the coupling capacitors [205]. For a weak coupling $q \ll 1$ (or $1 + q^2 \approx 1$), Y_s can be approximated to:

$$Y_s = \frac{q^2}{Z_0} + i\omega C_e. \quad (4.19)$$

Comparing this form of Y_s to Y_p it is clear that $Z'_0 = Z_0/q^2$ and $C'_e = C_e$. The parallel capacitance C'_e can then be taken into the cavity capacitance C , while Z'_0 can become the new characteristic load impedance of the transmission circuit, equivalent to taking Z'_0 inside the an RLC directly driven by a current source [141]. This leads to an equation for S_{21} of the same form as Equation 4.9, with the modifications $\beta \Rightarrow 2Rq^2/Z_0$ and $C \Rightarrow C + 2C_e$, where the process has been mirrored for an identical second port (discussion of asymmetry in [206]). With these modifications the equation for S_{21} can also be written as:

$$S_{21} = \frac{Q_L/Q_e}{1 + 2iQ_L\delta\omega'}, \quad (4.20)$$

where $Q_e = Z_0/2q^2\omega'_0 L$ and $\delta\omega' = (\omega - \omega'_0)/\omega'_0$, using $\omega_0'^2 = 1/L(C + 2C_e)$ as the modified resonant frequency of the cavity. The capacitance of the coupling is expected to be small compared to the cavity capacitance, therefore the modification to ω_0 can be largely ignored (or modelled for with FEM). S_{11} can be modified with the same substitutions into Equation 4.13, including $Z_0 \rightarrow Z'_0$. However, the fridge's microwave 'in' line to port 1 is heavily attenuated, and so direct measurement of S_{11} is not possible due to signal

strength below background noise.

The transformation of the quality factor can also be understood from the parallel RLC definition of $Q = R/\omega_0 L$, where the new R of the circuit is a parallel combination of R and two Z'_0 , giving a total quality factor:

$$\frac{1}{Q_L} = \omega_0 L \left(\frac{1}{R} + \frac{2}{Z'_0} \right), \quad (4.21)$$

which is of the form $1/Q_L = 1/Q_0 + 1/Q_e$, and gives the original Q_0 and modified Q_e above.

Note in [205] the approximation for q is given for ‘weak’ coupling, however with the coupled circuit q can be rewritten:

$$q^2 = \frac{Z_0 \beta}{2R}. \quad (4.22)$$

This is almost always very small for a high Q superconducting microwave resonator: $Z_0 = 50 \Omega$ and $R \approx 1 \times 10^{12} \Omega$, while β can vary a few order of magnitude around 1, it is therefore unlikely the approximation $q^2 + 1 \approx 1$ is never not valid. So the ‘weak’ coupling here then refers to an absolute weak coupling, meaning a high Q_e in absolute terms rather than its relationship to Q_0 . Additionally q is dependent on ω but this variation is assumed to be small close to resonance.

4.1.4 Cavity Photons

The average photon number within the cavity is a useful term in optomechanics. As the system has been generalised in terms of quality factors / linewidths, it is possible to use the general optomechanical expression [1] for photons circulating in the cavity:

$$\bar{n}_{\text{cav}} = |\langle \hat{a} \rangle|^2 = \frac{2}{\kappa_e} \frac{\kappa_e^2}{4\Delta\omega_p^2 + \kappa_L^2} \frac{P}{\hbar\omega_p}, \quad (4.23)$$

where \hat{a} is the intracavity field, P is the microwave power applied at one port, and ω_p is the ‘pump’ frequency of the applied power (giving $\Delta\omega_p = \omega_p - \omega_0$). This equation is valid close to resonance for the expected regime of two weakly coupled ports, with the

extra factor of $1/2$ coming from the second port losses being taken into κ_e , rather than losses through the second mirror of a Fabry-Perot being taken into κ_0 in an effective one port system.

Though photon number is important for the optomechanical coupling, it is also useful to know the voltage across, and field strengths within, the microwave cavity; the field within the central capacitor is especially important as a design consideration for nanofluidic chip. Therefore this section will cover a derivation of the cavity average photon number, through the cavity voltages, and using the transformed circuits in Section 4.1.3. The voltage across the cavity in terms of the transformed circuit is:

$$V_{\text{cav}} = I'_0 Z'_{\text{total}} , \quad (4.24)$$

where I'_0 is the transformed current source and Z'_{total} is the total impedance of the transformed circuit. As noted in the previous section the transformed current source is:

$$\begin{aligned} I'_0 &= 2V_0 \left(Z_0 + \frac{1}{i\omega C_e} \right)^{-1} \\ &= 2V_0 \cdot i\omega C_e , \end{aligned} \quad (4.25)$$

where the approximation $q \ll 1$ has been used (weaker than $q^2 \ll 1$). The total transformed impedance Z'_{total} can then be expressed as a parallel combination of all the components:

$$Z_{\text{total}} = \left(i\omega C + \frac{1}{i\omega L} + \frac{1}{R} + \frac{2}{Z'_0} \right)^{-1} . \quad (4.26)$$

Expressing this in terms of quality factors and resonances:

$$\begin{aligned} Z_{\text{total}} &= \left(i \frac{Q_0 \omega}{\omega_0 R} - i \frac{Q_0 \omega_0}{\omega R} + \frac{1}{Q_L \omega_0 L} \right)^{-1} \\ &\simeq \frac{R Q_L / Q_0}{1 + 2i Q_L \delta \omega} , \end{aligned} \quad (4.27)$$

where the approximation $\omega^2 - \omega_0^2 \approx 2\omega(\omega - \omega_0)$ and substitution $\delta\omega = (\omega - \omega_0)/\omega_0$ has been used to simplify the equation. Combining Z_{total} and I'_0 gives:

$$V_{\text{cav}} = 2V_0 \cdot i\omega C_e R \frac{Q_L/Q_0}{1 + 2iQ_L\delta\omega} . \quad (4.28)$$

It is also important to know the voltage out of the cavity V_{amp} , expressed as the voltage across the HEMT amplifier of characteristic impedance Z_0 . This voltage is the cavity voltage V_{cav} reduced by C_e and Z_0 acting as a voltage divider:

$$\begin{aligned} V_{\text{amp}} &= \frac{Z_0}{1 + \frac{1}{i\omega C_e}} V_{\text{cav}} \\ &\simeq iZ_0\omega C_e V_{\text{cav}} , \end{aligned} \quad (4.29)$$

where the approximation $q \ll 1$ has been used. Substituting in the cavity voltage gives:

$$\begin{aligned} V_{\text{amp}} &= 2V_0\omega^2 C_e^2 R Z_0 \frac{Q_L/Q_0}{1 + 2iQ_L\delta\omega} \\ &= -V_0 \frac{Q_L/Q_e}{1 + 2iQ_L\delta\omega} , \end{aligned} \quad (4.30)$$

dividing this by $-V_0$ recovers Equation 4.20, consistent with the definition of S_{21} . It is important to derive the complex forms of these transmission equations as it maintains information of the microwave signal's phase, and makes fitting measurement data more accurate. On resonance ($\omega = \omega_0$), this also returns expected expressions for voltage out and total quality factor:

$$V_{\text{amp}} = -V_0 \frac{Q_L}{Q_e} = -V_0 \frac{\kappa_e}{\kappa_L} , \quad (4.31)$$

$$Q_0 = \frac{1}{1 - \left| \frac{V_{\text{amp}}}{V_0} \right|} Q_L . \quad (4.32)$$

This can be useful for estimating Q_0 as Q_L is easily found through a fitting of the transmission spectrum, the limit of this estimation will be how well loss and gain are

known.

From the voltages V_{cav} and V_{amp} it is possible to calculate the average energy within the cavity and therefore the average photon number. To begin the average energy within a low loss RLC circuit or microwave cavity is:

$$e = \frac{1}{2}CV_{\text{rms}}^2 + \frac{1}{2}LI_{\text{rms}}^2 \approx CV_{\text{rms}}^2, \quad (4.33)$$

approximating close to resonance where there is equal energy in both fields. RMS voltage is used here while V_{cav} is complex amplitude so, so taking $V_{\text{rms}} \rightarrow \frac{1}{\sqrt{2}}|V_{\text{cav}}|$:

$$e_{\text{cav}} = \frac{1}{2}C|V_{\text{cav}}|^2, \quad (4.34)$$

where e_{cav} is the average microwave energy inside the cavity. Substituting for V_{cav} gives:

$$\begin{aligned} e_{\text{cav}} &= 2|V_0|^2\omega^2C_e^2R^2\frac{Q_L^2/Q_0^2}{1+4Q_L^2\delta\omega^2} \\ &= \frac{|V_0|^2}{Z_0}\frac{1}{\omega_0Q_e}\frac{Q_L^2}{1+4Q_L^2\delta\omega^2}. \end{aligned} \quad (4.35)$$

Using Equation 4.30 to substitute in for V_0 this can be written in terms of V_{amp} :

$$e_{\text{cav}} = \frac{|V_{\text{amp}}|^2}{Z_0}\frac{Q_e}{\omega_0}. \quad (4.36)$$

Using transmission line theory the power at each port's $x = 0$ reference plane can be written $P_1 = \frac{|V_0|^2}{2Z_0}$ and $P_2 = \frac{|V_{\text{amp}}|^2}{2Z_0}$, with P_1 being the incoming power at port 1 (LHS) and P_2 being the outgoing power at port 2 (RHS). This can be substituted into each e_{cav} equation:

$$e_{\text{cav}} = \frac{2P_1}{\omega_0Q_e}\frac{Q_L^2}{1+4Q_L^2\delta\omega^2}, \quad (4.37)$$

$$e_{\text{cav}} = \frac{2P_2Q_e}{\omega_0}. \quad (4.38)$$

The P_2 form is useful as the power out of the cavity may be simpler to measure than the power arriving at port 1. Note, it can be seen here that the cavity emits a power $\kappa_e e_{\text{cav}}/2$ from each power, while it dissipates $\kappa_0 e_{\text{cav}}$ internally. Combing these two expressions gives the transmitted power in terms of incident power:

$$P_2 = P_1 \frac{Q_L^2/Q_e^2}{1 + 4Q_L^2\delta\omega^2}, \quad (4.39)$$

recovering the fraction of transmitted power $|S_{21}|^2 = P_2/P_1$, equal to Equation 4.20. For a $\beta = 1$ critical coupling and a signal on resonance, this shows $|S_{21}|^2 = 1/4 = -6$ dBm as expected.

From the energies above it is simple to write the average photon number:

$$\bar{n}_{\text{cav}} = \frac{1}{\hbar\omega} \frac{2P_1}{\omega_0 Q_e} \frac{Q_L^2}{1 + 4Q_L^2\delta\omega^2}, \quad (4.40)$$

$$\bar{n}_{\text{cav}} = \frac{1}{\hbar\omega} \frac{2P_2 Q_e}{\omega_0}. \quad (4.41)$$

The first equation here is equivalent to 4.23 with the pump power being applied at port 1. Of course it is not always possible to work directly with the powers at the cavity's microwave ports, so the next section will cover a generalisation of the greater circuit.

4.1.5 Real Circuit Response

The microwave response outlined in the previous sections is for an idealised system, where the signal directly at the port's reference planes is known. However, even for a simple circuit, measurement data will be modified by the response of other components on the microwave line. For simple circuits it is often possible to directly measure and then calibrate to remove modifications. While for more complex circuits, and especially components at low temperature, it is not practical to accurately determine this response, and so instead a generalised real circuit response is added and fitted for. For the complex cavity transmission S_{21} (Equation 4.20), the modification from the greater circuit can be

written [207]:

$$\tilde{S}_{21} = (S'_{21} + X) e^{i\phi} , \quad (4.42)$$

\tilde{S}_{21} being the real measured response and S'_{21} the cavity transmission S_{21} including a factor of $\sqrt{\text{loss} \cdot \text{gain}}$, to account for effects of attenuation and amplification to signal strength. X is a complex factor representing the total cross talk of components, which introduces a translation to the centre point of a resonance on a circle plot (real vs imaginary axes), while $e^{i\phi}$ represents the total phase shift of components, leading to a rotation about the origin in complex space. In essence this accounts for the measurement's reference plane not being directly at the cavity ports. The phase ϕ can be broken up further into $\tau\omega + \phi'$, where τ is the time delay of the signal (mainly from cables), and ϕ' is any phase shift not dependent on frequency, e.g. any reflections. To simplify fitting, and as often only ϕ is of interest, this can be rewritten:

$$\tilde{S}_{21} = A + B e^{i\phi} \frac{Q_L/Q_e}{1 + 2iQ_L\delta\omega'} , \quad (4.43)$$

where A is the complex shift of the data after rotation by ϕ , and B is a real factor representing the total attenuation and amplification of the circuit. In principle both A and B may have some frequency dependence, usually approximated to the first order as $A = A_1 + A_2\omega$, where A_1 is the flat background and A_2 is the slope of the background. Then for $B = B_1 + B_2\omega$, B_1 is the constant attenuation plus amplification, and B_2 is the skew. For a high Q_L , close to ω_0 , and no other resonances near in frequency; both A and B can be approximated to constant values.

Without knowledge of B it is usually not possible to determine Q_0 or Q_e from a single transmission measurement. However, in a strongly over / under coupled regime Q_e / Q_0 respectively will dominate Q_L , allowing a reasonable estimate. Otherwise it may also be possible to determine both by varying the temperature, though only if Q_e and Q_0 are close enough that changing Q_0 via temperature will vary Q_L significantly.

All S_{21} resonances in this work are fitted to Equation 4.43, using a complex least squares fit. Simply fitting the raw data works well for a complex S_{21} , provided sufficient

data, while fitting $|S_{21}|$ provides much less accuracy. For data that is especially noisy or sparse, the points can be weighted in the least squares fit by either: their distance from the point opposite the resonance on a circle fit (for high background), or by the inverse of their distance from the centre of the resonance circle (for a noisy resonance).

Photon Number

A small A gives a transmission response close to S_{21} , only modified by constant phase and amplitude factors. When considering transmitted power, as in the previous section, the phase factor can be ignored while the B can be broken up into *gain* and *loss*. Considering the power applied by a signal generator P_{in} onto port one gives $P_1 = P_{\text{in}} \cdot \text{loss}$, where *loss* is the linear attenuation between the signal generator and port 1. Similarly the power out of the system (into a detector) via port 2 is $P_2 = P_{\text{out}}/\text{gain}$, where *gain* is the total linear gain of the amplified ‘out’ line (with some adjustment for any additional attenuation). In this way the photon noise can be rewritten in terms of powers in and out of the system:

$$\bar{n}_{\text{cav}} = \frac{1}{\hbar\omega} \frac{2P_{\text{in}} \cdot \text{loss}}{\omega_0 Q_e} \frac{Q_L^2}{1 + 4Q_L^2 \delta\omega^2}, \quad (4.44)$$

$$\bar{n}_{\text{cav}} = \frac{1}{\hbar\omega} \frac{2P_{\text{out}} Q_e}{\omega_0 \cdot \text{gain}}. \quad (4.45)$$

Giving two approaches to estimating the photons within the cavity, as it is difficult to accurately determine the attenuation and gain of components on the fridge at low temperature.

4.2 Fridge Circuit

4.2.1 Overview

The microwave measurement circuit inside the fridge follows a simple two line design for measurement at mK temperatures, using an attenuated ‘in’ line to bring signal down

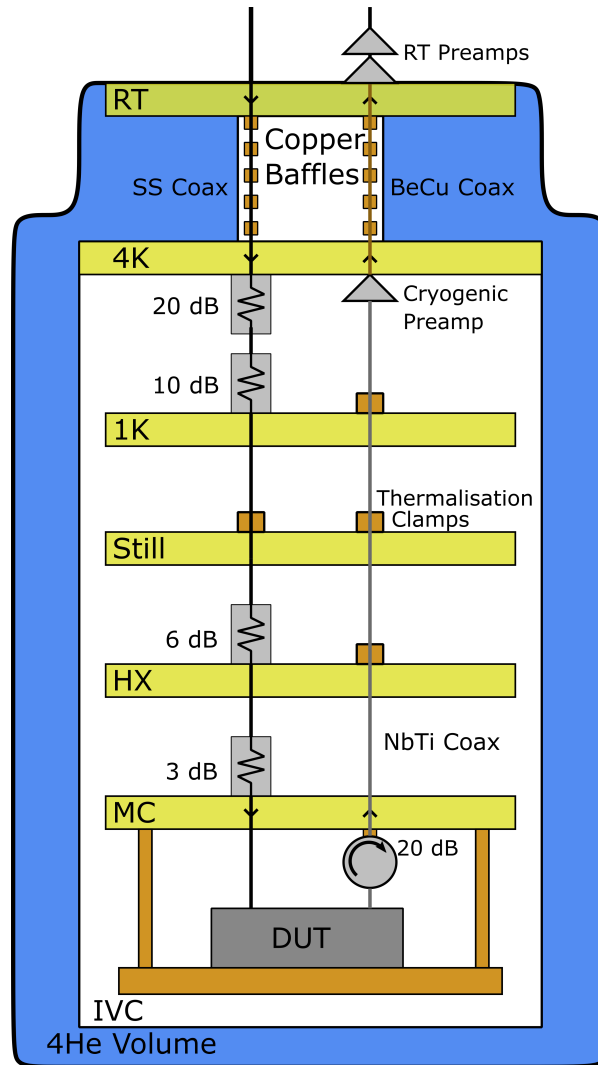


Figure 4.3: Figure showing microwave circuit inside the dilution fridge.

to the device under test (DUT), then an amplified low attenuation ‘out’ line to return the signal modified by the DUT to a detector. Figure 4.3 shows a diagram of this measurement setup, including all microwave components and thermalisation at each plate. The ‘in’ line is attenuated at each plate (except the still) to reduce the heating power applied to the lower plates and DUT. The attenuators have the effect of thermalising the cable core at each plate, reducing the signal intensity and thermal radiation noise. As attenuation is required on the ‘in’ line, cables can be chosen to minimise thermal conductivity without too much concern for their attenuation. For the ‘out’ line reducing signal losses is the priority, therefore superconducting coax is used up to 4K, then low loss BeCu coax to RT. The low power return signal is amplified at 4K by a HEMT amplifier from Low

Noise Factory (*LNF-LNC0.3 14A s/n 1628Z*), improving signal strength before coming into contact with higher thermal noise components. The ‘out’ line is also amplified by two preamps at RT, a Low Noise Factory (*LNF-LNR1 15A*), and a Mini-Circuits (*ZX60-83LN12+*). Amplifier noise, thermal noise, and reflected signal can easily travel back down the low attenuation ‘out’ line and into the DUT, disturbing the measurement. This signal is minimised by a 20 dB isolator (*LNF-ISC4-12A s/n 1901-15*) mounted on the EX plate.

4.2.2 Photon Noise

In addition to attenuators and amplifiers the properties of the coaxial cables must be taken into account for an accurate characterisation of the circuit. The properties of cables used for the ‘in’ and ‘out’ lines are shown in Table 4.1 below. All coax are *COAX CO. LTD* semi-rigid cables with SMA male connectors. All coaxial cables for the ‘in’ line are stainless steel (SS) SUS304 with lengths: 1400 mm RT-4K, 300 mm 4K-1K, 300 mm 1K-HX, 400 mm HX-EX and 400 mm EX-DUT. While on the ‘out’ line the 4K-RT cable is 1400 mm BeCu, then NbTi 1000 mm EX-4K and 300 mm DUT-EX.

Table 4.1: Comparison of coaxial cables used in microwave circuit. Both attenuations given for 5 GHz signal.

<i>Inner Material</i>	<i>Outer Material</i>	<i>Thermal Conductivity @4K (W cm/K)</i>	<i>Attenuation @300K(dB/m)</i>	<i>Attenuation @4K(dB/m)</i>
Ag Plate BeCu	BeCu	4.88E-04	1.8	0.6
SUS304	SUS304	4.30E-05	9.4	5.9
NbTi	NbTi	2.64E-05	9.6	<0.3

These lengths become important when calculating the thermal photon noise, at operating frequency, delivered to the DUT by the microwave lines. The noise photon occupation number $n_i(\omega)$ at stage i and frequency ω can be calculated according to [208]:

$$n_i(\omega) = \frac{n_{i-1}(\omega)}{A_i} + \frac{A_i - 1}{A_i} n_{\text{BE}}(T_{i,\text{att}}, \omega), \quad (4.46)$$

where $n_{i-1}(\omega)$ is the noise photon occupation number at the previous fridge stage, A_i is the attenuation at the i th stage, and $n_{\text{BE}}(T_{i,\text{att}}, \omega)$ is the Bose-Einstein distribution at the temperature of the i th stage's attenuator. This formula allows calculation of the noise photon occupation for each plate in turn down to the DUT itself. The formula does not explicitly consider the coaxial cables, however their effect can be estimated by splitting the attenuation of each cable between connected plates. From here it is a simple matter of calculating $n_i(\omega)$ at each plate, starting with $n_{\text{RT}}(\omega) = n_{\text{BE}}(300\text{K}, \omega)$. At 4.21 GHz this gives $n_{\text{DUT}}^{\text{in}} = 0.295$ for the 'in' line from Figure 4.3. For the 'out' line the isolator and HEMT preamp have isolations of approximately 20 dB at 4.21 GHz, giving $n_{\text{DUT}}^{\text{out}} = 0.337$. Combining these to gives a total photon noise number of $n_{\text{DUT}} = 0.632$. Originally the attenuation at HX and MC were 10 dB, giving a reasonable photon number down the 'in' line for quantum information experiments. However, this level of isolation is not required, and given the noise down the 'out' line would still be present, attenuation was removed to increase the range of powers that could be delivered to the MC.

4.2.3 Applied Powers

For the microwave circuit in Figure 4.3, there is ~ 58 dB of attenuation on the microwave line in. Then the two port microwave cavity at critical coupling adds another 6 dB of attenuation. Ignoring the attenuation of the superconducting microwave lines and other cables outside the fridge, this gives a total attenuation for the circuit of 64 dB.

The cryogenic HEMT preamp has a max input power of -10 dBm, meaning a power greater than 53 dBm at the input of the fridge circuit would overload it. Typically powers of -30 dBm to +26 dBm are used in the lab, so this is very safe. The HEMT preamp provides 36 dBm of gain, so the total attenuation plus gain is -28 dB reaching the second amplifier (Low Noise Factory). This amplifier has a max input power of 0 dBm, so sending 28 dBm at the fridge input would overload it. Similarly it provides 29 dB of gain, taking the circuit total to +1 dB at the last amplifier (Mini-Circuits), which has a 16 dBm input max, so limiting the sent power to 23 dBm or below. From this it is clear the amplifier chain is safe for all but the highest operating powers.

The VNA used to measure S_{21} through the fridge circuit has a maximum output power of 0 dBm in the region of interest (300 kHz to 8.5 GHz), and a maximum measured input power of 6 dBm (>26 dBm will damage the instrument). The last amplifier provides 22 dB of gain, which takes the total of the fridge circuit to +23 dB. Therefore the VNA will not be able to damage itself, especially as there is ~6 dB additional attenuation in the out of fridge cables. However signals should initially be sent around -15 dBm to keep the output within the operating range.

The attenuation before the MC is ~51.5 dB, assuming all power past this point is delivered to the MC, and that the signal at the MC should be kept below -10 dBm (~100 μ W). This means that a power delivered to the top of the fridge should not exceed 41.5 dBm, much higher than expected operational powers, though some care should be taken if amplifying the signal before it enters the fridge.

4.3 Cavity Transmission

This section will expand on the microwave cavity response outlined in Section 4.1. This expansion will include the optomechanical effect, as a modulation of the cavity's resonant frequency. The expected result for a direct measurement of the optomechanical sideband from the transmitted signal will be derived. This type of measurement was attempted but proved unsuccessful, however the relationship between carrier signal strength and sideband peak can then be used to calculate expected signal strength of a homodyne detection measurement, as in Section 5.2.2. The estimation of expected signals being important when determining whether a failure to measure the sideband is simply a lack of measurement sensitivity, or whether unexpected experimental factor must be considered. The effect of the cavity on a phase modulated signal will also be derived, as it is relevant to the calibration of homodyne detection. This section will use ω_0 to refer to unperturbed pure cavity resonance, and $\omega_c(t)$ to refer to the time varying resonance, varying due to the optomechanical coupling.

The physical picture of the modulation is that the pressure fluctuations of the sonic crystal's acoustic mode modifies the density of helium within the on-chip capacitor (be-

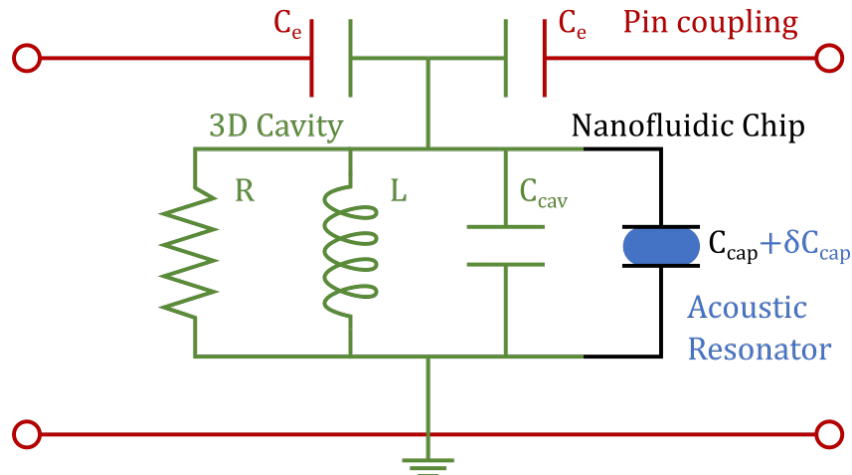


Figure 4.4: RLC circuit representation of the chip-cavity system, including the capacitive pin coupling. Red represents the external microwave coupling to the chip-cavity system, while green represents the cavity, black the nanofluidic chip’s capacitance. Then blue indicates the presence and contribution of the superfluid ^4He acoustic resonator.

tween the central electrodes). The fluctuation of density causes a change in the electric permittivity of the superfluid ^4He acting as a dielectric for the capacitor, which in turn changes the capacitance. Finally the varying capacitance varies the resonant frequency of the microwave cavity mode, which is the origin of the optomechanical coupling. Figure 4.4 shows a circuit representation of the chip-cavity system, including the empty cavity capacitance C_{cav} , the chip’s time varying capacitance $C_{\text{cap}}(t)$, and the external capacitances C_e from the pin coupling. The mechanics in this section is treated generally, with an abstract $x(t)$, and in this way is treated similarly to most microwave cavity optomechanical experiments, such as a coplanar waveguide capacitively coupled to a nano-mechanical beam [209]. For this work the $C_{\text{cav}}(t)$ is the dominant system capacitance, however its variation with time is small $C_{\text{cap}}(t) = C_{\text{cap}} + \delta C_{\text{cap}}(t)$.

Phase Modulation

For general treatments in this section, and especially in Section 4.4 on homodyne detection, the microwave signal is often represented as a real time varying voltage. This choice is to simplify the response of non-linear components involved in the microwave circuits, and also due to the detection methods used for the mechanical signal generally returning amplitudes. These microwave signals can carry information, either from

mechanics or intentionally for calibration, as a phase modulation. The form of a phase modulated signal used in this work is:

$$V(t) = V_0 \sin[\omega_0 t + \phi_{\text{pm}} \sin(\Omega_{\text{pm}} t)] , \quad (4.47)$$

where V_0 is the voltage amplitude, ω_0 is the signal or carrier frequency, ϕ_{pm} is the modulation amplitude in radians, and Ω_{pm} is the modulation frequency. Frequency modulation can be treated similarly, but is a special case where $\phi_{\text{pm}} = \Delta\omega/\Omega_f$, with $\Delta\omega$ the frequency deviation from ω_0 and Ω_f the modulation frequency. The phase modulated signal can be expanded to:

$$V(t) = V_0 \sin(\omega_0 t) \cos[\phi_{\text{pm}} \sin(\Omega_{\text{pm}} t)] + V_0 \cos(\omega_0 t) \sin[\phi_{\text{pm}} \sin(\Omega_{\text{pm}} t)] . \quad (4.48)$$

For small modulation amplitude $\phi_{\text{pm}} \ll 1$, the small angle approximations can be used, $\cos \theta \approx 1 - \theta^2$ and $\sin \theta \approx \theta$, for small θ . Discarding terms second order and higher in ϕ_{pm} gives:

$$V(t) = V_0 \sin(\omega_0 t) + V_0 \phi_{\text{pm}} \cos(\omega_0 t) \sin(\Omega_{\text{pm}} t) . \quad (4.49)$$

Expanding the last term gives:

$$V(t) = V_0 \sin(\omega_0 t) + \frac{1}{2} V_0 \phi_{\text{pm}} [\sin(\omega_0 + \Omega_{\text{pm}})t - \sin(\omega_0 - \Omega_{\text{pm}})t] . \quad (4.50)$$

Giving the approximation of a phase modulated signal into a carrier signal with two sidebands. The $\phi_{\text{pm}} \ll 1$ approximation is accurate as small couplings are expected, giving modulations equivalent to $\phi_{\text{pm}} < 1$ mrad. The full equation uses Bessel functions to expand rather than small angle approximations, giving additional sidebands every harmonic of $\pm\Omega_{\text{pm}}$, and is required for higher modulation amplitudes.

4.3.1 Mechanical Modulation

Time Varying Cavity Resonance

The microwave cavity alters both magnitude and phase of a microwave signal via its complex transmission function. This function has a small time dependence, from the time dependence of $\omega_c(t)$, in turn due to the optomechanical coupling to the mechanical mode. From Section 1.4.2, the coupling is electrostrictive, where the superfluid acoustic mode varies the dominant capacitance in the microwave mode, though the methodology in this section is general in terms of the mechanics. To a first order expansion around the unperturbed resonance ω_0 , the transmission function for the capacitively coupled cavity in Section 4.1 can be written:

$$S_{21}(\omega, \omega_c(t)) \approx S_{21}(\omega, \omega_0) + \frac{\partial S_{21}(\omega, \omega_0)}{\partial \omega_c(t)} \delta\omega_c(t), \quad (4.51)$$

where S_{21} is the complex transmission function, ω is the frequency of the probe signal or carrier wave, $\omega_c(t)$ is the time varying cavity resonance, ω_0 is the unperturbed cavity resonance, and $\delta\omega_c(t)$ represents the small variations around ω_0 . Which assumes that the optomechanical coupling is weak enough for $\delta\omega_c(t) \ll \kappa_L$. This complex transmission function can be broken up into magnitude and phase effects. With a probe approaching ω_0 the magnitude vanishes, giving a phase sensitive measurement. The phase shift expanded to first order around the unperturbed resonance is:

$$\arg[S_{21}(\omega, \omega_c(t))] \equiv \phi_c(\omega, \omega_c(t)) = \phi_c(\omega, \omega_0) + \frac{\partial \phi_c(\omega, \omega_0)}{\partial \omega_c(t)} \delta\omega_c(t). \quad (4.52)$$

From the definition of S_{21} used, the argument on resonance is zero, eliminating the first term. In practise the physical cavity will provide some constant phase shift, including some contribution from the carrier being off resonance, which can be taken into its constant phase term. From the derivation of S_{21} in Section 4.1.3, the differential in Eq. 4.52 can be calculated as:

$$\frac{\partial \phi_c(\omega, \omega_0)}{\partial \omega_c(t)} = \frac{2Q_L \omega}{\omega_0^2} \frac{1}{1 + 4Q_L^2 \delta\omega^2} . \quad (4.53)$$

For a phase sensitive measurement the differential Eq. 4.53 should be maximised, which is the slope of the phase of S_{21} . This is achieved when the carrier frequency is on resonance ($\omega = \omega_0$), giving:

$$\frac{\partial \phi_c(\omega_0, \omega_0)}{\partial \omega_c(t)} = \frac{2Q_L}{\omega_0} , \quad (4.54)$$

where Q_L is the loaded quality factor. Substituting back into Eq. 4.52 then gives:

$$\phi_c(\omega_0, \omega_c(t)) = \frac{2Q_L}{\omega_0} \delta\omega_c(t) . \quad (4.55)$$

Which can be converted to a general mechanical mode amplitude as:

$$\phi_c(\omega_0, \omega_c(t)) = \frac{2Q_L}{\omega_0} \frac{\partial \omega_c}{\partial x} \delta x(t) , \quad (4.56)$$

where $x(t)$ is the global amplitude function defined in Section 1.2.2, often treated as a displacement in optomechanics, $\delta x(t)$ then represents small deviations around the equilibrium position. Writing for the constant carrier frequency as $\Delta\phi_c$, the phase shift of an on peak carrier due to the varying cavity resonance, and also using $G = \partial\omega_c/\partial x$, gives a time dependent phase term of:

$$\Delta\phi_c(t) = \frac{2GQ_L}{\omega_0} \delta x(t) . \quad (4.57)$$

Generalised Mechanical Motion

For a mechanical harmonic oscillator with frequency Ω_m and dissipation Γ_m , acted on by no significant external forces, $\delta x(t)$ will originate from the thermal Brownian motion of the resonator as [210]:

$$\delta x(t) = X(t) \cos(\Omega_m t) + Y(t) \sin(\Omega_m t) . \quad (4.58)$$

The magnitude of $\Delta\phi_c(t)$ is small compared with the overall signal, and so these two quadrature components cause phase modulation similar to Section 4.3, which cause sidebands at $\omega \pm \Omega_m$. So a frequency domain power spectrum measurement, of the microwave signal from the cavity, would access the noise power spectral density of the acoustic mode. This is equivalent to the Fourier transform of the autocorrelation function for a mechanical oscillator, defined as [1]:

$$S_{xx}(\Omega) = \int_{-\infty}^{+\infty} \langle x(t)x(0) \rangle e^{i\Omega t} dt. \quad (4.59)$$

From fluctuation-dissipation theorem, the symmetrised (double-sided) spectral density for a mechanical oscillator in contact with a thermal bath at temperature T is given by [35, 211]:

$$\begin{aligned} S_{xx}(\Omega) &= \frac{\hbar\Omega\Omega_m}{Q_m m_{\text{eff}}} \frac{\coth\left(\frac{\hbar\Omega}{2k_B T}\right)}{(\Omega^2 - \Omega_m^2)^2 + (\Omega\Omega_m/Q_m)^2} \\ &\approx \frac{2k_B T \Omega_m}{m_{\text{eff}} Q_m [(\Omega^2 - \Omega_m^2)^2 + (\Omega\Omega_m/Q_m)^2]}, \end{aligned} \quad (4.60)$$

where the approximation has been made for large phonon occupation numbers $\bar{n}_m \approx k_B T / \hbar\Omega_m \gg 1$, and m_{eff} is the effective mass corresponding to the normalisation of $x(t)$, as discussed generally in Section 1.2.2 and specific to this work in Section 1.4.2. On the mechanical resonance Ω_m the mechanical noise power spectral density simplifies to:

$$S_{xx}(\Omega_m) = \frac{2k_B T Q_m}{m_{\text{eff}} \Omega_m}. \quad (4.61)$$

Another important result is that the integral of the mechanical noise gives the variance of x :

$$\int_{-\infty}^{+\infty} S_{xx}(\Omega) \frac{d\Omega}{2\pi} = \langle x^2 \rangle. \quad (4.62)$$

Meaning the area under the sideband peak in power spectral density is proportional to $\langle x^2 \rangle$. For a weakly damped oscillator in thermal equilibrium:

$$\langle x^2 \rangle = \frac{k_B T}{m_{\text{eff}} \Omega_m^2} . \quad (4.63)$$

Relation to Microwave Frequency Noise

For the cavity optomechanical experiments in this work, the mechanical motion is not measured directly, instead the mechanical motion is imprinted upon the cavity's microwave field. Given the definition of G , this is most simply seen in a relationship between the double sided noise spectral density of the cavity resonance frequency due to the optomechanical coupling $S_{\omega\omega}(\Omega)$, and the mechanical displacement spectral density $S_{xx}(\Omega)$:

$$S_{\omega\omega}(\Omega) = G^2 S_{xx}(\Omega) . \quad (4.64)$$

Writing in terms of g_0 , substituting in for $x_{\text{zpf}} = \sqrt{\hbar/2m_{\text{eff}}\Omega_m}$ and for $S_{xx}(\Omega)$ from Eq. 4.60 gives:

$$S_{\omega\omega}(\Omega) \approx g_0^2 \frac{4k_B T \Omega_m^2}{\hbar Q_m [(\Omega^2 - \Omega_m^2)^2 + (\Omega \Omega_m / Q_m)^2]} . \quad (4.65)$$

On the mechanical resonance Ω_m this simplifies to:

$$S_{\omega\omega}(\Omega_m) = g_0^2 \frac{4k_B T Q_m}{\hbar \Omega_m^2} = 4\bar{n}_m g_0^2 \frac{Q_m}{\Omega_m} , \quad (4.66)$$

giving a potential route for a direct measurement of g_0 if $S_{\omega\omega}(\Omega_m)$ can be measured. The integral of $S_{\omega\omega}(\Omega_m)$ over Ω gives another possible route of determining g_0 , and will be equivalent to the variance of $\delta\omega_c$, by using Eq.'s 4.62 and 4.63:

$$\langle \delta\omega_c^2 \rangle = \int_{-\infty}^{+\infty} S_{\omega\omega}(\Omega) \frac{d\Omega}{2\pi} = 2\bar{n}_m g_0^2 , \quad (4.67)$$

which is equal to the area under a measurement of the sideband peak in a measurement of $S_{\omega\omega}(\Omega)$. Both methods rely on a low enough dynamical back action, that is a low enough coupling or probe power, such that the occupation number \bar{n}_m can be directly related

to the bulk temperature of the experiment. These two calculations for determining g_0 can be used for a direct measurement of the carrier signal with a spectrum analyser, as outlined in the following Section 4.3.2. However, for a low coupling the sensitivity of a spectrum analyser may not be sufficient, which is where a homodyne detection method may be more successful, which is outlined in Section 4.4.

4.3.2 Direct Measurement

As mentioned above a spectrum analyser measures power spectral density, and so can be used to measure a noise power spectrum. For a simple cavity transmission of an on resonance carrier signal, the optomechanical coupling will result in a phase shift of the signal. Using the logic of phase modulation in Section 4.3, for a small modulation amplitude this will give two sidebands, with frequency $\omega_0 \pm \Omega_m$ and amplitude proportional to phase noise amplitude (e.g. ϕ_{pm} in Eq. 4.50). For now ignoring the relationship to the carrier wave with amplitude V_0 , the double sided phase noise spectral density $S_{\phi\phi}(\Omega)$, imparted on a carrier wave transmitting the cavity at its unperturbed resonance frequency ω_0 , by the optomechanical coupling, can be defined:

$$S_{\phi\phi}(\Omega) = \frac{|\Delta\tilde{\phi}_c(\Omega)|^2}{BW}, \quad (4.68)$$

where $|\Delta\tilde{\phi}_c(\Omega)|^2 = \mathcal{F}\{\Delta\phi_c(t) \star \Delta\phi_c(-t)\}$ is the Fourier transform of the convolution of the time dependent noise $\Delta\phi_c(t)$ (from Eq. 4.57) with $\Delta\phi_c(-t)$. Then BW is the bandwidth used to measure $\Delta\phi_c$, and originates from the convolution of the measurement specific envelope function [35]. This $S_{\phi\phi}(\Omega)$ can then be related to the noise of cavity resonant frequency and mechanical amplitude via Eq. 4.55 and 4.57, giving:

$$S_{\phi\phi}(\Omega) = \frac{4Q_L^2}{\omega_0^2} S_{\omega\omega}(\Omega) = \frac{4Q_L^2 G^2}{\omega_0^2} S_{xx}(\Omega). \quad (4.69)$$

Also from Section 4.3 on phase modulation, it can be seen that the phase noise voltage amplitude is equal to the carrier wave voltage multiplied by the phase noise amplitude. The additional 1/2 factor for a single sideband should not be involved as

the noise is measured at the level of Eq. 4.49, because of the choice of $S_{xx}(\Omega)$ being the symmetrised double sided noise spectrum. If the spectrum analyser measures microwave power spectral density, this is proportional to V^2/Hz , and so the measured power spectral density as a function of microwave frequency $S_{VV}(\omega)$, near the sideband $\Omega \approx \pm\Omega_m$, should then be:

$$S_{VV}(\omega_0 + \Omega) = S_{\phi\phi}(\Omega)S_{VV}(\omega_0) \cdot BW , \quad (4.70)$$

where $S_{VV}(\omega_0)$ is the measured power spectral density of the carrier signal at frequency ω_0 , whose actual spectral density should essentially be a delta function at ω_0 , with magnitude P_{out} from Eq. 4.45. The peak of the frequency noise can be calculated from Eq. 4.66, an equation g_0 can be written:

$$g_0^2 = \frac{S_{VV}(\omega_0 \pm \Omega_m)}{S_{VV}(\omega_0) \cdot BW} \frac{\omega_0^2 \Omega_m}{16Q_L^2 Q_m \bar{n}_m} , \quad (4.71)$$

This method is highly convenient as all factors can either be measured directly, quickly fitted from cavity transmission measurements, or calculated from temperature and other known factors in the case of \bar{n}_m . Although Q_m may be difficult to find accurately from a measurement with the sidebands close to the noise floor. The spectrum analyser may also automatically account for the BW dependent on settings, say if measuring in dBm or with a 1 Hz bandwidth, in this case $S_{VV} \rightarrow P$.

A similar method is possible by integrating the area under the sideband curve in S_{VV} , using a similar procedure as for the peak signal, but with Eq. 4.67:

$$\int_{\text{SSB}} S_{VV}(\omega_0 + \Omega) \frac{d\Omega}{2\pi} = \frac{1}{2} S_{VV}(\omega_0) \cdot BW \int_{-\infty}^{+\infty} S_{\phi\phi}(\Omega) \frac{d\Omega}{2\pi} , \quad (4.72)$$

where \int_{SSB} is over a single sideband region close to $|\Omega_m|$, which is the origin of the 1/2 factor. From Eq. 4.69 and 4.67, the integral above is:

$$\int_{-\infty}^{+\infty} S_{\phi\phi}(\Omega) \frac{d\Omega}{2\pi} = g_0^2 \frac{8Q_L^2 \bar{n}_m}{\omega_0^2} . \quad (4.73)$$

Which leads to another equation for g_0 :

$$g_0^2 = \frac{\omega_0^2}{4Q_L^2 \bar{n}_m S_{VV}(\omega_0) \cdot BW} \int_{\text{SSB}} S_{VV}(\omega_0 + \Omega) \frac{d\Omega}{2\pi}, \quad (4.74)$$

giving an alternative method for calculating g_0 , similar to [212]. These two direct measurement techniques have the advantage of being able to ignore the rest of the microwave measurement circuit, as the cavity modulated sideband signal can be calibrated against the carrier. However, for this to work the ratio of carrier to the sideband must be within the spectrum analyser's dynamic range, which may not be true for weak coupling or very low temperatures. The following Section 4.4 seeks to increase the measurement sensitivity, while maintaining a reference wave to calibrate any mechanical signal against.

4.4 Homodyne Detection

Homodyne detection was the main method used for searching for the mechanical resonance of the sonic crystal. A method which effectively a microwave interferometer, a phase sensitive detection technique where the time varying phase of one arm is isolated using a constant reference signal, at the same frequency, in the other arm. This method has been used in the Rojas Lab (paper in preparation) to detect thermomechanical motion of a silicon nitride membrane, using a microwave cavity at room temperature. It has the advantage of isolating the frequency around the mechanical frequency, and can be achieved with relatively inexpensive microwave equipment. However, the mechanical signal is isolated from the microwave carrier signal, and so cannot be calibrated against it, as in Section 4.3.2. So instead a calibration signal can be generated by adding a small phase modulation at the signal generator.

4.4.1 Principles of Lock-In Detection

Instead of a spectrum analyser to measure the output signal of the homodyne measurement setup, a Zurich Instruments lock-in amplifier is used. Lock-in amplifiers are especially effective at isolating signals at specific frequencies, with small measurement bandwidths around the given frequency. They tend to operate in the MHz or lower

frequency range, making them ideal for homodyne detection. The lock-in takes an input signal of form:

$$V_s(t) = A_s \cos(\Omega_s t + \theta) , \quad (4.75)$$

where $V_s(t)$ is the signal voltage into the lock-in, A_s is the amplitude of this signal, Ω_s its frequency, and θ its phase. This wave is then demodulated (down mixed) with two separate reference signals at Ω_{ref} , but out of phase by $\pi/2$, to produce the quadrature components [213]:

$$X + iY = \frac{A_s}{\sqrt{2}} F(\Omega_s - \Omega_{\text{ref}}) \exp\{i[(\Omega_s - \Omega_{\text{ref}})t + \theta]\} , \quad (4.76)$$

where $F(\Omega)$ is the frequency response of the filters. The simplest filters low-pass the signal, with the 3 dB point of filters being set by demodulation bandwidth, and the number of filters applied being set by the order. The most common use of the lock-in is to directly measure a signal by setting $\Omega_{\text{ref}} \approx \Omega_s$, which will be down converted to a near DC signal, then setting the filters to a low enough bandwidth to isolate the signal from a background. The amplitude of this isolated signal will then be $|A_s|/\sqrt{2}$, and will have power proportional to $|A_s|^2/2$, which are effectively values of the RMS amplitude. This function is used first to detect mechanical signals in the homodyne detection scheme, where Ω_{ref} is swept for the detection frequency and also the piezo drive, hoping to excite and then detect the mechanical resonance.

Once the mechanical resonance has been found, the piezo can be set to drive on or near the resonance Ω_m , and the lock-in's 'zoom FFT' detection method can be used. This produces the power spectral density of the input wave, functioning similarly to a spectrum analyser, with some key differences. The zoom FFT first uses the lock-in's regular functionality to demodulate the signal by its internal reference Ω_{ref} , producing and filtering the $X + iY$ quadrature components, which can then be Fourier transformed to produce a double sided spectrum centred at Ω_{ref} . Because the lock-in effectively isolates a small band and mixes it down near DC, it greatly decreases the number of data points required for FFT, reducing acquisition time.

As the FFT algorithm is applied to the $X + iY$ signal in Eq. 4.76 (functionally Fourier transforming it), its complex nature allows generation of a double sided spectrum around the reference. This spectrum can then be plotted as either: spectrum $FFT(X + iY)$, power spectrum $|FFT(X + iY)|^2$, spectral density $[V/\sqrt{\text{Hz}}]$, or power spectral density $[V^2/\text{Hz}]$. The signal described in Eq. 4.76 will give a peak in power spectrum [214]:

$$P_{\text{spec}}(\Omega_s - \Omega_{\text{ref}}) = \frac{|A_s|^2}{2} |F(\Omega_s - \Omega_{\text{ref}})|^2 . \quad (4.77)$$

The lock-in can give the spectrum either in absolute frequency Ω_s , or in frequency relative to Ω_{ref} . There is also the functionality to divide the output spectrum by $F(\omega)$, therefore giving the input signal in absolute terms.

This work will focus on spectral density measurements of signals related to the mechanical noise. For a lock-in measurement, accounting for the filters, the noise power spectral density is [215]:

$$S_{VV}(\Omega) = \frac{\Delta V_{\text{rms}}^2(\Omega)}{BW \text{ used to measure } \Delta V_{\text{rms}}} , \quad (4.78)$$

in V^2/Hz , where over bandwidth BW there is negligible change in $S_{VV}(\Omega)$. For completeness frequency noise spectral density can be written:

$$S_{\Omega\Omega}(\Omega) = \frac{\Delta \Omega_{\text{rms}}^2(\Omega)}{BW \text{ used to measure } \Delta \Omega_{\text{rms}}} , \quad (4.79)$$

in Hz^2/Hz . While the phase noise spectral density is:

$$S_{\phi\phi}(\Omega) = \frac{\Delta \phi_{\text{rms}}^2(\Omega)}{BW \text{ used to measure } \Delta \phi_{\text{rms}}} , \quad (4.80)$$

in rad^2/Hz . These definitions are equivalent to those in Section 4.3, for example the phases are related via $\Delta \phi_{\text{rms}}^2(\Omega) = |\Delta \tilde{\phi}_c(\Omega)|^2/2$. Measuring the example signal in Eq. 4.75, in power spectral density, with the automatic filter function removal, the lock-in will give a peak:

$$S_{VV}(\Omega_s) = \frac{|A_s|^2}{2BW} . \quad (4.81)$$

Though this frequency sweep and then zoom FFT method was normally used, it is also possible to send white noise to the piezo from a function generator, and then either sweep detection frequency, or zoom FFT around the expected mechanical frequency. The white noise can even be bandpass filtered to remove noise outside the frequency region of interest.

Measurement Circuit

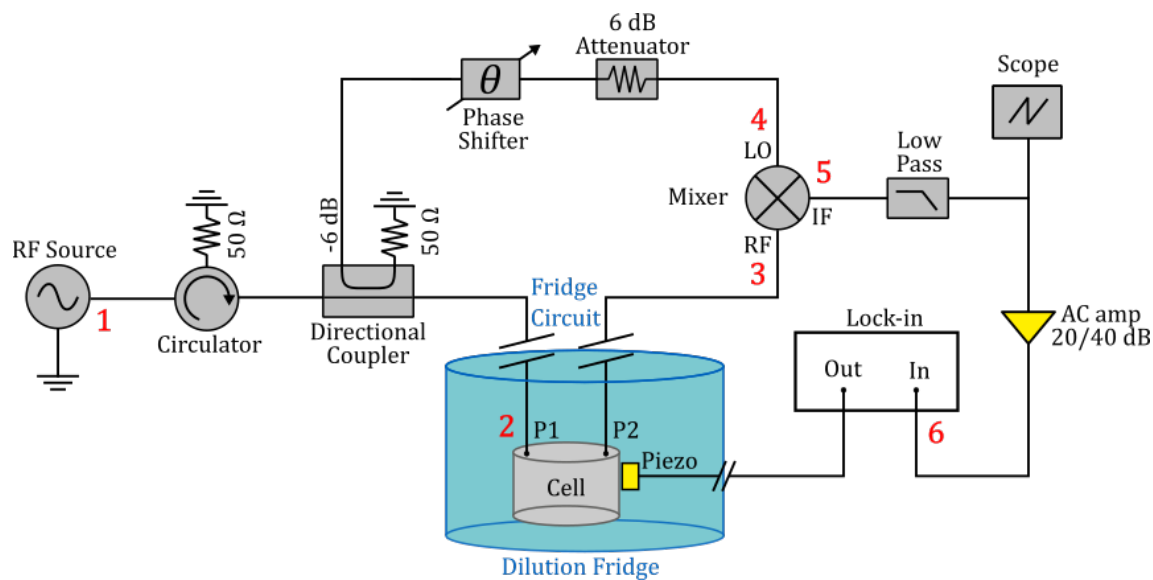


Figure 4.5: Diagram of microwave interferometer circuit used, with red numbers relating to voltages as positions around the circuit (e.g. $V_1(t)$). The microwave circuit from Figure 4.3 is present but omitted from the diagram for simplicity, instead labelled as ‘Fridge circuit’ in blue.

Figure 4.5 shows the homodyne detection microwave circuit. The RF signal is generated at ω_0 , is split into two arms, one that passes through a ‘delay’ arm with variable phase shifter, and the other which passes through the cavity, where the optomechanical coupling imparts phase noise. The two signals are then recombined at the mixer, with the phase shifter adjusted to quadrature in order to cancel the two carrier waves, leaving only the mechanical sidebands, down-mixed to the mechanical frequency. The signal is then low passed to remove any RF frequency components, and measured with the lock-in

as described above. The rest of Section 4.4 will give details of how this method is used to obtain g_0 , the vacuum optomechanical coupling strength.

4.4.2 Cavity Modulated Signal

This section will consider the cavity's effect on the carrier wave, what happens when the result is demodulated with the delay arm sight, and what is then measured at the lock-in. The small phase modulation added at the signal generator will be considered in the next Section 4.4.3.

At the signal generator, represented by 1 on Figure 4.5, ignoring the small phase modulation the carrier wave is:

$$V_1(t) = V_1 \cos(\omega_0 t + \phi_1) , \quad (4.82)$$

where ω_0 is the carrier frequency, set to the unperturbed cavity resonance to maximise phase sensitivity, V_1 is the voltage magnitude, and ϕ_1 the phase at the signal generator. After splitting at the directional coupling, on the lower arm and just before the cavity (2 on Figure 4.5), the signal has become:

$$V_2(t) = V_2 \cos(\omega_0 t + \phi_2) , \quad (4.83)$$

where V_2 represents V_1 after the circuit magnitude response of all components up to position 2; $\phi_2 = \omega_0 \tau_2 + \theta_2$ is then the phase at position 2, comprised of a time delay τ_2 due to cable length, and a constant phase term θ_2 , the sum of all frequency independent phase contributions up to position 2. Treating phase in this way is useful when calculating relative phase differences, as discussed in Section 4.4.6. Both the phase and amplitude response are assumed to be constant across the frequency window of interest.

The signal then passes through the cavity, and is modified by its transmission properties, including phase noise from the variation in cavity resonance due to the optomechanical coupling. The signal after the cavity is then:

$$V_3(t) = V_3 |S_{21}(\omega_0)| \cos[\omega_0 t + \Delta\phi_c(t) + \phi_3] , \quad (4.84)$$

where V_3 is magnitude excluding cavity transmission, and $\Delta\phi_c(t)$ is the phase noise on resonance from the coupling, as defined in Eq. 4.57, and ϕ_3 is the total constant phase, including the constant transmission term. This also is the signal into the RF port of the frequency mixer. For the top arm of the circuit the signal into the LO is simply:

$$V_4(t) = V_4 \cos[\omega_0 t + \phi_4] , \quad (4.85)$$

where V_4 is the combined circuit magnitude effects to this point, and ϕ_4 is the phase shift from the signal generator to the LO port through this arm. Given Eq. 4.84 and 4.85 above into the RF and LO ports of the frequency mixer, and ignoring higher harmonics, the expected signal out the IF port is of the form:

$$V_5(t) = K'_m(V_3, V_4) |S_{21}(\omega_0)| (\cos[2\omega t + (\phi_3 + \phi_4) + \Delta\phi_c(t)] + \cos[(\phi_3 - \phi_4) + \Delta\phi_c(t)]) , \quad (4.86)$$

where $K'_m(V_3, V_4)$ is the transfer function of the frequency mixer with amplitudes V_4 on the LO port and amplitude $V_3/|S_{21}(\omega_0)|$ on the RF port, written in this way as the RF signal should be well below the 1 dB compression point of the mixer. In this form $K'_m(V_3, V_4)$ will be frequency independent in the region of interest, a few MHz around ω_0 . After low pass filtering and amplifying the signal at the input of the lock-in is:

$$V_6(t) = K_m |S_{21}(\omega_0)| \cos[\phi_r + \Delta\phi_c(t)] , \quad (4.87)$$

where the total circuit transfer function K_m , has absorbed additional attenuation and amplification up to the lock-in, dropping the V_3 and V_4 dependences for simplicity; and $\phi_r = (\phi_3 - \phi_4)$ has been used to signify the relative phase difference between the two arms. Expanding the cos term gives:

$$\cos[\phi_r + \Delta\phi_c(t)] = \cos(\phi_r) \cos[\Delta\phi_c(t)] - \sin(\phi_r) \sin[\Delta\phi_c(t)] . \quad (4.88)$$

The scope in Figure 4.5 can be used to monitor the relative phase of the two waves at the mixer, and the phase shifter used to shift them into quadrature (0V DC). This sets $\phi_r = (2n + 1)\pi/2$ where $n \in \mathbb{Z}$, meaning only the sin term remains. Then using $\Delta\phi_c(\Omega) \ll 1$ (weak optomechanical coupling), allows simplification of Equation 4.87 to:

$$V_6(t) = -K_m |S_{21}(\omega_0)| \Delta\phi_c(t) . \quad (4.89)$$

From here the measurement scheme becomes important to the form of $\Delta\phi_c(t)$. In the case where the mechanics is being driven by the piezo at Ω , an approximation to a simple cosine wave can be used $\Delta\phi_c(t) \approx \phi_d(\Omega) \cos(\Omega t + \psi_d)$, where $\phi_d(\Omega)$ will depend on settings and acoustic transmission of the piezo drive, and $\phi_d(\Omega)$ is an arbitrary constant phase term. This is demodulated by the lock-in reference to

$$V_{\text{lock-in}}(\Omega) = \frac{K_m \phi_d(\Omega) |S_{21}(\omega_0)|}{\sqrt{2}} \exp(i[(\Omega - \Omega_{\text{ref}})t + \theta]) , \quad (4.90)$$

for an arbitrary phase θ . This is measured and displayed as either $X + iY$ quadrature terms, or as R and θ the amplitude and phase of the wave. A simple lock-in measurement of the magnitude will therefore retrieve:

$$V_{\text{lock-in}}^R(\Omega) = \frac{K_m \phi_d(\Omega) |S_{21}(\omega_0)|}{\sqrt{2}} . \quad (4.91)$$

Simultaneously sweeping the piezo drive and measurement frequency Ω across membrane resonance Ω_0 , should produce the expected Lorentzian type peak of a mechanical resonance. Note here that the amplitude of R is the RMS value of the signal voltage, represented by the $\sqrt{2}$.

Without the presence of a drive tone, the time varying voltage at the lock-in in Eq. 4.89 will be due to the phase noise induced by the thermochemical noise of the superfluid acoustic mode. The lock in will then measure this as a RMS voltage noise spectral density:

$$S_{VV}(\Omega) = \frac{K_m^2 |S_{21}(\omega_0)|^2 |\Delta\tilde{\phi}_c(\Omega)|^2}{2BW}, \quad (4.92)$$

similar to 4.68. The signal here is double sided in Ω , due to the complex nature of $X + iY$, though for any detection method of a symmetric spectrum any factor of 2 here will cancel with the same factor in the modulated signal. This is also true for the 1/2 factor from RMS measurement. Comparing Eq. 4.92 and the phase noise spectral density in Eq. 4.80, the measured signal is effectively:

$$S_{VV}(\Omega) = K_m^2 |S_{21}(\omega_0)|^2 S_{\phi\phi}(\Omega), \quad (4.93)$$

where the factor of 1/2 has been taken into $S_{\phi\phi}(\Omega)$ to account for the phase noise spectral density being in terms of RMS values. As the carrier is on the cavity resonance, Eq. 4.69 relating $S_{\phi\phi}(\Omega)$ to $S_{\omega\omega}(\Omega)$ and $S_{xx}(\Omega)$ can then be used:

$$\begin{aligned} S_{VV}(\Omega) &= K_m^2 |S_{21}(\omega_0)|^2 \frac{4Q_L^2}{\omega_0^2} S_{\omega\omega}(\Omega) \\ &= K_m^2 |S_{21}(\omega_0)|^2 \frac{4Q_L^2 G^2}{\omega_0^2} S_{xx}(\Omega), \end{aligned} \quad (4.94)$$

which will be used in Section 4.4.4, along with the equations derived in the rest of Section 4.4. Having the carrier signal at ω_0 gives maximum phase sensitivity. Being off resonance will alter the conversion $S_{\phi\phi}(\Omega) \rightarrow S_{\omega\omega}(\Omega)$, through $\partial\phi_c/\partial\omega_c$, and the full form of Eq. 4.53 would need to be used.

4.4.3 Source Modulated Signal

If a mechanical signal can be found using homodyne detection, especially in the absence of piezo drive, it would be advantageous to separate the greater circuit response from the optomechanical coupling. This is simple for a direct measurement as in Section 4.3.2, however in homodyne detection the carrier is removed. Instead a known amplitude of phase modulation ϕ_{pm} can be added at the microwave source, at a modulation fre-

quency Ω_{pm} near the mechanical resonance, and the resulting signal be used to calibrate the measurement. This method was attempted, however it decreased the sensitivity of the measurement, via phase noise, and so was not used for the data shown in Chapter 5. Once a clear optomechanical signal can be found, the method outlined in the rest of this section can then be used to help determine g_0 .

Following the same process as Section 4.53 above, where the subscripts for signal refer to positions in Figure 4.5, but this time starting with a phase modulated signal from the signal generator:

$$V_1(t) = V_1 \cos[\omega t + \phi_{\text{pm}} \cos(\Omega_{\text{pm}} t + \psi_1) + \phi_1] , \quad (4.95)$$

where Ω_{pm} is the modulated frequency, close to the mechanical resonance Ω_m but off the peak, and ϕ_{pm} is the modulation amplitude, chosen to be of similar order to $\Delta\phi_c$. Then $\psi_1 = \Omega_{\text{pm}}\tau_1 + \hat{\theta}_1$ is the phase of the modulation at position 1, this is related to ϕ_1 as discussed in Section 4.4.6 later, note $\hat{\theta}_1 \neq \theta_1$. Then on the lower arm before the cavity:

$$V_2(t) = V_2 \cos[\omega t + \phi_{\text{pm}} \cos(\Omega_{\text{pm}} t + \psi_2) + \phi_2] . \quad (4.96)$$

Then just before the mixer, again taking non-cavity magnitude change into V_3 , and all phase effects into ϕ_3 , the signal at position 3 is:

$$V_3(t) = V_3 |S_{21}(\omega_0)| \cos[\omega t + \phi_{\text{pm}} s_{21}(\Omega_{\text{pm}}) \cos(\Omega_{\text{pm}} t + \psi_3) + \phi_3] , \quad (4.97)$$

where $s_{21}(\Omega_{\text{pm}}) = |S_{21}(\omega_0 \pm \Omega_{\text{pm}})/S_{21}(\omega_0)|$, and accounts for the sidebands from phase modulation travelling through the cavity away from resonance. For now the phase response of the cavity is assumed constant within the modulated window $\pm\Omega_m$ around ω_0 , which will be explored in Section 4.4.5. The optomechanical effect on the modulated sidebands is ignored as this will be second order (e.g. order $\phi_{\text{pm}}\Delta\phi_c$, both of which are small). The signal through the upper arm, on the LO port, is then:

$$V_4(t) = V_4 \cos[\omega t + \phi_{\text{pm}} \cos(\Omega_{\text{pm}} t + \psi_4) + \phi_4] . \quad (4.98)$$

Mixing these two signals and low passing out the higher frequencies gives signal out the IF port of:

$$V_6(t) = K_m(V_3, V_4)|S_{21}(\omega_0)| \cos[(\phi_3 - \phi_4) + s_{21}(\Omega_{\text{pm}})\phi_{\text{pm}} \cos(\Omega_{\text{pm}}t + \psi_3) - s_{21}(\Omega_{\text{pm}})\phi_{\text{pm}} \cos(\Omega_{\text{pm}}t + \psi_4)] . \quad (4.99)$$

Note K_m here is identical to the K_m in Equation 4.87, as all components other than the microwave cavity are assumed to have an approximately constant response within the modulation window around the carrier. This can be expanded as in Eq. 4.88 for the cavity modulated signal, and quadrature assumed for the $\phi_4 - \phi_5$ term while keeping the phase of the ψ terms:

$$V_6(t) = K_m|S_{21}(\omega_0)| \sin[s_{21}(\Omega_{\text{pm}})\phi_{\text{pm}} \cos(\Omega_{\text{pm}}t + \psi_3) - s_{21}(\Omega_{\text{pm}})\phi_{\text{pm}} \cos(\Omega_{\text{pm}}t + \psi_4)] . \quad (4.100)$$

Here, similarly to Eq. 4.89 for the mechanical modulation, ϕ_{pm} can be assumed to be small giving:

$$V_6(t) = K_m|S_{21}(\omega_0 \pm \Omega_{\text{pm}})|\phi_{\text{pm}}[\cos(\Omega_{\text{pm}}t + \psi_3) - \cos(\Omega_{\text{pm}}t + \psi_4)] . \quad (4.101)$$

These last two terms can be combined to give:

$$V_6(t) = -2K_m|S_{21}(\omega_0 \pm \Omega_{\text{pm}})|\phi_{\text{pm}} \sin[\Omega_{\text{pm}}t + (\psi_3 + \psi_4)/2] \sin[(\psi_3 - \psi_4)/2] . \quad (4.102)$$

When this signal is measured with with the zoom FFT feature of the lock-in, a sharp peak in the power spectral density at Ω_{pm} is produced, of height:

$$S_{VV}(\Omega_{\text{pm}}) = \frac{2K_m^2|S_{21}(\omega_0 \pm \Omega_{\text{pm}})|^2\phi_{\text{pm}}^2 \sin^2(\psi_r/2)}{BW} , \quad (4.103)$$

where $\psi_r = \psi_3 - \psi_4$ is the relative phase difference between the two arms. This is of similar form to Eq. 4.92, and should allow calibration of K_m , to extract g_0 . Then ϕ_{pm} and BW are known, $|S_{21}(\omega_0 \pm \Omega_{pm})|$ can be determined from a transmission measurement, and then methods of determining ψ_r are discussed in Section 4.4.6.

4.4.4 Optomechanical Coupling Calibration

Given the expressions for the S_{VV} for both the cavity and source modulated signals, similar calculations to the direct measurement methods in Section 4.3.2 are possible. Firstly the transfer function can be calibrated by the source modulated signal, from Eq. 4.103, giving:

$$K_m^2 = \frac{BW \cdot S_{VV}(\Omega_{pm})}{2|S_{21}(\omega_0 \pm \Omega_{pm})|^2 \phi_{pm}^2 \sin^2(\psi_r/2)}. \quad (4.104)$$

Which can be used to either calibrate for a measurement of the mechanical signal peak at Ω_m , or the integral over this peak. Then from Eq. 4.94 expected mechanical peak is:

$$S_{VV}(\Omega_m) = K_m^2 |S_{21}(\omega_0)|^2 \frac{4Q_L^2}{\omega_0^2} g_0^2 \frac{4\bar{n}_m Q_m}{\Omega_m}. \quad (4.105)$$

Substituting in for K_m^2 from Eq. 4.104, and rewriting in terms of g_0^2 gives:

$$g_0^2 = \phi_{pm}^2 \sin^2(\psi_r/2) \frac{\Omega_m \omega_0^2 |s_{21}(\Omega_{pm})|^2}{8\bar{n}_m Q_m Q_L^2} \frac{S_{VV}(\Omega_m)}{BW \cdot S_{VV}(\Omega_{pm})}. \quad (4.106)$$

This is simplified slightly with linewidths: $\kappa_L = \omega_0/Q_L$ and $\Gamma_m = \Omega_m/Q_m$. Then for the on-resonance carrier $s_{21}(\Omega_{pm}) = \kappa_L/(\kappa_L + 2i\Omega_{pm})$. Using these substitutions, the above equation becomes:

$$g_0^2 = \phi_{pm}^2 \sin^2(\psi_r/2) \frac{\Gamma_m \kappa_L^4}{8\bar{n}_m (\kappa_L^2 + 4\Omega_{pm}^2)} \frac{S_{VV}(\Omega_m)}{BW \cdot S_{VV}(\Omega_{pm})}. \quad (4.107)$$

A similar method can be employed for the area under one of the sidebands in $S_{VV}(\Omega)$:

$$\int_{\text{SSB}} S_{VV}(\Omega) \frac{d\Omega}{2\pi} = g_0^2 \cdot K_m^2 |S_{21}(\omega_0)|^2 \frac{4\bar{n}_m Q_L^2}{\omega_0^2}, \quad (4.108)$$

where \int_{SSB} is over the mechanical sideband, ignoring any contribution from the source modulated signal nearby. Substituting in for K_m^2 and rearranging in terms of g_0^2 then gives:

$$g_0^2 = \phi_{\text{pm}}^2 \sin^2(\psi_r/2) \frac{\omega_0^2 |s_{21}(\Omega_{\text{pm}})|^2}{2\bar{n}_m Q_L^2} \frac{\int_{\text{SSB}} S_{VV}(\Omega) \frac{d\Omega}{2\pi}}{BW \cdot S_{VV}(\Omega_{\text{pm}})}. \quad (4.109)$$

With the same substitutions as Eq. 4.107:

$$g_0^2 = \phi_{\text{pm}}^2 \sin^2(\psi_r/2) \frac{\kappa_L^4}{2\bar{n}_m(\kappa_L^2 + 4\Omega_{\text{pm}}^2)} \frac{\int_{\text{SSB}} S_{VV}(\Omega) \frac{d\Omega}{2\pi}}{BW \cdot S_{VV}(\Omega_{\text{pm}})}, \quad (4.110)$$

giving two methods for determining g_0 from the same measurement. There is an additional phase factor ψ_m , covered in the next Section 4.4.5, which can be taken into ψ_r , and the method for calculating ψ_r covered in Section 4.4.6. Then all other factors in both Eq. 4.107 and 4.110 are either known or fairly simply determined from measurements. This is advantageous as trying to measure rigorously the transfer function K_m is difficult, especially for a setup where the microwave lines include the fridge circuit. This method has been used in the Rojas Lab (paper in preparation) to measure the optomechanical coupling of re-entrant microwave cavities, with gold plated silicon nitride membranes over the re-entrant stub. The method successfully measured thermomechanical motion at room temperature, and found a vacuum optomechanical coupling of $g_0 \approx 100 \mu\text{Hz}$ for a 72 kHz mode.

4.4.5 Cavity Phase Effect on Modulated Sideband

As derived in Section 4.1.3, $S_{21}(\omega)$ the transmission parameter, or the ratio of microwave voltage in to microwave voltage out of the cavity is:

$$S_{21}(\omega) = \frac{Q_L/Q_e}{1 + 2iQ_L\delta\omega}. \quad (4.111)$$

On resonance the phase shift is zero, and is then antisymmetric for frequencies either side of ω_0 . For a carrier signal through the cavity on resonance, the two modulated sidebands at $\pm\Omega_m$ will be modulated by $\mp\psi_m$ respectively. Assuming an incident wave of the standard phase modulated form, split into a carrier and two sidebands as in Equation 4.50, the signal out of the cavity will have the form:

$$V_t(t) = V_t \sin(\omega t) + \frac{1}{2} V_t s_{21}(\Omega_{pm}) \phi_m (\sin[(\omega + \Omega_m)t - \psi_m] - \sin[(\omega - \Omega_m)t + \psi_m]) . \quad (4.112)$$

With a symmetric transmission and on resonance carrier this is just $\Omega_m t \rightarrow \Omega_m t - \psi_m$, which back into the phase modulated form is:

$$V_t(t) = V_t \cos[\omega t + s_{21}(\Omega_{pm}) \phi_m \cos(\Omega_m t - \psi_m)] . \quad (4.113)$$

This only alters the lower cavity arm, resulting in an additional phase term within the modulation cos term. This results in an altered lock-in voltage magnitude of:

$$V_{\text{lock-in}}^{R'}(\Omega_m) = \frac{2}{\sqrt{2}} K_m |S_{21}(\omega_0 \pm \Omega_{pm})| \phi_m |\sin[(\psi_r - \psi_m)/2]| . \quad (4.114)$$

This alteration is only to the modulation, and will therefore not be factored into a calculation of time delay τ or additional phase shift θ . The extra phase ψ_m tends to increase the magnitude of the sin term, as ψ_r tends to be negative with a longer cavity arm. If the carrier signal is not centred exactly at the cavity resonance but is close, then it is still possible to approximate the phase shift to $\pm\psi_m$, but with an additional $+\delta\psi_m$ for both side-bands and the central frequency. This will give an altered signal of:

$$V_t(t) = V_t \sin(\omega t + \delta\psi_m) + \frac{1}{2} V_t s_{21}(\Omega_{pm}) \phi_m (\sin[(\omega + \Omega_m)t - \psi_m + \delta\psi_m] - \sin[(\omega - \Omega_m)t + \psi_m + \delta\psi_m]) . \quad (4.115)$$

This time the additional factor is effectively $\omega t \rightarrow \omega t + \delta\psi_m$. This will lead to an addi-

tional factor in the quadrature term of the resulting mixed wave, giving a $\cos(\phi_r + \delta\psi_m)$ term instead of the $\cos(\phi_r)$ term in Equation 4.88. This does not actually affect the end result, as by experimentally minimising the dc component this entire term becomes $(2n + 1)\pi/2$. Generally all of these additional phase effects should be minimal, as the time delay will be the greatest element in the relative phase.

4.4.6 Determination of Delay

The transfer function K_m must be determined in absolute terms to give full access to the vacuum optomechanical coupling strength of the system, otherwise it will be obscured behind the various experimental factors of the microwave circuit. This can be achieved or at least estimated with many different methods.

One method that does not require a calibration signal, is calculating K_m by varying τ_5 using the phase shifter, by mapping the change in length of the phase shifter to its phase shift at ω_0 , then varying the phase by a known amount, while recording the DC voltage on the scope. The DC response could then be fitted to $K_m \cos(\phi_r)$, the DC quadrature term, giving direct access to K_m . However, any variation to components, including phase and resonance drift due to temperature can affect this measurement.

The method used in this work is to send a weakly phase modulated microwave signal which causes another peak in $S_{VV}(\Omega)$ to calibrate against. This calibration signal should be offset from the mechanical signal such that it does not disturb the measurement, either by directly obscuring the mechanical signal in frequency space, or by causing additional driving to the mechanics. The advantage of this method is that it provides a calibration signal for each individual measurement within the measurement window, making it resilient to transfer function drift. A transmission measurement of the microwave cavity, plus the noise power spectral density, is enough to then calculate all factors in determining g_0 , other than ψ_r which must be determined separately.

For most measurement circuits $\psi_r \approx \tau_r \Omega_m$, where it is dominated by the time difference to travel the upper arm vs the lower arm. Ignoring θ for this case, the total length of each arm can be measured, then calculation of the difference in length divided by the speed of light in the cable dielectric will give an approximate answer for τ_r . The

assumption that $\omega_0\tau_r = (2n + 1)\pi/2$ then allows rounding of the rough τ_r to the closest quadrature value.

A more precise method is to use the VNA to measure each arm, looking at the gradient of the phase to determine $\omega\tau$, then finding the relative delay between arms. This method is simplified by using extended phase to measure a whole arm at once, θ can then be extracted from an offset at $\omega \approx 0$, or more rigorously by measuring each component expected to give a constant offset near ω_0 . Note here that $\hat{\theta}_1 \neq \theta_1$, so while θ can be determined in this way $\hat{\theta}_1$ cannot. However, all phase shifts are expected to be frequency independent in $\pm\Omega_m$ around ω_0 , then any constant phase shift to a modulated sideband can be absorbed into the carrier phase by $\omega t \rightarrow \omega t + \theta$, leaving $\psi_r = \Omega_m\tau$. This method is dependent on the circuit components, but not any other parameters. It is also possible for this method to take the phase shift to the nearest $\phi_r = (2n + 1)\pi/2$, if the measurement is close to quadrature.

4.5 Summary

This chapter has developed the theoretical framework for microwave measurement of the chip-cavity system. With Section 4.1 giving the microwave transmission response near resonance, used experimentally to characterise the microwave system, treating the chip-cavity system as a capacitively coupled RLC circuit. This treatment has then been expanded to include the general response of a greater microwave circuit, and used to provide equations for photon number within the cavity at base temperature, dependent on power supplied or measured at room temperature. Section 4.2 then details the microwave circuit mounted on the dilution fridge, including estimations of photon noise delivered to the cavity and the maximum powers that can be safely applied. These first two sections of Chapter 4 deal exclusively with the microwave system, ignoring the optomechanical coupling as it's effect on the microwave characterisation is expected to be negligible.

Section 4.3 introduces the effects of the optomechanical coupling, treated as a time dependent variation on the cavity resonance. The measurement schemes used in this work are all phase sensitive, so the time varying resonant frequency (due to mechanical oscilla-

tions) is used to write the phase shift on a constant microwave signal at the unperturbed resonance $\Delta\phi_c(t)$ in terms of the generalised mechanical motion $\delta x(t)$. This relationship is then used for the direct measurement scheme, where the vacuum optomechanical coupling strength g_0 can be calculated from the relative size of the optomechanical sideband to the carrier signal strength. A simple measurement scheme where a constant signal from a microwave source, at the unperturbed cavity resonance, can be transmitted through the cavity and then measured on a spectrum analyser. Though direct measurement was attempted for the chip-cavity system, the optomechanical coupling was too weak for direct detection.

Section 4.4 outlines the theory for a homodyne detection technique, which provides greater sensitivity than direct detection, and is the primary method used to measure optomechanical systems in this work. This section begins with the general circuit response of homodyne detection, using a microwave interferometer circuit to detect small phase noise signals on a carrier wave. The theory is then developed to create a methodology for a calibrated phase sensitive detection measurement, using a phase modulated signal from the microwave source, which is capable of directly determining g_0 from a single measurement.

Chapter 5:

Experimental Results

This chapter covers the experimental results, split into fridge runs. The completed nanofluidic chips described at the end of Section 3.3 were fitted into the aluminium microwave cavity and copper cell designed in Section 3.2. The chip-cavity system was then successfully cooled to base temperature, around 23 mK, and filled with Superfluid ^4He . Using the microwave transmission derived in Section 4.1, the microwave properties of the system were characterised. Run 2 measured the highest microwave quality factor of 81,900, while Run 3 found increasing quality factor with higher cavity photon number (a possible indication of two-level systems), and a pressure dependence of the quality factor when the cell was filled with ^4He . The microwave transmission was also used to identify and eliminate sources of noise from the measurement, specifically a sensitivity to magnetic fields.

Run 1 and Run 3 used the homodyne detection scheme developed in Section 4.4 to measure a mechanical signal close to the expected defect mode frequency of 1.34 MHz, though the signal was too weak for a full characterisation and measurement of g_0 . Run 1 suffered from the magnetic field dependent noise, while Run 3 found lower microwave quality factors and a reduced max input power before observing nonlinearities. A run without these constraints should be able to measure with sufficient signal to noise to determine g_0 , and by increasing the external microwave coupling (decreasing Q_e) it will be possible to increase signal strength by 30 dB.

5.1 Overview

This chapter will cover experimental results from the fridge ‘runs’, where each run denotes a distinct change to the experiment, involving warming to room temperature,

opening the IVC, and modifying the experiment in some way. The runs are presented in chronological order, with modifications discussed in light of the previous run. All runs involve the ‘best’ nanofluidic chips from Section 3.3.5, inserted into the cavity designed in Section 3.2, with the fridge circuit of Section 4.2.

Run 1 used the chip Si3(5), successfully reached base temperature, but suffered from significant microwave noise and instability in the chip-cavity resonant frequencies. This instability was present for all temperatures, microwave signal powers and resonant peaks, and was insensitive to the presence of helium. The instability was only visible near the microwave resonances and not for transmission far from the peaks. It was eventually discovered that this instability was highly sensitive to magnetic fields outside of the fridge, even to those outside the lab. The decision was made to warm up and inspect the cell.

Once warm it was discovered that the aluminium cavity was not sufficiently sealed to the volume of the greater copper cell, leading to some coupling between the field inside the aluminium and the volume between the aluminium and copper, which caused a much higher background and magnetic flux penetrating into the superconducting microwave cavity. Run 2 then sought to better seal and then shield the superconducting cavity. The nanofluidic chip was also swapped to chip Si2(5), in case the old chip was contributing to the problems. The shielding for this run involved wrapping the still plate radiation shield with lead foil; which, along with a better sealed aluminium cavity, eliminated the sensitivity to external magnetic field, and greatly reduced signal noise. However the lead foil was not sufficiently tight to the radiation shield, causing a significant heat leak between the IVC at 4 K and the still plate, which limited base temperature to ~ 500 mK for continuous running. This is too high to take the ^4He sufficiently far into the superfluid regime, and so the fridge was warmed back to room temperature.

Run 3 kept the chip Si2(5), replaced the piezo with one for higher frequency, removed the lead foil from the shield and instead wrapped the cell directly. Extra care was also taken ensure the aluminium cell was well closed, given the hermetic feedthrough in the copper cell lid needed resoldering from thermal cycling. Other than these changes Run 3 was essentially a repeat of Run 2. This run was the most promising, as base temperature

was achieved with little to no peak instability and noise. However a deterioration of the first mode's Q_L , from Run 2's Q_L of 81,900 at 189 mK, to 14,600 at 23 mK for this run, significantly decreased the power transmitted through the fridge; which, coupled with the resonant peaks becoming nonlinear at lower photon numbers, made measurement with sufficient sensitivity difficult. An interesting peak splitting effect was discovered depending on helium pressure, along with an increasing Q_L with photon number, possibly indicating two-level systems. Unfortunately time constraints required abandoning this run.

There is currently, at the time of writing, a Run 4 underway. This time using the quartz chip Q4(A2), which may have a better quality of evaporated aluminium, and should eliminate some variables associated with fabrication. Also planned is a fabrication of a new aluminium cavity, altering the intended Q_e closer to the Q_L 's measured in the experimental runs, which should increase transmitted signal strength. This and other continuations of the project are outlined in Section 5.6.1.

5.1.1 Expected Transmission Strength

It is useful here to estimate the signal strength of the mechanical sidebands, in relation to the signal strength of a carrier signal. This can be used to directly assess whether a signal analyser measurement is sensitive enough to detect the optomechanical coupling, or indirectly to assess the same thing for a homodyne measurement. Rearranging Eq. 4.71, for direct measurement of g_0 from peak heights, in terms of the ratio of sideband peak to carrier peak, and using $\bar{n}_m \approx k_B T / \hbar \Omega_m$, gives:

$$\frac{S_{VV}(\omega_0 \pm \Omega_m)}{S_{VV}(\omega_0)} = \frac{16k_B g_0^2}{\hbar \Omega_m^2} \frac{Q_m Q_L^2 T}{\omega_0^2}, \quad (5.1)$$

for a measurement with 1 Hz measurement bandwidth. Using the estimated $g_0/2\pi$ of 6.3×10^{-4} Hz from Section 1.4.3, which is for the fundamental acoustic and microwave modes of: $\Omega_m/2\pi = 1.34$ MHz and $\omega_0/2\pi = 4.21$ GHz, then choosing a measured $Q_L = 2 \times 10^4$, gives a relative peak amplitude of:

$$\frac{S_{VV}(\omega_0 \pm \Omega_m)}{S_{VV}(\omega_0)} = P_{\text{ratio}} = 4.12 \times 10^{-16} \cdot Q_m T, \quad (5.2)$$

where the fraction of powers is shortened to P_{ratio} . For a base temperature of 25 mK it may be possible to achieve a mechanical quality factor of 10^8 , giving an upper estimate for P_{ratio} of 1.03×10^{-9} which is equivalent to ~ -90 dB. A more conservative estimate would be a mechanical quality factor of 10^6 at 100 mK, giving a P_{ratio} of 4.122×10^{-11} or a difference of ~ -105 dB. The spectrum analyser (*R&S-FSW-43*) in the lab measures a noise floor of ~ -125 dBm, for a 1 Hz measurement bandwidth and a large number of averages, meaning a carrier signal of at least -35 dBm would be required to see the optomechanical sideband, or carrier greater than -20 dBm for the more conservative estimate.

This highlights the major problem with the direct detection scheme, and current experimental cell, where resonant peaks tend to measure less than -40 dB on S_{21} transmission measurements through the fridge circuit, which would require signal into the fridge of over +5 dBm and +20 dBm for the two cases, powers that are into the nonlinear peak regime. For a given chip-cavity system and temperature, the nonlinearity is expected to depend on photon number in the cavity. Looking at Eq. 4.45, $P_{\text{out}} \propto \bar{n}_{\text{cav}}/Q_e$. So increasing the microwave coupling strength to give Q_e closer to 10^5 , from 10^7 , would give a 20 dB increase to the signal out while maintaining the same photon number and similar Q_L . Homodyne detection expected signal is outlined in Run 1, and then calculated for the specific parameters of each run.

5.2 Run 1

Run 1 was the first run of the dilution fridge to base temperature with a nanofluidic chip, using the superconducting aluminium cavity, and superfluid leak tight copper cell, corresponding to the technical drawings in Appendix A. Along with the nanofluidic chip Si3(5), as described in Section 3.3.5, mounted inside the aluminium cavity. Figure 5.1 shows a labelled image of this cell fitted to the experimental stage of the dilution fridge.

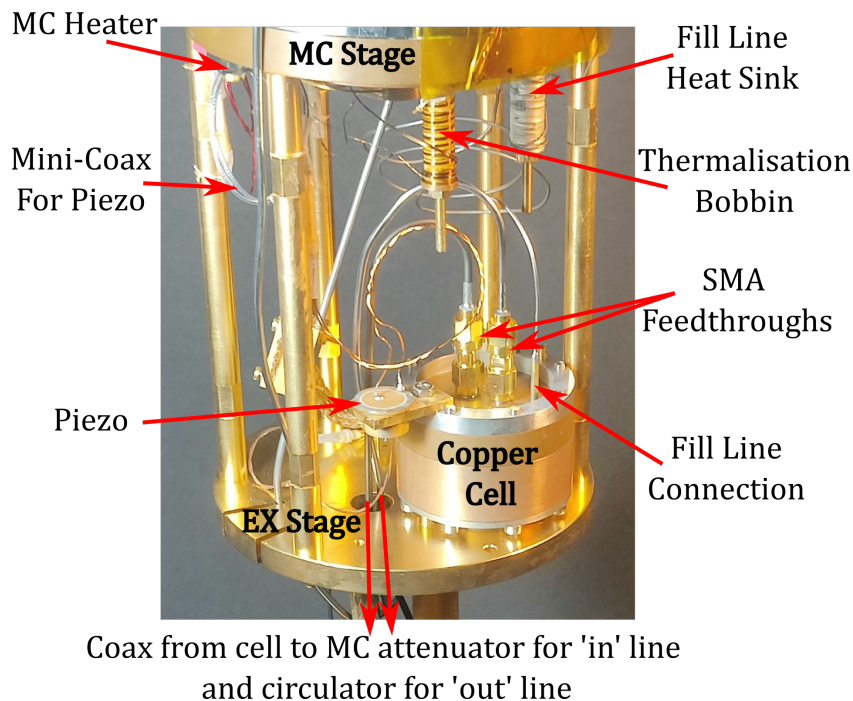


Figure 5.1: Photo of the experimental cell attached to the experimental stage of the dilution fridge. The different components mounted at this level are labelled. The in microwave line passes the MC, through a slot on the EX stage, to the 3 dB attenuator thermalised at base temperature, then back up through the hole in the EX stage to the cavity SMA feedthrough. The out line then exits the cavity, passes through the EX hole, to the circulator, back up through the EX stage slot, and through the centre of the MC all the way to the HEMT amplifier at 4K. The MC thermometer and heater leads are thermalised at the bobbin shown, the thermometer cannot be seen in this photo but is attached similarly to the MC heater. The mini-coax for the piezo is thermalised at another bobbin which is also not in view.

The fridge successfully reached an initial base temperature of 28 mK, with the cell under vacuum. Filling the cell with helium to 168 mbar in the fill line increased the MC temperature to 34 mK, which was reduced to 22 mK by reducing the fill line pressure towards SVP, indicating some heat leak to MC through the helium within the fill line at higher pressure. Below about 750 mK on the MC thermometer three sharp microwave resonances were found at 4.21 GHz, 7.35 GHz and 10.18 GHz, within 10% of those predicted when designing the cavity in Section 3.2.1. Figure 5.2 shows a transmission measurement of the fundamental 4.2 GHz resonance at base temperature, with and without ^4He in the cell.

The total loaded quality factor for the first resonance tended to be around 20,000 near base temperature, lower than anticipated, and into a regime where the total quality factor is dominated by internal losses. Though this is assuming Q_e is around 10^7 as de-

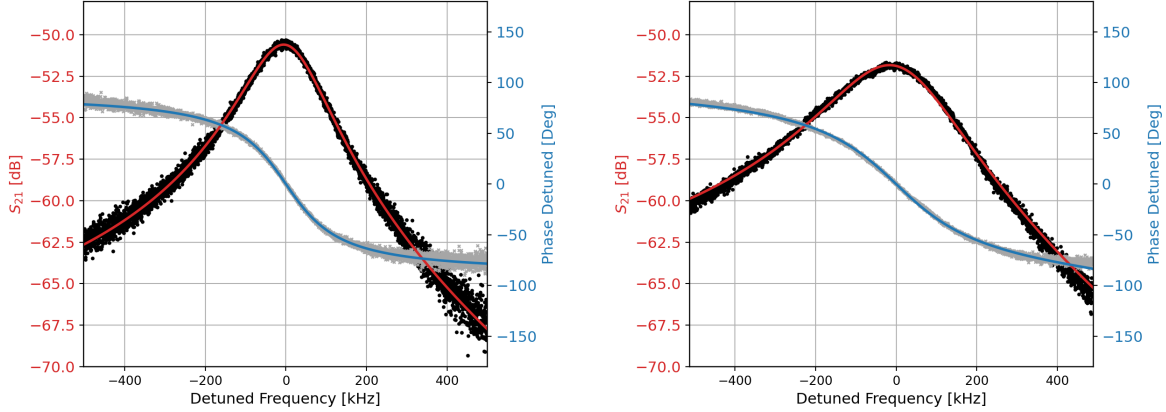


Figure 5.2: Left: S_{21} logmag and phase detuned around the 4.24 GHz fundamental microwave mode, at 30 mK under vacuum. Black and grey dots are logmag and phase of the data respectively. The red and blue lines are then logmag and phase respectively, for a complex transmission fit of the data. This fit gives $Q_L = 2.14 \times 10^4$. Right: S_{21} logmag and phase detuned around the 4.21 GHz fundamental microwave mode, at 34 mK and filled with ^4He pressurised to ~ 250 mbar. Data and fit represented as in the LHS figure. The fit here gives $Q_L = 1.32 \times 10^4$. The data for the filled cell corresponds to a higher number of averages and lower IF bandwidth, leading to lower noise.

signed, which is discussed in more detail in Run 3. These values of Q_L seem characteristic for the system, indicating some chip related loss is dominant.

5.2.1 Instability and Noise

The graphs in Figure 5.2 also show the first signs of the major noise / instability problem, which over many averages becomes a slight broadening of the peak. When moving from VNA transmission to spectrum analyser measurements, it was noticed that the carrier signal strength would jump around in real time. This noise, in the transmitted signal strength of a tone at constant frequency and source power, was qualitatively much larger than expected from electrical noise in the circuit. Once observed, cavity transmission against time was tracked, with a constant frequency and power probe signal.

Figure 5.3 shows the result of one of these measurements, over a series of weekdays while a homodyne measurement occurred. This level of noise is extreme, over 15 dB of change in some cases. The data presented is for a reasonable ‘worst case’, during the week in the lab, with people entering and exiting the screen room housing the fridge. However with the screen closed, noise is limited to less than 10 dB of change, and in the best case of nobody in the lab over the weekend, it was occasionally possible to

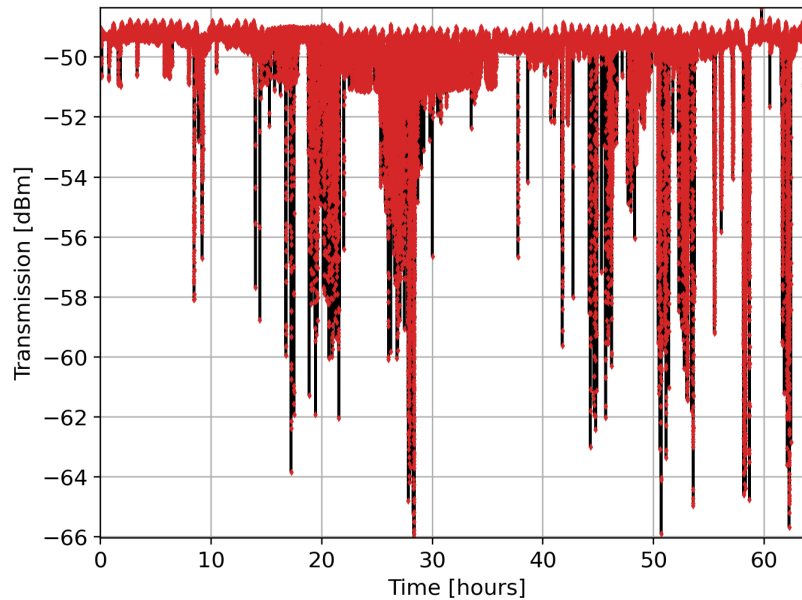


Figure 5.3: Power transmission through the cavity vs time, with a probe signal at 4.21 GHz and a power of 25 dBm, showing a severe level of noise not expected for the system. Red diamonds indicate data points, which have been connected with black lines to show the severity of the noise. The time between data points was approximately one second. The transmission is low as the measurement is taken from the cavity arm via a -20 dB directional coupler during a homodyne measurement.

get less than 5 dB for extended periods. Figure 5.3 also shows small periods of very low noise amplitude, which are around 1 dB and have some frequency components, that the transmission appears to return to after a spike. In fact it seems as though some ‘event’ causes a spike in the noise, which may put the transmission into a noisy regime for a period, before eventually returning to a low noise regime. Observing fast VNA measurements of the 4.21 GHz resonance peak, the peak would flutter back and forth in frequency over a range of roughly the linewidth, accounting for the noise with some apparent frequency component. Then seemingly randomly the peak would disappear for a short period of at most a few seconds, before reappearing within the same region as before, accounting for the large dips in transmission.

To analyse the frequency dependence of the noise, the microwave source was set to constant power at the cavity resonance, and the spectrum analyser was used to take a time domain measurement at the same frequency, similar to the measurement in Figure 5.3 but with a much faster sampling rate. This data was then fast fourier transformed (FFT), giving the frequency components of the noise. Figure 5.4 shows the FFT of one

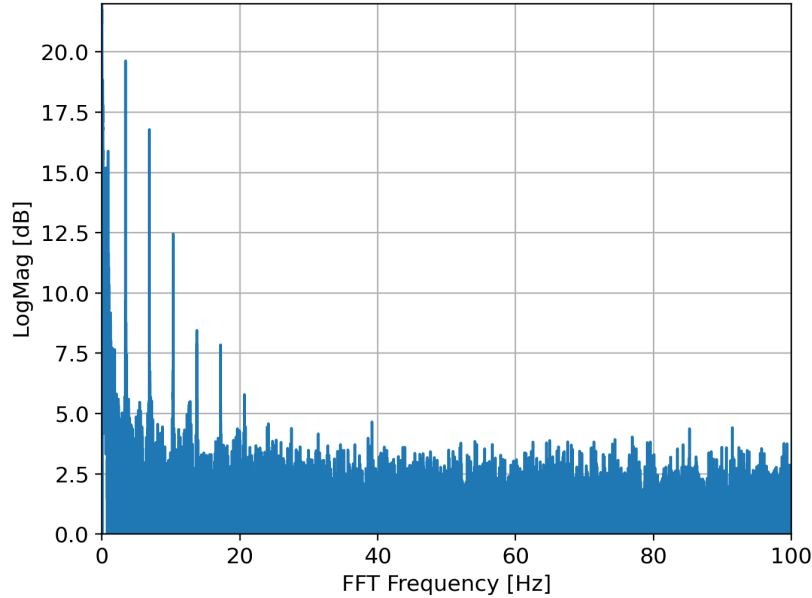


Figure 5.4: FFT spectrum of a time domain spectrum analyser measurement at the carrier frequency, which is set to the cavity resonance. The amplitude has been normalised to the average value of the spectrum, ignoring the large unperturbed signal near 0 Hz, and then converted into dB.

such measurement, with a sampling rate of 200 s^{-1} , and so a maximum frequency of 100 Hz [216]. There is a clear frequency component at 3.4 Hz, with harmonics of increasing frequency. It is unclear what causes this noise, and there is no component at 50 Hz which could indicate an issue in isolation from mains noise.

Initially vibrational isolation as considered as a possible noise source, as moving around close to the fridge would cause spikes in noise. However it was soon realised that the spikes correlated most strongly with movement of metal objects within the screen room, and with aid of a magnet it was confirmed that the noise was originating from a sensitivity to magnetic fields. The most probable cause of this is vortices becoming trapped in one of the superconducting materials when passing through T_c . Then if the superconducting cavity is not sufficiently closed to outside magnetic flux, it could produce a resonance which is very sensitive to small changes in magnetic field.

To attempt to rule out flux frozen into the aluminium, from the presence of say a pump electromagnet, the fridge was warmed to 1.5 K and then cooled back to base temperature, in a more magnetically clean environment (closing the screen room and removing additional pumps). This seemingly had no effect on the noise, and so the

process was repeated up to 5 K and then 15 K, to rule out indium and NbTi respectively. With no effect after these two warming and cooling cycles, it is likely the thin aluminium on the chip in combination with a poorly sealed aluminium cavity is the cause of the noise. The vortices being on the chip near areas of the highest magnetic and electric field would also explain the extreme sensitivity.

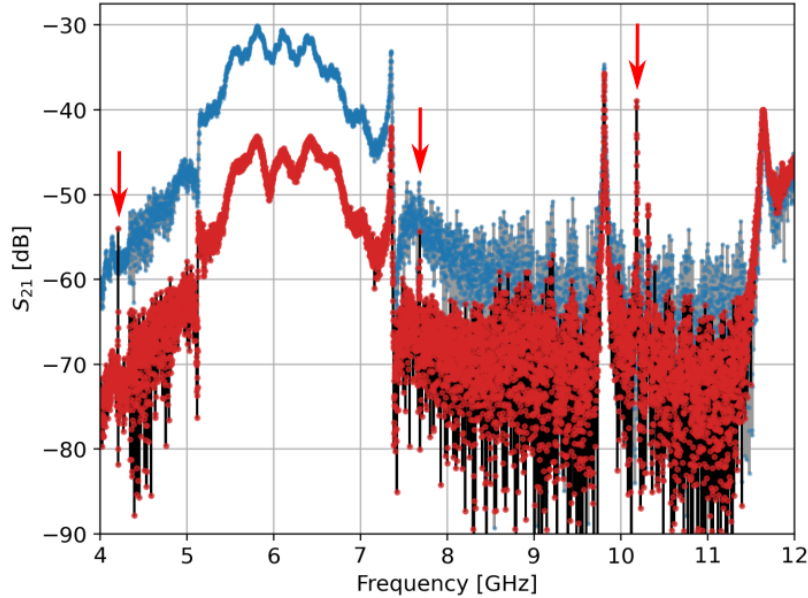


Figure 5.5: S_{21} transmission spectrum on the 4 - 12 GHz operational range of the microwave circuit. Blue data points connected by grey lines are for 1.4 K, while red data points connected by black lines are for 37 mK. At least three superconducting chip-cavity modes, highlighted with red arrows, can be seen at 37 mK, at 4.2 GHz, 7.4 GHz and 10.2 GHz. Distinct due to their delta function like appearance on this large frequency range.

Figure 5.5 shows the transmission spectrum over the entire operating range of the microwave circuit, above and below the superconducting transition of the aluminium. This shows the significant background structure not expected for the chip-cavity system, and which was still present above all T_c 's. The structure is likely due to the copper cell volume, which the aluminium cavity is not sufficiently isolated from, allowing the copper cavity to mediate coupling between magnetic fields within the lab and the chip-cavity resonant modes. This is corroborated by the instability and noise being present only near chip-cavity resonances, but for all temperatures, with and without the presence of ^4He , and for all incident microwave powers.

5.2.2 Homodyne

Considering the homodyne measurement circuit in Figure 4.5 of Section 4.4.1, and the expected homodyne circuit response from Section 4.4.2, for a carrier signal at the unperturbed cavity resonance. A directional coupler is added at position 3, just before the RF port of the microwave mixer, with a spectrum analyser on the couplers -20 dB arm. This allows reading of the power into the RF port, from which the power in the mechanical sideband can be estimated using the the calculations in Section 5.1.1. Therefore with a source power of 21 dBm, a carrier signal of -30 dBm is measured at the RF port of the mixer, which for the strongest coupling case corresponds to a -120 dBm mechanical sideband peak. Including the mixer’s conversion loss, and the max gain from the low frequency amplifier, gives an expected sideband signal strength into the lock-in of -87 dBm. For the lock-in input with 1 M Ω this corresponds to a measured voltage of 3.99 mV. For the more conservative case of lower mechanical quality factor, this would be reduced to around 0.7 mV.

Though these signal strengths are significantly above the sensitivity of the lock-in, they are difficult to resolve over the background noise of the homodyne measurement. The mechanical linewidth is also expected to be very small, which searching with a wider measurement bandwidth may miss in the noise. Driving with the piezo would hopefully increase \bar{n}_m and so increase the effective coupling strength, provided energy can be transmitted through the cavity and chip into the defect region. This method is also hampered by the low mechanical linewidth as the piezo may need to be very close to the mechanical resonance (within a Hz or less) to have a significant effect. For these reason the mechanical resonance was searched for using the piezo drive with the cavity at higher temperatures, broadening the linewidth while hopefully increasing the coupling strength.

The mechanical signal was primarily searched for via homodyne detection, where the detection frequency and piezo drive frequency are swept simultaneously. Different combinations of temperature, piezo drive, and lock-in measurement settings, were trialled. Figure 5.6 shows one of the ‘best’ measurements, clearly indicating some signal

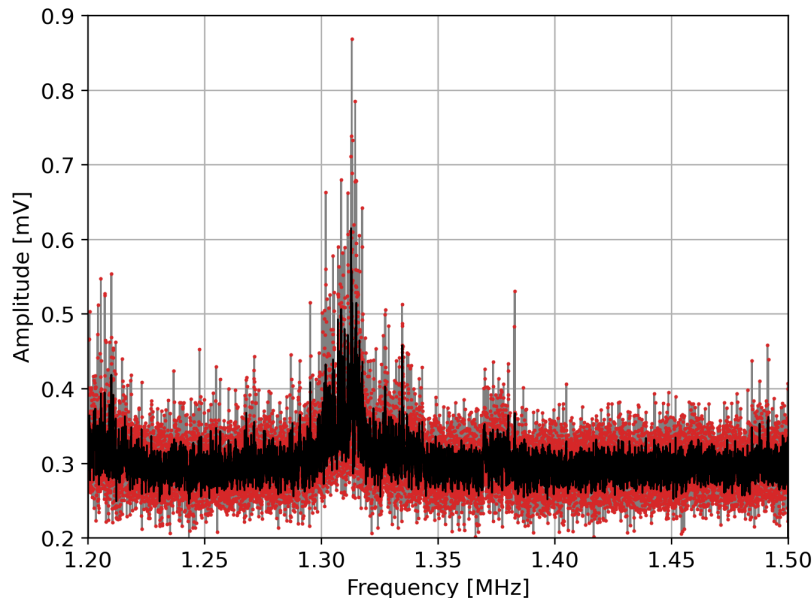


Figure 5.6: ‘Best’ homodyne measurement of mechanical signal, signal amplitude vs lock-in and piezo frequency. Red dots indicate data points, linked by grey lines, black lines are the 5 point moving averages of the data points. Measurements were taken at 200 mK, with a piezo drive of 400 mV, and a lock-in bandwidth of 3 Hz, over a 300 kHz frequency window with 20,000 points. Shown data points are the average of 30 sweeps.

around 1.32 MHz, close to the COMSOL predicted frequency. This measurement’s data points were 15 Hz apart, and at 200 mK the expected three-phonon limited linewidth is expected to be ~ 21 Hz. So this feature has much greater width than expected, although 400 mV piezo drive is large and a significant broadening of the peak would be expected. Measurements with sufficient sensitivity, piezo drive, and averaging found similar spectrum. The piezo drive dependence indicating the feature was in fact a mechanical signal, though too high of a drive increased the measurement noise.

It is difficult to extract a coupling strength from these graphs as the peak structure is not clear, and it is especially challenging to extract g_0 , as the transmission from the piezo to the defect is not known. Adding the phase modulated calibration signal would increase the noise floor and so was avoided when searching for the mechanics. The homodyne results were not reproducible enough to measure the effects of varying temperature or piezo drive on the feature, primarily because the measurement times are too long for the measurement stability (Figure 5.6 representing a four day measurement time), and because the feature does not show up on ever sweep.

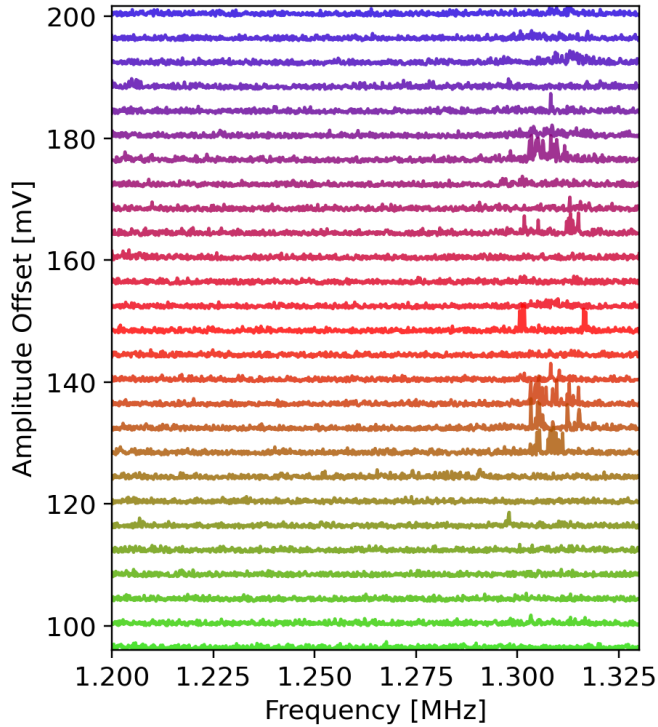


Figure 5.7: Individual homodyne measurements, amplitude offset by a constant factor for each sweep vs lock-in and piezo frequency, taken at 500 mK, with 1 V piezo drive, and 800 points per sweep. Sweeps are plotted from top to bottom in chronological order, successive sweeps start as the previous sweep finishes.

Figure 5.7 shows a set of individual homodyne frequency sweeps, where some sweeps show increased amplitude in the region of interest and others do not. The cause of the feature not always being measured could be related to the microwave instability from magnetic sensitivity, as sudden drops in transmission did correlate to drops in lock-in signal. There may also be fluctuations in the superfluid ^4He pressure, which would cause the mechanical resonance frequency to shift significantly, and so an individual sweep may miss this moving resonance. Temperature instability should not cause the resonance to move, as speed of first sound is not sensitive to temperature far below 1 K [119], though local heating from cavity mode dissipation may drive some second sound. Homodyne measurement with the lock-in zoom FFT spectrum was also attempted, using a constant piezo drive or a function generator to supply white noise, which could also be bandpass filtered to only supply noise in the frequency region of interest. These measurements did not produce clear mechanical signals.

Given the variability of measured signal it was difficult to optimise the set of measurement parameters, and unclear whether any single frequency sweep could be trusted. With the sensitivity of this run it may have been possible to measure a clean signal with a very long integration time. However, due to the difficulty optimising parameters for such a measurement, time constraints due to nanofab delays, and the realisation the aluminium cell was insufficiently sealed; it was decided to warm the fridge back to room temperature, primarily to investigate sealing the aluminium cell, but also allowing the nanofluidic chip to be swapped out, to rule out some fabrication defect.

5.3 Run 2

5.3.1 Room Temperature Investigations

Before the second nanofluidic chip run of the dilution fridge, the experimental cell was investigated at room temperature for the source of the magnetic instability. Aluminium expels magnetic flux as it transitions to a superconductor, so physical gaps in the cavity are the only way for magnetic fields from outside to enter. The possible gaps are: the microwave ports, the slot in the lid for securing the chip, the small slot for helium to fill, and the seam between the two aluminium pieces.

Removing the nanofluidic chip the empty aluminium cavity resonance can be measured at room temperature, not possible for the chip-cavity mode. A measurement of the aluminium cavity tightened to the copper lid, but the copper base not attached, would yield a transmission spectrum with no peaks before the first aluminium cavity mode around 13.5 GHz. However, also attaching the copper base would raise the background noise and introduce spurious peaks, indicating some coupling between the aluminium cavity and copper cell volumes. Further tightening the aluminium cell would then reduce this background noise, and magnitude of additional peaks, which is shown in Figure 5.8. Upon further inspection it was found that the aluminium lid and base did not quite fit together flush, a danger of external fabrication from non-specialists.

While the fridge was at room temperature, the opportunity was taken to measure

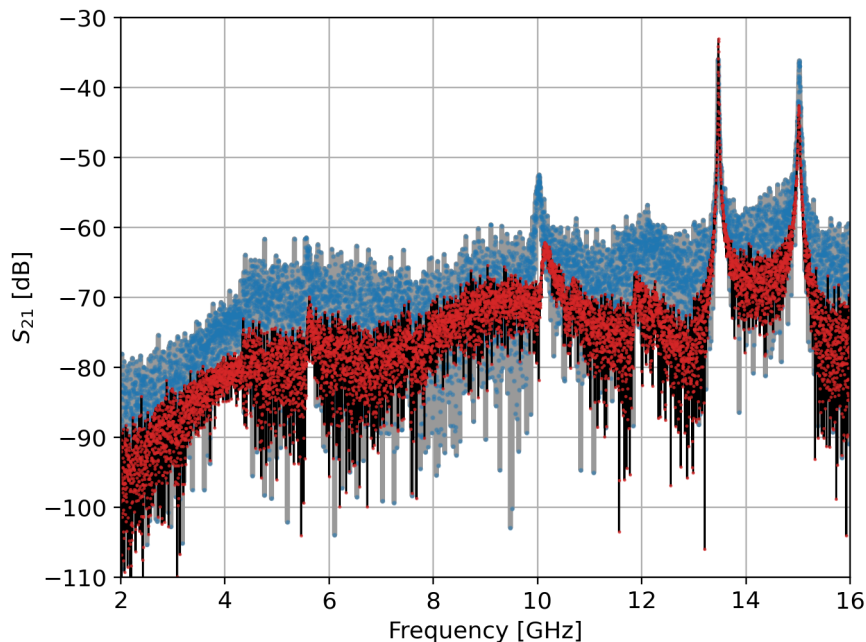


Figure 5.8: Transmission spectrum through the empty aluminium cavity, with the VNA directly connected to the copper cell lid. Blue data points linked by grey lines are from a measurement of the aluminium cavity, with the copper cell closed. Then red data points linked with black lines are from the same measurement but with the aluminium cells additionally tightened to the copper lid.

phase noise associated with carrier signals passing through different sections of the fridge circuit, potentially significant as the expected optomechanical signal strengths are so close to the noise floor of associated measurements. Figure 5.9 shows relevant phase noise measurements. The amplified ‘out’ line with only the HEMT amplifier gives noise equivalent to that of the source above 30 Hz. For the attenuated ‘in’ line thermal noise is dominant over source noise at around 100 Hz, due to the attenuation bringing the carrier signal strength close to that of RT thermal noise. Of most significance here is that a through measurement returns a noise floor around -100 dBc/Hz around 1 MHz, for two and three amplifiers, indicating the signal gain is equal to the noise gain, maintaining signal to noise through the amplifiers. Similar to a measurement of just the ‘in’ line, the source noise is seen up to around 30 Hz, then thermal noise becomes dominant. For a 1 Hz bandwidth measurement, the through noise of -100 dBc/Hz at 1 MHz corresponds to a sensitivity to signals -100 dB compared to the carrier, which is sufficient for the best case coupling scenario from Section 5.1.1 of -90 dB for the mechanical sideband peaks, but insufficient for the more conservative estimate of -105

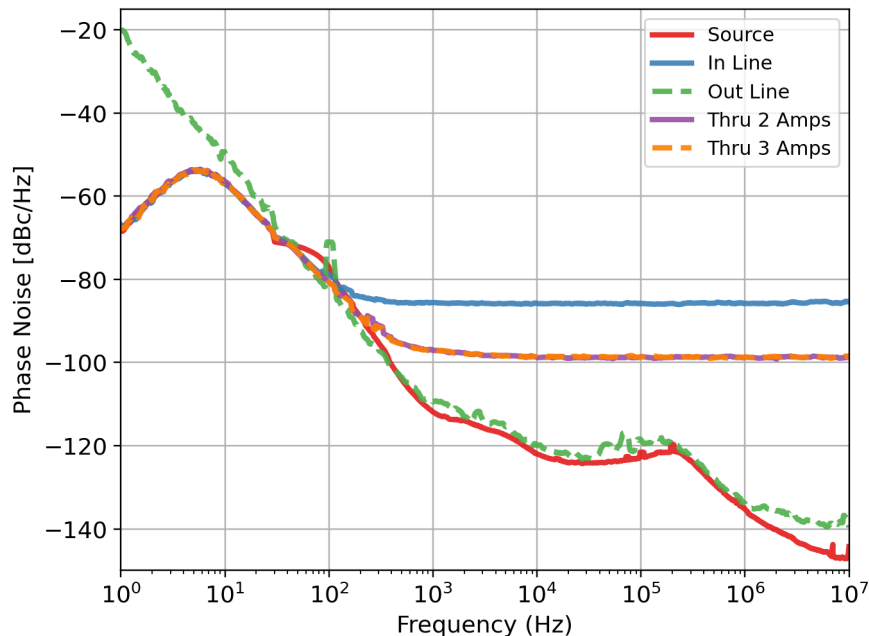


Figure 5.9: Room temperature phase noise measurements using the spectrum analyser, on a 4.21 GHz carrier signal, as transmitted through different sections of the microwave circuit. Red line represents the signal generator directly connected. Blue line represents transmission through the attenuated in line of the microwave circuit. Green dashed line transmission through the HEMT amplified out line. Purple line transmission through the entire fridge circuit, with in line directly connected to out line at the EX stage, and amplified by the HEMT and low noise amplifiers. Orange dashed line is an identical measurement but with the Mini-Circuits amplifier added.

dB. For a low temperature measurement this noise floor should be improved as the NbTi coax become superconducting and the HEMT amplifier amplifies the signal at 4 K, where the thermal noise is roughly 20 dB lower than at room temperature. However, if the cavity transmission is too low the mechanical sideband amplitude may still be below thermal noise at 4K, or the sideband signal may be reduced below the -125 dBm minimum noise of the spectrum analyser, either of which may have been the regime of Run 1.

5.3.2 Cooling

For Run 2, the experimental cell was altered by: swapping the nanofluidic chip to Si2(5), polishing the aluminium cavity to reduce microwave losses, further tightening the aluminium cavity, covering the aluminium lid window with indium foil, and wrapping the outer aluminium cavity seam with indium foil. The last three alterations were made

to help improve the cavity's isolation from external magnetic fields. To further shield the cavity, lead foil was wrapped around the thermal radiation shield attached to the still plate, which encloses the lower temperature stages.

Initial stages of cooling were successful, however upon starting circulation the fridge failed to reach base temperature, instead reaching a minimum temperature of 500 mK. This likely due to the lead foil making contact with the IVC at 4K, so creating a significant heat leak between 4K and the still. 500 mK is too high a temperature regime for the ^4He to be considered sufficiently superfluid, for detection of the optomechanical coupling, so the decision was made to warm up.

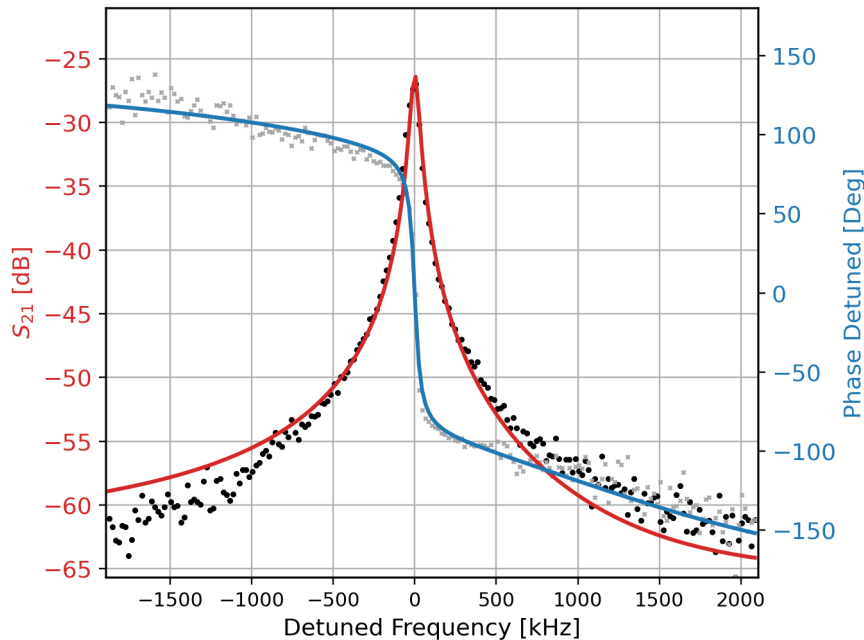


Figure 5.10: S_{21} VNA transmission measurement at 189 mK, during single shot operation of the fridge. Black dots are magnitude data, with red line its fit. Then grey dots represent phase, and blue line their fit. The data represents an average of six sweeps. The peak frequency detuned around was 4.20 GHz.

As part of the warming up procedure the fridge was put into a ‘single-shot’ configuration, where the condensation arm of the ^3He circuit is closed. This reduces the heat load on the lower stages of the fridge, and allows lower temperatures than in the continuous running configuration. Furthermore, as the fridge reached a minimum temperature the continuous fill of the 1K pot was closed, further reducing the temperature. Using this method a minimum temperature a little below 200 mK was achieved, while

the cavity transmission spectrum was continuously measured.

Figure 5.10 represents one of these transmission measurements with maximum Q_L , recorded at a MC temperature of 189 mK. The resonant frequency for this measurement was 4.20 GHz, and the external quality factor Q_L extracted from the fit was 81,900, which should be approximately the internal quality factor Q_0 . The significant increase of microwave quality factor could be due to the polishing, more closed cavity environment, some aspect of the nanofluidic chip, or the contact between the chip and cavity. A four fold increase of the quality factor relates to a sixteen fold increase to the relative mechanical sideband signal, or a roughly 12 dB increase in signal strength, perhaps enough to directly measure the mechanics. The cavity resonance showed no signs of the magnetic instability, however it was difficult to assess the noise level as the cavity temperature was not stable.

5.4 Run 3

5.4.1 Cool and Fill

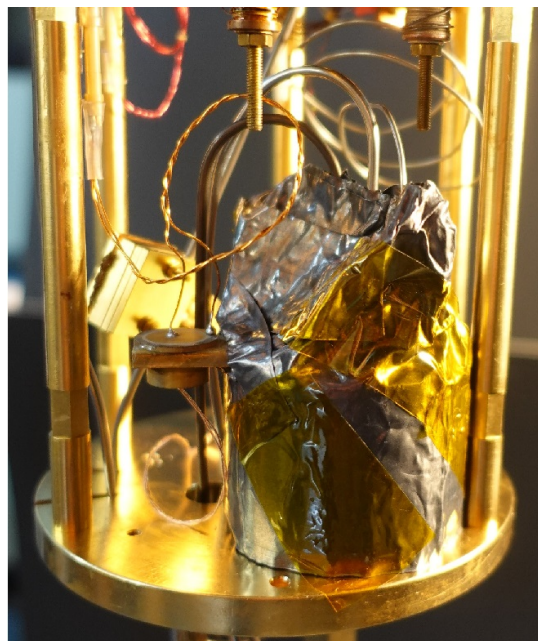


Figure 5.11: Photo of the experimental stage of the dilution fridge, showing the experimental cell wrapped in lead foil. The photo was taken before closing the IVC during Run 3.

Run 3 was essentially a repeat of Run 2 but with the lead foil removed from the radiation shield, and instead the cell directly wrapped, which can be seen in Figure 5.11. The Si2(5) chip was kept, and the aluminium cell was not opened, although the copper cell was opened to resolder the feedthroughs which had started leaking after thermal cycling.

After successfully cooling to a base temperature of 23 mK, and again detecting three chip-cavity modes, measurements were taken of the transmission of each peak at different probe powers, both at 23 mK and 300 mK. This data is used to check the microwave resonances for the instability characteristic of Run 1. Moving metal objects and magnets close to the fridge had no apparent effect on the transmission, and repeated measurements of the peaks showed no movement in frequency. Figure 5.12 shows a colour map of repeated transmission measurements across the first resonance, with no sudden losses of signal, and no significant movement of the resonance.

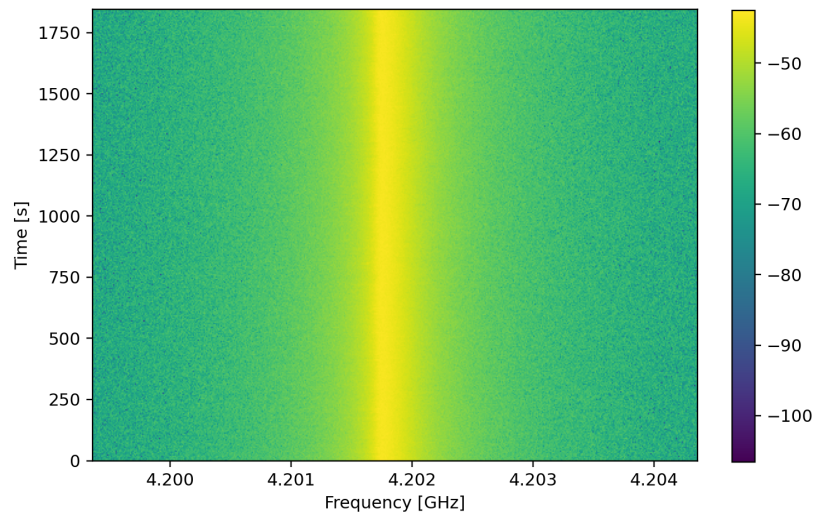


Figure 5.12: Colour plot of continuous single S_{21} measurements over the first cavity resonance, for Run 3 at 23 mK, with the cell under vacuum. Sweeps are taken from low to high frequency, with one the next sweep starting upon the previous sweep finishing. The sweep start time relative to the first sweep is plotted on the y axis, the colour scale refers to the values of S_{21} in dB.

Once it was established that the instability had been eliminated, the cell was again filled with ^4He . Applying ~ 20 mbar each time from the smallest volume of the GHS (digital gauge plus connected tubing). This enabled monitoring of the 4.2 GHz mode

frequency with filling, whereas during the first run the change occurred with the first volume applied. The 10 GHz mode changes slightly slower but still quickly, and the 7.7 GHz mode much slower, consistent with the simulated results of a thin helium film in Section 3.2.1. Table 5.1 shows a comparison of the simulated frequencies and those measured for this run. The 7.7 GHz mode may prove useful to assessing the filling of the cavity, as its frequency is more directly related to the overall level of ^4He inside.

Table 5.1: Comparison of simulated chip-cavity resonant frequencies with experimental values. All values for a ~ 250 nm electrode gap chip, with $60 \mu\text{m}$ electrode. Simulated values are from COMSOL simulations in Section 3.2.1. Experimental values are from the initial filling at base temperature, with ‘film’ values being taken after the initial sharp change in the first resonance.

Result From	Mode No.	$\omega_c^{\text{vac}}/2\pi$ GHz	$\omega_c^{\text{film}}/2\pi$ GHz	$\omega_c^{\text{full}}/2\pi$ GHz
Sim.	1	4.125	4.095	4.088
Exp.	1	4.202	4.163	4.152
Sim.	2	7.767	7.7674	7.717
Exp.	2	7.785	7.781	7.730
Sim.	3	11.412	11.407	11.311
Exp.	3	10.399	10.391	10.298

While filling the cell with ^4He it was noticed that the first resonant peak split into two separate resonances, split by ~ 20 MHz. The splitting occurred immediately upon the first volume of ^4He introduced to the cell, then as the filling was increase the higher frequency peak was suppressed, until the cell was near full and this upper peak returned. This behaviour can be seen in Figure 5.13, though it is difficult to draw direct conclusions as the cell did not reach equilibrium before each ^4He volume was introduced. Either addition of a needle valve to apply ^4He very slowly, or allowing sufficient time between shots for the system to equilibrate, would be required to study the relationship between peak splitting and ^4He level. The peak splitting behaviour was also observed with the 7.7 GHz peak, though one of the peaks quickly became dominant and the second remained suppressed. No splitting was observed for the 10 GHz peak. It is currently unclear what causes the splitting, COMSOL simulations breaking the various geometric

symmetries of the microwave system have not caused any of the modes to split.

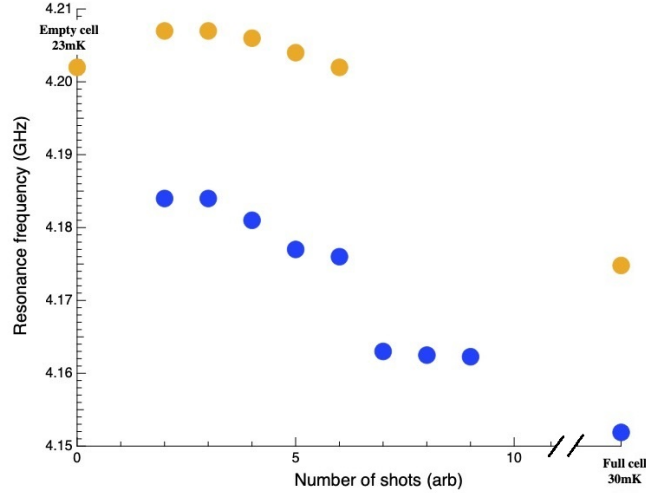


Figure 5.13: Plot of the chip-cavity’s first microwave mode resonant frequency, vs ^4He filling in arbitrary number of small volumes applied. The initial single peak of the mode splits with the presence of helium, the upper and lower split modes are shown by orange and blue dots respectively. Data was taken at the start of Run 3, moving from 23 mK in vacuum, to 34 mbar of pressure on the ^4He and at 30 mK.

5.4.2 Microwave Power Dependence

Once the cell was full with 34 mbar of pressure on the ^4He , and the temperature had been stabilised to 30 mK, a probe power transmission study was undertaken across all four peaks (including both 4.2 GHz). Figure 5.14 shows the resulting spectrum from this study, including fits to the complex S_{21} in Eq. 4.43. Qualitatively the transmission and quality factor for the first peak has dropped greatly from previous runs, especially the second. Comparing this 30 mK ^4He filled cell data with the 23 mK vacuum data, the 4.2 GHz peak’s quality factor Q_L drops and splits from $\sim 10,000$ to $\sim 3,000$ under the presence of helium. The story is similar with the 7.7 GHz mode, which drops from around 50,000 to 25,000; and not as severe for the 10 GHz mode which drops from 25,000 to 20,000. It is unclear the cause of this drop in Q_L , as it was not the case for Run 1, and the helium should not introduce significant dielectric loss, so it may therefore be related to the peak splitting. The quality factor has also dropped greatly since Run 2 with the same chip, so may be related to the galvanic contact’s deteriorating through

thermal cycling, or perhaps some impurity introduced to the chip when returning the chip to atmosphere.

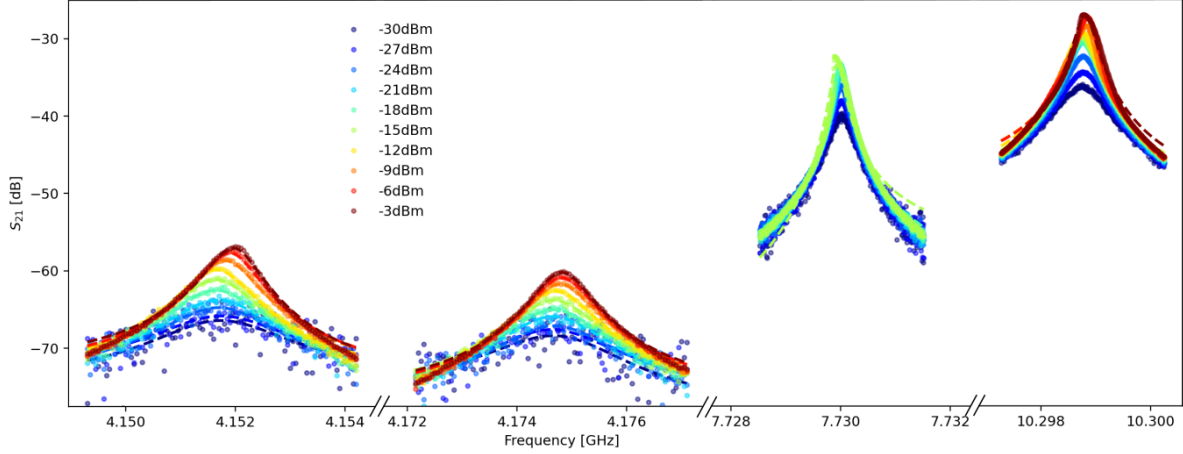


Figure 5.14: S_{21} transmission data over all four resonances for the chip-cavity system of Run 3, for a temperature of 30 mK and ^4He pressure 34 mbar. The same scale is kept on the x axis but the data cut down to only the resonances. Each resonance measured at a specific power, represented by a single colour of dot, is the average of 12 sweeps over the individual resonance. The averaged data is then fitted to S_{21} , and used to plot the dashed lines of same colour as associated data. The higher power sweeps where the resonance becomes highly nonlinear are not included (especially for the 7.7 GHz mode).

As mentioned previously, transmission data of each resonance at different source powers, was taken at 23 mK and 300 mK with the cell under vacuum. This is repeated for the full cell at 30 mK, and then for every new pressure and temperature, where these parameters were being varied to search for a mechanical signal using homodyne detection. Prior to this run the microwave circuit had been calibrated at 4.2 GHz, with an overall $loss \cdot gain$ of 12 dB being calculated, which ignores the cavity contribution. This value can then be used to calibrate the S_{21} fit and extract Q_0 the internal chip-cavity quality factor. The Q_0 's of the 4.2 GHz modes, at various pressures and temperatures, are presented in Figure 5.15.

Interestingly, of the filled cell peaks the 30 mK ones do not have the highest internal quality factor, even though they are by far the lowest temperatures. Instead the second 11 mbar and first 941 mbar peaks have the highest Q_L , which are both at 200 mK, which points towards another feature of the peak splitting, that the dominance of one peak over the other is pressure dependent. This switching of dominance appears to occur at

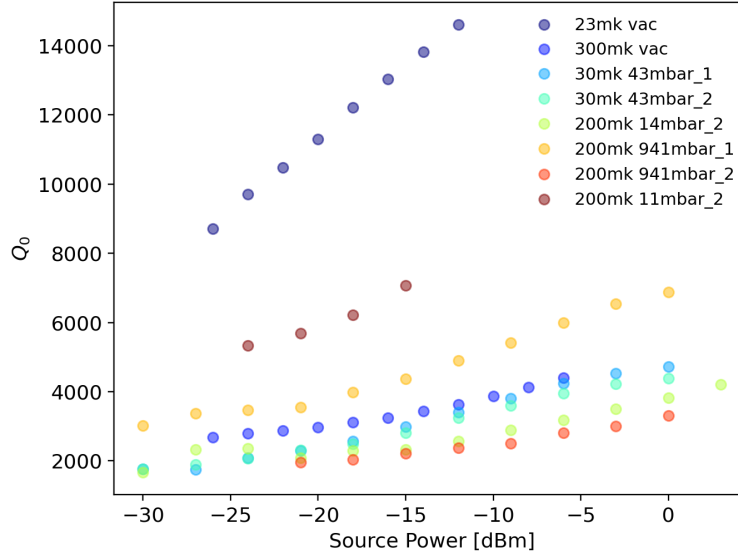


Figure 5.15: Q_0 vs source power, for the 4.2 GHz mode/s, extracted from fits of S_{21} transmission data taken at various temperatures and helium pressures. Temperature and pressure of data is indicated in the legend, vac refers to vacuum, and the _1 / _2 indicates whether the data is from the lower (_1) or higher (_2) frequency peak. Data is plotted for fits of linear resonances only, discarding any nonlinear resonances.

low pressure, where the 30 mbar peaks at 34 mbar represent a fair balance between the two peaks, while at 11 and 14 mbar the second peak is so dominant the first cannot be seen. Then at 941 mbar the first peak is almost completely dominant. The pressure dependence from this run may prove an interesting prospect for further study if the behaviour is reproducible.

Not mentioned yet, but clear from the resonances in Figure 5.14 and then the fitted Q_0 's in Figure 5.15, is that for all peaks the internal quality factor is enhanced by increasing source power. Using the calibration of the circuit and the fit parameters, this source power can be transformed, via Eq. 4.44 or 4.45, into n_{cav} the number of photons in the cavity. Figure 5.16 shows photon number against source power, calculated using P_{out} and *gain*. For consistency the calculation is repeated with P_{in} and *loss*, retrieving near identical results, indicating an accurate calibration of the circuit at 4.2 GHz.

Clearly the Q_0 increases with n_{cav} , indicating the number of photons suppresses some internal microwave loss mechanism of the chip-cavity system. This may be an indication that Two-Level Systems (TLS) are a significant loss channel for the system.

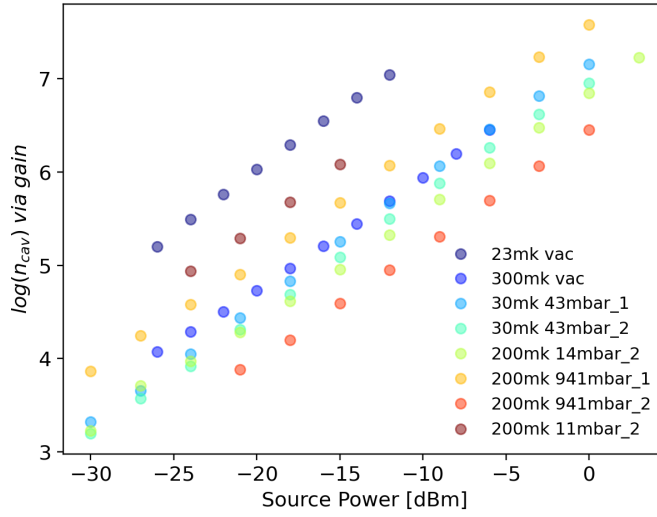


Figure 5.16: Number of photons in the microwave cavity n_{cav} against source power, for 4.2 GHz modes, taken at various temperatures and helium pressures. Calculated from fits of S_{21} , P_{out} and the *gain* calibration at 4.2 GHz. Temperature, pressure, and peak of data is indicated in the legend.

5.4.3 Two-Level Systems

Parasitic TLS provide a common unwanted loss channel for nanofabricated circuits, especially those for quantum technologies intended to operate at low photon number, where the TLS are most significant [137]. Figure 5.16 shows the chip-cavity system is operating in a regime of low enough photon number for TLS processes to become significant, and 5.15 shows the characteristic increase in intrinsic quality factor with cavity photon number, where the higher cavity field increases the polarization of the TLS. Note quality factor still increases with decreasing temperature in vacuum, indicating TLS are not the dominant loss channel at higher temperatures.

The relative strength of parasitic TLS are not only dictated by photon number but also by temperature, whereas with other quantum effects they become more significant at lower temperature. Figure 5.17 effectively shows the relative change of quality factor with source power. If TLS are more significant to the total Q_L at lower temperature, the increase in quality factor with photon number should be larger at lower temperatures. This is suggested in Figure 5.17, though a study with more data where the Q_L vs n_{cav} curves are fitted and then normalised to some n_{cav} would be more conclusive.

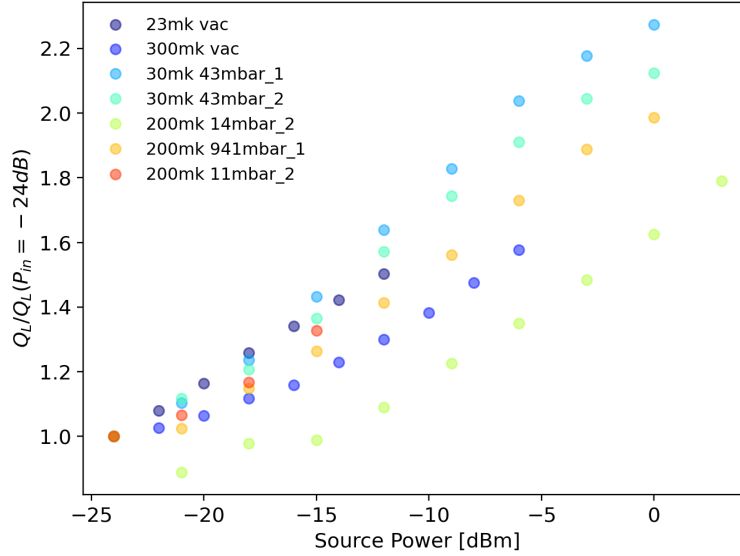


Figure 5.17: Loaded quality factor Q_L of the 4.2 GHz peaks, normalised to Q_L for a -24 dBm source power, for each temperature and pressure combination, plotted against source power. Calculated from fits of S_{21} , with pressure, temperature and peak indicated in the legend.

Generally, this behaviour suggests some TLS likely located within the electrode region of the cavity, where the electric fields are highest, though it is possible the thin wires to the electrodes also contribute. TLS are common to dielectrics that thin superconducting circuits have been deposited onto. So it may be TLS in the thermal oxide causing the parasitic effect, or some surface OH groups [137], to which recessing the aluminium may have increased sensitivity. It could also be the surface aluminium, either the oxide or impurities from fabrication. As similar behaviour was not observed in Run 2, it may be that impurities such as water have been introduced when breaking the cell vacuum. For future fabrications it may be advisable to use a high purity aluminium only evaporator, or to switch to depositing niobium. Additionally a thicker layer of metal may help to reduce sensitivity to TLS.

If there is a significant parasitic coupling to TLS, a measurement at constant cavity photon number should see the quality factor begin to increase below a certain temperature, while resonant frequency should also start to decrease around this temperature, with perhaps a small increase at very low temperature [137]. Figure 5.18 shows data taken over the first resonance during the initial cooling to base temperature, unfortunately the labview recording the temperature ceased to function at 600 mK, and so only

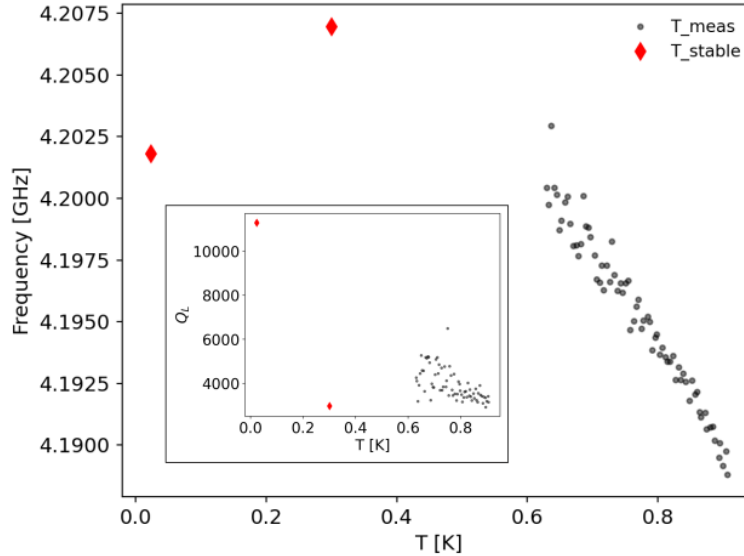


Figure 5.18: Main Figure: Resonant frequency of the 4.2 GHz peak vs temperature. Insert: Loaded quality factor of the 4.2 GHz peak vs temperature. Black dots represent data taken during the initial cooldown, while red dots are taken at stable temperatures, during the power studies. Parameter values are extracted using S_{21} fits.

stabilised points are shown below this. The resonant frequency behaviour somewhat follows the expected trend, with a maximum around 300 mK, and the quality factor potentially has a local maximum above base temperature; however, due to an insufficient number of data points over the resonance the fit of Q_L is not very accurate. Looking at both graphs there appears to be multiple peaks, especially in the resonant frequency graph, suggesting multiple significant effects.

The data in Figure 5.18 is not ideal, and if the behaviour of increasing Q_L with source power proves reproducible, then a more careful study should be undertaken. A study where the system is allowed to stabilise between measurements, and the photon number in the cavity is kept constant by adjusting the source power relative to Q_L . This measurement could then be repeated with ^4He filling the cell to determine the effect of superfluid ^4He on the mechanism [103]. Decreasing Q_e would also improve sensitivity to lower photon numbers, which may also be aided by reducing the attenuation of the microwave in line.

5.4.4 Homodyne

Homodyne detection was tried at the various temperature and pressure combinations, though the low Q_L and decreased source power at which nonlinearity occurred, made detection difficult. For this run there appeared to be no magnetic instability, and in general the signal noise was low. With the instability eliminated it was now possible to investigate the effect of the piezo drive on the transmission noise. Figure 5.19 shows a measurement of this, where the transmission noise clearly increase with piezo drive, though even at its highest the noise is much lower than Run 1. The data in this figure was taken with the piezo drive frequency swept over a region around 170 kHz, where mechanical peaks were consistently seen, to give a reasonable worst case for the noise. Of note is the sudden jump during the 5 mV drive sweeps. Investigations of these features found a jump in the DC component for homodyne measurements, when the drive frequency matched a mechanical resonance, which could indicate a shift in the cavity resonance causing a step change in the phase of the cavity arm, thus altering the quadrature.

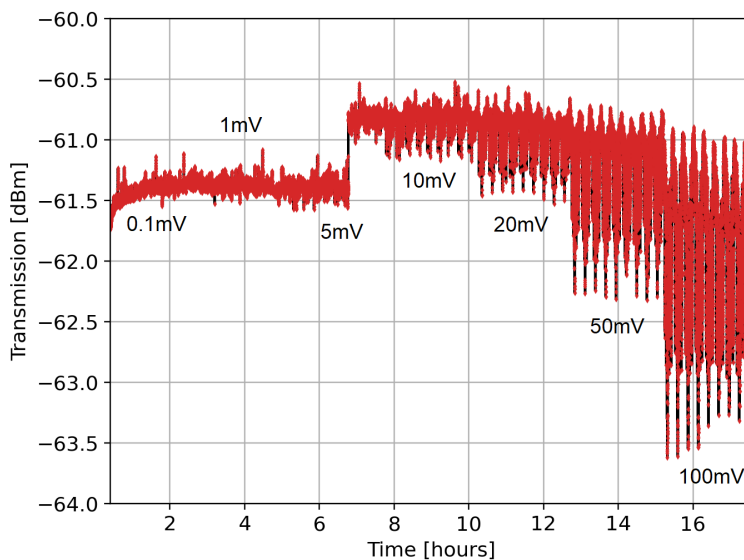


Figure 5.19: Transmission of a carrier signal on the second 4.2 GHz peak vs time, at 200 mK and 14 mbar. Data points in red, connected by black lines to show severity of change. Data is taken with the piezo sweeping a region around 170 kHz, and the piezo drive voltage is increased in steps, which are indicated on the graph.

Because of the significantly reduced Q_L and transmission of the first mode, the 10

GHz mode was also used for homodyne measurement in this run. From Section 3.2.1 the g_0 of the third mode is expected to be an order of magnitude less than the first. Using Eq. 5.1 for the ratio of sideband peak to carrier peak, g_0^2 is proportional to the relative height of the sideband, meaning a roughly two order of magnitude reduction in signal. At 200 mK the loaded quality factor of the 10 GHz mode tended to be 3-4 time larger than the 4.2 GHz, though the frequency is ~ 2.5 times larger, so the Q_L^2/ω_0^2 factor should lead to a roughly 2.5 times increase in sideband signal. The mechanics should then be the same, so the sideband's relative peak height should be roughly 17 dB lower. Looking at Figure 5.14 the 10 GHz peak is roughly 30 dB higher than either of the 4.2 GHz peaks, meaning that even though the relative height of the sideband will be lower, overall the power in the sideband will be higher. This is not as extreme at higher temperatures, and pressures that give a higher Q_L , however the difference in peak transmission is still around 20 dB, making the chance of detecting a mechanical signal similar between the two peaks.

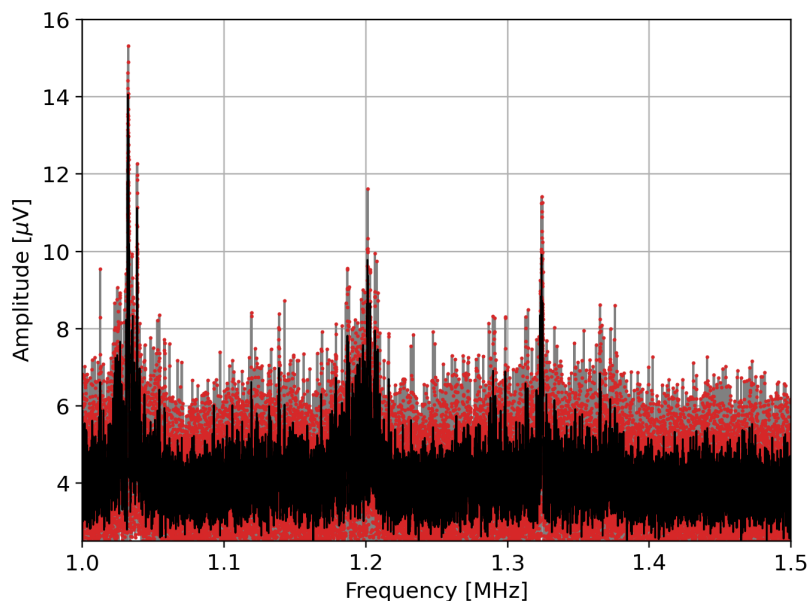


Figure 5.20: ‘Best’ homodyne measurement set for Run 3, signal amplitude vs lock-in and piezo drive frequency. Red dots indicate data points, linked by grey lines, black lines are the 5 point moving averages of the data points. Measurements taken at 300 mK, with a piezo drive of 100 mV, using the 10 GHz peak, and with a thin film of ^4He ; measured with a lock-in bandwidth of 6 Hz, over a 500 kHz frequency window with 50,000 points. Shown data points are the average of 5 sweeps taken overnight.

Figure 5.20 shows some of the ‘best’ homodyne data from Run 3, using the 10 GHz

mode. This data is from a partially filled cell, referred to as ‘thin film’, where the cell is filled enough to account for the initial jump of the 4.2 GHz mode, then stopped when the rate of change slows (see Figure 5.13). If the three peaks in the figure are mechanical signals, the thin film regime may prove interesting for study with the current system, removing possible attenuation from the bulk ^4He outside the chip. For these sweeps the signal into the fridge was reduced to around -3 dBm, to maintain a linear microwave peak, and the low frequency amplifier was reduced from 40 dB to 20 dB gain. This is what accounts for the μV signal in Figure 5.20. The lock-in can detect μV signals, so the low noise amplifier is free to be set to 20 dB gain, as it also amplifies the noise background the signal to noise will not be significantly affected. Being able to increase the signal into the fridge (as in earlier runs) would be beneficial, as the signal to noise at the HEMT amplifier is the most significant point for the overall signal.

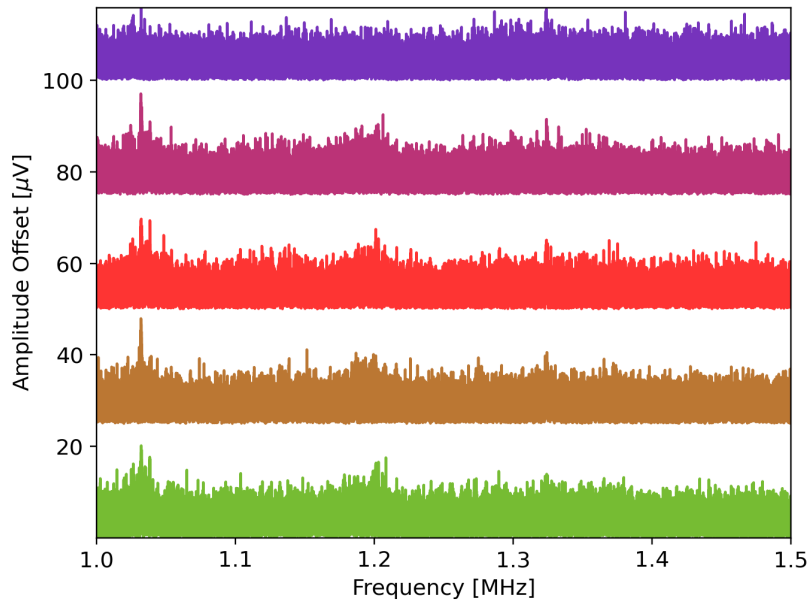


Figure 5.21: Individual sweeps for the best homodyne measurement set of Run 3, signal amplitude vs lock-in and piezo drive frequency. The individual sweeps which average to Figure 5.20 are shown, subsequent sweeps offset by an additional $25 \mu\text{V}$.

Figure 5.21 shows the individual sweeps which when averaged give the spectrum in Figure 5.20. The structure of the signal is much more consistent across individual sweeps than Figure 5.7 for the first run. Looking at Figures 5.20 and 5.21, there seem to be three signals present in each of the five sweeps, which are more clearly shown

by the average. No other signals were found around 0.5 - 2 MHz. With the current data it is not possible to determine with certainty the origin of these peaks, though the peaks appear to be mechanical due to their Lorentzian shape. Furthermore the highest frequency peak, as seen in Figure 5.20, is very close to 1.34 MHz the expected value for the resonant frequency of the nanofluidic chip's sonic crystal defect mode. Also all three peaks feature multiple consecutive data points well above the noise floor, something not seen in Run 1. This run was eventually ended due to time constraints, and the low transmission of the 4.2 GHz mode, which reduced quality of measurement data below a level where g_0 could be determined within the time available.

5.5 Run 4

A fourth run is currently underway, with the switch being made to the Q4(A2) quartz chip, needing a slightly different aluminium cavity for the orientation of the contact pads, but with otherwise the same microwave cavity dimensions. The Quartz chips were fabricated using a different evaporator for the aluminium, which should hopefully rule out the possibility of poor quality aluminium depositions at SuperFab. A much larger electrode gap may also improve signal strength, as a higher photon number will be possible with the same electric field strength at the electrode surfaces, which is likely related to the nonlinear effect. A larger gap will also increase the frequency of the fundamental chip-cavity resonance, which may improve the optomechanical signal, though the increase acoustic mode volume will reduce g_0 . The run has been delayed slightly by the need to resolder the microwave feedthroughs after thermally cycling, which may be replaced with Stycast feedthroughs for later runs.

5.6 Conclusion

This project has created an experimental platform for modern microwave based superfluid optomechanics. Nanofluidic sonic crystal chips have been designed and then fabricated using cleanroom techniques, with special emphasis on developing techniques

for room temperature plasma activated direct wafer bonding. Simulations in COMSOL Multiphysics have been used to design the superfluid optomechanical system, both of the sonic crystal acoustic environment, and the chip-cavity microwave system. The results of these simulations have then been used to predict a vacuum optomechanical coupling of $g_0/2\pi = 0.63$ mHz.

The chip-cavity system has then been incorporated into an experimental cell, cooled to base temperature and filled with superfluid ^4He . The first experimental run of this system found a strong instability affecting the microwave resonance, sensitive to external magnetic fields, which was effectively eliminated in later runs. During this run measurements of the optomechanical coupling were attempted, primarily using direct detection and homodyne phase sensitive measurements. These measurement techniques found weak signals when measurement sensitivity was maximised. Ruling out spurious peaks due to electrical noise, the peaks appear to be mechanical in origin. However the appearance of these peaks was not consistent, possibly due to the microwave instability, which prevented determination of g_0 and other optomechanical parameters.

The second experimental run eliminated the microwave instability, and achieved a much higher quality factor of $Q_L = 81,900$ at 189 mK. This microwave quality factor was roughly four times larger than the highest value for the first run of 21,400, which would have increased the height of the mechanical sideband by a factor of 16. Unfortunately a thermal contact between 4K and the still plate prevented cooling to base temperature and the run had to be abandoned.

A third run with the same chip-cavity system as Run 2 successfully cooled to base temperature, while also eliminating the microwave instability. This run was able to measure more consistent signals using homodyne detection, though the microwave quality factor had deteriorated to well below 10,000 in the presence of ^4He , reducing the overall signal strength to a point where determination of g_0 was not possible in the remaining time. During Run 3 it was discovered that microwave quality factor increased with the number of photons in the cavity, a behaviour common to parasitic two-level systems, giving a possible route to expand the scope of the project to study two level systems in the presence of superfluid ^4He .

5.6.1 Outlook

From the current data sets, it seems as though the mechanical signal is on the edge of the homodyne detection sensitivity. So a run with a quality factor of Run 2, that could reach base temperature without the instability of Run 1, should be able to detect the mechanical signal with enough clarity to move forward with analysis. A consistent signal that was trusted could also be averaged over a longer measurement time. Once the mechanical signal was clearly detected, the piezo could be set to drive on or near the resonance, and the lock-in's zoom FFT function used to measure the optomechanical coupling. Then by varying the system parameters such as temperature a value for g_0 could be extracted.

Even without measuring the optomechanical coupling, it may prove interesting to study the TLS-like dependencies of the resonances. The system may be well suited for studying dissipation of on-chip superconducting circuits in the presence of helium [137, 217] There are three cavity modes to examine, with cavity temperature and ^4He pressure dependencies which can be measured. If the splitting of the modes with the presence of the ^4He is a feature of the chip-cavity system, and not an issue afflicting only Run 3, the dependence of the splitting on the ^4He pressure can be investigated.

A quick solution to the low optomechanical signal may be to increase the strength of the microwave pin couplers, reducing Q_e to around 10^5 , which would increase the signal strength P_{out} by a factor of 100 at the same cavity photon number. This may also be an opportunity to move to Stycast feedthroughs, which should be more resistant to thermal cycling. Vibrationally isolating the cavity from the rest of the fridge may also help homodyne detection [91], though at 1.34 MHz this should not be too much of a concern.

A new fabrication run may be required to produce more chips. This would provide an opportunity to switch the on-chip aluminium for niobium, which may provide a better microwave environment [209], and would allow dip testing of the chip-cavity system's microwave properties at liquid ^4He temperature. A new fabrication could greatly increase the scale of sonic crystal geometry on the nanofluidic chip, moving towards more of a

bulk ^4He mode volume. This would significantly decrease the g_0 , but allow for much higher microwave power, and hopefully increase acoustic transmission from the piezo to the defect mode. It may also be productive to make direct electrical connection from the measurement lines to the contact pads, moving the system away from optomechanics and towards a more direct electromechanical detection [148].

As a significant extension of the project, it may be possible to incorporate a SiN membrane into the top chip piece over the defect [126]. This should significantly increase g_0 , however would greatly reduce the maximum possible Q_m . The microwave cavity could also be moved on chip [218], though this would take significant development of the chip designs and nanofabrication process. Starting with a more simple on-chip bulk ^4He cavity may be a simpler way to begin these studies. The cavity could then be developed into an on-chip re-entrant cavity, and eventually a joint sonic crystal plus on-chip cavity.

Maintaining the same or similar chip design, creating a cell capable of withstanding high pressure may enable measurement of four-phonon processes [75], though it will likely prove difficult to isolate the acoustic mode from extrinsic losses. A more achievable extension may be to use the system to study confined ^3He [99, 106], requiring a dilution fridge with nuclear demagnetisation capabilities. The system may also be suitable for measurements of ^4He confined to thin slabs near its correlation length [107, 109, 110]; or, given Run 3's ability to measure mechanical modes with only a little ^4He inside the cavity, it may be possible to study ^4He thin-film modes [28, 112]. Of course moving towards the quantum regime is always an appealing prospect when working at dilution fridge temperatures and with on-chip superconducting circuits. Currently at 23 mK and $\Omega_m = 1.34$ MHz there should be ~ 2500 phonons in the point defect mode. With the current system and a weak coupling, optomechanical cooling to the quantum regime is not possible [1], however reducing the crystal unit cell size and temperature by a combined three orders of magnitude (achievable with a combination of nuclear demagnetisation for cooling, and electron beam lithography for chip fabrication), would put the phonon occupation number into the single digits, entering the regime of quantum optomechanics.

Bibliography

- [1] M. Aspelmeyer, T. J. Kippenberg, and F. Marquardt, “Cavity optomechanics,” *Reviews of Modern Physics*, vol. 86, no. 4, p. 1391, 2014.
- [2] W. P. Bowen and G. J. Milburn, *Quantum optomechanics*. CRC press, 2015.
- [3] L. De Lorenzo and K. Schwab, “Superfluid optomechanics: coupling of a superfluid to a superconducting condensate,” *New Journal of Physics*, vol. 16, no. 11, p. 113020, 2014.
- [4] W. Hartung, J. Bierwagen, S. Bricker, C. Compton, T. Grimm, M. Johnson, D. Meidlinger, D. Pendell, J. Popielarski, L. Saxton, *et al.*, “RF performance of a superconducting s-band cavity filled with liquid helium,” *Vacuum*, vol. 10, p. 10, 2006.
- [5] L. De Lorenzo and K. Schwab, “Ultra-high Q acoustic resonance in superfluid He,” *Journal of Low Temperature Physics*, vol. 186, no. 3-4, pp. 233–240, 2017.
- [6] A. Shkarin, A. Kashkanova, C. Brown, S. Garcia, K. Ott, J. Reichel, and J. Harris, “Quantum optomechanics in a liquid,” *Physical Review Letters*, vol. 122, no. 15, p. 153601, 2019.
- [7] A. Kashkanova, A. Shkarin, C. Brown, N. Flowers-Jacobs, L. Childress, S. Hoch, L. Hohmann, K. Ott, J. Reichel, and J. Harris, “Superfluid Brillouin optomechanics,” *Nature Physics*, vol. 13, no. 1, pp. 74–79, 2017.
- [8] F. Souris, X. Rojas, P. H. Kim, and J. P. Davis, “Ultralow-dissipation superfluid micromechanical resonator,” *Physical Review Applied*, vol. 7, no. 4, p. 044008, 2017.

- [9] A. H. Safavi-Naeini and O. Painter, “Design of optomechanical cavities and waveguides on a simultaneous bandgap phononic-photonic crystal slab,” *Optics Express*, vol. 18, no. 14, pp. 14926–14943, 2010.
- [10] J. Kepler, “De cometis,” *Libelli tres. Mylius: Augustae Vindelicorum*, vol. 1619.
- [11] S. Stenholm, “The semiclassical theory of laser cooling,” *Rev. Mod. Phys.*, vol. 58, pp. 699–739, Jul 1986.
- [12] J. Aasi, J. Abadie, B. Abbott, R. Abbott, T. Abbott, M. Abernathy, C. Adams, T. Adams, P. Addesso, R. Adhikari, *et al.*, “Enhanced sensitivity of the LIGO gravitational wave detector by using squeezed states of light,” *Nature Photonics*, vol. 7, no. 8, p. 613, 2013.
- [13] J. McKeever, J. Buck, A. Boozer, A. Kuzmich, H.-C. Nägerl, D. Stamper-Kurn, and H. Kimble, “State-insensitive cooling and trapping of single atoms in an optical cavity,” *Physical Review Letters*, vol. 90, no. 13, p. 133602, 2003.
- [14] M. Li, W. Pernice, C. Xiong, T. Baehr-Jones, M. Hochberg, and H. Tang, “Harnessing optical forces in integrated photonic circuits,” *Nature*, vol. 456, no. 7221, p. 480, 2008.
- [15] M. Kang, A. Nazarkin, A. Brenn, and P. S. J. Russell, “Tightly trapped acoustic phonons in photonic crystal fibres as highly nonlinear artificial Raman oscillators,” *Nature Physics*, vol. 5, no. 4, p. 276, 2009.
- [16] G. Anetsberger, E. Gavartin, O. Arcizet, Q. P. Unterreithmeier, E. M. Weig, M. L. Gorodetsky, J. P. Kotthaus, and T. J. Kippenberg, “Measuring nanomechanical motion with an imprecision below the standard quantum limit,” *Physical Review A*, vol. 82, no. 6, p. 061804, 2010.
- [17] J. D. Teufel, T. Donner, M. Castellanos-Beltran, J. W. Harlow, and K. W. Lehnert, “Nanomechanical motion measured with an imprecision below that at the standard quantum limit,” *Nature Nanotechnology*, vol. 4, no. 12, pp. 820–823, 2009.

- [18] A. D. O’Connell, M. Hofheinz, M. Ansmann, R. C. Bialczak, M. Lenander, E. Lucero, M. Neeley, D. Sank, H. Wang, M. Weides, *et al.*, “Quantum ground state and single-phonon control of a mechanical resonator,” *Nature*, vol. 464, no. 7289, p. 697, 2010.
- [19] J. D. Teufel, T. Donner, D. Li, J. W. Harlow, M. Allman, K. Cicak, A. J. Sirois, J. D. Whittaker, K. W. Lehnert, and R. W. Simmonds, “Sideband cooling of micromechanical motion to the quantum ground state,” *Nature*, vol. 475, no. 7356, pp. 359–363, 2011.
- [20] J. Suh, A. Weinstein, C. Lei, E. Wollman, S. Steinke, P. Meystre, A. A. Clerk, and K. Schwab, “Mechanically detecting and avoiding the quantum fluctuations of a microwave field,” *Science*, vol. 344, no. 6189, pp. 1262–1265, 2014.
- [21] F. Lecocq, J. B. Clark, R. W. Simmonds, J. Aumentado, and J. D. Teufel, “Quantum nondemolition measurement of a nonclassical state of a massive object,” *Physical Review X*, vol. 5, no. 4, p. 041037, 2015.
- [22] T. Palomaki, J. Harlow, J. Teufel, R. Simmonds, and K. W. Lehnert, “Coherent state transfer between itinerant microwave fields and a mechanical oscillator,” *Nature*, vol. 495, no. 7440, pp. 210–214, 2013.
- [23] A. Reed, K. Mayer, J. Teufel, L. Burkhart, W. Pfaff, M. Reagor, L. Sletten, X. Ma, R. Schoelkopf, E. Knill, *et al.*, “Faithful conversion of propagating quantum information to mechanical motion,” *Nature Physics*, vol. 13, no. 12, pp. 1163–1167, 2017.
- [24] E. E. Wollman, C. Lei, A. Weinstein, J. Suh, A. Kronwald, F. Marquardt, A. A. Clerk, and K. Schwab, “Quantum squeezing of motion in a mechanical resonator,” *Science*, vol. 349, no. 6251, pp. 952–955, 2015.
- [25] J.-M. Pirkkalainen, E. Damskäg, M. Brandt, F. Massel, and M. A. Sillanpää, “Squeezing of quantum noise of motion in a micromechanical resonator,” *Physical Review Letters*, vol. 115, no. 24, p. 243601, 2015.

- [26] T. Palomaki, J. Teufel, R. Simmonds, and K. W. Lehnert, “Entangling mechanical motion with microwave fields,” *Science*, vol. 342, no. 6159, pp. 710–713, 2013.
- [27] LIGO Laboratory, “New movie on LIGO’s mirror suspensions.” <https://www.ligo.caltech.edu/news/ligo20170216>, 2017.
- [28] G. S. MacCabe, H. Ren, J. Luo, J. D. Cohen, H. Zhou, A. Sipahigil, M. Mirhosseini, and O. Painter, “Nano-acoustic resonator with ultralong phonon lifetime,” *Science*, vol. 370, no. 6518, pp. 840–843, 2020.
- [29] X. He, G. I. Harris, C. G. Baker, A. Sawadsky, Y. L. Sfondla, Y. P. Sachkou, S. Forstner, and W. P. Bowen, “Strong optical coupling through superfluid Brillouin lasing,” *Nature Physics*, vol. 16, no. 4, pp. 417–421, 2020.
- [30] R. Riedinger, A. Wallucks, I. Marinković, C. Löschnauer, M. Aspelmeyer, S. Hong, and S. Gröblacher, “Remote quantum entanglement between two micromechanical oscillators,” *Nature*, vol. 556, no. 7702, pp. 473–477, 2018.
- [31] Y. Seis, T. Capelle, E. Langman, S. Saarinen, E. Planz, and A. Schliesser, “Ground state cooling of an ultracoherent electromechanical system,” *arXiv preprint arXiv:2107.05552*, 2021.
- [32] H. Ren, M. H. Matheny, G. S. MacCabe, J. Luo, H. Pfeifer, M. Mirhosseini, and O. Painter, “Two-dimensional optomechanical crystal cavity with high quantum cooperativity,” *Nature Communications*, vol. 11, no. 1, pp. 1–10, 2020.
- [33] B. Hauer, C. Doolin, K. Beach, and J. Davis, “A general procedure for thermo-mechanical calibration of nano/micro-mechanical resonators,” *Annals of Physics*, vol. 339, pp. 181 – 207, 2013.
- [34] M. Pinard, Y. Hadjar, and A. Heidmann, “Effective mass in quantum effects of radiation pressure,” *The European Physical Journal D-Atomic, Molecular, Optical and Plasma Physics*, vol. 7, no. 1, pp. 107–116, 1999.

- [35] M. Gorodetsky, A. Schliesser, G. Anetsberger, S. Deleglise, and T. J. Kippenberg, “Determination of the vacuum optomechanical coupling rate using frequency noise calibration,” *Optics Express*, vol. 18, no. 22, pp. 23236–23246, 2010.
- [36] F. Souris, A. D. Fefferman, H. J. Maris, V. Dauvois, P. Jean-Baptiste, J. R. Beamish, and S. Balibar, “Movement of dislocations dressed with He 3 impurities in He 4 crystals,” *Physical Review B*, vol. 90, no. 18, p. 180103, 2014.
- [37] P. Kapitza, “Viscosity of liquid helium below the λ -point,” *Nature*, vol. 141, no. 3558, pp. 74–74, 1938.
- [38] B. Abraham, Y. Eckstein, J. Ketterson, M. Kuchnir, and J. Vignos, “Sound propagation in liquid He 4,” *Physical Review*, vol. 181, no. 1, p. 347, 1969.
- [39] K. Dransfeld, “Ultrasonic absorption in liquid helium at temperatures below 0.6 K,” *Physical Review*, vol. 127, no. 1, p. 17, 1962.
- [40] S. Spence, Z. Koong, S. Horsley, and X. Rojas, “Superfluid optomechanics with phononic nanostructures,” *Physical Review Applied*, vol. 15, no. 3, p. 034090, 2021.
- [41] J. Wilhelm, A. Misener, and A. Clark, “The viscosity of liquid helium,” *Proceedings of the Royal Society of London. Series A-Mathematical and Physical Sciences*, vol. 151, no. 873, pp. 342–347, 1935.
- [42] J. F. Allen and A. Misener, “Flow of liquid helium II,” *Nature*, vol. 141, no. 3558, pp. 75–75, 1938.
- [43] L. Tisza, “Transport phenomena in helium II,” *Nature*, vol. 141, no. 3577, pp. 913–913, 1938.
- [44] L. Landau, “Theory of the superfluidity of helium II,” *Physical Review*, vol. 60, no. 4, p. 356, 1941.
- [45] S. Balibar, “Laszlo Tisza and the two-fluid model of superfluidity,” *Comptes Rendus Physique*, vol. 18, no. 9-10, pp. 586–591, 2017.

- [46] A. Schmitt, “Introduction to superfluidity,” *Lect. Notes Phys*, vol. 888, no. 1, 2015.
- [47] J. Yarnell, G. Arnold, P. Bendt, and E. Kerr, “Excitations in liquid helium: neutron scattering measurements,” *Physical Review*, vol. 113, no. 6, p. 1379, 1959.
- [48] P. Nozieres and D. Pines, “Theory of quantum liquids volume II: Superfluid bose liquids., advanced book classics,” 1994.
- [49] S. Eckstein, Y. Eckstein, J. Ketterson, and J. Vignos, “The propagation of sound in condensed helium,” in *Physical Acoustics*, vol. 6, pp. 243–372, Elsevier, 1970.
- [50] K. Beauvois, J. Dawidowski, B. Fåk, H. Godfrin, E. Krotscheck, J. Ollivier, and A. Sultan, “Microscopic dynamics of superfluid He 4: A comprehensive study by inelastic neutron scattering,” *Physical Review B*, vol. 97, no. 18, p. 184520, 2018.
- [51] R. P. Feynman, “Chapter II application of quantum mechanics to liquid helium,” in *Progress in Low Temperature Physics*, vol. 1, pp. 17–53, Elsevier, 1955.
- [52] A. Miller, D. Pines, and P. Nozieres, “Elementary excitations in liquid helium,” *Physical Review*, vol. 127, no. 5, p. 1452, 1962.
- [53] R. Feynman and M. Cohen, “Energy spectrum of the excitations in liquid helium,” *Physical Review*, vol. 102, no. 5, p. 1189, 1956.
- [54] P. Nozieres, “Is the roton in superfluid 4 He the ghost of a Bragg spot?,” *Journal of Low Temperature Physics*, vol. 137, no. 1, pp. 45–67, 2004.
- [55] G. R. Pickett and S. N. Fisher, “Superfluid 3He in the zero-temperature limit,” *Physica B: Condensed Matter*, vol. 329, pp. 75–79, 2003.
- [56] A. Leanhardt, T. Pasquini, M. Saba, A. Schirotzek, Y. Shin, D. Kielpinski, D. Pritchard, and W. Ketterle, “Cooling bose-einstein condensates below 500 picokelvin,” *Science*, vol. 301, no. 5639, pp. 1513–1515, 2003.
- [57] C. Enss and S. Hunklinger, *Low-Temperature Physics*. Springer Science and Business Media, 2005.

- [58] I. M. Khalatnikov, *An introduction to the theory of superfluidity*. CRC Press, 2018.
- [59] J. Allen and H. Jones, “New phenomena connected with heat flow in helium II,” *Nature*, vol. 141, no. 3562, pp. 243–244, 1938.
- [60] J. Jäckle and K. Kehr, “High-frequency ultrasonic attenuation in superfluid helium under pressure,” *Physical Review Letters*, vol. 27, no. 10, p. 654, 1971.
- [61] T. O. Woodruff, “Sound absorption in liquid helium II, $t < 0.5$ K,” *Physical Review*, vol. 127, no. 3, p. 682, 1962.
- [62] C. Pethick and D. Ter Haar, “On the attenuation of sound in liquid helium,” *Physica*, vol. 32, no. 11-12, pp. 1905–1920, 1966.
- [63] Y. Disatnik, “Single-collision-time theory of sound propagation in liquid He 4 below 0.6 K,” *Physical Review*, vol. 158, no. 1, p. 162, 1967.
- [64] G. Waters, D. Watmough, and J. Wilks, “Absorption of sound in helium II below 0.6 K,” *Physics Letters A*, vol. 26, no. 1, pp. 12–13, 1967.
- [65] C. Chase, “Ultrasonic propagation in liquid helium,” *American Journal of Physics*, vol. 24, no. 3, pp. 136–155, 1956.
- [66] N. E. Phillips, C. Waterfield, and J. Hoffer, “Calorimetric evidence for positive phonon dispersion in liquid helium-4,” *Physical Review Letters*, vol. 25, no. 18, p. 1260, 1970.
- [67] P. R. Roach, J. Ketterson, and M. Kuchnir, “Ultrasonic attenuation in liquid He 4 under pressure,” *Physical Review A*, vol. 5, no. 5, p. 2205, 1972.
- [68] C. Anderson and E. Sabisky, “Positive linear dispersion in the velocity of sound in He II,” *Physical Review Letters*, vol. 28, no. 2, p. 80, 1972.
- [69] P. R. Roach, J. Ketterson, and M. Kuchnir, “New relaxation effect in the sound attenuation in liquid He 4 under pressure,” *Physical Review Letters*, vol. 25, no. 15, p. 1002, 1970.

- [70] H. J. Maris and W. E. Massey, “Phonon dispersion and the propagation of sound in liquid helium-4 below 0.6 K,” *Physical Review Letters*, vol. 25, no. 4, p. 220, 1970.
- [71] H. J. Maris, “Hydrodynamics of superfluid helium below 0.6 K. II. velocity and attenuation of ultrasonic waves,” *Physical Review A*, vol. 8, no. 5, p. 2629, 1973.
- [72] D. Rugar and J. Foster, “Accurate measurement of low-energy phonon dispersion in liquid He 4,” *Physical Review B*, vol. 30, no. 5, p. 2595, 1984.
- [73] A. Isihara, “Attenuation coefficient of first sound in liquid He 4,” *Physical Review B*, vol. 40, no. 1, p. 698, 1989.
- [74] B. Abraham, Y. Eckstein, J. Ketterson, M. Kuchnir, and P. R. Roach, “Velocity of sound, density, and Grüneisen constant in liquid He 4,” *Physical Review A*, vol. 1, no. 2, p. 250, 1970.
- [75] H. Kurkjian, Y. Castin, and A. Sinatra, “Three-phonon and four-phonon interaction processes in a pair-condensed Fermi gas,” *Annalen der Physik*, vol. 529, no. 9, p. 1600352, 2017.
- [76] K. Beauvois, H. Godfrin, E. Krotscheck, and R. Zillich, “Transport and phonon damping in ^4He ,” *Journal of Low Temperature Physics*, vol. 197, no. 3, pp. 113–129, 2019.
- [77] H. Godfrin, K. Beauvois, A. Sultan, E. Krotscheck, J. Dawidowski, B. Fak, and J. Ollivier, “Dispersion relation of landau elementary excitations and thermodynamic properties of superfluid He 4,” *Physical Review B*, vol. 103, no. 10, p. 104516, 2021.
- [78] L. Landau and I. Khalatnikov, “Theory of viscosity of helium II. 1. collisions of elementary excitations in helium II.,” *Zhurnal Eksperimentalnoi i Teoreticheskoi Fiziki*, vol. 19, p. 637, 1949.

- [79] M. Tucker and A. Wyatt, “Four-phonon scattering in superfluid He 4,” *Journal of Physics: Condensed Matter*, vol. 4, no. 38, p. 7745, 1992.
- [80] H. J. Maris, “Phonon-phonon interactions in liquid helium,” *Reviews of Modern Physics*, vol. 49, no. 2, p. 341, 1977.
- [81] J. Bardeen, G. Baym, and D. Pines, “Interactions between He 3 atoms in dilute solutions of He 3 in superfluid He 4,” *Physical Review Letters*, vol. 17, no. 7, p. 372, 1966.
- [82] J. Bardeen, G. Baym, and D. Pines, “Effective interaction of He 3 atoms in dilute solutions of He 3 in He 4 at low temperatures,” *Physical Review*, vol. 156, no. 1, p. 207, 1967.
- [83] G. Baym, W. Saam, and C. Ebner, “Phonon-quasiparticle interactions in dilute solutions of He 3 in superfluid He 4: Iii. attenuation of first sound above 0.2 K,” *Physical Review*, vol. 173, no. 1, p. 306, 1968.
- [84] G. Baym and C. Pethick, *Landau Fermi-liquid theory: concepts and applications*. John Wiley & Sons, 2008.
- [85] G. Baym, “Theory of first sound in dilute solutions of He 3 in He 4 at very low temperatures,” *Physical Review Letters*, vol. 18, no. 3, p. 71, 1967.
- [86] G. Baym and C. Ebner, “Phonon-quasiparticle interactions in dilute solutions of He 3 in superfluid He 4: I. phonon thermal conductivity and ultrasonic attenuation,” *Physical Review*, vol. 164, no. 1, p. 235, 1967.
- [87] G. Baym, D. Beck, and C. Pethick, “Low-temperature transport properties of very dilute classical solutions of ^3He in superfluid ^4He ,” *Journal of Low Temperature Physics*, vol. 178, no. 3, pp. 200–228, 2015.
- [88] P. Hendry and P. V. McClintock, “Continuous flow apparatus for preparing isotopically pure He 4,” *Cryogenics*, vol. 27, no. 3, pp. 131–138, 1987.
- [89] D. Ter Haar, *Collected papers of LD Landau*. Elsevier, 2013.

- [90] H. Kerscher, M. Niemetz, and W. Schoepe, “Viscosity and mean free path of very diluted solutions of He 3 in He 4,” *Journal of Low Temperature Physics*, vol. 124, no. 1, pp. 163–168, 2001.
- [91] L. A. De Lorenzo, *Optomechanics with superfluid helium-4*. PhD thesis, California Institute of Technology, 2016.
- [92] G. Baym, D. Beck, and C. J. Pethick, “Transport in very dilute solutions of 3 He in superfluid 4 He,” *Physical Review B*, vol. 88, no. 1, p. 014512, 2013.
- [93] G. Baym, D. Beck, and C. J. Pethick, “Transport in ultradilute solutions of He 3 in superfluid He 4,” *Physical Review B*, vol. 92, no. 2, p. 024504, 2015.
- [94] C. Boghosian and H. Meyer, “Density of a dilute He 3-He 4 solution under pressure,” *Physics Letters A*, vol. 25, no. 5, pp. 352–353, 1967.
- [95] G. Watson, J. Reppy, and R. Richardson, “Low-temperature density and solubility of He 3 in liquid He 4 under pressure,” *Physical Review*, vol. 188, no. 1, p. 384, 1969.
- [96] B. Abraham, O. Brandt, Y. Eckstein, J. Munarin, and G. Baym, “Relative molar volume and limiting solubility of He 3 in superfluid He 4,” *Physical Review*, vol. 188, no. 1, p. 309, 1969.
- [97] S. Tholen and J. Parpia, “Slip and the effect of He 4 at the silicon 3 interface,” *Physical Review Letters*, vol. 67, no. 3, p. 334, 1991.
- [98] J. M. Ziman, *Electrons and phonons: the theory of transport phenomena in solids*. Oxford University Press, 2001.
- [99] P. Heikkinen, A. Casey, L. Levitin, X. Rojas, A. Vorontsov, P. Sharma, N. Zhelev, J. Parpia, and J. Saunders, “Fragility of surface states in topological superfluid 3 He,” *Nature Communications*, vol. 12, no. 1, pp. 1–8, 2021.

- [100] L. Childress, M. Schmidt, A. Kashkanova, C. Brown, G. Harris, A. Aiello, F. Marquardt, and J. Harris, “Cavity optomechanics in a levitated helium drop,” *Physical Review A*, vol. 96, no. 6, p. 063842, 2017.
- [101] S. Singh, L. De Lorenzo, I. Pikovski, and K. Schwab, “Detecting continuous gravitational waves with superfluid He 4,” *New Journal of Physics*, vol. 19, no. 7, p. 073023, 2017.
- [102] V. Vadakkumbatt, M. Hirschel, J. Manley, T. Clark, S. Singh, and J. Davis, “Prototype superfluid gravitational wave detector,” *Physical Review D*, vol. 104, no. 8, p. 082001, 2021.
- [103] J. R. Lane, *Integrating Superconducting Qubits with Quantum Fluids and Surface Acoustic Wave Devices*. PhD thesis, Michigan State University, 2021.
- [104] K. Schwab, J. Steinhauer, J. Davis, and R. E. Packard, “Fabrication of a silicon-based superfluid oscillator,” *Journal of microelectromechanical systems*, vol. 5, no. 3, pp. 180–186, 1996.
- [105] X. Rojas, B. Hauer, A. MacDonald, P. Saberi, Y. Yang, and J. Davis, “Ultrasonic interferometer for first-sound measurements of confined liquid He 4,” *Physical Review B*, vol. 89, no. 17, p. 174508, 2014.
- [106] L. Levitin, R. Bennett, A. Casey, B. Cowan, J. Saunders, D. Drung, T. Schurig, and J. Parpia, “Phase diagram of the topological superfluid He 3 confined in a nanoscale slab geometry,” *Science*, vol. 340, no. 6134, pp. 841–844, 2013.
- [107] E. Varga and J. P. Davis, “Electromechanical feedback control of nanoscale superflow,” *New Journal of Physics*, vol. 23, no. 11, p. 113041, 2021.
- [108] F. M. Gasparini, M. O. Kimball, K. P. Mooney, and M. Diaz-Avila, “Finite-size scaling of He 4 at the superfluid transition,” *Reviews of Modern Physics*, vol. 80, no. 3, p. 1009, 2008.

- [109] J. Perron, M. Kimball, and F. Gasparini, “A review of giant correlation-length effects via proximity and weak-links coupling in a critical system: He 4 near the superfluid transition,” *Reports on Progress in Physics*, vol. 82, no. 11, p. 114501, 2019.
- [110] E. Varga, V. Vadakkumbatt, A. Shook, P. Kim, and J. Davis, “Observation of bistable turbulence in quasi-two-dimensional superflow,” *Physical Review Letters*, vol. 125, no. 2, p. 025301, 2020.
- [111] Y. P. Sachkou, C. G. Baker, G. I. Harris, O. R. Stockdale, S. Forstner, M. T. Reeves, X. He, D. L. McAuslan, A. S. Bradley, M. J. Davis, *et al.*, “Coherent vortex dynamics in a strongly interacting superfluid on a silicon chip,” *Science*, vol. 366, no. 6472, pp. 1480–1485, 2019.
- [112] Y. L. Sfindla, C. G. Baker, G. I. Harris, L. Tian, R. A. Harrison, and W. P. Bowen, “Extreme quantum nonlinearity in superfluid thin-film surface waves,” *NPJ Quantum Information*, vol. 7, no. 1, pp. 1–12, 2021.
- [113] D. M. Pozar, *Microwave Engineering*. John Wiley & Sons, 2009.
- [114] L. Bruch and F. Weinhold, “Diamagnetism of helium,” *The Journal of Chemical Physics*, vol. 113, no. 19, pp. 8667–8670, 2000.
- [115] J. J. Niemela and R. J. Donnelly, “Density and thermal expansion coefficient of liquid helium-4 from measurements of the dielectric constant,” *Journal of Low Temperature Physics*, vol. 98, no. 1, pp. 1–16, 1995.
- [116] E. Talebian and M. Talebian, “A general review on the derivation of Clausius–Mossotti relation,” *Optik-International Journal for Light and Electron Optics*, vol. 124, no. 16, pp. 2324–2326, 2013.
- [117] R. Harris-Lowe and K. Smee, “Thermal expansion of liquid helium II,” *Physical Review A*, vol. 2, no. 1, p. 158, 1970.

- [118] S. W. Rienstra and A. Hirschberg, “An introduction to acoustics,” *Eindhoven University of Technology*, vol. 18, p. 19, 2004.
- [119] R. J. Donnelly and C. F. Barenghi, “The observed properties of liquid helium at the saturated vapor pressure,” *Journal of Physical and Chemical Reference Data*, vol. 27, no. 6, pp. 1217–1274, 1998.
- [120] B. T. McAllister, Y. Shen, G. Flower, S. R. Parker, and M. E. Tobar, “Higher order reentrant post modes in cylindrical cavities,” *Journal of Applied Physics*, vol. 122, no. 14, p. 144501, 2017.
- [121] M. Reagor, W. Pfaff, C. Axline, R. W. Heeres, N. Ofek, K. Sliwa, E. Holland, C. Wang, J. Blumoff, K. Chou, *et al.*, “Quantum memory with millisecond coherence in circuit QED,” *Physical Review B*, vol. 94, no. 1, p. 014506, 2016.
- [122] M. Goryachev and M. E. Tobar, “Creating tuneable microwave media from a two-dimensional lattice of re-entrant posts,” *Journal of Applied Physics*, vol. 118, no. 20, p. 204504, 2015.
- [123] J. Barroso, P. Castro, O. Aguiar, and L. Carneiro, “Reentrant cavities as electromechanical transducers,” *Review of Scientific Instruments*, vol. 75, no. 4, pp. 1000–1005, 2004.
- [124] K. Fujisawa, “General treatment of Klystron resonant cavities,” *IRE Transactions on Microwave Theory and Techniques*, vol. 6, no. 4, pp. 344–358, 1958.
- [125] J.-M. Le Floch, Y. Fan, M. Aubourg, D. Cros, N. Carvalho, Q. Shan, J. Bourhill, E. Ivanov, G. Humbert, V. Madrangeas, *et al.*, “Rigorous analysis of highly tunable cylindrical transverse magnetic mode re-entrant cavities,” *Review of Scientific Instruments*, vol. 84, no. 12, p. 125114, 2013.
- [126] M. Yuan, V. Singh, Y. M. Blanter, and G. A. Steele, “Large cooperativity and microkelvin cooling with a three-dimensional optomechanical cavity,” *Nature Communications*, vol. 6, no. 1, pp. 1–6, 2015.

- [127] A. Noguchi, R. Yamazaki, M. Ataka, H. Fujita, Y. Tabuchi, T. Ishikawa, K. Usami, and Y. Nakamura, “Ground state cooling of a quantum electromechanical system with a silicon nitride membrane in a 3D loop-gap cavity,” *New Journal of Physics*, vol. 18, no. 10, p. 103036, 2016.
- [128] D. Alesini, C. Braggio, G. Carugno, N. Crescini, D. D’Agostino, D. Di Gioacchino, R. Di Vora, P. Falferi, U. Gambardella, C. Gatti, *et al.*, “Realization of a high quality factor resonator with hollow dielectric cylinders for axion searches,” *Nuclear Instruments and Methods in Physics Research Section A: Accelerators, Spectrometers, Detectors and Associated Equipment*, vol. 985, p. 164641, 2021.
- [129] X. Liu, L. P. Katehi, W. J. Chappell, and D. Peroulis, “High-Q tunable microwave cavity resonators and filters using SOI-based RF MEMS tuners,” *Journal of Microelectromechanical Systems*, vol. 19, no. 4, pp. 774–784, 2010.
- [130] F. Biquard and A. Septier, “Amelioration de la conductivite superficielle du cuivre et de l’aluminium en hyperfréquences, par abaissement de temperature,” *Nuclear Instruments and Methods*, vol. 44, no. 1, pp. 18–28, 1966.
- [131] M. Kudra, J. Biznárová, A. Fadavi Roudsari, J. Burnett, D. Niepce, S. Gasparinetti, B. Wickman, and P. Delsing, “High quality three-dimensional aluminum microwave cavities,” *Applied Physics Letters*, vol. 117, no. 7, p. 070601, 2020.
- [132] M. Reagor, H. Paik, G. Catelani, L. Sun, C. Axline, E. Holland, I. M. Pop, N. A. Masluk, T. Brecht, L. Frunzio, *et al.*, “Reaching 10 ms single photon lifetimes for superconducting aluminum cavities,” *Applied Physics Letters*, vol. 102, no. 19, p. 192604, 2013.
- [133] D. F. Bogorin, D. T. McClure, M. Ware, and B. Plourde, “Copper waveguide cavities with reduced surface loss for coupling to superconducting qubits,” *IEEE Transactions on Applied Superconductivity*, vol. 24, no. 4, pp. 1–7, 2014.
- [134] J. M. Pierce, “Residual microwave surface resistance of superconducting lead,” *Journal of Applied Physics*, vol. 44, no. 3, pp. 1342–1347, 1973.

- [135] R. Eichhorn, D. Gonnella, G. Hoffstaetter, M. Liepe, and W. Weingarten, “On superconducting niobium accelerating cavities fired under N₂-gas exposure,” *arXiv preprint arXiv:1407.3220*, 2014.
- [136] M. Allen, Z. Farkas, H. Hogg, E. Hoyt, and P. Wilson, “Superconducting niobium cavity measurements at SLAC,” *IEEE Transactions on Nuclear Science*, vol. 18, no. 3, pp. 168–172, 1971.
- [137] A. Bruno, G. De Lange, S. Asaad, K. Van Der Eenden, N. Langford, and L. Di-Carlo, “Reducing intrinsic loss in superconducting resonators by surface treatment and deep etching of silicon substrates,” *Applied Physics Letters*, vol. 106, no. 18, p. 182601, 2015.
- [138] M. J. Reagor, *Superconducting cavities for circuit quantum electrodynamics*. PhD thesis, 2016.
- [139] T. L. Brecht, *Micromachined quantum circuits*. PhD thesis, Yale University, 2017.
- [140] J. Gao, *The physics of superconducting microwave resonators*. PhD thesis, 2008.
- [141] A. D. O’Connell, M. Ansmann, R. C. Bialczak, M. Hofheinz, N. Katz, E. Lucero, C. McKenney, M. Neeley, H. Wang, E. M. Weig, *et al.*, “Microwave dielectric loss at single photon energies and millikelvin temperatures,” *Applied Physics Letters*, vol. 92, no. 11, p. 112903, 2008.
- [142] C. Wang, C. Axline, Y. Y. Gao, T. Brecht, Y. Chu, L. Frunzio, M. Devoret, and R. J. Schoelkopf, “Surface participation and dielectric loss in superconducting qubits,” *Applied Physics Letters*, vol. 107, no. 16, p. 162601, 2015.
- [143] O. Dial, D. T. McClure, S. Poletto, G. Keefe, M. B. Rothwell, J. M. Gambetta, D. W. Abraham, J. M. Chow, and M. Steffen, “Bulk and surface loss in superconducting transmon qubits,” *Superconductor Science and Technology*, vol. 29, no. 4, p. 044001, 2016.

- [144] J. Turneaure, J. Halbritter, and H. Schwettman, “The surface impedance of superconductors and normal conductors: The Mattis-Bardeen theory,” *Journal of Superconductivity*, vol. 4, no. 5, pp. 341–355, 1991.
- [145] P. K. Day, H. G. LeDuc, B. A. Mazin, A. Vayonakis, and J. Zmuidzinas, “A broadband superconducting detector suitable for use in large arrays,” *Nature*, vol. 425, no. 6960, pp. 817–821, 2003.
- [146] J. P. Turneaure and N. T. Viet, “Superconducting Nb TM₀₁₀ mode electron-beam welded cavities,” *Applied Physics Letters*, vol. 16, no. 9, pp. 333–335, 1970.
- [147] T. Brecht, M. Reagor, Y. Chu, W. Pfaff, C. Wang, L. Frunzio, M. H. Devoret, and R. J. Schoelkopf, “Demonstration of superconducting micromachined cavities,” *Applied Physics Letters*, vol. 107, no. 19, p. 192603, 2015.
- [148] X. Rojas and J. Davis, “Superfluid nanomechanical resonator for quantum nanofluidics,” *Physical Review B*, vol. 91, no. 2, p. 024503, 2015.
- [149] A. Duh, A. Suhel, B. Hauer, R. Saeedi, P. Kim, T. Biswas, and J. Davis, “Microfluidic and nanofluidic cavities for quantum fluids experiments,” *Journal of Low Temperature Physics*, vol. 168, no. 1, pp. 31–39, 2012.
- [150] N. Zhelev, T. Abhilash, R. Bennett, E. Smith, B. Ilic, J. Parpia, L. Levitin, X. Rojas, A. Casey, and J. Saunders, “Fabrication of microfluidic cavities using si-to-glass anodic bonding,” *Review of Scientific Instruments*, vol. 89, no. 7, p. 073902, 2018.
- [151] S. Forstner, Y. Sachkou, M. Woolley, G. I. Harris, X. He, W. P. Bowen, and C. G. Baker, “Modelling of vorticity, sound and their interaction in two-dimensional superfluids,” *New Journal of Physics*, vol. 21, no. 5, p. 053029, 2019.
- [152] G. I. Harris, A. Sawadsky, Y. L. Sfindla, W. W. Wasserman, W. P. Bowen, and C. G. Baker, “Proposal for a quantum traveling Brillouin resonator,” *Optics Express*, vol. 28, no. 15, pp. 22450–22461, 2020.

- [153] L.-Y. Wu and L.-W. Chen, “Wave propagation in a 2d sonic crystal with a helmholtz resonant defect,” *Journal of Physics D: Applied Physics*, vol. 43, no. 5, p. 055401, 2010.
- [154] “Semiconductor wafer inc.” <http://www.semiwafer.com/>, Feb. 2022.
- [155] H. Zhang, W. Pang, H. Yu, and E. S. Kim, “High-tone bulk acoustic resonators on sapphire, crystal quartz, fused silica, and silicon substrates,” *Journal of Applied Physics*, vol. 99, no. 12, p. 124911, 2006.
- [156] S.-F. Wang, Y.-F. Hsu, J.-C. Pu, J. C. Sung, and L. Hwa, “Determination of acoustic wave velocities and elastic properties for diamond and other hard materials,” *Materials Chemistry and Physics*, vol. 85, no. 2-3, pp. 432–437, 2004.
- [157] A. Khelif and A. Adibi, *Phononic crystals*. Springer, 2015.
- [158] M. S. Kushwaha, P. Halevi, L. Dobrzynski, and B. Djafari-Rouhani, “Acoustic band structure of periodic elastic composites,” *Physical Review Letters*, vol. 71, no. 13, p. 2022, 1993.
- [159] D. P. Elford, L. Chalmers, F. V. Kusmartsev, and G. M. Swallowe, “Matryoshka locally resonant sonic crystal,” *The Journal of the Acoustical Society of America*, vol. 130, no. 5, pp. 2746–2755, 2011.
- [160] P. A. Deymier, *Acoustic metamaterials and phononic crystals*, vol. 173. Springer Science & Business Media, 2013.
- [161] A. Fathi, L. F. Kallivokas, and B. Poursartip, “Full-waveform inversion in three-dimensional pml-truncated elastic media,” *Computer Methods in Applied Mechanics and Engineering*, vol. 296, pp. 39–72, 2015.
- [162] W. Frei, “Using perfectly matched layers and scattering boundary conditions for wave electromagnetics problems.” <https://www.comsol.com/blogs/using-perfectly-matched-layers-and-scattering-boundary-conditions-for-wave-electromagnetics-problems>, Jan. 2015.

- [163] J. Gaffney, “How to automate meshing in frequency bands for acoustic simulations.” <https://www.comsol.com/blogs/how-to-automate-meshing-in-frequency-bands-for-acoustic-simulations/>, June 2019.
- [164] “Material properties database.” <http://matweb.com/index.aspx/>, Feb. 2022.
- [165] D. McGuigan, C. Lam, R. Gram, A. Hoffman, D. Douglass, and H. Gutche, “Measurements of the mechanical q of single-crystal silicon at low temperatures,” *Journal of Low Temperature Physics*, vol. 30, no. 5, pp. 621–629, 1978.
- [166] M. Goryachev, D. L. Creedon, E. N. Ivanov, S. Galliou, R. Bourquin, and M. E. Tobar, “Extremely low-loss acoustic phonons in a quartz bulk acoustic wave resonator at millikelvin temperature,” *Applied Physics Letters*, vol. 100, no. 24, p. 243504, 2012.
- [167] S. D. Penn, G. M. Harry, A. M. Gretarsson, S. E. Kittelberger, P. R. Saulson, J. J. Schiller, J. R. Smith, and S. O. Swords, “High quality factor measured in fused silica,” *Review of Scientific Instruments*, vol. 72, no. 9, pp. 3670–3673, 2001.
- [168] D. Senkal, M. J. Ahamed, M. H. A. Ardakani, S. Askari, and A. M. Shkel, “Demonstration of 1 million Q -factor on microglassblown wineglass resonators with out-of-plane electrostatic transduction,” *Journal of Microelectromechanical Systems*, vol. 24, no. 1, pp. 29–37, 2014.
- [169] M. Mitchell, D. P. Lake, and P. E. Barclay, “Realizing $Q > 300\,000$ in diamond microdisks for optomechanics via etch optimization,” *APL Photonics*, vol. 4, no. 1, p. 016101, 2019.
- [170] W. Bogaerts, P. Bienstman, and R. Baets, “Scattering at sidewall roughness in photonic crystal slabs,” *Optics Letters*, vol. 28, no. 9, pp. 689–691, 2003.
- [171] J. D. Joannopoulos, S. G. Johnson, J. N. Winn, and R. D. Meade, *Photonic Crystals*. Princeton University Press, 2011.

- [172] R. Doolittle, H. Überall, and P. Uginčius, “Sound scattering by elastic cylinders,” *The Journal of the Acoustical Society of America*, vol. 43, no. 1, pp. 1–14, 1968.
- [173] L. W. Schmerr Jr and A. Sedov, “An elastodynamic model for compressional and shear wave transducers,” *The Journal of the Acoustical Society of America*, vol. 86, no. 5, pp. 1988–1999, 1989.
- [174] F. Pobell, *Matter and Methods at Low Temperatures*, vol. 2. Springer, 2007.
- [175] B. Baudouy, “Heat transfer and cooling techniques at low temperature,” *arXiv preprint arXiv:1501.07153*, 2015.
- [176] LakeShore, “Cryogenic wire / technical - specifications.” <https://www.lakeshore.com/products/categories/specification/temperature-products/cryogenic-accessories/cryogenic-wire>, Feb. 2019.
- [177] P. R. Roach, J. Ketterson, and M. Kuchnir, “Hydraulically actuated valve for very low temperatures,” *Review of Scientific Instruments*, vol. 43, no. 6, pp. 898–899, 1972.
- [178] R. B. Hallock, “A bellows seal superfluid valve,” *Review of Scientific Instruments*, vol. 43, no. 11, pp. 1713–1714, 1972.
- [179] V. Dotsenko and N. Mulders, “A really simple cryogenic valve,” *Journal of Low Temperature Physics*, vol. 134, no. 1, pp. 443–446, 2004.
- [180] WIKA Instruments. <https://www.wika.com/>, 2022.
- [181] C. Lim, “Indium seals for low-temperature and moderate-pressure applications,” *Review of Scientific Instruments*, vol. 57, no. 1, pp. 108–114, 1986.
- [182] R. J. Corruccini and J. J. Gniewek, *Thermal expansion of technical solids at low temperatures: A compilation from the literature*, vol. 29. US Department of Commerce, National Bureau of Standards, 1961.
- [183] B. C. Coalmon, “CNST nanolithography toolbox,” 2016.

- [184] H. Moriceau, F. Rieutord, F. Fournel, Y. Le Tiec, L. Di Cioccio, C. Morales, A. Charvet, and C. Deguet, “Overview of recent direct wafer bonding advances and applications,” *Advances in Natural Sciences: Nanoscience and Nanotechnology*, vol. 1, no. 4, p. 043004, 2011.
- [185] P. Mao and J. Han, “Fabrication and characterization of 20 nm planar nanofluidic channels by glass–glass and glass–silicon bonding,” *Lab on a Chip*, vol. 5, no. 8, pp. 837–844, 2005.
- [186] Y.-K. Lin and J.-N. Kuo, “Fabrication of sub-40 nm nanofluidic channels using thin glass-glass bonding,” in *2011 6th IEEE International Conference on Nano/Micro Engineered and Molecular Systems*, pp. 351–354, IEEE, 2011.
- [187] Q.-Y. Tong, G. Cha, R. Gafiteanu, and U. Gosele, “Low temperature wafer direct bonding,” *Journal of Microelectromechanical Systems*, vol. 3, no. 1, pp. 29–35, 1994.
- [188] T. Plach, K. Hingerl, S. Tollabimazraehno, G. Hesser, V. Dragoi, and M. Wimplinger, “Mechanisms for room temperature direct wafer bonding,” *Journal of Applied Physics*, vol. 113, no. 9, p. 094905, 2013.
- [189] C. Gui, M. Elwenspoek, N. Tas, and J. G. Gardeniers, “The effect of surface roughness on direct wafer bonding,” *Journal of Applied Physics*, vol. 85, no. 10, pp. 7448–7454, 1999.
- [190] N. Miki and S. Spearing, “Effect of nanoscale surface roughness on the bonding energy of direct-bonded silicon wafers,” *Journal of Applied Physics*, vol. 94, no. 10, pp. 6800–6806, 2003.
- [191] N. Chiem, L. Lockyear-Shultz, P. Andersson, C. Skinner, and D. J. Harrison, “Room temperature bonding of micromachined glass devices for capillary electrophoresis,” *Sensors and Actuators B: Chemical*, vol. 63, no. 3, pp. 147–152, 2000.

- [192] Z.-J. Jia, Q. Fang, and Z.-L. Fang, “Bonding of glass microfluidic chips at room temperatures,” *Analytical Chemistry*, vol. 76, no. 18, pp. 5597–5602, 2004.
- [193] H. Moriceau, F. Rieutord, F. Fournel, L. Di Cioccio, C. Moulet, L. Libralesso, P. Gueguen, R. Taibi, and C. Deguet, “Low temperature direct bonding: An attractive technique for heterostructures build-up,” *Microelectronics Reliability*, vol. 52, no. 2, pp. 331–341, 2012.
- [194] X. Ma, W. Liu, Z. Song, W. Li, and C. Lin, “Void-free low-temperature silicon direct-bonding technique using plasma activation,” *Journal of Vacuum Science & Technology B: Microelectronics and Nanometer Structures Processing, Measurement, and Phenomena*, vol. 25, no. 1, pp. 229–234, 2007.
- [195] R. He, M. Fujino, A. Yamauchi, and T. Suga, “Novel hydrophilic SiO₂ wafer bonding using combined surface-activated bonding technique,” *Japanese Journal of Applied Physics*, vol. 54, no. 3, p. 030218, 2015.
- [196] R. He, M. Fujino, A. Yamauchi, and T. Suga, “Combined surface-activated bonding technique for low-temperature hydrophilic direct wafer bonding,” *Japanese Journal of Applied Physics*, vol. 55, no. 4S, p. 04EC02, 2016.
- [197] R. He, A. Yamauchi, and T. Suga, “Sequential plasma activation methods for hydrophilic direct bonding at sub-200°C,” *Japanese Journal of Applied Physics*, vol. 57, no. 2S1, p. 02BD03, 2018.
- [198] C. Wang, Y. Wang, Y. Tian, C. Wang, and T. Suga, “Room-temperature direct bonding of silicon and quartz glass wafers,” *Applied Physics Letters*, vol. 110, no. 22, p. 221602, 2017.
- [199] L. Pasternak and Y. Paz, “Low-temperature direct bonding of silicon nitride to glass,” *RSC Advances*, vol. 8, no. 4, pp. 2161–2172, 2018.
- [200] A. Quade, H. Wulff, H. Steffen, T. Tun, and R. Hippler, “Investigation of the aluminium oxidation in an oxygen plasma excited by microwaves,” *Thin Solid Films*, vol. 377, pp. 626–630, 2000.

- [201] K. R. Williams, K. Gupta, and M. Wasilik, “Etch rates for micromachining processing-part II,” *Journal of Microelectromechanical Systems*, vol. 12, no. 6, pp. 761–778, 2003.
- [202] G. B. Airy, “VI. on the phænomena of Newton’s rings when formed between two transparent substances of different refractive powers,” *The London, Edinburgh, and Dublin Philosophical Magazine and Journal of Science*, vol. 2, no. 7, pp. 20–30, 1833.
- [203] J. Aitken, “Swept-frequency microwave Q-factor measurement,” in *Proceedings of the Institution of Electrical Engineers*, vol. 123, pp. 855–862, IET, 1976.
- [204] J. B. Hertzberg, *Back-action evading measurements of nanomechanical motion approaching quantum limits*. PhD thesis, 2009.
- [205] D. I. Schuster, *Circuit quantum electrodynamics*. PhD thesis, 2007.
- [206] K. L. Geerlings, *Improving coherence of superconducting qubits and resonators*. PhD thesis, 2013.
- [207] P. J. Petersan and S. M. Anlage, “Measurement of resonant frequency and quality factor of microwave resonators: Comparison of methods,” *Journal of Applied Physics*, vol. 84, no. 6, pp. 3392–3402, 1998.
- [208] S. Krinner, S. Storz, P. Kurpiers, P. Magnard, J. Heinsoo, R. Keller, J. Luetolf, C. Eichler, and A. Wallraff, “Engineering cryogenic setups for 100-qubit scale superconducting circuit systems,” *EPJ Quantum Technology*, vol. 6, no. 1, p. 2, 2019.
- [209] S. Kumar, *Low temperature microwave optomechanics: anomalous force noise and optomechanically induced transparency*. PhD thesis, Université Grenoble Alpes, 2021.
- [210] A. A. Clerk, M. H. Devoret, S. M. Girvin, F. Marquardt, and R. J. Schoelkopf, “Introduction to quantum noise, measurement, and amplification,” *Reviews of Modern Physics*, vol. 82, no. 2, p. 1155, 2010.

- [211] P. R. Saulson, “Thermal noise in mechanical experiments,” *Physical Review D*, vol. 42, no. 8, p. 2437, 1990.
- [212] A. J. Weinstein, *Quantum Electromechanics with Two Tone Drive*. PhD thesis, California Institute of Technology, 2016.
- [213] Zurich Instruments, “Principles of lock-in detection and the state of the art,” *CH-8005 Zurich, Switzerland, Accessed*, 2016.
- [214] Zurich Instruments, “HF2 user manual - LabOne edition.” <https://www.zhinst.com/manuals/hf2>, 2019.
- [215] H. Packard, “Phase noise characterization of microwave oscillators,” *Frequency Discriminator Method*, 1985.
- [216] M. Cerna and A. F. Harvey, “The fundamentals of FFT-based signal analysis and measurement,” tech. rep., Application Note 041, National Instruments, 2000.
- [217] J. R. Lane, D. Tan, N. R. Beysengulov, K. Nasyedkin, E. Brook, L. Zhang, T. Stefanski, H. Byeon, K. W. Murch, and J. Pollanen, “Integrating superfluids with superconducting qubit systems,” *Phys. Rev. A*, vol. 101, p. 012336, Jan 2020.
- [218] C. U. Lei, L. Krayzman, S. Ganjam, L. Frunzio, and R. J. Schoelkopf, “High coherence superconducting microwave cavities with indium bump bonding,” *Applied Physics Letters*, vol. 116, no. 15, p. 154002, 2020.
- [219] COMSOL, “Structural mechanics module user’s guide.” <https://doc.comsol.com/5.3/StructuralMechanicsModuleUsersGuide.pdf>, Feb. 2017.
- [220] COMSOL, “Acoustics module user’s guide.” <https://doc.comsol.com/5.5/AcousticsModuleUsersGuide.pdf>, Feb. 2019.

Appendices

Appendix A: Experiment Cell Drawings

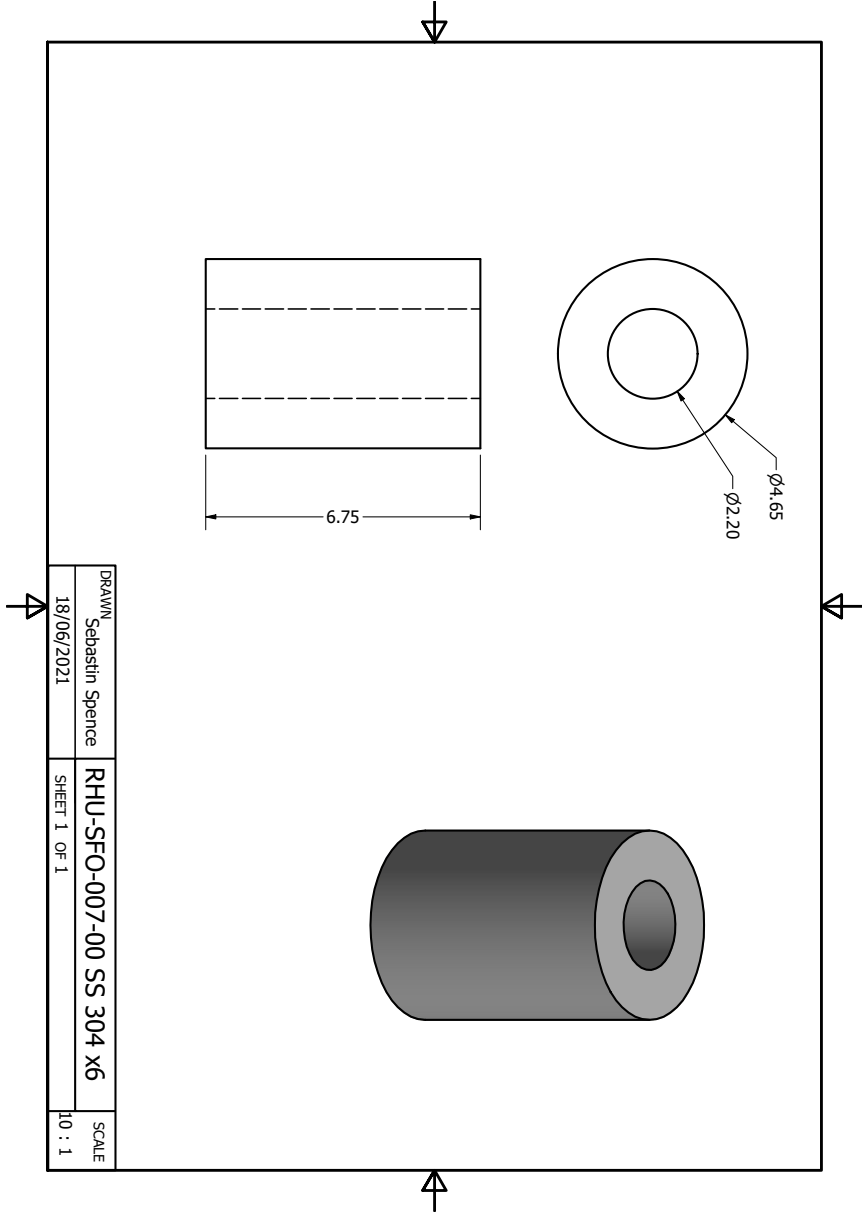


Figure A.1: Stainless steel washer for fitting inside aluminium base.

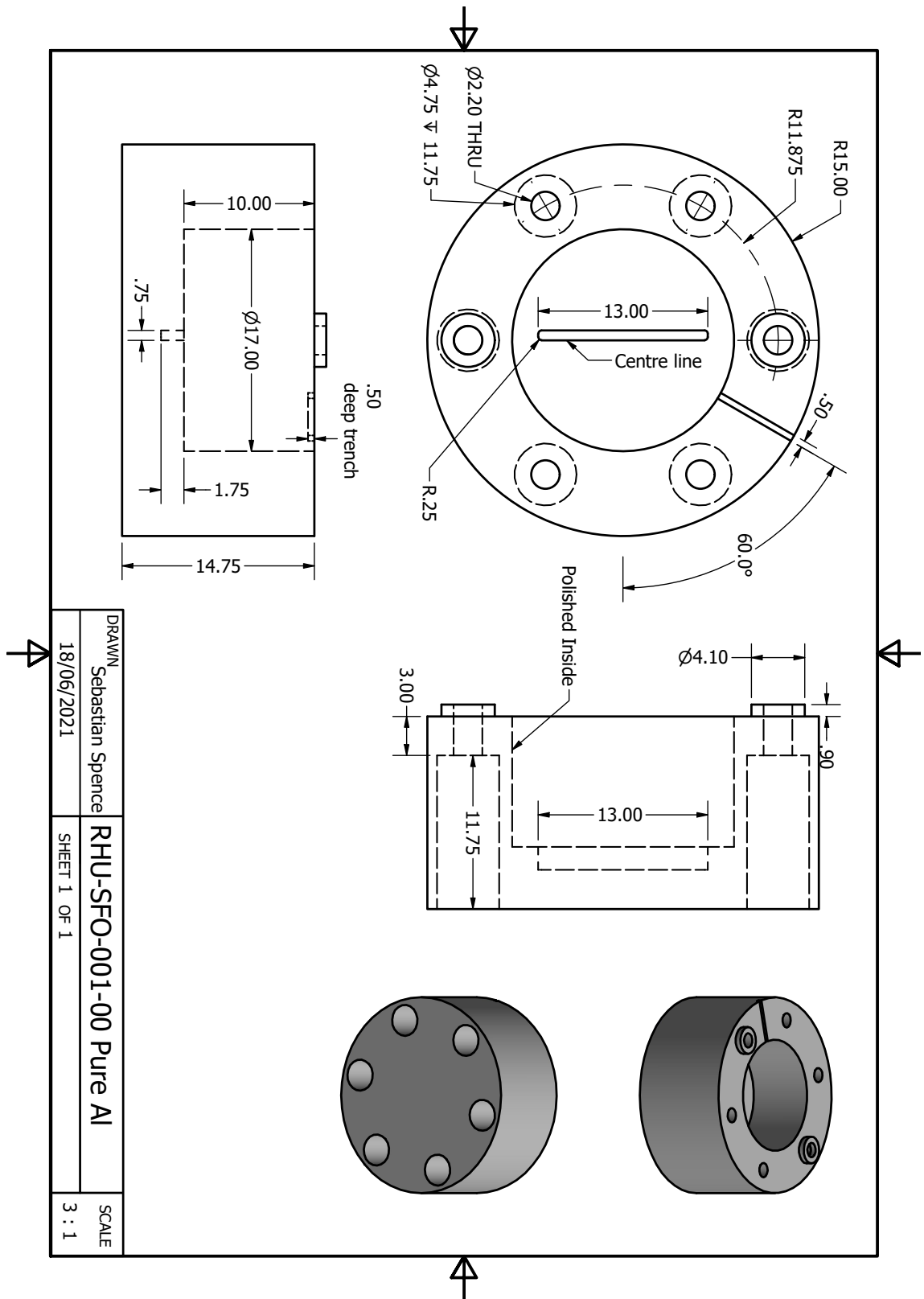


Figure A.2: Aluminium cavity base for D type chips.

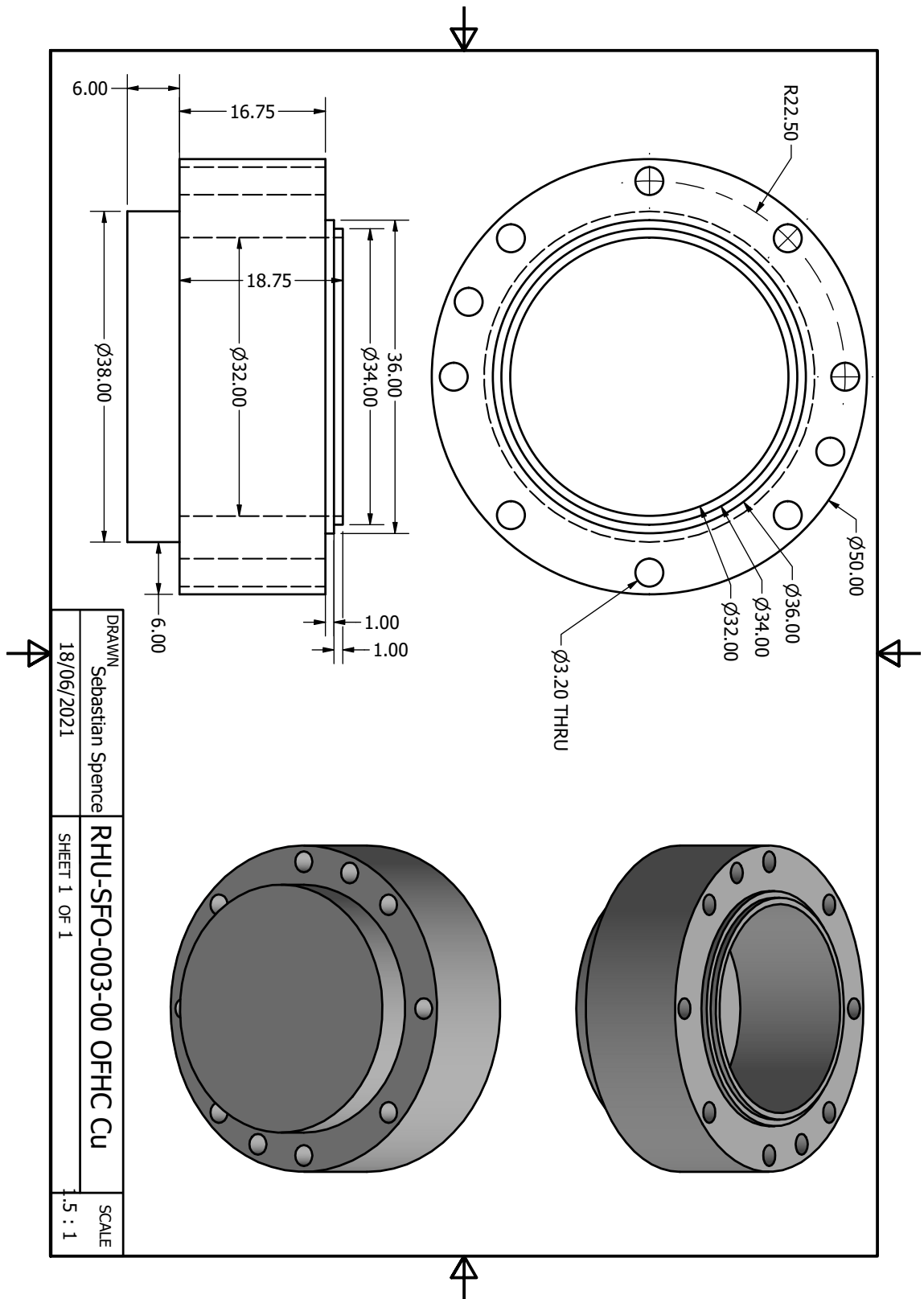


Figure A.4: Copper experimental cell base.

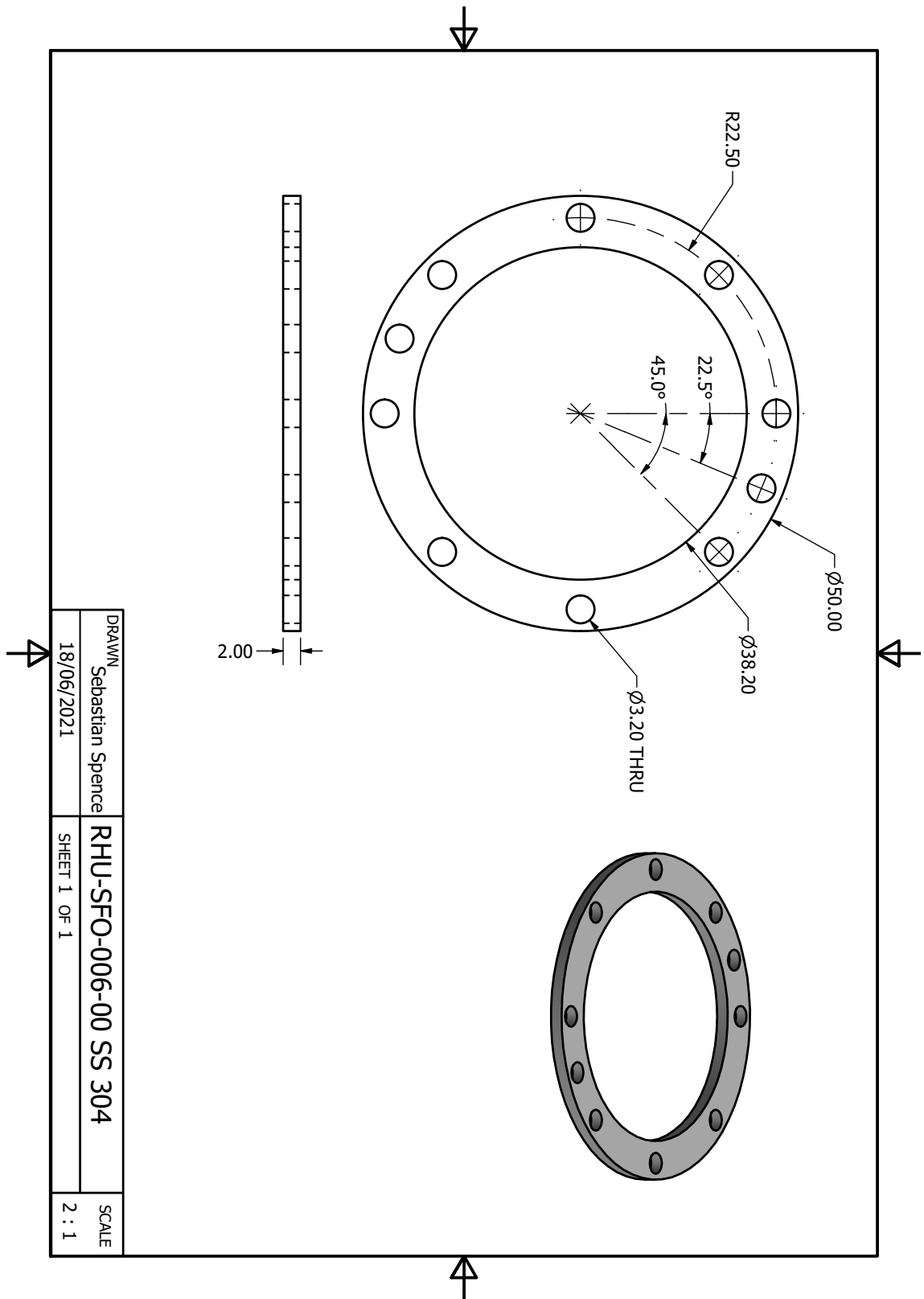


Figure A.6: Stainless steel clamp for copper cell base.

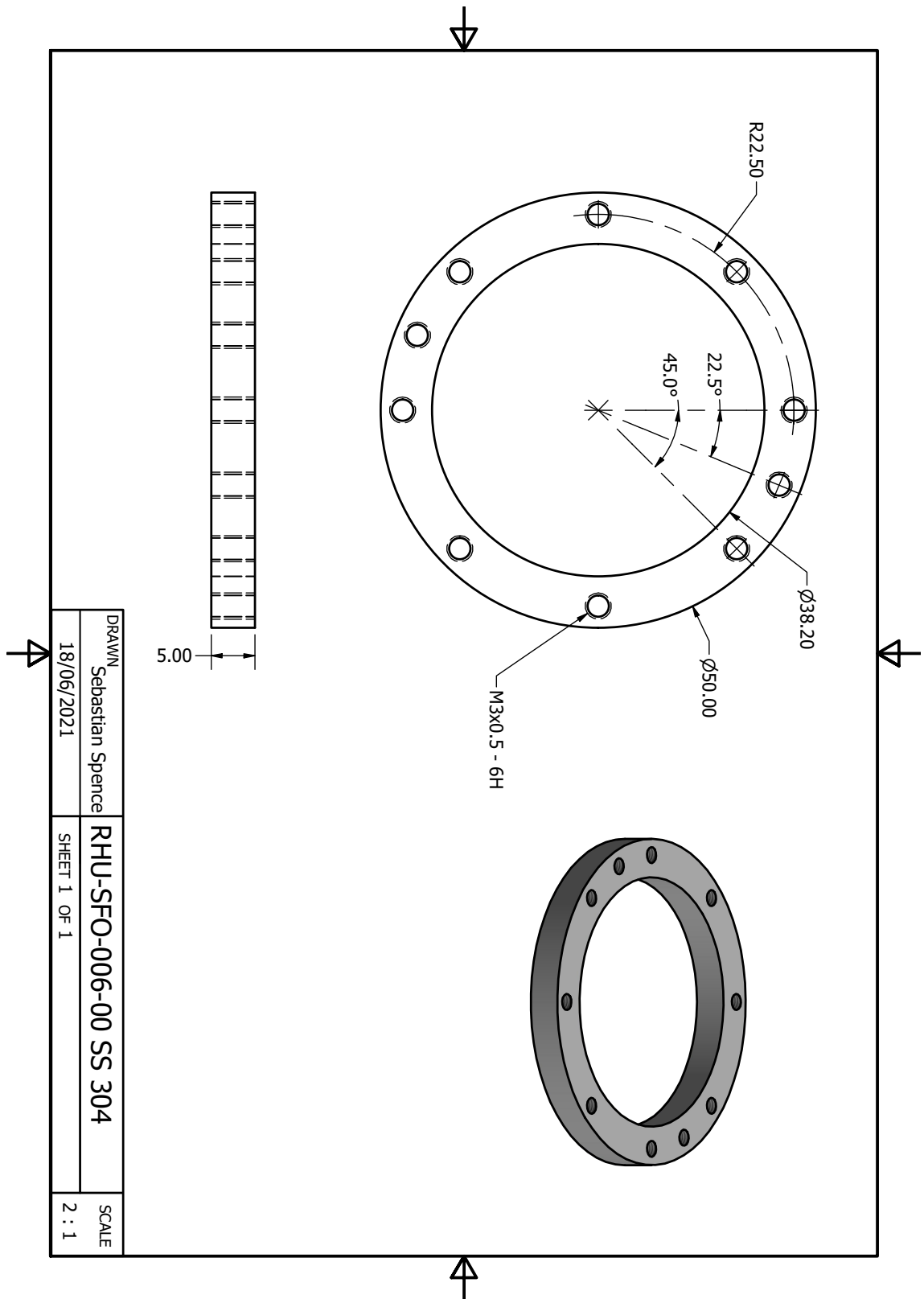


Figure A.7: Stainless steel clamp for copper cell lid.

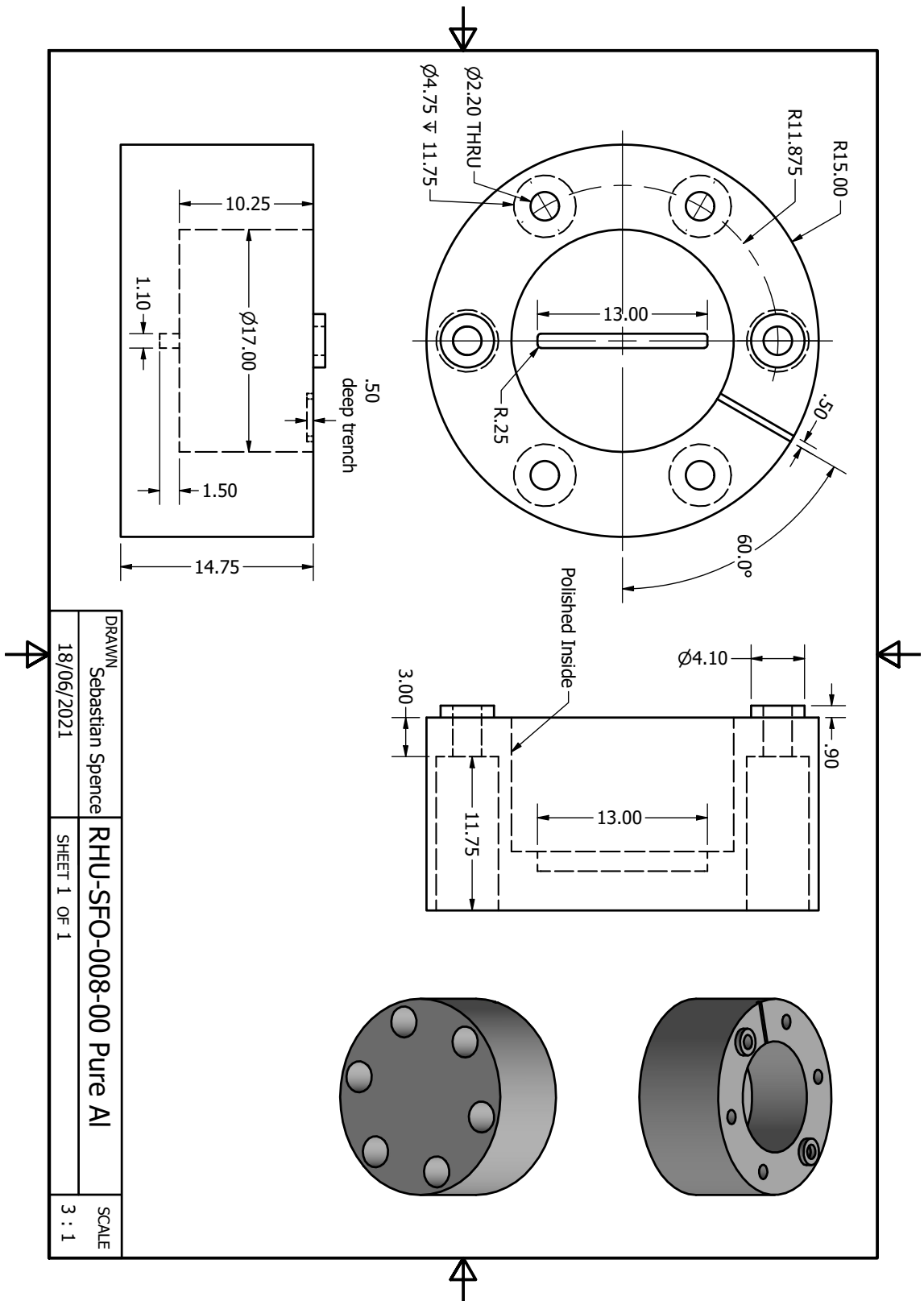


Figure A.8: Aluminium cavity base for A/B/C type chips.

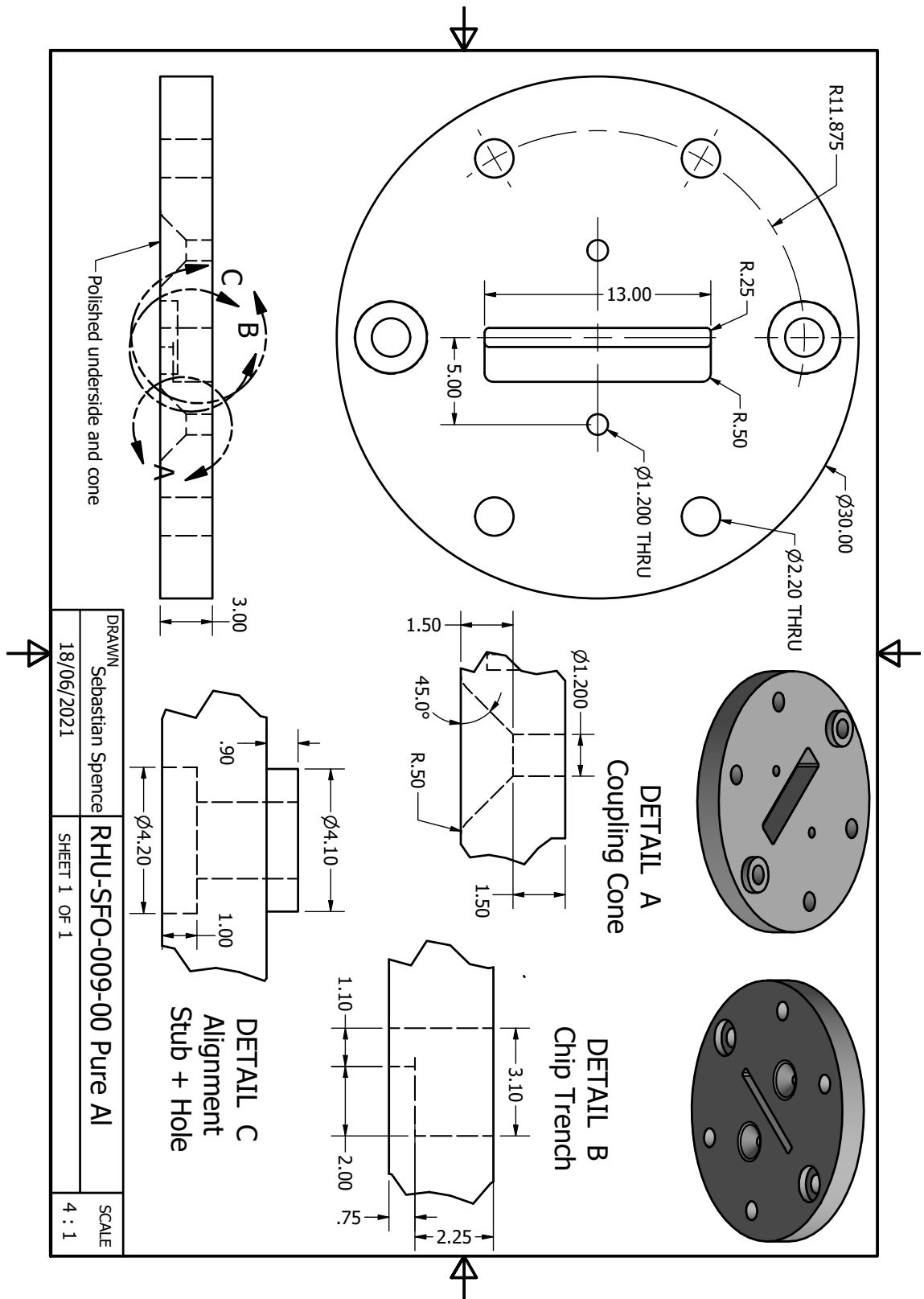


Figure A.9: Aluminium cavity lid for A/B/C type chips.

Appendix B: COMSOL Abstracted Q

This appendix gives the full derivation from equations of motion for the method of abstracting quality factors from Sections 2.3.6, for the purpose of isolating ^4He and substrate internal losses from significant boundary condition related errors, for 3D sonic crystal simulations in COMSOL. The quality factors described here are Q 's of the total mode, not the bulk material quality factors due to intrinsic losses, instead these are labelled Q' . These are not accessible variables in COMSOL and so to transform into a form consisting of accessible terms start with the COMSOL specific equations of motion. For the substrate mechanical system this is [219]:

$$\mathbf{M}\ddot{\mathbf{u}} + \mathbf{C}\dot{\mathbf{u}} + \mathbf{K}\mathbf{u} = \mathbf{f}(t) , \quad (\text{B.1})$$

where \mathbf{u} is the displacement vector, \mathbf{M} is the mass matrix, \mathbf{C} is the viscous damping matrix, \mathbf{K} is the stiffness matrix, and $\mathbf{f}(t)$ is the force vector. Assuming the excitation and response are harmonic this can be written in the frequency domain as:

$$(-\Omega\mathbf{M} + i\Omega\mathbf{C} + \mathbf{K})\tilde{\mathbf{u}} = \tilde{\mathbf{f}}(t) , \quad (\text{B.2})$$

where $\tilde{\mathbf{u}}$ and $\tilde{\mathbf{f}}(t)$ are both complex. For the case of isotropic losses, \mathbf{C} can be understood as a complex multiplier to the stiffness matrix:

$$\mathbf{C} = \frac{\alpha_{\text{sub}}\mathbf{K}}{\Omega} , \quad (\text{B.3})$$

where α_{sub} is the substrate's dimensionless isotropic loss factor, defined for a complex Young's modulus as the ratio of its real and complex parts. Equation B.2 then becomes:

$$(-\Omega^2\mathbf{M} + (1 + i\alpha_{\text{sub}})\mathbf{K})\tilde{\mathbf{u}} = \tilde{\mathbf{f}}(t) . \quad (\text{B.4})$$

There is a quick way to relate α_{sub} to $Q_{\text{m}}^{\text{sub}}$ via the complex stress-strain relation:

$$\tilde{\sigma} = \tilde{E}\tilde{\varepsilon} = (E' + iE'')\tilde{\varepsilon} , \quad (\text{B.5})$$

where $\tilde{\sigma}$ is the complex stress, \tilde{E} is the complex Young's Modulus, $\tilde{\epsilon}$ is the complex strain, E' is the storage modulus and E'' is the loss modulus. In the case of low losses e.g. small E'' then $E \approx E'$ and the above equation can be written:

$$\tilde{\sigma} = E(1 + i\alpha_{\text{sub}})\tilde{\epsilon}. \quad (\text{B.6})$$

If E'' is not small then a $1/\sqrt{1 + (\alpha_{\text{sub}})^2}$ factor must be added. For an isotropic solid defined in this way, the energy dissipated per loading cycle is:

$$D = \pi E'' \epsilon_A^2, \quad (\text{B.7})$$

where ϵ_A is the strain amplitude. Similarly the maximum elastic potential energy in the cycle can be defined:

$$W = \frac{1}{2} E' \epsilon_A^2. \quad (\text{B.8})$$

Inserting both these equations into the definition of quality factor yields:

$$Q_m^{\text{sub}'} = 2\pi \frac{\frac{1}{2} E' \epsilon_A^2}{\pi E'' \epsilon_A^2}, \quad (\text{B.9})$$

where $Q_m^{\text{sub}'}$ is the intrinsic bulk quality factor of the substrate. Which reduces to:

$$Q_m^{\text{sub}'} = \frac{E'}{E''} = \frac{1}{\alpha_{\text{sub}}}, \quad (\text{B.10})$$

showing that, for an isolated system with isotropic attenuation, the attenuation factor is the inverse of the quality factor. However for the coupled system this $Q_m^{\text{sub}'}$ will be altered by the distribution of energy throughout the system.

To instead calculate Q_m^{sub} , assuming the attenuation factor is only applied to the energy participation of the substrate, the decay of the amplitude can be used. Assuming $\alpha_{\text{sub}} \ll 1$ solutions to Eq. B.1 will be of the form:

$$\mathbf{u}(\mathbf{r}, t) = \mathbf{u}_0(\mathbf{r}) e^{-\frac{1}{2}\alpha_{\text{sub}}\Omega t - i\Omega t}, \quad (\text{B.11})$$

or in terms of period as:

$$\mathbf{u}(\mathbf{r}, t) = \mathbf{u}_0(\mathbf{r})e^{-\pi\alpha_{\text{sub}}t/T_0-2i\pi t/T_0} , \quad (\text{B.12})$$

where T_0 is the period. As strain is proportional to displacement:

$$\boldsymbol{\varepsilon}(\mathbf{r}, t) = \boldsymbol{\varepsilon}_0(\mathbf{r})e^{-\pi\alpha_{\text{sub}}t/T_0-2i\pi t/T_0} . \quad (\text{B.13})$$

Taking this at two points a single period apart, arbitrarily $t = 0$ and $t = T_0$ yields:

$$\boldsymbol{\varepsilon}(\mathbf{r}, t = 0) = \boldsymbol{\varepsilon}_0(\mathbf{r}) , \quad (\text{B.14})$$

$$\boldsymbol{\varepsilon}(\mathbf{r}, t = T_0) = \boldsymbol{\varepsilon}_0(\mathbf{r})e^{-\pi\alpha_{\text{sub}}} . \quad (\text{B.15})$$

Taking $t = 0$ to be the point of peak amplitude, Eq. B.8 can then be used to give maximum elastic potential energy at the start and end of a cycle:

$$W(\mathbf{r}, t = 0) = \frac{1}{2}E'|\boldsymbol{\varepsilon}_0(\mathbf{r})|^2 , \quad (\text{B.16})$$

$$W(\mathbf{r}, t = T_0) = \frac{1}{2}E'|\boldsymbol{\varepsilon}_0(\mathbf{r})|^2e^{-2\pi\alpha_{\text{sub}}} . \quad (\text{B.17})$$

The dissipated energy in one cycle is then $W(\mathbf{r}, t = 0) - W(\mathbf{r}, t = T_0)$. Taking $U_{\text{sub}} = \int \frac{1}{2}E'|\boldsymbol{\varepsilon}_0(\mathbf{r})|^2d^3r$ as the initial maximum elastic potential energy within the substrate. $Q_{\text{m}}^{\text{sub}}$ can then be written as:

$$Q_{\text{sub}} = 2\pi \frac{U_0}{U_{\text{sub}}(1 - e^{2\pi\alpha_{\text{sub}}})} , \quad (\text{B.18})$$

where U_0 is the energy in the entire coupled system. Using a Taylor approximation and $\mathcal{R}_{\text{sub}} = U_{\text{sub}}/U_0$ the maximum fraction of energy during a cycle within the substrate, $Q_{\text{m}}^{\text{sub}}$ can be written as:

$$Q_{\text{m}}^{\text{sub}} = \frac{1}{\alpha_{\text{sub}}\mathcal{R}_{\text{sub}}} . \quad (\text{B.19})$$

This is then the quality factor of the entire coupled acoustic mode due to internal material loss of the substrate. A similar method can be followed for the acoustics [220], starting with the frequency domain 1D definition of the complex wave vector k :

$$k = \frac{\Omega}{c} - i\alpha_{\text{int}} , \quad (\text{B.20})$$

where c is the speed of sound in helium and α_{int} is the loss factor, though some care should be taken with α_{int} as this is not necessarily equivalent to the isotropic loss factor in the solid mechanics model domain. Using this complex k and the equations of motion for acoustics yields a pressure of the form:

$$p(x, t) = p_0(x)e^{-\alpha_{\text{int}}x}e^{-i((\Omega/c)x - \Omega t)} , \quad (\text{B.21})$$

where $p(x, t)$ is the complex pressure, $p_0(x)$ is the initial amplitude at a point in x , α is a general attenuation factor, and c is the speed of sounds in the acoustic medium. However as α_{int} is defined along x it is not directly accessible in COMSOL as a dimensionless factor, instead a number of definitions are possible. Isotropic attenuation defined in dB/λ is chosen for simplicity, as this leaves density as a real factor (converted to a dimensionless α_{int} in Section 2.3.6). This choice of α_{int} gives the complex k :

$$k = \frac{\Omega}{c} \left(1 - i \ln(10) \frac{\alpha_{\text{dB}}}{2\pi \cdot 20} \right) , \quad (\text{B.22})$$

where α_{dB} denotes this attenuation being defined in dB/λ . As the complex pressure encodes all information of the mode, the maximum acoustic energy density in a cycle can be defined defined:

$$W(x) = \frac{1}{2} \frac{|p(x, t)|^2}{\rho_{\text{h}} c_{\text{h}}^2} , \quad (\text{B.23})$$

where ρ_{h} is the ^4He density, simplified by choice to α_{dB} to the real density, and c_{h} is the complex helium speed of sound defined $c_{\text{h}} = \Omega/k$. Combining Eq.'s B.21 and B.22 and substituting into the energy gives:

$$W(x) = W_0(x)10^{-\frac{\alpha_{dB}\Omega}{10 \cdot 2\pi c_h}x}, \quad (B.24)$$

with the initial energy density:

$$W_0(x) = \frac{1}{2} \frac{p_0(x)^2}{\rho_h c_h^2}. \quad (B.25)$$

Taking this energy at $x = 0$ and after one cycle at $x = \lambda = 2\pi c_h/\Omega$ gives:

$$W(x = 0) = W_0, \quad (B.26)$$

$$W(x = 2\pi c_h/\Omega) = W_0 10^{-\frac{\alpha_{dB}}{10}x}. \quad (B.27)$$

It can be helpful to define a conversion from attenuation in dB/λ to an equivalent isotropic attenuation factor here via:

$$\alpha_{dB} = -10 \log_{10}(1 - 2\pi\alpha_{int}), \quad (B.28)$$

where α_{int} is the equivalent to the isotropic loss factor for solid mechanics. Note this definition encodes the Taylor approximation from the solid mechanics, which is only relevant at high attenuation. Using this $W(x = 2\pi c_h/\Omega)$ can be rewritten:

$$W(x = 2\pi c_h/\Omega) = W_0(1 - 2\pi\alpha_{int}). \quad (B.29)$$

Again using the definition of quality factor, the difference between $W(x = 2\pi c_h/\Omega)$ and $W(x = 0)$ gives the energy density lost over one cycle, and using $U_{int} = \int W_0 d^3r$ gives the maximum acoustic potential energy of the harmonic. The Q factor applied by the acoustic domain can be written:

$$Q_m^{int} = 2\pi \frac{U_0}{U_{int} - U_{int}(1 - 2\pi\alpha_{int})}, \quad (B.30)$$

which is equivalent to:

$$Q_{\text{int}} = \frac{1}{\alpha_{\text{int}} \mathcal{R}_{\text{int}}}, \quad (\text{B.31})$$

where $\mathcal{R}_{\text{int}} = U_0/U_{\text{int}}$ is the maximum fraction of energy during a cycle within the helium. Giving a similar form to Eq. B.19 due to the conversion to isotropic loss factor equivalent. Note $U_0 \leq U_{\text{sub}} + U_{\text{int}}$, where the sum of the maximum energies is larger when the peak acoustic energy does not coincide with zero solid mechanical energy, and vice versa. Now using the quality factors described by variables accessible in COMSOL, the more general equation 2.35 can be rewritten using Eq.'s B.19 and B.31 to:

$$Q_{\text{m}} \alpha_{\text{int}} = \frac{1}{\mathcal{R}_{\text{int}}} \left(1 + \frac{\alpha_{\text{sub}} \mathcal{R}_{\text{sub}}}{\alpha_{\text{int}} \mathcal{R}_{\text{int}}} \right)^{-1}, \quad (\text{B.32})$$

where α_{sub} and α_{int} have been used to represent the intrinsic attenuation in the substrate and helium respectively. As $Q_{\text{m}}^{\text{sub/int}'} = 1/\alpha_{\text{sub/int}'}$ expresses the quality factor of an isolated material with only intrinsic losses, the above expression can be thought of as $Q_{\text{m}}/Q_{\text{m}}^{\text{int}'}$, the ratio of whole system mode quality factor to the unspoilt ${}^4\text{He}$ quality factor, or as the suppression of the ${}^4\text{He}$ quality factor due to the presence of the substrate. Assuming that \mathcal{R}_{int} and \mathcal{R}_{sub} are constant over varying α 's, both α 's can be varied without affecting $Q_{\text{m}}/Q_{\text{m}}^{\text{int}'}$, so long as their ratio $\alpha_{\text{sub}}/\alpha_{\text{int}}$ is maintained. This then allows both attenuations to be taken to much higher values, suppressing the total system Q_{m} , but keeping $Q_{\text{m}}/Q_{\text{m}}^{\text{int}'}$ intact. This should work up to fairly high attenuations, provided both $\alpha^2 \ll 1$.

Note the inverse of equation B.28 is:

$$\alpha_{\text{isotropic}} = \frac{1}{2\pi} (-10^{-\alpha_{\text{dB}}/10}) \quad (\text{B.33})$$

B.1 Energy Definitions in COMSOL

In COMSOL the physics is often defined through complex variables, especially for harmonic studies, where the real and imaginary part encode information about the mode. For solid mechanics this is complex displacement / strain, whilst acoustics uses complex pressure. This can be thought of as the real part of the variable representing the potential

energy terms and the imaginary representing the kinetic, though this is a simplification. Some of these complex terms are used in the equations above. This complex nature becomes important when calculating the energy distribution and estimating the quality factor. COMSOL factors attenuation as an exponential decay to the amplitude of the complex key variables, and can therefore be thought of as a loss factor applied to the maximum potential energy in a cycle of that section of the physics. This means that U_{int} and U_{sub} are the maximum potential energy in the helium and substrate respectively, as calculated from the complex pressure and strain. These do not necessarily occur at the same point in the cycle and so the sum of these two energies can be greater than the total system energy U_0 . This means taking U_0 as the sum of these two energies can introduce small errors to calculations. To get the most accurate quality factors U_0 should be calculated from the average energies of the different physics, a sum of the average kinetic and potential energies of both the helium and the substrate. A physical interpretation of this is that some energy is transferred back and forth between the two mediums each cycle, and therefore both the solid and acoustic attenuations are applied to this quantity of energy. The result is a quality factor that is slightly lower (due to more effective attenuation) than one calculated by using average energies.

Appendix C: Minor Fridge Alterations

The following is a list of more minor alternations to the dilution fridge not covered in the main text, mostly to create space or decrease thermal contact:

- Remove older low frequency coax to 1K, replacing plugs and O-rings at RT.
- Removal of the rotatable shield, which covers the toploading hole through the centre of the fridge plates within the IVC volume. This was to make room for the out microwave line. The pole down from RT, its handle and O-ring were also replaced with a plug and new O-rings.
- Card to break thermal contact between the spirals of the continuous heat exchanger (improved base temp by a few mK).
- Hermetic Stycast 1266 feedthroughs at RT for DC and AC lines.
- Teflon collar around the central hole of the 1K pot to stop thermal contact between 4K coax and 1K stage.
- Silver tape to cover holes between plates inside the IVC to reduce base temperature, and silver tape over the holes in the liquid helium bath baffles to increase evaporation efficiency .
- RT to 4K coax thermalisation + radiation shield down the central top loading tube.
- Design and replacement of experimental stage.
- Isolation of the ^3He pumping system from the 'B' system and the old GHS system.

Appendix D: Fridge Pumping Systems

Figure D.1 shows the ^3He circuit gas handling system for the fridge. Not shown are the 4 K cold trap and dilution unit within the fridge, this figure shows the RT sections of the circuit outside of the OVC. Shown in red is the circuit taken by the ^3He in normal circulation mode, and shown in grey is the OVC with condensing and return side labelled. The main pumping force is provided by a large turbo pump (housed behind the ^3He gas handling board) backed by the ^3He rotary (located in the pit below the fridge). There are two cold traps to allow cleaning of one whilst the other is used in circulation, enabling continuous running for long periods. Valve 5 is left open along with the dumps during circulation in case of a blockage within the fridge. When the pressure on G4 exceeds 800 mbar the power is cut to both pumps and the bypass opens, allowing gas to flow from the condenser side of the circuit into the dump. There is no bypass on the still side of the circuit as the running pressure is low enough and volume large enough to avoid overpressure.

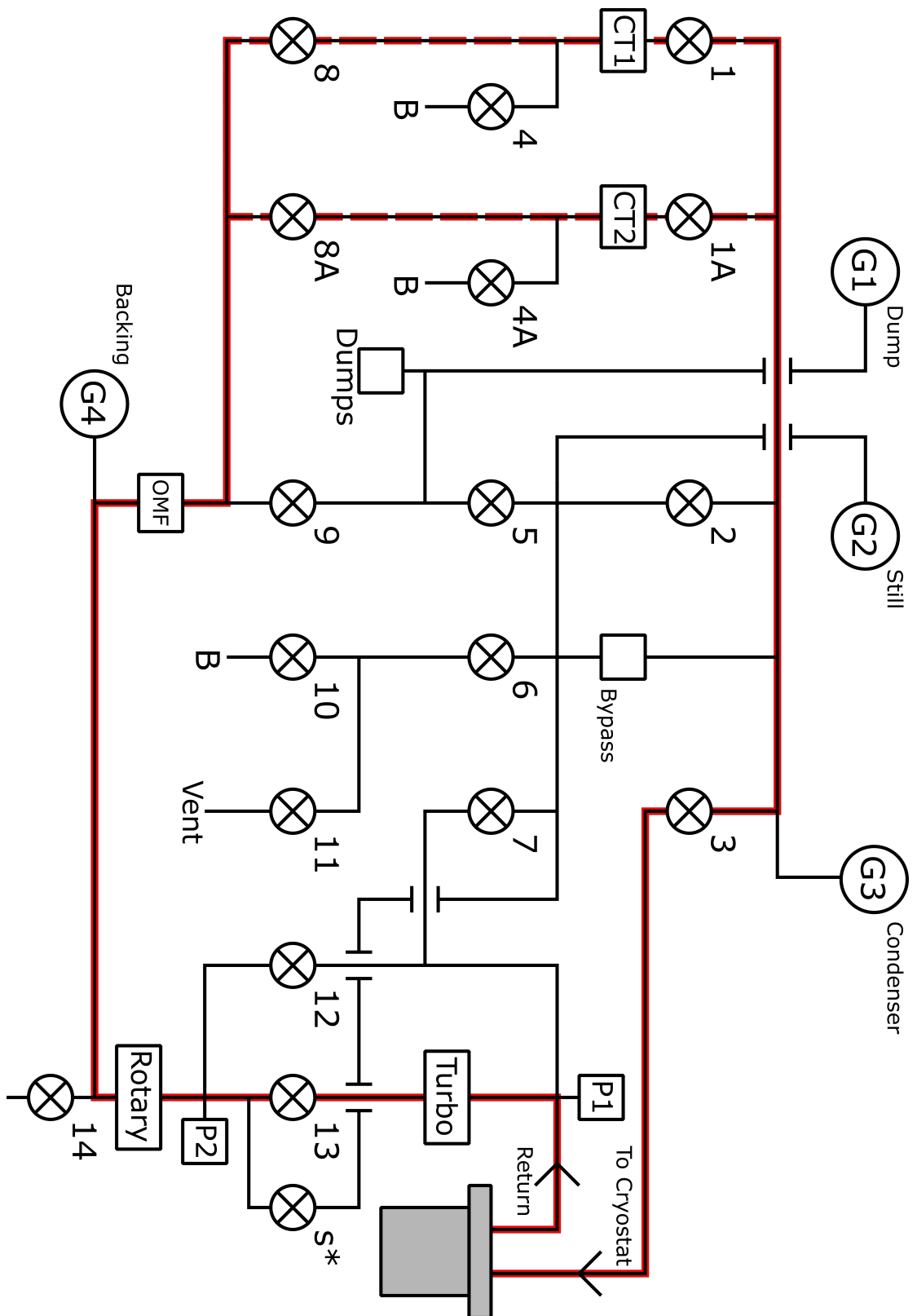


Figure D.1: ³He pumping system, inside of fridge not shown.

G1-4 are pressure gauges from 0 - 1000 mbar. P1 is the pressure in front of the turbo measuring pressure down to 1×10^{-3} mbar, and P2 is the pressure behind the turbo

/ in front of the ^3He rotary and measuring pressure down to 1×10^{-2} mbar. The ‘Vent’ labelled section ends in an external KF flange allowing a pumping trolley to be attached. This allows the pumping out of any air in the system and the cleaning of the cold traps through the connected ‘B’ system. All valves bar 14 are found on the main ^3He gas handling board along with all pressure gauges. There are two dumps to help extraction of all mix and to avoid overpressure within the system.

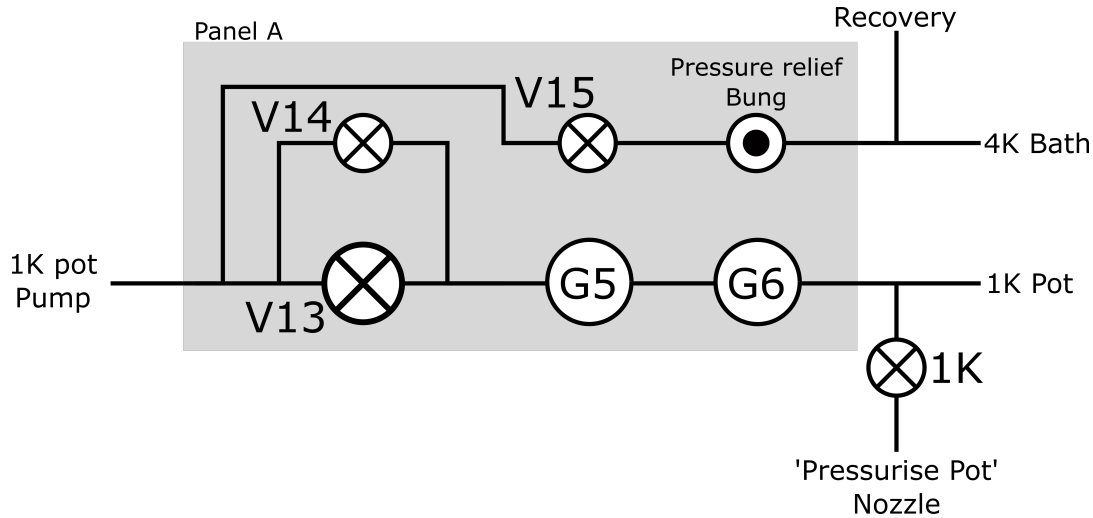


Figure D.2: 1K pot pumping system, which is linked to the 4K helium bath.

Figure D.2 shows the gas handling system for the 1K pot pumping line outside the OVC. It also shows a section of the ^4He recovery system, for the recycling of ^4He used for the 4K bath and 1K pot. The bath is connected to the pressure relief bung at all times which prevents overpressure at around 1.5 bar, though this safety feature is mainly used to protect the OVC when pressuring the bath to blow out LN_2 . When full of liquid ^4He the bath is also left open to the recovery, creating a path for boil off. G5 is the rough 1K pot gauge from 0 - 1000 mbar whilst G6 is the fine gauge from 25 0 Torr. The 1K pot pump is housed beneath the fridge in the pit, and the recovery leads through gas meters and to the cryogenics facility where the ^4He is re-liquefied.

Appendix E: Hermetic Pin Solder Recipe

290-02G glass bead seals were used, in holes drilled by specialised drill piece *T-291-4*. The pins were connected to using *214-522SF* super SMA jacks which are mounted by small screws either side, which are also used by the solder tool *T-212-5*, having similar form to the SMA jack.

Once the correct hole profiles are drilled the beads must be soldered in place. This process is designed for non-accessible specific solder split rings, so to achieve a hermetic seal while maintaining a good impedance match requires careful handling. The current process used in the lab is:

- Heat copper piece with holes on hot plate to 100°C (the copper piece with holes is to allow the coupling pins to stick down without the base of the hot plate pushed the beads out).
- Apply acid flux to brass drilled hole.
- Place brass piece on top of the copper and allow the flux to fully melt.
- Remove the brass piece, clean with IPA and allow to cool.
- Heat hot plate and copper to 300°C.
- Place brass piece onto another room temperature copper piece with holes such that beads can be fully inserted (long pin down).
- With the bead in place create a solder wire split ring by wrapping around the insert part of the solder tool and cutting.
- With solder tool place this ring over bead and use a wooden stick to push it into the groove around the bead.
- Repeat this process until three rings have been pushed into the groove, flux can be applied lightly to the rings.
- The solder tool can be screwed on to push the last split ring into place.
- Once the last ring is in place use a cotton bud to remove any excess flux.
- Tighten the solder tool onto the piece and place onto the hot plate.

- Leave for ~5 mins or until the solder tool is hot enough to melt solder on contact.
- Remove the piece from the hot plate and cool by dipping edge in water (not getting the feedthrough area wet).
- Remove the solder tool when cool and clean with IPA.
- Gaps in the solder join can be filled by placing a small amount of solder and flux into the area and placing back on the hot plate.
- Excess solder spilling out onto the brass can be carefully filled away without affecting the impedance matching, provided the outer metal of the bead is not damaged.

0.23 mm diameter tin-silver solder is used with a melting point of 217 °C, 300 °C is used as the solder must be heated through the copper and brass pieces. This soldering can also be performed inside a helium / nitrogen environment when soldering into copper to prevent oxidation.

Appendix F: Transparent Bonding Pictures



Figure F.1: Four chip pieces (to create two full chips), suspended on Nalgene forceps into a beaker of 1165 remover, which is itself in a heated bath with sonication. This method was used also for cleaning individual chips with IPA and DI.

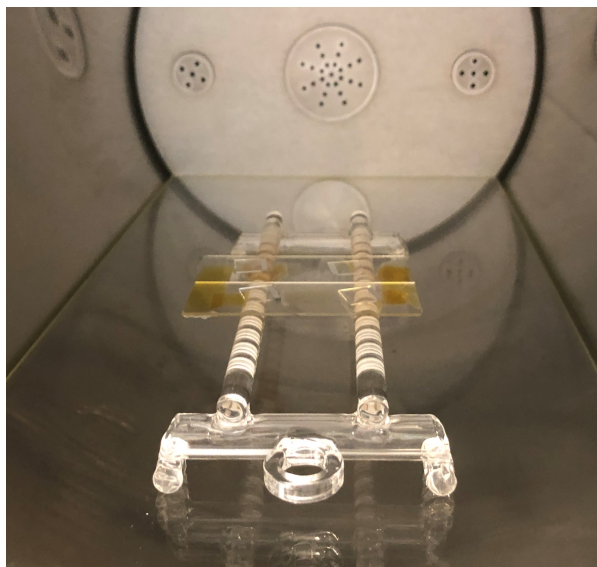


Figure F.2: Four chip pieces (to create two full chips), placed on a quartz chip holder, within the Diener Plasma Asher, ready to be plasma activated prior to bonding.

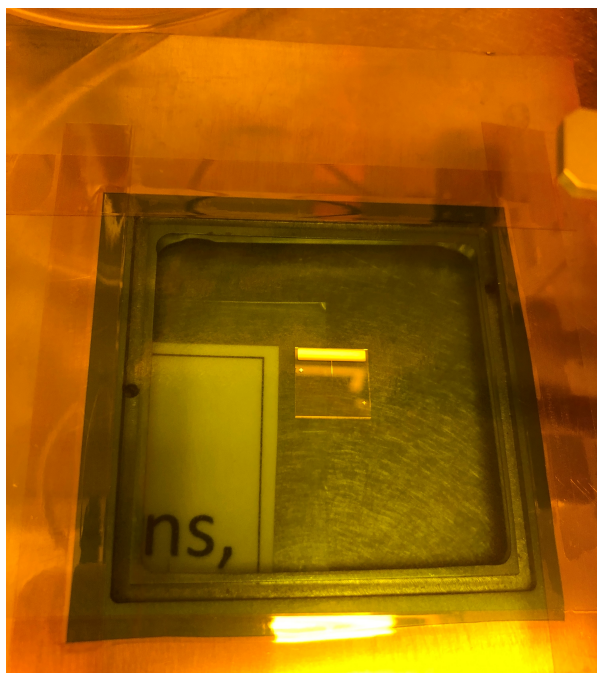


Figure F.3: Chip piece held on bonding tape, which it Kapton taped to the photomask holder of the mask aligner used for bonding. Ready to be flipped and inserted under the aligner microscope.

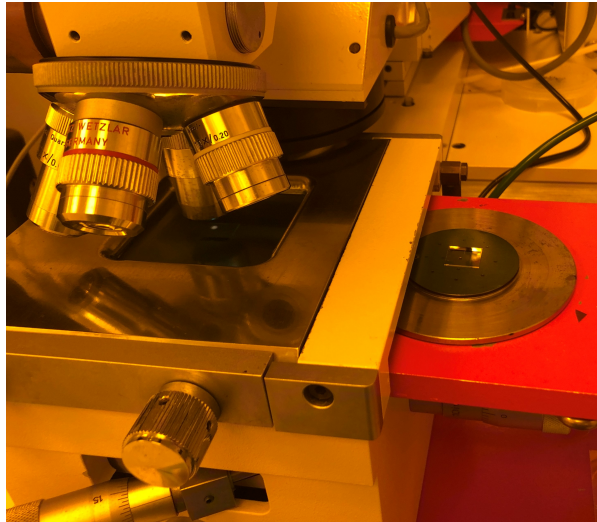


Figure F.4: Mask aligner used for bonding. Top chip piece is suspended facing downwards under the microscope. The bottom chip piece can be seen on the chuck on the right. Care must be taken with the vacuum settings when bonding.